

2015-01-21

Improved GNSS Carrier Phase Tracking for Hand Held Receivers

Bhaskar, Srinivas

Bhaskar, S. (2015). Improved GNSS Carrier Phase Tracking for Hand Held Receivers (Doctoral thesis, University of Calgary, Calgary, Canada). Retrieved from <https://prism.ucalgary.ca>. doi:10.11575/PRISM/26478
<http://hdl.handle.net/11023/2011>

Downloaded from PRISM Repository, University of Calgary

UNIVERSITY OF CALGARY

Improved GNSS Carrier Phase Tracking for Hand Held Receivers

by

Srinivas Bhaskar

A THESIS

SUBMITTED TO THE FACULTY OF GRADUATE STUDIES
IN PARTIAL FULFILMENT OF THE REQUIREMENTS FOR THE
DEGREE OF DOCTOR OF PHILOSOPHY

GRADUATE PROGRAM IN GEOMATICS ENGINEERING

CALGARY, ALBERTA

JANUARY, 2015

© Srinivas Bhaskar 2015

Abstract

Despite constituting a prime portion of GNSS applications, pedestrian hand held users still cannot achieve centimetre-level carrier phase based solutions; rather, they currently provide code phase based metre-level solutions. The limiting factors that inhibit the provision of kinematic solutions include poor antenna quality, harsh operating environments, poor receiver components, especially low-cost oscillators, to name a few. Many of these factors needs to be addressed to improve the performance of kinematic solutions to hand held users.

To this end, the first phase of this research is aimed at understanding the pedestrian GNSS signal propagation channel. A study of the effects of pedestrian dynamics on GNSS signal parameters, namely carrier frequency and phase, is conducted. A theoretical relationship is established between the dynamics measured by inertial sensors and GNSS signal parameters, also considering the oscillator g -sensitivity, and verified empirically using live GPS L1 C/A signals. Considering this relationship, pedestrian dynamics is characterized using appropriately processed inertial sensors data to understand the effects on GNSS signal parameters. The oscillator g -sensitivity and line-of-sight dynamics are identified to be two major sources of carrier phase disruptions. Pedestrian dynamics are characterized in the frequency domain in terms of power spectral densities and cumulative spectral densities. One of the important results of this research phase is that the pedestrian dynamics exhibit quasi-periodicity; this is proven to be useful in developing improved tracking architectures that reduce the impact of pedestrian dynamics in subsequent research phases. A study of signal attenuation due to the presence of human body is also conducted and impact of such attenuation on the

carrier phase tracking performance is empirically measured. The second phase of this research addresses oscillator g -sensitivity issues. Existing theoretical models are used to quantify the carrier frequency perturbations due to changes in acceleration. A method of laboratory calibration of g -sensitivity using GPS signals is employed. A novel tracking architecture that compensates for g -sensitivity induced carrier frequency perturbations using accelerometers measurements via feed-forward correction is proposed. The method is tested using live GPS L1 C/A signals in a pedestrian environment with various accelerometer specifications ranging from tactical to MEMS grade. Performance is also evaluated for vehicular navigation.

The third phase of this research results in a novel tracking architecture that measures pedestrian dynamics and implements a feed-forward compensation technique. A simple short term Fourier transform based technique is used to isolate harmonics inherent to pedestrian dynamics and predict the dynamics ahead of time. The prediction is proven useful in delivering improved carrier phase tracking performance, again, evaluated with live GPS signals. The final phase of the research performs a comparative analysis of carrier phase continuity in pedestrian environment between a software-defined receiver and a survey-grade receiver. It is also demonstrated, by comparing kinematic solutions performance, that a software-defined receiver can also deliver comparable performance to a commercial survey-grade receiver when properly tuned.

Overall, this thesis is aimed at addressing some of the key issues arising in pedestrian environments that are detrimental to carrier phase tracking, so that GNSS receiver design progresses one step closer to the possibility of ubiquitous kinematic solutions.

Preface

This thesis, in part, contains materials from three previously published conference papers and one journal paper that are referenced below.

Bhaskar, S. (2014) "Exploiting quasi-periodicity in receiver dynamics to enhance GNSS carrier phase tracking," *in Proceedings of ION GNSS+2014*, Tampa, FL, 08-12 Sep, The Institute of Navigation, 15 pages

Bhaskar, S., J. T. Curran and G. Lachapelle (2014) "Improving GNSS Carrier Phase Tracking via Oscillator g-Sensitivity Compensation," accepted for publication in *IEEE Transactions on Aerospace and Electronic Systems*, in press

Bhaskar, S., J. T. Curran and G. Lachapelle (2013) "Optimal PLL Design for Pedestrian Hand-Held GNSS Receivers," *in Proceedings of National Conference on Applications and Challenges in Space Based Navigation*, Indian Space Research Organization, Bangalore, April 17-18, 6 pages

Bhaskar, S., J. T. Curran and G. Lachapelle (2012) "Effect of Oscillator Quality on Ultra-Tight GPS/INS Aided Carrier Phase Tracking," *in Proceedings of ION GNSS 2012* , Nashville, TN, 18-21 Sep, The Institute of Navigation, 11 pages

Acknowledgements

Firstly, I express my sincere gratitude to my supervisor, Professor Gérard Lachapelle, for his continuous support and guidance throughout my doctoral studies. I was fortunate to have my graduate studies done under his vast expertise. He was never short of motivating words that encouraged me to succeed in my research. His constant appreciation of the research progress further motivated me to improve the quality of the thesis.

My sincere thanks to my co-supervisor Dr. James Curran for sharing his knowledge in signal processing, for all the time and patience invested in technical discussions, which were mostly spent answering basic questions. His research curiosity and ability to generate new ideas served as an engine of motivation during my doctoral studies. Thank you, James.

I also thank Dr. Tao Lin for being my advisor and for his technical discussions.

Dr. Jayanta Kumar Ray and Murali Krishna are acknowledged for suggesting to pursue my studies in the PLAN group. I thank Accord Software & Systems Pvt. Ltd, India for introducing me to the field of GNSS through interesting projects.

My past three+ years has been an enjoyable experience in Calgary. I thank past and current students of the PLAN Group for providing a friendly atmosphere during my studies. I thank Dr. Pratibha Anantharamu and Dr. Shashank Satyanarayana for helping me during the initial days of my arrival in Calgary. Thanks to Dr. Vyasraj Gururao for providing additional motivation to pursue my research. I acknowledge the help of many students in data collections and processing, my apologies for not mentioning all their names. Vimal is specially acknowledged for his efforts on the carrier phase positioning software. A special thanks to Anup, Billy, Rasika, Naveen, Rakesh, Vimal, Vijay, Suvarna,

Sujay, Niranjana, Shruthi, Thyagaraja, Ranjeeth, Ashwitha, Ahmad, Nahal, Aruna, Samtha, Tantry, Shashi and Pavana for providing me with a “home away from home” experience. I was fortunate to have you guys as friends for life!

Alberta Innovates Technology Futures are acknowledged for their financial support during my studies.

Finally, I thank my parents and my entire family for their boundless love, support and encouragement.

Table of Contents

Abstract	ii	
Preface	iv	
Acknowledgements	v	
Table of Contents	vii	
List of Tables	xi	
List of Figures and Illustrations	xii	
List of Abbreviations	xvii	
List of Symbols	xix	
CHAPTER ONE: INTRODUCTION TO PEDESTRIAN HAND-HELD GNSS		
RECEIVERS	1	
1.1 An overview of GNSS signal propagation	2	
1.2 Satellite-based non-idealities	4	
1.2.1 Satellite output power	4	
1.2.2 Satellite output bandwidth	4	
1.2.3 Satellite antenna Design	5	
1.2.4 Satellite clock stability	6	
1.2.5 Equipment group delay	6	
1.2.6 Satellite orbital errors	7	
1.3 Environmental effects	7	
1.3.1 Ionospheric effects	8	
1.3.2 Tropospheric effects	9	
1.3.3 Multipath	10	
1.3.4 Signal attenuation	11	
1.3.5 Line-of-sight dynamics	12	
1.3.6 Interference	12	
1.4 Receiver-based non-idealities	14	
1.4.1 Receiving antenna	14	
1.4.2 Thermal noise	15	
1.4.3 Front-end filtering and quantization	16	
1.4.4 Local oscillator	17	
1.5 Literature survey related to pedestrian GNSS receivers	18	
1.6 Limitations of previous work	25	
1.7 Objectives and contributions	28	
1.8 Assumptions on data collection and processing	28	
1.9 Thesis flow and organization	29	
CHAPTER TWO: GNSS SIGNAL PROCESSING AND CARRIER PHASE TRACKING		32
2.1 Introduction	32	
2.2 GNSS signal structure	32	
2.2.1 Received signal power	34	
2.2.2 Navigation data	34	
2.2.3 Spreading code	35	
2.2.4 Carrier	36	

2.3 An overview of receiver signal processing	37
2.3.1 The front-end	38
2.3.1.1 Antenna.....	38
2.3.1.2 Low Noise Amplifiers	39
2.3.1.3 Band Pass Filters	40
2.3.1.4 Down-conversion to Intermediate Frequency.....	40
2.3.1.5 Reference oscillator	41
2.3.1.6 Sampling and ADC	41
2.3.1.7 Signal model at the RF front-end output	42
2.3.2 Baseband signal processing	46
2.3.2.1 Signal acquisition	46
2.3.3 Navigation signal processing	48
2.4 Fundamentals of GNSS signal tracking.....	49
2.4.1 Code lock loop	52
2.4.2 Carrier lock loop.....	53
2.4.2.1 Phase lock loop.....	53
2.4.3 Kalman filter-based tracking	54
2.4.3.1 Dynamic performance of Kalman filter	58
2.5 Benefits of carrier phase tracking	58
2.6 Tracking performance indicators	59
2.6.1 C/N_0 as a tracking performance indicator.....	59
2.6.2 Phase Lock Indicator (PLI).....	61
2.6.3 Frequency Lock Indicator.....	63
2.7 Summary	64
CHAPTER THREE: PEDESTRIAN ENVIRONMENT CHARACTERIZATION	66
3.1 Introduction.....	66
3.2 Dynamics Characterization	66
3.2.1 Accelerometer model	67
3.2.2 Time series analysis	68
3.2.3 Interpolation to get uniformly sampled data	70
3.2.4 Double integration of acceleration.....	71
3.2.5 Estimation of power spectral density.....	72
3.2.6 Resolution versus spectral dynamic range trade-off	74
3.2.7 Spectrum analysis of pedestrian dynamics	76
3.2.8 Pedestrian dynamics and GNSS signal parameters	87
3.3 Effect of human attenuation of GNSS signals on carrier phase tracking ...	93
3.3.1 Data collection setup.....	94
3.3.2 Signal attenuation analysis	95
3.4 Summary	99
CHAPTER FOUR: OSCILLATOR G-SENSITIVITY EFFECTS ON GNSS CARRIER PHASE TRACKING	101
4.1 Introduction.....	101
4.2 Laboratory calibration of oscillator g -sensitivity	101
4.3 Proposed compensation technique.....	105
4.4 Experimental validation.....	109

4.4.1 Demonstrating g-sensitivity compensation.....	111
4.4.2 Isolating oscillator induced carrier disruptions	115
4.4.3 Vehicular navigation.....	116
4.4.4 Navigation domain performance analysis	119
4.4.5 Phase tracking sensitivity and cycle slips	121
4.5 Design considerations	123
4.5.1 Accelerometer quality	124
4.5.2 IMU data rate	125
4.5.3 IMU and oscillator g-sensitivity calibration	126
4.6 Summary	128
CHAPTER FIVE: PEDESTRIAN DYNAMICS PREDICTION	
EXPLOITING QUASI-PERIODICITY.....	129
5.1 Introduction.....	129
5.2 Proposed dynamics compensation technique	129
5.2.1 A few possible alternatives to STFT.....	138
5.3 Experimental validation with LOS dynamics only	139
5.3.1 Experimental setup and data processing	139
5.3.2 Performance demonstration.....	143
5.3.3 Heuristic cycle slip detection	148
5.3.4 Effect of dynamic compensation on the noise equivalent bandwidth	151
5.4 Details of the prediction algorithm	152
5.5 Influence of observation data length and feed-forward gain	156
5.6 Performance evaluation in regular pedestrian environments.....	160
5.6.1 Experimental validation with LOS dynamics and oscillator g-sensitivity	161
5.6.2 Compensation with low-cost equipment across pedestrian subjects.....	164
5.7 Summary	166
CHAPTER SIX: INVESTIGATION OF KINEMATIC POSITIONS	
FOR PEDESTRIAN RECEIVERS.....	167
6.1 Introduction.....	167
6.2 Cycle slips analysis using known receiver location.....	167
6.3 Phase rate method	180
6.3.1 Limitations of phase rate method	182
6.4 Kinematic positioning.....	185
6.5 Effect of human proximity on carrier phase residuals	193
6.6 Summary	195
CHAPTER SEVEN: CONCLUSIONS AND FUTURE RECOMMENDATIONS..	197
7.1 Conclusions	197
7.1.1 Characterization of pedestrian Environment	197
7.1.2 Oscillator g-sensitivity effects on GNSS carrier phase tracking	199
7.1.3 Exploiting quasi-periodicity in pedestrian dynamics	201
7.1.4 Investigation of kinematic solutions for pedestrian receivers	203

7.2 Recommendations for future work	204
7.2.1 Pedestrian environment characterization	204
7.2.2 Oscillator g-sensitivity compensation	205
7.2.3 STFT based dynamics prediction.....	206
7.2.4 Kinematic solutions in a pedestrian environment.....	207
REFERENCES.....	208

List of Tables

Table 1-1 Signal attenuation in dB for various antenna types and locations	20
Table 3-1 Accelerometer Specifications	68
Table 3-2 Datasets corresponding to dynamics characterization	77
Table 4-1 Measured g -sensitivity for a selection of oscillators	105
Table 4-2 Data collection scenarios	110
Table 4-3 Velocity component standard deviations for scenario B.....	120
Table 5-1: Datasets collected with various pedestrian motions.....	140
Table 5-2 Comparison of the mean power in the Doppler process, when the pedestrian is in motion, with mean powers in individual harmonics for PRN 14, normalized for the dominant harmonic.	154
Table 5-3: Datasets with regular pedestrian motion with various patterns and antenna placements.....	161

List of Figures and Illustrations

Figure 1-1 Illustration of pedestrian GNSS signal propagation channel	3
Figure 1-2 Thesis flow chart – flow of information across chapters.....	30
Figure 2-1 Generic block diagram of a GNSS receiver	37
Figure 2-2 Schematic representation of two dimensional acquisition search space.....	48
Figure 2-3 DRC process corresponding to i^{th} satellite signal.....	50
Figure 2-4 Basic components of a GNSS scalar tracking loop architecture	52
Figure 2-5 Traditional code tracking with early, prompt and late correlator arms	53
Figure 2-6 PLI simulation results using Matlab™ and a hardware GNSS simulator.....	62
Figure 3-1 Acceleration patterns based on the pedestrian motion mode for pocket data	69
Figure 3-2 Acceleration patterns based on the pedestrian motion mode for wrist dataset	70
Figure 3-3 (a) The plot shows that the durations between successive samples are non-uniform; (b) the effect of interpolation on acceleration measurements is shown for a portion of the pocket dataset - interpolation is used to obtain uniformly sampled signal.....	71
Figure 3-4 Welch's method of spectrum estimation of a random process	73
Figure 3-5 (a) spectral properties of window functions (b) Effect of windows on spectral estimation	75
Figure 3-6 Spectrogram corresponding to datasets containing several motion modes .	77
Figure 3-7 Data collection setup showing sensor locations and data collection scenarios.....	78
Figure 3-8 Acceleration process over time corresponding to all datasets; the colors blue, green and red represent X, Y and Z-axis respectively.....	79
Figure 3-9 PSDs of position, velocity and acceleration corresponding to all datasets; blue, green and red represent the X, Y and Z-axis.....	83
Figure 3-10 Cumulative power distributions of position, velocity and acceleration corresponding to all datasets; blue, green and red represent the X, Y and Z-axis .	84

Figure 3-11 (a) position, (b) velocity and (c) acceleration bandwidths and total measured power for all datasets; blue, green and red represent the X, Y and Z-axis.....	86
Figure 3-12 Data collection setup, location and skyplot used to establish relationship between processed inertial sensors data and GNSS carrier signal.....	89
Figure 3-13 PSDs and CSDs of carrier frequency and phase processes due to receiver dynamics	92
Figure 3-14 Individual contribution of g -sensitivity and LOS receiver dynamics.....	93
Figure 3-15 Data collection setup used for human attenuation characterization	94
Figure 3-16 Variations in C/N_0 and carrier phase misalignments for selected antenna levels.....	95
Figure 3-17 Trade-off between dynamic response of signal variations versus smoothness.....	98
Figure 3-18 The <i>maximum (blue)</i> , <i>mean (red)</i> and <i>minimum (black)</i> values of C/N_0 and phase misalignment variations. The statistics are computed across 6-7 available satellites for the corresponding antenna level as per	98
Figure 4-1 Observed GPS L1 frequency change corresponding to the 2- g tip-over test conducted for each axis of the Morion MV89A OCXO	104
Figure 4-2 Generic block diagram of a GNSS receiver supporting scalar-based, vector-based or ultra-tight architecture with optional g -sensitivity compensation .	106
Figure 4-3 Equipment configuration for pedestrian data collection in Scenarios A and B.....	113
Figure 4-4 Carrier phase tracking performance of the scalar and ultra-tight receivers with and without oscillator compensation for scenario A for PRN 8	113
Figure 4-5 (a) Mean PLI values for all satellites in view for various receiver configurations in Scenario A (b) Estimated carrier frequency for various receiver configurations in the same scenario.....	114
4-6 Carrier phase tracking performance of the scalar receiver with and without oscillator g -sensitivity compensation for scenario B for PRN 8	116
Figure 4-7 (a) Equipment configuration for vehicular navigation data collection, (b) Norm of three-dimensional velocity errors for the g -sensitivity isolated dataset...	118
Figure 4-8 Phase tracking performance of the scalar and ultra-tight receivers with and without oscillator compensation for scenario C	118

Figure 4-9 Carrier phase cycle-slip test statistics for selection of spectral density values for compensated and uncompensated receivers in Scenario B	122
Figure 4-10 PLI for selection of spectral densities depicting phase misalignment below the phase-lock threshold for compensated receiver in scenario B	123
Figure 4-11 (a) PLI values for scenario A with no compensation and with compensation using HTC and LCI IMUs (b) Corresponding pedestrian accelerations recorded by LCI and HTC IMUs	125
Figure 4-12 Mean PLI value versus IMU data rate for a selection of IMUs examined in both Scenario A and B.....	126
Figure 4-13 Maximum observed phase errors for a receiver operating in Scenario B for a range of scale factor calibration errors	128
Figure 5-1 Proposed tracking architecture illustrated as an augmentation to the traditional tracking architecture	132
Figure 5-2 Details of STFT-based feed-forward compensation algorithm	133
Figure 5-3 (a) Test setup to isolate the effect of pedestrian dynamics on carrier signal from other sources (b) Computation of differential residual ranges due to satellite motion for the given baseline	142
Figure 5-4 PLI corresponding to PRN 14 for Scenario-A and Scenario-B datasets	144
Figure 5-5 C/N ₀ corresponding to PRN 14 for Scenario-A and Scenario-B datasets ..	145
Figure 5-6 Between-receivers difference Doppler corresponding to PRN 14 Scenario-A dataset for the compensated and uncompensated receivers	145
Figure 5-7 (a) Mean PLI and (b) Mean C/N ₀ for all satellites in view for Scenario-A and Scenario-B datasets	146
Figure 5-8 Mean PLI and C/N ₀ for all satellites in view corresponding to the Scenario-C dataset	147
Figure 5-9 Carrier phase between-receivers single difference plots for all satellites in view corresponding to Scenario-A dataset for various feed-forward gains.....	149
Figure 5-10 Carrier phase between-receivers single differences for PRN 14 serving as qualitative cycle slip test statistics	152
Figure 5-11 Time variation of the Doppler process and its corresponding PSD for a portion of Scenario-A dataset for PRN 14	153
Figure 5-12 (a) Time-variation and (b) Time-correlation of dominant frequency components for PRN 14 corresponding to Scenario-A dataset	153

Figure 5-13 Variation of mean phase error over various input data lengths for feed-forward gains namely (a) 0.2, (b) 0.4 and (c) 0.6 for dataset Scenario-A. Losses-of-lock were observed for a feed-forward gain of 0.8.	158
Figure 5-14 LOS Doppler variation patterns across satellites as a function of satellite locations.....	159
Figure 5-15 PLI and C/N_0 plots corresponding to Ped-A dataset for PRN 14.....	161
Figure 5-16 Mean PLI and C/N_0 values computed across all visible satellites for regular pedestrian motion datasets	163
Figure 5-17 Mean PLI and C/N_0 values computed across all visible satellites for different pedestrian subjects corresponding to Ped-D datasets	165
Figure 6-1 (a) Antenna snap-locking device used to precisely locate the pedestrian antenna (b) Pedestrian exhibited hand held dynamics during data collection.....	170
Figure 6-2 Differential GPS data collection setup to detect and quantify cycle slips in pedestrian hand held environment	171
Figure 6-3 Phase difference plots for NovAtel receiver described by Eq. 6-3 shown with gradual reduction in vertical scales from the top to the middle to the bottom subplots.....	173
Figure 6-4 Phase difference plots for the modified GSNRx TM receiver, as described by Eq. 6-3 shown with gradual reduction in vertical scales from the top to the bottom subplots.....	174
Figure 6-5 Raw and filtered C/N_0 values corresponding to PRN 27 computed from correlation values output by GSNRx TM	177
Figure 6-6 Correlation values corresponding to PRN 27 obtained from GSNRx TM	177
Figure 6-7 Acceleration norm for the time duration corresponding to the spikes observed in correlation values and C/N_0 . IMU time was manually synchronized with GPS time and deemed sufficient for the analysis conducted herein	177
Figure 6-8 A short portion of accelerations in the pedestrian antenna-frame corresponding to the third dynamic segment.....	180
Figure 6-9 Phase rate test statistic for PRN 5 for pedestrian receivers and corresponding PDFs under static and dynamic conditions.....	183
Figure 6-10 Carrier frequency process for PRN 5 for the pedestrian receiver.....	184
Figure 6-11 Overview of the flow of software developed for kinematic solution analysis and the flow chart for recursive ambiguity resolution.....	186

Figure 6-12 Position differences obtained from float solutions when the antenna was static at its initial location..... 187

Figure 6-13 Position differences are shown for float solutions after convergence. No noticeable jumps in positions when one half cycle slip happened for PRN 27, but the overall divergence of float solution is apparent 188

Figure 6-14 Position differences obtained from fixed kinematic solution with NovAtel and GSNRx™ observations at (a) full scale and (b) magnified vertical scales. Notice the change of unit from metres in (a) to centimetres in (b)..... 191

Figure 6-15 Least-squares phase residuals corresponding to two versions of GSNRx™ measurements. The base satellite used was PRN 29 in both cases.. 192

Figure 6-16 Number of satellites used for fix, HDOP and VDOP corresponding to NovAtel and GSNRx™ receivers..... 192

Figure 6-17 Least-squares phase residuals for three pedestrian-antenna distances corresponding to Novatel receiver..... 195

List of Abbreviations

ADC	Analog to Digital Converter
AGC	Automatic Gain Controller
AWGN	Additive White Gaussian Noise
BER	Bit Error Rate
BPF	Band Pass Filter
C/A	Coarse/Acquisition
C/N ₀	carrier-to-noise-density ratio
CBOC	Composite Binary Offset Carrier
CDMA	Code Division Multiple Access
CSD	Cumulative Spectral Distribution
DCM	Direction Cosine Matrix
DD	Double-Difference
DRA	Dielectric Resonator Antenna
DSSS	Direct Sequence Spread Spectrum
ESA	European GNSS Agency
FLI	Frequency Lock Indicator
GEO	Geostationary Earth Orbit
GLRT	Generalized Likelihood Ratio Test
GNSS	Global Navigation Satellite Systems
GPS	Global Positioning System
GSM	Global System for Mobile
IDFT	Inverse Discrete Fourier Transform
INS	Inertial Navigation Systems
ITU	International Telecommunication Union
LAMBDA	Least-Squares AMBIGUITY Decorrelation Adjustment
LBS	Location Based Services
LHCP	left hand circularly polarized
LNA	Low Noise Amplifier
MA	Moving Average
MEMS	Micro-electro-mechanical systems

MEO	Medium Earth Orbit
MLE	Maximum Likelihood Estimation
MMSE	minimum mean squared error
NCO	numerical controlled oscillator
NEU	north east up
NLOS	Non-Line-Of-Sight
OEXO	Oven Compensated Crystal Oscillator
PLAN	Position, Location and Navigation
PLI	Phase Lock Indicator
PPP	Precise Point Positioning
PRN	pseudorandom number
PSD	Power Spectral Density
PVT	Position, Velocity and Time
RAIM	Receiver Autonomous Integrity Monitoring
RF	Radio Frequency
RHCP	right hand circular polarized
SNR	Signal-to-Noise Ratio
TCXO	Temperature Compensated Crystal Oscillator
TOA	Time of Arrival

List of Symbols

Symbol	Definition
r_a	Received analog signal at the antenna
t	Time variable
s_i	Incoming satellite signal of i^{th} satellite
η_a	Analog thermal noise
N_{sig}	Number of GNSS signals arriving at the antenna
P_i	Received signal power
d_i	Data bit
c_i	PRN code chip
τ_i	Transit delay
f_{C_i}	Centre frequency
θ_i	Carrier phase of the incoming analog signal
r_{IF}	Down-converted signal at IF
f_{IF}	IF frequency
$\theta_{i,IF}$	Signal phase at IF
η_{IF}	Analog noise at IF
r	Received signal in discrete-time
n	Discrete-time index
$\tilde{\tau}_i$	Transit delay in discrete-time samples
θ_i^{LOS}	LOS component of carrier phase
θ^g	Oscillator g-sensitivity induced carrier phase
θ^T	Temperature dependent carrier phase
θ^{ST}	Carrier phase variations due to oscillator short-term stability
θ^{LT}	Carrier phase variations due to oscillator long-term stability
θ_i^η	Random variations of carrier phase due to ionospheric effects
θ_i^0	Carrier phase arbitrary initial offset
$CN()$	Circular normal random variable
σ^2	Variance of a quantity
I_k	In-phase correlation value
Q_k	Quadrature correlation value
$\hat{\phi}_i$	Estimate of the carrier phase
$\hat{\tau}_i$	Estimate of the code delay
\hat{f}_{d_i}	Estimate of the carrier frequency
F_s	Sampling rate

N_0	Noise spectral density
k	Boltzmann constant
T_{coh}	Coherent integration period
$\text{sinc}(\)$	Sinc function
$\text{exp}(\)$	Exponential function
$R(\)$	PRN code autocorrelation function
$\arctan(\)$	Arc tangent function
δx	Kalman filter error state vector
z	Kalman filter observations vector
H	Kalman filter design matrix
Φ	Kalman filter state transition matrix
A	Signal amplitude
$\delta\tau$	PRN code delay error state
$\delta\phi$	Carrier signal phase error state
δf	Carrier signal frequency error state
δa	Carrier signal frequency-rate error state
Δt	Kalman filter update period
β	GPS L1 C/A code-to-carrier frequency ratio
Q	Kalman filter process noise matrix
R	Kalman filter measurement noise matrix
$\overline{\delta F}$	Average carrier frequency error over a loop update period
$\overline{\delta\Phi}$	Average carrier phase error over a loop update period
C / N_0	Carrier-to-noise-density-ratio
FLI	Frequency lock indicator
a_x	Accelerometer measurement along x axis
a_x^f	Specific force along x axis
$b_{a,x}$	Accelerometer bias along x axis
S_x	Accelerometer scale factor - x axis
N_{xy}	Non-orthogonality factor along x-y axes
$\eta_{a,x}$	Accelerometer noise – x axis
$S_{p_x p_x}^n(f)$	PSD estimate of a signal p_x
$\vec{\Gamma}$	3-dimensional g -sensitivity vector
\vec{a}_{NEU}	3-dimensional acceleration vector in NEU frame
R_{XYZ}^{NEU}	Rotation matrix from XYZ to NEU frame
$\ \vec{V}\ $	Norm of a 3-dimensional vector
\vec{A}	Acceleration vector in the oscillator frame
\vec{V}	Velocity vector in the oscillator frame

f_{OSC}	Actual frequency output of the local oscillator
g	Acceleration due to gravity
Δf	Feed-forward g-sensitivity frequency correction
$\Delta \dot{t}$	Feed-forward g-sensitivity code phase correction
$\vec{\Omega}$	Angular acceleration
T_{coh}	Coherent integration period
I_k^E	In-phase early correlation values
Q_k^E	Quadrature phase early correlation values
I_k^P	In-phase prompt correlation values
Q_k^P	Quadrature phase prompt correlation values
I_k^L	In-phase late correlation values
Q_k^L	Quadrature phase late correlation values
PLI_k	Phase lock indicator value computed from prompt correlation values
PLI_k^{MA}	Time averaged phase lock indicator value
$a_{(\bullet)}$	Acceleration measurements
$f_{a,(\bullet)}$	Specific force
$b_{a,(\bullet)}$	Measurement bias
$S_{(\bullet)}$	Scale factor error
N_{xy}	Non-orthogonally component
$\eta_{a,(\bullet)}$	White measurement noise
$F_{S,IMU}$	IMU data logging rate
\mathbf{a}	Three-dimensional acceleration vector
\mathbf{v}	Three-dimensional velocity vector
\mathbf{p}	Three-dimensional position vector
T_s	Sampling rate after interpolation
$\bar{\mathbf{q}}$	Sample mean vector
$\widehat{S}_{p_x p_x}^n(f)$	Estimated PSD of the data segment
w	Window function
$\widehat{S}_{a_x a_x}^n(f)$	PSD of x-axis acceleration process
$\widehat{S}_{v_x v_x}^n(f)$	PSD of x-axis velocity process
$\widehat{S}_{p_x p_x}^n(f)$	PSD of x-axis position process
f_i^{LOS}	LOS component of carrier frequency
f_i^η	Stochastic frequency disruptions based on signal propagation channel effects

f^g	Oscillator g-sensitivity induced frequency disruptions
f^T	Clock drift variations due to temperature
f^{ST}	Short term clock variations
f^{LT}	Long term clock variations
$f_i^{LOS,rx}$	Receiver LOS dynamics component
f_i^{Rx}	Total receiver dynamics dependent carrier frequency disruption on the i^{th} satellite
ε_i	Elevation angle of the i^{th} satellite
α_i	Azimuth angle of the i^{th} satellite
$\mathbf{v}_{rx,NEU}$	Receiver velocity vector in local-level NEU frame
$\vec{\Gamma}$	Local oscillator g-sensitivity vector
\vec{a}_{NEU}	Acceleration vector in the body frame
R_{XYZ}^{NEU}	Rotation matrix to convert from body frame to local-level frame
$\theta^g(\vec{A})$	Sensitivity of the local oscillator to applied acceleration
Δf_{2g}	Observed carrier frequency change due to 2 g acceleration
\vec{A}_{OSC}	3-axis acceleration in oscillator frame
$\dot{\tau}_o$	Nominal chipping rate of the GNSS signal
Δf	Carrier frequency correction factor
$\Delta \dot{\tau}$	Chipping rate correction factor
θ_{qp}^{rx}	Quasi-periodic carrier phase component due to LOS pedestrian dynamics
θ_{qp}^g	Quasi-periodic carrier phase component due to oscillator g-sensitivity
θ_{ap}^{rx}	Aperiodic carrier phase component due to LOS pedestrian dynamics
θ_{ap}^g	Aperiodic carrier phase component due to oscillator g-sensitivity
$\theta_{qp}^{rx,g}$	Quasi-periodic carrier phase component due to LOS pedestrian dynamics and oscillator g-sensitivity
$\theta_{qp}^{rx,g}$	Aperiodic carrier phase component due to LOS pedestrian dynamics and oscillator g-sensitivity
$\theta_{ap}^{rx,g,T,ST,LT,\eta}$	Other aperiodic carrier phase components
$f_{qp}^{rx,g}$	Quasi-periodic carrier frequency component due to LOS pedestrian dynamics and oscillator g-sensitivity
$f_{ap}^{rx,g,T,ST,LT,\eta}$	Other aperiodic carrier frequency components
\hat{f}_i	Carrier frequency estimate
$\eta_{\hat{f}_i}$	Error due to thermal noise effects in the estimated carrier frequency
$\widehat{F}_{i,k}[l]$	Sequence of DFT coefficients
$F_{S,STFT}$	Sampling frequency of the carrier frequency process

$S_{f_i,k} [l]$	PSD of the carrier frequency process
a_j^{FFT}	Amplitude of the selected harmonic
f_j^{FFT}	Frequency of the selected harmonic
ϕ_j^{FFT}	Phase of the selected harmonic
$\tilde{f}_i[k]$	Reconstructed carrier frequency process
α	Feed-forward correction gain
$\Delta\theta$	Carrier-phase single difference between the reference and pedestrian receiver
ΔN	Carrier-phase ambiguity
$\Delta\varepsilon_{MP,\theta}$	Error due to multipath
$\Delta\eta$	Error due to noise
$\delta\rho_{ped}$	Carrier-phase changes due to pedestrian motion
ρ_{ped}^{known}	Geometric range that corresponds to the known snap-locked location
ΔcdT_{const}	Clock-bias due to difference in receiver time initializations across reference and rover receivers
t_{ped}^{begin}	Pedestrian receiver switch-on time
t_{ref}^{begin}	Reference receiver switch-on time
$\delta\nabla\Delta\theta$	Double-difference carrier phase measurement
ζ_{CS}	Test statistic for cycle-slip detection
λ_{CS}	Cycle-slip detection threshold

Chapter One: Introduction to Pedestrian Hand-held GNSS Receivers

The use of Global Navigation Satellite Systems (GNSS) in hand-held receivers is becoming increasingly popular due to increased smartphone usage over the past decade. There are numerous applications for hand-held GNSS receivers which include personal navigation, geo-caching, tracking personal assets and people, search and rescue operations of individuals involved in high-risk professions, recovery of stolen items such as mobile phones and so on. Another category of GNSS receivers used in hand-held applications is the camera industry. GNSS receivers are being built-in to cameras for geo-tagging purposes. Interestingly, the GNSS market report by the European GNSS Agency (ESA) indicates that the smartphone market constitutes a growing prime share, of about 40% in the year 2010 to about 47% in 2013, of all the GNSS applications, which is predominantly due to ever increasing applications based on Location Based Services (LBS). The number of receiver units employed for LBS are expected to increase from one billion in 2013 to over two billions by the year 2019.

Although other methods such as inertial sensors, optical sensors, WiFi signals, etc., can be used for pedestrian navigation, GNSS is by far the favorite due to its long-term accuracy. The Global Positioning System (GPS) is the first and, currently, the most used GNSS. However, there are a number of significant issues which result in a deterioration of the navigation performance of hand-held pedestrian GNSS receivers, owing to their unique operating environment. These challenges limit the pedestrian GNSS applications to metre level code phase based positioning accuracy. In order to improve the pedestrian receiver design to provide centimetre level carrier phase based positioning accuracy, a

number of issues need to be addressed both at the product design level and at the signal processing level. This chapter provides a detailed introduction to the challenges involved in carrier phase tracking in pedestrian hand held GNSS receivers and describes the motivation for the research work presented in this thesis.

The remainder of this chapter is organized as follows. A brief introduction to GNSS is provided. The *non-idealities* associated with GNSS pedestrian signal propagation channel and their effects on carrier phase tracking are discussed. The term *non-idealities* is used in this thesis to describe the following: (a) undesirable signal propagation effects; (b) limitations of the system design and implementation; (c) effects which involve an element of chance and hence which are modeled as random processes. The existing methods to combat non-idealities are discussed. The motivation for the current research is derived from the challenges that are either inadequately met or where it is not feasible to employ existing solutions in pedestrian GNSS receivers. Finally, the chapter concludes with the thesis outline.

1.1 An overview of GNSS signal propagation

GNSS mainly consists of the space segment, the control segment and the user segment. The space segment is a network of time-synchronized satellites orbiting around the earth in precisely predictable paths. The control segment consists of several ground-based monitoring stations that accurately monitor the positions, health and clock correction parameters of satellites. The control segment also performs prediction of future satellite data required for navigation and periodically uploads to respective satellites via their telemetric channels. The satellites transmit navigation data by modulating them on their

allocated carriers. The transmitted data are demodulated by the user segment, which consists of a large number of GNSS receivers generally operating on or near the surface of the earth to provide Position, Velocity and Time (PVT) solution.

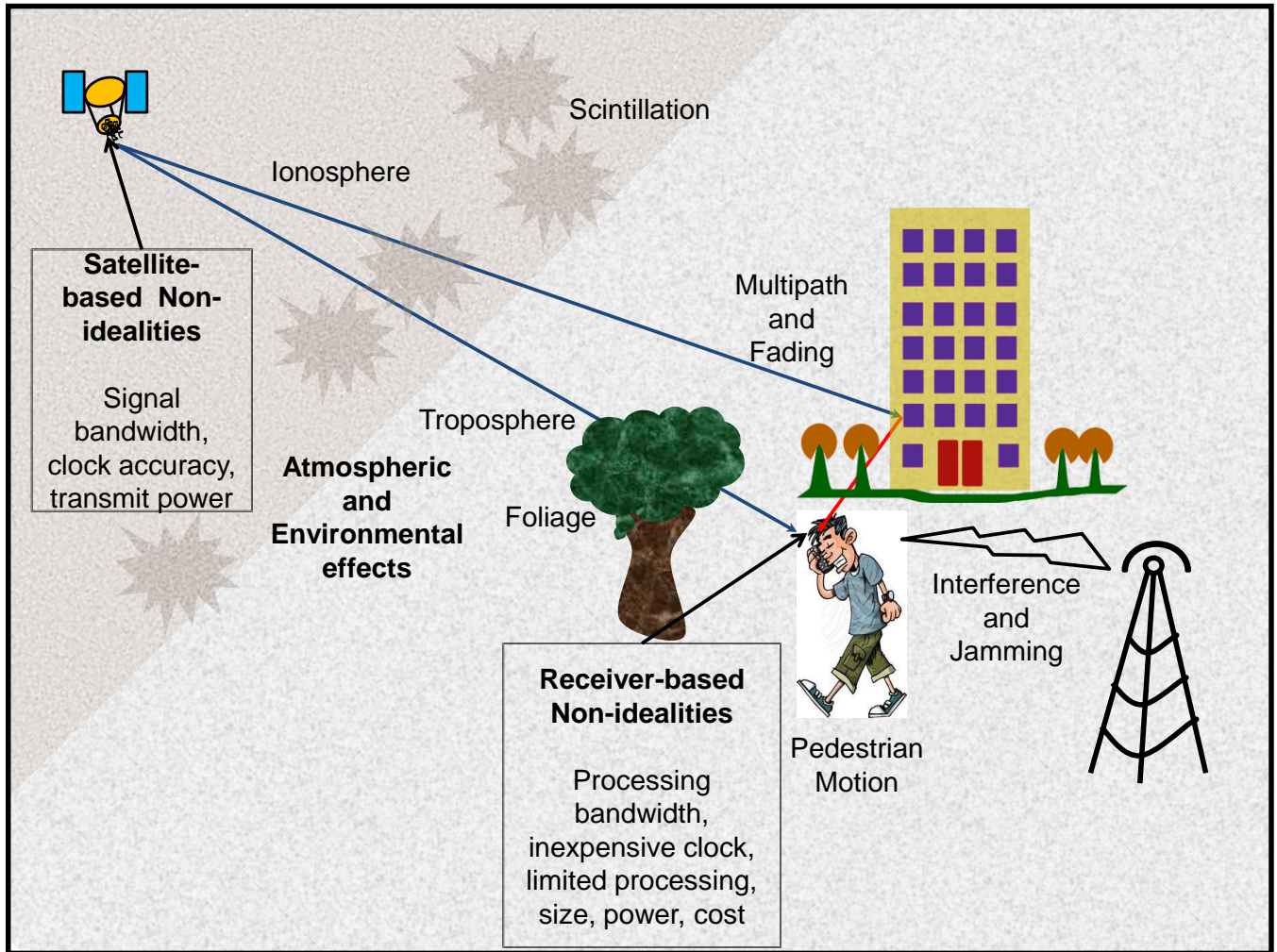


Figure 1-1 Illustration of pedestrian GNSS signal propagation channel

GNSS signal propagation is briefly explained in the following sections starting from the origin of signals — the satellites, until their final intended destination — the navigation solution in the receiver. GNSS signal propagation non-idealities can be broadly divided into the following sections as shown in Figure 1-1: (a) satellite-based non-idealities; (b)

atmospheric and environmental effects; (c) receiver-based non-idealities. The first category of non-idealities is typically negligible for pedestrian applications; however the other two require explicit mitigation techniques in the receiver design.

1.2 Satellite-based non-idealities

The satellite-based non-idealities include the constraints imposed on satellite design, which limits the operation of GNSS. The key issues which constrain the receiver design, albeit non-detrimental to navigation, are discussed below. Also mentioned are the ways receiver designers cope with respective constraints.

1.2.1 Satellite output power

The transmit power of a GNSS satellite is limited primarily due to two reasons: (a) firstly, the regulation by the International Telecommunication Union (ITU) limits the flux density generated by satellite-to-earth link to avoid interference with signals from other communication systems in the same frequency band. For example, in the 1.525-2.5 GHz frequency band used to transmit GPS L1 signals, the flux density limit is -154 dBW/m^2 (Spilker 1996a) (b) secondly, the cost involved in powering up the satellite in space limits the transmission power (Misra & Enge 2011). In order to cope with limited satellite output power, the receiver designers generally need to increase the signal-to-noise ratio at the receiver via enhanced coherent integration in the receiver assuming appropriate design choices of the receiver antenna gain, LNA and noise figure.

1.2.2 Satellite output bandwidth

Theoretically, GNSS signals occupy infinite bandwidths due to the presence of binary data and pseudorandom codes resulting in sharp carrier phase changes when they are

modulated onto the carrier signal. However, physically realisable systems have a finite bandwidth and this bandwidth constraint results in correlation losses depending on the amount of signal power being discarded by the transmitting antenna. For example, GPS L1 C/A signals are band-limited to a 20 MHz transmission bandwidth. However, it is shown that there is no significant performance deterioration as almost all signal power is confined for GPS L1 C/A to within 20 MHz (Spilker 1996a). It only bounds the theoretical limit on the possible correlator chip spacing during code phase tracking.

1.2.3 Satellite antenna Design

GNSS uses Right Hand Circular Polarized (RHCP) signals. The choice of circular polarization is mainly for the following reasons: (a) ionospheric Faraday rotation introduces a shift in the polarization of the signal. For circularly polarized signals the shift is merely rotation thus leaving the polarization of passing satellite signals unchanged. Consequently, the circular polarization does not put a constraint on the orientation of the receiver antenna, which is important as the angles of arrival of the multiple satellite signals are different and no satellite-based orientation is necessary for standard operation of GNSS receivers; (b) the RHCP signals have a distinct advantage from the linearly polarized signals that reflections either from ground or from nearby structures become either linearly polarized or left hand circularly polarized (LHCP) based on the dielectric constant of the reflecting surface (Dierendonck 1996). The gain of a well-designed RHCP antenna for LHCP signals is very low and hence this offers a built-in protection against single reflection multipath signals. However, due to the antenna design and manufacturing limitations it is difficult to build perfect RHCP antennas. In case of satellite antennas, the axial ratio, a measure of circularity of the antenna polarization, is

maintained within 1.2 dB for GPS antennas (Spilker & Parkinson 1996) thus deviating from the ideal RHCP axial ratio of 0 dB and hence incurring polarization mismatch losses. Although this loss is negligible for standard receiver operations, it can be compensated by increased signal processing gains.

1.2.4 Satellite clock stability

GNSS operates on the principle of Time of Arrival (TOA) ranging; the network of satellites should be time-synchronized to obtain accurate navigation solution. In this regard, atomic clocks used in satellites play a crucial role. Unlike ground control stations where the clocks can be regularly maintained and even relatively easily replaced, it is difficult to monitor on-board satellite clocks due to the distance and operating conditions. GNSS satellites generally have a redundant ensemble of atomic clocks consisting of rubidium and caesium based clocks. These clocks are radiation hardened as they should withstand heavy radiation storms mainly from the sun and the outer space. However, the satellites clocks instabilities in GNSS are only a few parts in 10^{12} per day (Parkinson 1996 and Daly et al 1991), and hence do not affect the standard signal processing performance of the receiver. The satellite time offsets from the standard GPS time, however, are regularly monitored by the control stations and transmitted to the user equipment through the navigation message.

1.2.5 Equipment group delay

The signal propagation delay through the satellite electronic circuitry from the frequency source to the transmission antenna is known as *equipment group delay*, which needs to be precisely known to the user receiver for accurate ranging. The equipment delay across different frequencies, such as L1 and L2, is known as *group delay differential* (GPS ICD

2012). The bias part of the equipment group delay is transmitted to receivers via clock correction parameters. However, the group delay uncertainties can cause ranging inaccuracies for single-frequency receivers. For example, for GPS receivers the group delay uncertainties can be up to 3.0 nanoseconds or 0.9 m (GPS ICD 2012). However, these errors can be cancelled via differential GNSS techniques.

1.2.6 Satellite orbital errors

The navigation message contains satellite orbital models, which are regularly revised by the control segment, to be used by user receivers to compute the satellite positions needed for PVT solution. However, the accuracy of these models dictates the overall positioning accuracy. A total of about 1.5 m of error prevails due to the orbital and satellite clock estimation in case of GPS (Misra & Enge 2011). However, these errors are easily removed by differential techniques by forming between-receivers difference measurements. Post-mission positioning applications have access to more accurate ephemeris data which are available for free from IGS products' data centres if required. However, for real-time applications another technique known as Precise Point Positioning (PPP) in the GNSS community provides real-time orbital and clock data among other corrections; for differential operations, transmitted orbits have sufficient accuracy for most applications.

1.3 Environmental effects

After the GNSS signal is converted to electromagnetic waves by the satellite transmitter antenna, it interacts with several particles on its way to the receiver antenna where it is converted into electrical signals again and transported to electronic circuitry for further

processing. Most of these interactions are detrimental to accurate navigation and hence it is necessary to understand these effects to help in appropriate receiver design.

1.3.1 Ionospheric effects

The ionosphere extends from 50 km to 1000 km approximately above the earth surface (Misra & Enge 2011) and it contains free ions which interact with the GNSS electromagnetic waves slowing down the code phase and navigation data, whereas advancing their carrier phase. The ionosphere is a dispersive medium, meaning the signal modulation delays and phase advances depend on the carrier frequency of the electromagnetic signals passing through the medium. These interactions cause group delay, phase advance, attenuation and phase distortions of GNSS signals passing through the ionosphere. Fortunately, these effects are predictable to a certain extent and can be accounted for in GNSS receivers. As such the ionosphere is not a significant source of GNSS signal attenuation always. However, in addition to these predictable effects the ionosphere exhibits spatially localized chaotic free-ion distribution referred to as *ionospheric scintillation*. Ionospheric scintillation causes unpredictable changes in the GNSS signal amplitude and phase which is responsible for some carrier and code tracking errors, sometimes leading to losses-of-lock (Fortes et al 2014, Ghafoori 2012, Klobuchar 1996). The ionospheric signal modulation delays and phase advances are handled in GNSS receivers by incorporating suitable models to estimate the ionospheric delays (Klobuchar 1996 and Angrisano et al 2013). It is also shown that differential GNSS positioning removes a major portion of delays introduced by the ionosphere depending on the baseline length and the significance of scintillation (Misra & Enge 2011). Owing to dispersive nature of the ionosphere, by appropriate frequency combinations of GNSS

measurements taken at various frequencies, the effect of ionospheric delays can be reduced (Klobuchar 1996). However, special signal processing methods are required to address scintillation in GNSS receiver at signal detection and tracking levels. One of the elementary methods to address the phase scintillation problem is to set the tracking loop bandwidth to an 'optimal' value so that the variation of the phase is appropriately handled by the tracking loop. Furthermore, a recent comparative study of scintillation effects during 2002 and 2013 solar maximums, conducted by Fortes et al (2014), shows that the carrier phase tracking performance has significantly improved due to enhanced receiver hardware and tracking algorithms.

1.3.2 Tropospheric effects

The troposphere is the lowest layer of the earth's atmosphere extending to about 12 km from the earth's surface (Spilker 1996a). The troposphere is not a significant source of GNSS signal attenuation. For GPS signals, the attenuation is mostly below 0.5 dB (Spilker 1996c). However, the total delay caused by troposphere can range from 2-25 m which must be taken into account while estimating navigation solutions. Unlike the ionosphere, the troposphere is a non-dispersive medium. The tropospheric delay can be further divided into the effects of dry and wet tropospheric components. The dry components constitute about 90% of the total delay and their modeling provides zenith delay estimation accuracies better than 1 cm. However, the wet tropospheric delay due to water vapour distribution along the GNSS signal path is highly variable. The zenith estimation accuracy of the wet delay is about 1-2 cm if local metrological data is used, about 5-10 cm if average metrological data is used. Although the estimation of zenith tropospheric delays is accurate to a few centimetres, the use of mapping functions to estimate the

delays for satellites at other elevation angles will contribute to increased estimation errors. It has been shown that 5-10 cm of residual errors in zenith delay estimates bloats up to about 0.5-1 m at a 5 degree elevation (Misra & Enge 2011). There are several models that are used to estimate the dry and wet tropospheric delays, such as Saastamoinen's (1973), Hopfield's (1969), etc. A survey of available tropospheric models is available in Shrestha (2003). In addition to models-based delay corrections, GNSS receivers can also obtain tropospheric corrections through SBAS satellites. Apart from using models, the tropospheric errors can be mitigated by using differential GNSS, specifically by performing between-receivers differencing. However, the achievable accuracy extensively depends on the length of the baseline, humidity and height differences between base station and rover receivers. In addition to tropospheric delays, tropospheric scintillations are caused by turbulence of troposphere. However, these scintillations result in a 0.9 dB RMS variation in signal power and hence are not a significant hurdle for GNSS signal processing (Spilker 1996c). The delays introduced by the ionosphere and troposphere do not affect the carrier phase tracking of GNSS signals. In contrast, the ionospheric amplitude and phase scintillations cause signal attenuation and carrier phase distortions, which must be handled by the receiver tracking algorithms.

1.3.3 Multipath

When GNSS receivers are operated in environments such as urban canyons and indoors the receiver antenna picks up multiple reflections of signals leading to erroneous estimation of pseudoranges. In addition to ranging inaccuracies, constructive and destructive combinations of LOS and NLOS signals, based on their relative carrier phases, result in time varying signal power fluctuations known as fading. However, for

carrier phase tracking, the effect of multipath is limited to carrier phase measurement errors up to one quarter of a cycle, which is about 5 cm for GPS L1 C/A signals when LOS signal is stronger than NLOS signals (Misra & Enge 2011). The code phase measurement errors due to multipath depends on the path and power differences between LOS and NLOS signals and code tracking strategies employed (Ray 2000). Therefore, one of the advantages of using carrier phase measurements for position compared to code phase measurements is a comparatively lower multipath effect. However, maintaining reliable carrier phase lock in multipath environments is a key challenge to be addressed during the receiver design (Misra & Enge 2011).

1.3.4 Signal attenuation

In addition to low received power levels, GNSS signals are further attenuated by structures in environments such as glass windows, brick walls, concrete buildings, forest canopy and human proximity. It is shown in Stone (1997) that building materials, namely reinforced concrete, can attenuate GNSS signals up to 35 dB and the indoor environments are shown to attenuate signals by 10's of dB. Reliable carrier phase tracking under such conditions requires extremely long coherent integration periods, which often limit the receiver dynamics and, consequently, requires reduction in the tracking loop bandwidth (Razavi et al 2008). For pedestrian applications under reasonably open sky scenarios the signal attenuation due to human proximity should be known and addressed in the tracking loop design. To this end, it is shown by Bancroft et al (2011) that about 12 dB of signal attenuation is noticeable for satellites at 85 degrees elevation. Measurements were made by placing a human model in close proximity to an antenna to

obtain this result. Signal attenuation forces a reduction in GNSS carrier tracking loop bandwidth in order to restrict thermal noise from corrupting measurements.

1.3.5 Line-of-sight dynamics

The Doppler frequency shift in the received signal caused by relative velocity between the satellite and receiver antennas is one of the concerns of GNSS receiver design. The GNSS signal acquisition phase has to consider the maximum possible Doppler frequency while detecting GNSS signals. The satellite motion is accurately predictable and so are the Doppler frequency changes due to satellite motion. For a stationary user, the Doppler frequency range due to satellite motion is typically within +/- 5 kHz, which also depends on the location of the user (Diggelen 2009 and Curran 2010). The Doppler frequency due to satellite motion varies slowly over time, and therefore is not an issue for carrier tracking loops. In contrast, the receiver dynamics generally induce significant stress on the carrier tracking loops demanding wider bandwidth to track the changes in Doppler frequency. The demand for wider bandwidth contradicts the lower bandwidth requirement to keep the effect of thermal noise low thus forcing a trade-off.

1.3.6 Interference

Any undesired signals entering the GNSS receiver signal processing chain, either through the antenna or through inappropriate hardware design, for example clock signal leakage on the receiver circuit board picked up by the Radio Frequency (RF) front-end, are considered as interference signals. There are two categories based on the intent of the interference source (Ward et al 2006b, Daneshmand 2013): (a) intentional interference, including GNSS jammers and spoofers; (b) unintentional interference, including cross talk between RF sections of a multi-application platform such as mobile phones. The

interference signals can be in-band or out of band. Although out of band interference is removed by filtering, the vast difference in power between GNSS signals and other ground-based interfering signals can be significant depending on the stop band attenuation of filters employed in the GNSS RF front-end (Borio 2008, Ward et al 2006b). Another possible classification of interference is whether the interfering signals are narrow band or wide band (Ward et al 2006b). Narrow band signals can affect GNSS signal detection and tracking via strong harmonics and intermodulation products causing false frequency locks and erroneous measurements, whereas wide band interference elevates the GNSS noise floor thus making signal detection a challenging task. One of the mildest in-band wide-band white noise interference is the atmospheric microwave background noise in the GNSS frequency band; this is usually neglected during the receiver design as the receiver-generated thermal noise, discussed in the next section, is much higher in magnitude compared to atmospheric microwave background noise.

Although there are sophisticated techniques such as adaptive beam-forming to reduce the impact of interference and jamming (Daneshmand et al 2013), the units are typically bulky and expensive, and hence not suitable for portable GNSS receivers such as in cell phones. There are however other signal processing methods which are generally performed on the digitised incoming GNSS signal samples and can be used for interference mitigation on portable GNSS receivers. These methods include signal spectrum monitoring to detect and filter out interfering signals (Borio 2008), the vector tracking approach with aiding from a navigation processor (Benson 2007), a combined vector architecture with notch filtering to build more robust tracking loops (Lin et al 2011),

use of the ultra-tight integration of inertial sensors with GNSS to further immunize GNSS signal tracking against interference (Groves et al 2007).

1.4 Receiver-based non-idealities

The receiver-based non-idealities are the limitations of the receiver design technology which further limits achievable navigation performance. The following discussion is focused on low-cost, portable hand held pedestrian GNSS receiver designs such as in cell phones. GNSS hand held receiver design is limited by the requirements of low cost, low power consumption and compact size; the discussion is emphasized on the impact of such limitations on the carrier phase tracking.

1.4.1 Receiving antenna

The issues faced by antenna designers of pedestrian hand held GNSS receiver are discussed by Chen et al (2012). The compact size of the portable antennas puts severe design constraint on the expected radiation pattern and phase centre stability of the antenna. The phase centre stability is one of the concerns of GNSS receivers employing carrier phase-based solution, also known as *kinematic positioning* in the GNSS community (Misra & Enge 2011). The requirements such as compact size, power consumption and rapid changes in device orientation limit advanced antenna design technologies such as antenna arrays and choke ring from being employed in portable applications, which in turn leads the portable GNSS receiver to be susceptible to multipath and interference, thus degrading the navigation performance. In addition, the human proximity to these antennas will reduce the radiation efficiency leading to reduced

antenna gain, deteriorate the radiation pattern and disturb the impedance matching at its feed point, causing further degradations in signal reception (Chen et al 2012).

1.4.2 Thermal noise

The thermal noise originates from unwanted motion of the electrons in the receiver along the RF signal processing chain from the antenna until Analog to Digital Converter (ADC). It is a common practice to model thermal noise as white Gaussian noise, more commonly known as Additive White Gaussian Noise (AWGN). In most cases, white noise is not a major problem in communication receivers as its effect on the estimated parameters can be reduced by averaging. However, the white thermal noise has interesting implications on GNSS carrier phase tracking. The carrier phase tracking loop needs to estimate the carrier phase from the incoming samples. It is shown in the literature (e.g. Peters & Kay 2004) that the unbiased estimator of the carrier phase of a sinusoid corrupted by AWGN does not exist. This causes a major problem to the carrier phase tracking in the following two ways: (1) the carrier phase discriminators used in GNSS are generally non-linear functions which convert correlation values to the corresponding phase error (Ward et al 2006a). The non-linearity of phase estimators results in erroneous carrier phase tracking. The phase lock loops are mostly operating within the linear region of discriminators, which resolves the problem under high SNR conditions (Ward et al 2006a, Curran 2010). However, under low SNR conditions, the linear region shrinks causing frequent losses of phase lock (Curran 2010); (2) the measure of phase tracking performance also suffers from non-linearity. For example, the Phase Lock Indicator (PLI) discussed by Dierendonck (1996) also suffers non-linearity issues at low SNR values. This poses a

significant problem in both carrier phase tracking and subsequently, carrier phase loss-of-lock detection, which is analyzed in more detail in Chapter 2.

1.4.3 Front-end filtering and quantization

The filtering of GNSS signals is usually performed in multiple stages through the RF front-end signal processing chain to remove out-of-band interference and mainly to constrain the signal within a specified bandwidth before sampling to avoid aliasing effects. However, the combined filtering effect can be summarised by an effective filtering loss factor which is primarily the results of GNSS signal attenuation outside the filter bandwidth. The front-end filter bandwidth has a direct impact on the number of samples to be processed by the receiver. In low cost pedestrian receivers limited by computation resources, lower processing bandwidth is desired. Fortunately, in GNSS the front-end filtering will not introduce significant losses owing to the power spectral density (PSD) of GNSS signals. For example, front-end bandwidth of 2 MHz on GPS L1 C/A will contain about 90 % of the signal power, which is adequate for many portable GNSS applications. The disadvantage of choosing a lower front-end bandwidth is the limited correlator chip spacing for code tracking loops, thus the code measurement accuracy is limited. However, for carrier phase tracking loops, no such significant degradations occur. After quantizing the sampled signal, the discrete time signal is converted to digital signal using ADC. The non-linear process of quantization introduces quantization noise which further degrades the effective SNR. Recent studies have shown that the front-end bandwidth and quantization must be considered as a joint design problem for GNSS receivers to obtain an optimal choice for the signal loss versus processing resources trade-off (Curran 2010).

1.4.4 Local oscillator

The local oscillator in GNSS receivers is a key choice, which dictates all the receiver events from signal processing to navigation solution. It is a common practice to use either temperature controlled crystal oscillators (TCXO) or oven controlled crystal oscillators (OCXO). The major quality parameters affecting the receiver design are the following:

1. The crystal stability indicates the ability of the oscillator to maintain the nominal output frequency. It is further divided into short term and long term stabilities. For carrier phase tracking, a clock with good short terms stability is preferred so as to perform coherent integration without incurring losses due to oscillator phase and frequency drift (Gaggero 2008, Watson et al 2007, Watson et al 2006). The oscillator stabilities are generally expressed as Allan or Hadamard variances (Allan 1987, Sullivan et al 1990).
2. The phase noise of the oscillator affects the carrier phase tracking jitter in pedestrian receivers and is arguably more important than that of the crystal stability mainly depending on the duration of coherent integration (Razavi et al 2008). A polynomial model in frequency is generally employed to express phase noise (Leeson 1966). The coefficients of the polynomial models, known as h -parameters, dictate the phase noise of the oscillator (Gaggero 2008).
3. The g -sensitivity of oscillator measures the shift in oscillator's output frequency when the oscillator is subject to changes in acceleration. This parameter also plays a crucial role in precise carrier phase tracking, as the tracking loops have to handle the total dynamics of the carrier phase whether it is due to the LOS dynamics or to the local

clock. It is usually expressed in parts-per-billion per g , ppb/ g , for each axis of the crystal where g is the acceleration due to gravity. Oscillator g -sensitivity is one of the main focuses of this thesis and will be discussed in detail in Chapter 4.

1.5 Literature survey related to pedestrian GNSS receivers

In this section some of the previous work related to pedestrian navigation is discussed. The section begins with discussion of previous work on the pedestrian environment characterization in terms of the human gait analyses and human attenuation of GNSS signals. A review of the existing literature on the effects of oscillators on GNSS signal processing is then presented. Finally, the existing methods to combat receiver dynamic stress on tracking loops are discussed.

The human gait is well researched for a variety of medical and recreational purposes such as for making bone implants, prosthetic legs, better shoes, improved military gears for soldiers, etc. (Kavanagh & Menz 2008, Kwakkel 2008, Antonsson & Mann 1985, Ladetto et al 2001, and Terrier et al 2000). The data can be used to build improved pedestrian navigation technologies. To this end, some of the relevant findings from previous work are discussed. The average pedestrian walking speed is typically of the order of 1.2 m/s (Moe-Nilssen 2004) with up to about 52 % variation across subjects (Terrier et al 2000). The average pedestrian step duration is about 0.53 s with up to 6.64 % variation across subjects (Terrier et al 2000). The accelerations due to walking have been reported to be about 1.5 g on the torso (Takeda et al 2009), about 3.7 g on tibia (Lafortune 1991), more than 24 g on heels (Bancroft & Lachapelle 2012a). These dynamics will induce LOS dynamics and oscillator induced apparent dynamics due to g -sensitivity and challenge

GNSS carrier phase tracking. The frequency domain analysis of human gait shows that more than 99 % of the signal energy is concentrated within 15 Hz (Antonsson & Mann 1985), and the accelerations are characterized by peak frequency at about 1.5-2 Hz which coincides with the average step frequency (Kavanagh et al 2005). Although these numbers depend exclusively on the sensor location and motion modes, the pedestrian dynamics pose significant challenge to carrier tracking loops. For example, stark changes in accelerations of about 30 g recorded on foot mounted accelerometers occur within about 90 ms since the heel strike (Bancroft & Lachapelle 2012a), which can prove to be detrimental to GNSS carrier phase tracking. The situation is worst when a pedestrian is walking downhill. Much work have been done on the human gait analysis pertaining to pedestrian motion mode classification, also known as pedestrian context awareness, and subsequently using the recognized mode to improve pedestrian navigation. The context awareness can be established by a variety of techniques ranging from simple context dependent periodicity analysis (Susi et al 2011, Chowdhary et al 2009), temporal signal analysis including mean, maximum and minimum accelerations (Kantola et al 2010), zero crossing rate analysis (Susi 2012, Kantola et al 2010) to complicated sensor data fusion techniques utilizing most sensors available on cell phones (Saeedi et al 2014). The availability of context awareness can be readily exploited to improve GNSS carrier tracking by adaptive techniques such as adaptive bandwidth tracking loops. The context awareness in GNSS receivers can also be extracted from other context dependent parameters such as C/N_0 (Groves et al 2013, Lin et al 2011) and fading level (Lin et al 2011).

In addition to pedestrian dynamic stress on the GNSS tracking loops, human proximity to the GNSS antenna results in significant effects, which potentially degrade the navigation performance by lowering the effective SNR. The important human proximity effects on antennas are as follows (Chen et al 2012, Buckley et al 2010, Bancroft et al 2011): (a) The lossy nature of human body results in electromagnetic absorption in the tissues leading to significant signal attenuation; (b) Impedance mismatch between antenna output element and the succeeding RF front-end load results in incomplete RF power coupling lowering the effective signal power propagated to further stages of processing; (c) Change in resonant frequency, bandwidth, and radiation pattern of the antenna; (d) Multipath effects due to signal reflections from the skin.

The relevant effects pertaining to this thesis are the signal attenuation and multipath. The signal attenuation due to human proximity has been studied under multipath environments (Chen et al 2012) and there is a strong dependence of the overall signal attenuation on the type and location of the antenna. Signal attenuations for Planar Inverted-F Antennas (PIFA), Dielectric Resonator Antennas (DRA) and helical antennas, for various antenna locations are mentioned in Table 1-1.

Table 1-1 Signal attenuation in dB for various antenna types and locations

Antenna Type → Antenna Location↓	PIFA	DRA	Helical
Pocket	2.5	1.5	1.5
Hand-held (typing)	5.1	19.1	2.7
Hand-held (talking)	9.3	12.8	8

It is apparent from Table 1-1 that helical antennas perform better in terms of signal attenuation in human proximity. Another research pertaining to the human effects on GNSS signal attenuation is reported by Bancroft et al (2011), which show that there is a strong dependence of antenna distance from the subject and a maximum attenuation of about 12 dB was observed for the antenna-subject distance of 22 mm. The signal attenuation results in overall reduction in post coherent SNR that has to be addressed in tracking loops by reducing the loop bandwidth. The reduction in loop bandwidth limits the allowable receiver dynamics.

The cost, size and power consumption constraints usually lead to low-quality oscillators being employed in pedestrian GNSS receivers. The effect of oscillator phase noise is known to increase the carrier phase tracking jitter (Dierendonck 1996) and it is shown that the phase noise is the dominant error source in the absence of LOS dynamic stress (Razavi et al 2008). There are two categories of oscillator phase noise identified by GNSS researchers, namely the natural phase noise and the vibration-induced phase noise (Dierendonck 1996, Ward et al 2006a, and Misra & Enge 2011).

Rudimentary tracking loop designs consider the oscillator phase noise as one of the fundamental limits of GNSS tracking performance forcing a trade-off between thermal noise and oscillator phase noise (Dierendonck 1996). However, there are sophisticated approaches to the problem by modeling the vibration-induced phase noise in terms of its PSD (Curran et al 2012 and Razavi et al 2008). For example, in Curran et al (2012) the problem is formulated as a Weiner filter design where a known oscillator PSD model is separated from the thermal noise effects to achieve minimum carrier phase mean squared error. Although the oscillator phase noise is shown to be a limiting factor for

extended coherent integration (Nebel & Lankl 2010), it is only applicable for extreme high sensitivity GNSS applications such as indoor receivers and the limiting case does not apply for carrier phase tracking in pedestrian receivers operating in more hospitable operating conditions such as open sky. The g-sensitivity of oscillators is the cause of vibration-induced oscillator phase noise and it is handled in various ways. The loop bandwidth trade-off is mentioned in Dierendonck (1996). Although Ward et al (2006a) mention the usage of vibration isolators to reduce this effect, they do not offer a processing solution. Several techniques directed towards manufacturing low acceleration sensitive crystals are listed in Filler (1988). However, it was demonstrated that these methods cannot yield crystals with acceleration sensitivities less than a few parts per billion per g. Much work is done at the signal processing level which can be broadly classified into active and passive compensation techniques. The passive method, in which no feedback control signal is applied to the crystal oscillator directly, is also explored in (Fry & Burnett 2010, Milliren et al 1988) where two resonators with the same acceleration sensitivities are placed in such a manner that their effective acceleration sensitivity vectors are in opposite direction and hence cancel each other. One of the straightforward active compensation methods is the application of control voltage corresponding to the acceleration experienced by the crystal to steer the oscillator's output frequency to its nominal value, as discussed in (Emmons 1984 and Przyjanski 1978). Another active compensation scheme measures the acceleration experienced by the oscillator using 3-axis accelerometers mounted on the oscillator itself, using additional circuitry, and electronically adjusts the oscillator output (Bloch et al 2009).

The simplest of methods to address the dynamic stress imposed by receiver dynamics is via optimal choices of loop order, loop bandwidth and the coherent integration period according to the receiver dynamics specifications (Ward et al 2006a, Dierendonck 1996, Misra & Enge 2011). However, such simplistic tracking loop designs fail to consider time-varying receiver dynamics as it can happen in pedestrian applications; a pedestrian can be stationary, walking or running while the receiver can be hand held, kept in the pocket or put inside a backpack. To this end, much work has been done to improve GNSS tracking performance while accounting for time-varying receiver dynamics, in other words use adaptive tracking loops. Lee et al (2007) presented an adaptive tracking loop where the bandwidth was estimated from the signal-to-noise ratio (SNR), satellite elevation angle and receiver's acceleration. It was also shown (Muthuraman et al 2010) that the bandwidth can be modeled as a function of C/N_0 and discriminator output to improve carrier tracking performance. It is shown in Sokolova et al (2011) that constraining the so-called *Doppler bandwidth* to match the required dynamics yields better tracking performance. Kamel (2010) proposed an adaptive tracking loop with a variable bandwidth where the filter gains were determined directly by processing integrated navigation estimates using a fuzzy controller. In addition to the adaptive methods mentioned above, context awareness can be utilized to tune tracking loop parameters such as bandwidth to achieve performance enhancement. There are also tracking architectures based on dynamics compensation to improve tracking performance by reducing tracking loop dynamic stress. One of the well-established methods of dynamic compensation technique is the vector-based tracking architecture proposed by Spilker (1996b). Vector-based tracking architectures measure the receiver dynamics using information from all satellites

in view via the navigation solution and aid tracking loops with signal parameter estimates such as code phase and carrier Doppler frequency. The ultra-tight or deep-coupling of GNSS and Inertial Navigation Systems (INS) provide additional robustness and improved accuracy in a receiver employing vector-based tracking architecture by bridging GNSS data outages (Petovello et al 2007, O'Driscoll et al 2008, Petovello et al 2008a, b). Petovello et al (2007) demonstrated an average tracking sensitivity improvement of about 7 dB with ultra-tight coupling for vehicular navigation scenario.

When the traditional methods of strapdown ultra-tight integration fails due to, for example insufficient attitude estimation due to gyroscope bias instabilities (Pany et al 2009), alternative methods such as Pedestrian Dead Reckoning (PDR) can be employed (Pany et al 2009, Mezentsev et al 2005). The PDR technique uses human gait information and accelerometer data to detect steps and estimate the pedestrian step length, and update the user position by utilizing heading derived from either gyroscopes or magnetometers. This method of integration has been proven accurate compared to the conventional strapdown integration technique. The benefits of PDR for carrier tracking performance enhancement is explored in the so-called DINGPOS system (Niedermeier 2009, Pany et al 2009a, b). The DINGPOS work described by Pany et al (2009a) focused on extending the coherent integration for indoor operating conditions, where a strapdown ultra-tight system was constrained by the PDR technique to evaluate the user motion in short segments over time, which were called μ -trajectories. The estimated user motion, in turn, was used to control the local code and carrier replicas used in GNSS signal tracking. This method of ultra-tight integration was referred to as *partially coherent ultra-tight integration*. The reconstructed carrier phase trajectory using this method was demonstrated for up to

2 seconds for a walking user using a representative satellite. It was reported that the accuracy of the estimated carrier phase trajectory depends on the accuracy of step detection and estimated heading (Pany et al 2009a). Also, it was reported that the carrier phase estimation of lower elevation satellites are comparatively more affected than the higher elevation satellite, mainly due to heading inaccuracies. However, no results were presented across satellite elevations, but it was mentioned that occasional gross errors were noticed that result in large correlation errors (Pany et al 2009a).

1.6 Limitations of previous work

In this section the limitations of previous work, as it appears to the author, are discussed and lead to the motivation for the author's research.

Much work is done on GNSS/INS integration for pedestrian applications, which focus on the use of inertial sensors at the measurement level to provide accurate navigation solution. However, little effort is invested towards providing accurate GNSS carrier phase measurements by exploiting the operating conditions in pedestrian receivers. In this regard, this thesis is aimed towards identifying the major hurdles to carrier phase tracking thus providing a carrier phase based solution in pedestrian receivers. Where these hurdles persist, this thesis attempts to push the low-cost consumer grade receivers a few steps towards the carrier phase based solution, which is currently obtained only in high quality survey grade receivers, by bridging the technological gap via signal processing techniques.

The available literature on human gait models lacks focus on the analysis of dynamic stress imposed on tracking loops due to pedestrian motion patterns. Specifically, no effort

has been made toward establishing the relationship between pedestrian acceleration and the GNSS carrier phase process. Such an analysis is important to understand the type and severity of dynamic stress imposed by pedestrian dynamics on the tracking loops which will help in building appropriate tracking architectures conditioned on pedestrian motion patterns. Similarly, although several GNSS signal attenuation models due to human proximity are available, little analysis is done on the impact of such attenuation on carrier phase tracking performance.

Pedestrian dynamics have a two-fold effect on the overall dynamic stress on carrier phase tracking: (a) LOS dynamics; (b) vibration-induced oscillator phase noise due to oscillator's g-sensitivity. The existing adaptive tracking loop methods and high sensitivity tracking techniques are restricted to carrier frequency tracking as it is sufficient for code phase solution. Hand held devices such as cell phones now host MEMS based inertial sensors that meet the required specifications in terms of dynamic range and sensor bandwidth; previous work by Niedermeier (2009) and Pany et al (2009a,b) shows the potential of using IMUs for carrier phase recovery. Nevertheless, the case for not using an ultra-tight tracking architecture remains an interesting and relevant one from at least an academic perspective and for practical reasons, namely:

(a) Occurrence of IMU failure.

(b) GNSS chipsets and IMUs are generally not integrated into a single integrated circuit, but mounted separately as can be inferred from the handsets technology product line, for example by CSR (2015), u-blox (2014). It is therefore of interest to examine potential solutions which can be employed by a GNSS chipset both in the presence and in the absence of inertial sensors.

(c) Power consumption is a critical factor in hand-held devices and many features and components are switched to a power-saving mode whenever possible. In the context of navigation, MEMS sensors can consume significantly more power than the GNSS ASIC itself. Indeed, many MEMS units offer hibernation- or sleep-modes and motion-induced wake-up functions. Thus, in the interest of reducing power-consumption and preserving battery life, signal processing techniques that can offer an alternative to the constant use of MEMS sensors are of interest. If and when the technology evolves in future to produce batteries with improved capacity or MEMS devices that consume less power, it would become more realistic to have MEMS devices operating continuously.

(d) Unlike a standalone GNSS/INS navigation product, ultra-tight integration in cell phones calls for a collaboration of host processor manufacturers and GNSS chipset manufacturers. The GNSS equipment manufacturers need to be know the type of MEMS, specifications such as stability and noise spectral density values, and calibration data (if necessary). Also, GNSS chipset should be designed for three cases: (1) IMU not present; (2) IMU is present, but the specifications are not good enough for ultra-tight; (3) IMU is present and specifications are good enough for ultra-tight. Therefore, it can be hypothesised that, for the above reasons, ultra-tight integrated solutions are not realized in currently evolving cell phones despite the encouraging results in support of ultra-tight integration as reported by Pany et al (2009);

The limitations discussed in this section require more understanding of the pedestrian operating environment and necessitate new signal processing techniques for carrier

phase tracking in pedestrian receivers appropriately designed for the pedestrian operating environment.

1.7 Objectives and contributions

The objectives of this thesis is to understand the pedestrian operating environment from the perspective of GNSS carrier phase tracking, identify the major challenges to carrier phase tracking based on the characterization results, propose signal processing methods to enhance the carrier phase tracking performance and finally apply the enhancements to investigate the possibility of a carrier phase based solution under the environment considered. The objectives of this thesis can thus be summarized as the following question:

“How to utilize knowledge of the pedestrian operating environment to improve GNSS carrier phase tracking performance?”

Thus, the thesis shall attempt to propose new signal processing methods exclusively designed for pedestrian GNSS receivers while drawing upon the limited resources available in consumer grade receivers.

1.8 Assumptions on data collection and processing

- Although the methods developed in this thesis are equally applicable to all types of GNSS, for the sake of simplicity, and due to its global and permanent availability, the GPS L1 C/A signal is used.
- Live GPS data is used for performance evaluation of developed algorithms to ensure validity of the proposed methods.

- Although consumer quality hardware is assumed for the development of algorithms, adequate availability of computational resources is assumed for proposed methods.
- The data processing corresponding to this research shall be conducted offline, using GSNRx™ (Petovello et al 2008) - a C++ based software GNSS receiver developed and maintained by the Position, Location and Navigation (PLAN) group, University of Calgary.

1.9 Thesis flow and organization

The chapters in this thesis are organized as shown in Figure 1-2. The signal and system model used in this thesis is described in Chapter 2, which focuses on the mathematical models for carrier phase tracking loops in GNSS and the metric used to assess carrier phase tracking performance.

The overall objective of this thesis is to improve the carrier phase tracking performance in GNSS pedestrian hand-held receivers. The problem is formulated by characterising the pedestrian operating environment described in Chapter 3. An understanding of the effects of pedestrian dynamics and human body attenuation on GNSS signals and on carrier phase tracking performance is derived from experiments using inertial sensors and live data.

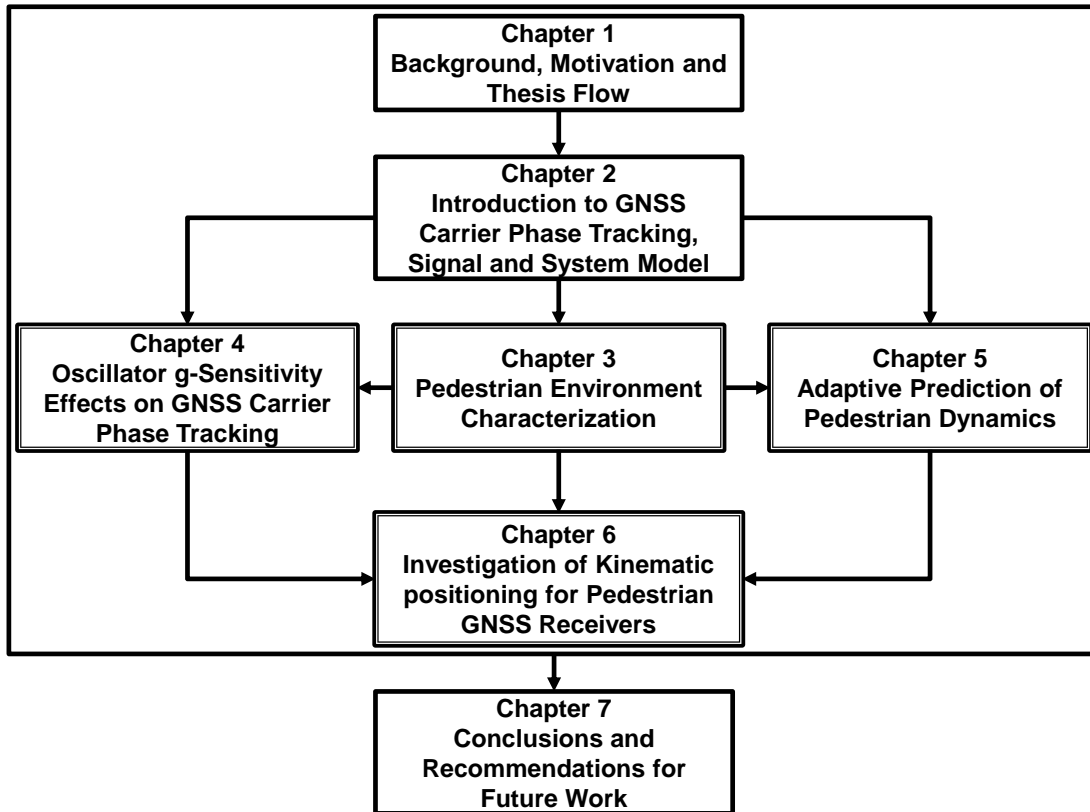


Figure 1-2 Thesis flow chart – flow of information across chapters

In principle, appropriately designed carrier phase tracking algorithms should handle the issues arising from the operating environment. To this end, chapters 4 and 5 recognize the aspects of the pedestrian environment that have a profound impact on the carrier phase tracking performance and propose methods to address these issues. The local oscillator's g -sensitivity combines with the pedestrian dynamics to induce additional dynamic stress in the carrier phase tracking loops. Fortunately, the accelerations experienced by the oscillator can be measured by accelerometers. A novel method to utilize these measurements to compensate for oscillator-induced errors is proposed in Chapter 4. The next dominant error source is recognized as the pedestrian LOS dynamics itself. The understanding derived from characterization is used to predict and compensate

for the pedestrian dynamics in tracking loops. A novel compensation algorithm via online measurement of dynamics in carrier tracking loops is proposed in Chapter 5.

Although the enhancements achieved using the proposed techniques in chapters 4 and 5 are assessed using relevant metrics at the tracking loop level, detailed analysis is needed to assess the overall performance at the positioning level. In this regard, Chapter 6 attempts to provide a differential carrier phase based GNSS solution using the enhanced carrier phase measurements from the proposed methods. Also, a comparative performance analysis of navigation solutions will be done between a survey grade commercial receiver and a software-defined receiver that implements the tracking algorithm developed in this research.

Chapter Two: GNSS signal processing and carrier phase tracking

2.1 Introduction

Current GNSS contains medium earth orbit satellites with a nominal orbital radius of 25,560 km for GPS, 25478 km for GLONASS, 29600 km for Galileo and from 21528 km in case of medium earth orbit (MEO) to 35786 km for BeiDou geostationary earth orbits (GEO) (Misra & Enge 2011, Galileo ICD 2014 and BeiDou ICD 2012). Due to such long distances signals are buried in the receiver thermal noise and therefore require enormous processing gains to decode their information content. To this end, GNSS use direct sequence spread spectrum (DSSS) signals due to the following advantages given the satellite-receiver communication channel: (a) noise-like appearance of GNSS signal due to bandwidth spreading enable encryption of signals for unintended receivers; (b) enable precise TOA measurements owing to the properties of pseudorandom number (PRN) code used; (c) offer interference and jamming immunity to a certain extent; (d) enable multiple access - GPS, Galileo and BeiDou use code division multiple access (CDMA) signals where the all the satellites of a particular constellation transmit their signals in the same frequency band at the same time. This chapter deals with processing of DSSS CDMA signals in a receiver typically on or near the surface of the earth while focusing on carrier phase tracking in pedestrian GNSS propagation channel. The discussion focuses on GPS L1 C/A signals used herein.

2.2 GNSS signal structure

The composite signal entering the GNSS receiver's antenna can be modeled as

$$r_a(t) = \sum_{i=1}^{N_{sig}(t)} s_i(t) + \eta_a(t) \quad \text{2-1}$$

where $r_a(t)$ is the composite GNSS signal at the user antenna at time t , $s_i(t)$ is the received signal from the i^{th} satellite, $N_{sig}(t)$ is the total number of GNSS signals from various carrier frequencies and various constellations reaching the receiver antenna either directly or upon reflections, and the term η_a models the composite additive noise comprised of atmospheric background noise, receiver thermal noise and interference, the subscript 'a' denotes the analog nature of the signal. The term $s_i(t)$ can be further expanded as

$$s_i(t) = \sqrt{2P_i(t)} d_i(t - \tau_i) c_i(t - \tau_i) \cos(2\pi f_{C_i} t + \theta_i(t)) \quad \text{2-2}$$

where $P_i(t)$ is the received total signal power in [W], d_i is the bipolar navigation data which takes values from the set $\{-1, 1\}$, c_i is the spreading code which takes various shapes based on the modulation scheme, namely bipolar for BPSK as in GPS L1 C/A, tripolar for modernized GPS signals such as L2CM and multi-level sequence for other modulations such as CBOC used in Galileo, τ_i is the signal transmission time from the satellite to the receiver antenna, f_{C_i} is the signal centre frequency in [Hz], and θ_i is the composite phase process of the satellite signal in [rad] and is the focus of this thesis. The composite phase process θ_i accounts for the Doppler frequency shift due to the relative motion between user antenna and the satellite transmission antenna and the other signal propagation effects through the atmosphere including an arbitrary constant phase offset. These parameters are explained in detail below.

2.2.1 Received signal power

Although the RF power allocated to C/A signals at the GPS satellite antenna input is about 25 W, the nominal received power level at ground is only about -128.5 dBm for LOS signals (Misra & Enge 2011 and GPS ICD 2012) where the free space propagation results in about 182 dB of signal loss (Misra & Enge 2011) and other atmospheric effects incur less than 2 dB of loss (Klobuchar 1996 and Spilker 1996c). However, the effective received signal power available for processing depends on the complex pedestrian GNSS signal propagation channel with the following significant sources of signal attenuation: (a) signal blockage by structures such as foliage, urban canyons and buildings; (b) amplitude fading due to multipath; (c) human proximity to the receiving antenna; (d) poor quality antennas employed in pedestrian receivers (Wang 2012) with degraded radiation gain patterns influencing the effective conversion of electromagnetic signal power to electrical signal incurring losses. Overall, for pedestrian receivers, the received signal power can vary between -128.5 when operated outdoors to -160 dBm in indoors (Lachapelle 2004, Diggelen 2002).

2.2.2 Navigation data

The navigation data is termed as *bits* and it can be modeled as

$$d_i(t) = \sum_{k=-\infty}^{\infty} b_k^i \delta(t - kT_b) * \text{rect}(t/T_b - k) \quad \mathbf{2-3}$$

where b_k^i is the bipolar navigation data sequence, $\delta(t)$ is the Dirac delta function, $\text{rect}(t)$ is the rectangular pulse, $*$ is the convolution operator, T_b is the data bit duration [s]. The $\text{rect}(t)$ function is defined as

$$rect(t) = \begin{cases} 1 & 0 \leq t < 1 \\ 0 & otherwise \end{cases}$$

2-4

For GPS L1 C/A signals T_b is 20 ms, while it varies for other signals. The navigation data contains the information about the long term and short term satellite orbital parameters, satellite health, satellite clock correction parameters and atmospheric error correction parameters. The navigation data in case of GNSS receivers with Internet connectivity can be readily downloaded from Assisted-GNSS service providers (Diggelen 2009). However, when the receivers are operated in areas devoid of network connectivity, the navigation data needs to be demodulated from the satellite signals. The uncertainty in navigation data bits dictates the upper limit on the coherent integration thus limiting the achievable sensitivity; such scenarios demand the network connectivity to supply navigation data bits.

2.2.3 Spreading code

The spreading code or simply referred to as the "code" is the satellite-dependent bipolar pseudorandom sequence modulated onto non-return to zero digital waveforms. These nearly orthogonal codes are generated by linear feedback shift registers and are designed to possess sharp autocorrelation properties. The naming is derived from its spreading of the signal spectrum to a wider bandwidth. The spreading codes can be represented as

$$c_i(t) = \sum_{k=-\infty}^{\infty} c_k^i \delta(t - kT_c) * sc(t - k)$$

2-5

where c_k^i is the periodic bipolar spreading code sequence, T_c is the duration of a spreading code pulse termed as a *chip*, $sc(t)$ is the sub-carrier signal corresponding to the spreading code. The periodicity of the sequence c_k^i and sub-carrier shapes vary based on the GNSS signal.

The GPS L1 C/A signals employ a class of codes known as *gold codes* named after their inventor. The code repeats itself after 1023 chips and, the code frequency being 1.023 MHz, this corresponding to a repetition period of 1 ms. This implies that there are 20 code periods or 20460 chips within a data bit. The peak value of autocorrelation of one period is 1023, which occurs only when the sequence is correlated with itself without any shift. However, when there is a shift or when the sequence is correlated with code from any other satellite, the resulting correlation taken on values from the set $\{-1, -65, 63\}$ which occurs for about $\{50\%, 12.5\%, 12.5\%\}$ of the time respectively. The subcarrier takes the shape of the $rect(t)$ function defined in Eq. 2-4. The C/A code exhibits line spectrum following a sinc shaped envelope with line spacing of 1 KHz due to a 1 ms periodicity.

2.2.4 Carrier

GPS L1 C/A transmits at 1575.42 MHz carrier centre frequency which is 1540 times the code frequency. This implies that there are 1540 carrier cycles within a chip. The carrier signal should allow transmission of information from the medium earth satellites to users on the earth surface. In this regard, the frequency band must be chosen carefully to avoid atmospheric losses and disruptions. The L-band chosen for GPS signals is a compromise between little atmospheric attenuation and feasible design of user antennas based on the technology existing at the time (Parkinson 1996). However, the ionospheric delays and scintillation are still one of the major challenges to precise navigation. The ionospheric delays are effectively handled by differential techniques for reasonably short baselines and utilizing frequency diversities for longer baselines (Misra & Enge 2011).

2.3 An overview of receiver signal processing

The electromagnetic signal propagation channel ends as the GNSS signal enters the receiver antenna and the GNSS receiver components mediate further electrical signal flow until the PVT solution. An overview of the signal processing performed on the electrical signals from the antenna to the position solution is provided in this section. A generic signal processing block diagram of a GNSS receiver is shown in Figure 2-1.

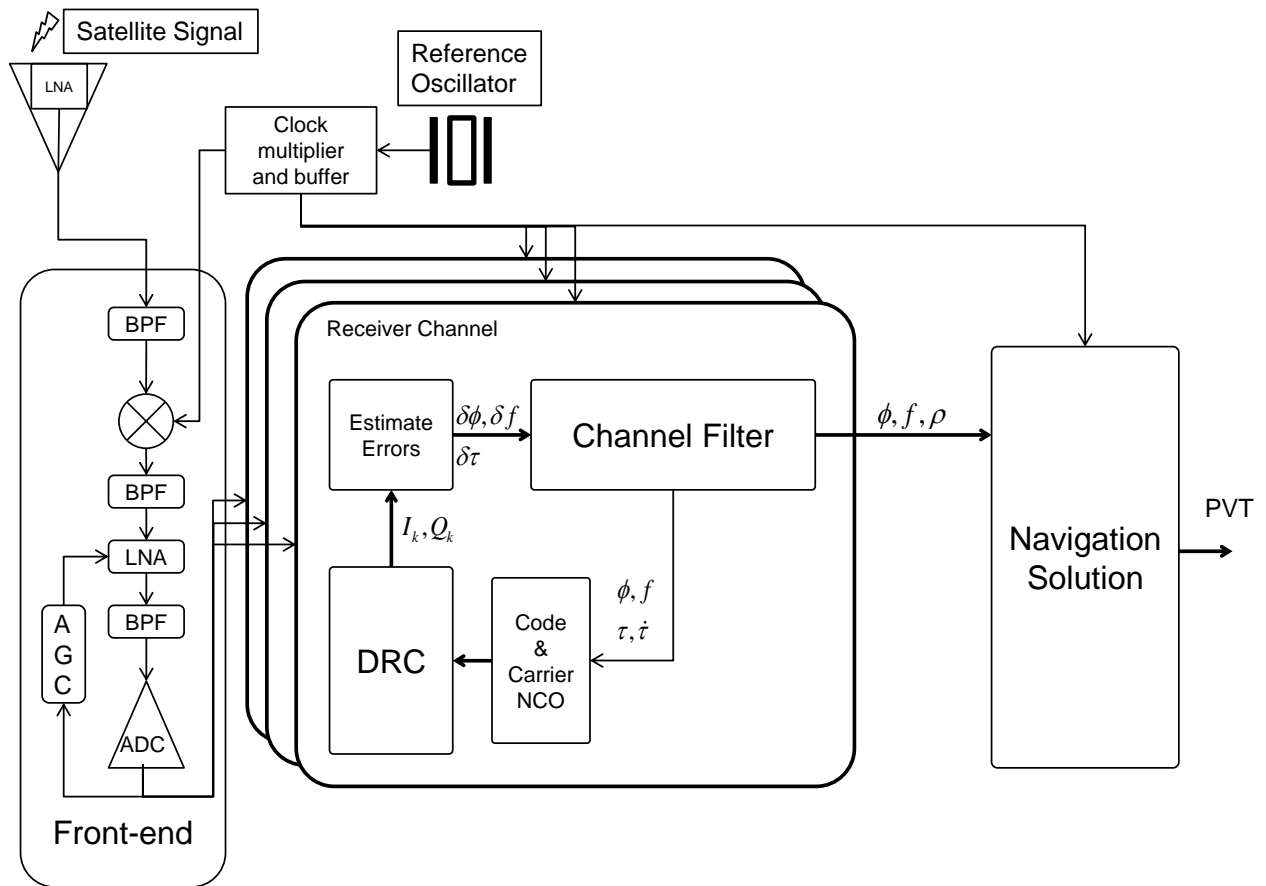


Figure 2-1 Generic block diagram of a GNSS receiver

2.3.1 The front-end

The front-end performs signal conditioning on the weak analog signal and converts it to a digital signal. A brief description of the characteristics and functions of the front-end components are sequentially explained according to the signal flow.

2.3.1.1 Antenna

The antenna converts weak GNSS electromagnetic signals to electrical signals. For standard GNSS receiver operation a single antenna is sufficient; however, research is also done to exploit the benefits of multiple antennas such as attitude determination (Wang et al 2004), multipath mitigation (Ray et al 1999), enhanced signal detection performance using polarization and spatial diversities (Zaheri et al 2012), interference and spoofing mitigation (Daneshmand et al 2012), etc. However, pedestrian portable applications such as cell phones and wrist watches generally cannot employ multiple antennas.

While survey grade antennas are bulky, heavy and consume significant amount of power, pedestrian hand held applications employ very small, low-cost, patch antennas integrated into cell phones. In standard GNSS receivers, omnidirectional antennas are used to receive signals from satellites from all direction with constant gain desired over the entire azimuth range at the user end. However, antenna gain over the range of elevation is not constant; NLOS signals and ground based interference impose a gain reduction for lower elevation satellites. A commercial GNSS antenna has about +4-5 dBc gain at the zenith and drops to about -10 dBc at 10 degree elevation (GPS-703-GGG 2014 and ANN-MS 2006). Survey grade antennas generally have clean radiation pattern, good LHCP rejection and better phase centre stability compared to consumer grade antennas used

in pedestrian receivers. In particular, the phase centre instability is a major issue for carrier phase based positioning. Also, it is especially challenging for multi-frequency GNSS antenna designers for pedestrian applications to incorporate survey grade features while keeping a compact size (Chen et al 2012). However, these issues are not addressed in this thesis and the antennas used in the experiments are assumed to have good phase centre stability. The effect of low grade antenna quality such as in cellphones on carrier phase based positioning performance is studied by Pesyna et al (2014).

2.3.1.2 Low Noise Amplifiers

Low Noise Amplifiers (LNAs) are designed to boost the incoming signal power while introducing less noise of their own. Typically, LNAs are the first components following the antenna that dictate the overall noise figure of the system using Friis' formula (Haykin 2001). They can be either built into so-called "active antennas" or mounted on the RF circuitry along with other components. The amplifiers are generally distributed throughout the RF signal path to provide enough amplification, of at least about 100 dB, to convert the RF signal power to the operating range of the Analog to Digital converter (ADC). The LNAs in subsequent RF front-end stages can be replaced by power amplifiers while trading low noise factor of the component for linearity. The ADC acts upon the incident thermal noise as the GNSS signal is buried in noise and therefore the amount of amplification required depends on the thermal noise power only. The non-ideal characteristics of LNAs such as generation of intermodulation products demand additional filtering after amplification.

2.3.1.3 Band Pass Filters

The band pass filters (BPFs) play the following three major roles: (1) pass only the GNSS signals of interest and attenuate out-of-band spurious signals, interference and jamming signals; (2) attenuate the image frequency after down-conversion; (3) prepare the RF signal for sampling by eliminating aliasing losses. The major drawback of filtering is the attenuation GNSS signals outside the pass-band. However, for GPS L1 C/A signals 2 MHz of BPF bandwidth, also known as the *RF bandwidth* to distinguish from the tracking loop bandwidth, this results in about 0.5 dB loss only (Dierendonck 1996). In addition to the signal loss, code tracking accuracy is affected by the RF bandwidth by limiting the correlator chip spacing. However, the higher the filter bandwidth the higher is the sampling rate; this amounts to more samples to process, resulting in increased utilization of computational resources which is not a desirable design choice for pedestrian receivers. Therefore, low-cost consumer grade receivers face a trade-off between code phase inaccuracies versus computational resource limitations.

2.3.1.4 Down-conversion to Intermediate Frequency

Down-conversion of L-band GNSS signals to a much lower IF is required to enable conversion of signals from analog to digital domain for further digital processing. The down-conversion involves the following three steps: (a) removal of any image frequency present in the signal by a suitable BPF; (b) Mixing of the incoming L-band signal with centre frequency f_c with a locally generated carrier signal at a frequency f_{lo} thus resulting in sum and difference frequencies $(f_c + f_{lo})$ and $(f_c - f_{lo})$; (c) removal of the sum frequency component and other harmonics generated by mixing using a BPF thus centring the GNSS signal at IF which is calculated as $f_{IF} = f_c - f_{lo}$. Although direct down-conversion

from L-band to baseband is possible via intentional aliasing, it is practically challenging due to the following reasons: (a) difficulty in realising bandpass filters with high Q-factor at L-band frequencies; (b) sampling clock instabilities; (c) a phenomenon known as self-mixing resulting in leakage of sampling clock which is in turn picked up by either the antenna or other components (Svitek & Raman 2005). The choice of IF at each stage of down-conversion should not coincide with any of the harmonics of the local oscillator to avoid undesired electronic interference within the RF front-end.

2.3.1.5 Reference oscillator

The reference oscillator is the heart of the receiver with which all events are timed. The reference oscillator is used either directly or input to the clock synthesizer circuit which in turn generates clocks for various tasks that include the following: (1) generation of the local frequency signal for down-conversion; (2) sampling clock; (3) clock for baseband processing such as acquisition and tracking via correlation; (4) generation of PTTI pulse; and (5) timing for all subsequent digital processing events up to the estimation of PVT solution. While the GNSS timing applications can employ high quality atomic clocks or OCXOs as reference oscillators, pedestrian receivers typically use low quality TCXOs which are prone to non-idealities such as frequency instability, phase noise, the g -sensitivity issue which is one of the topics of this thesis, etc. However, TCXOs provide benefits such as being low-cost, compact in size, consume lower power and require shorter warm up time, and are therefore more suited for pedestrian applications.

2.3.1.6 Sampling and ADC

When an IF signal is bandpass sampled it becomes aliased into the baseband, thereby converting the IF signal from the continuous-time domain to the baseband signal in the

discrete-time domain. The sampling frequency should be chosen such that the ratio of sampling frequency to the PRN code frequency is an irrational number to enable unambiguous detection of the chip transition (Akos & Pini 2006). The discrete-time signal is converted to a digital one by ADC through quantization process. GNSS receivers employ uniform quantization meaning that uniform step sizes are chosen to convert continuous amplitude to discrete amplitude values. The sampling process is linear and reversible, at least in principle, whereas the non-linear quantization process involves irreversible truncation of signal amplitude to nearby quantization levels introducing *quantization noise*. The thermal noise excursions at the input of ADC should ideally be equal to the ADC dynamic range for minimum quantization noise for given levels of quantization. This can be achieved by continuously monitoring the signal level with an Automatic Gain Controller (AGC) and correspondingly adjusting the gain of the preceding amplifier. The quantization noise can also be reduced by increasing the number of quantization levels so that truncation errors are reduced; however, more quantization levels lead to more digital data for further processing.

2.3.1.7 Signal model at the RF front-end output

In a multi-frequency GNSS receiver, the RF front-end structure replicates multiple times based on the number of frequency bands supported by the receiver. For example, two RF front-ends are required in a GPS-GLONASS L-band receiver for conditioning GPS L1 C/A and GLONASS L1 signals as the centre frequencies of the two constellations are different. However, only GPS L1 C/A single frequency receivers are assumed in this research. In this section, the changes to the signal model as the signal propagates through the RF front-end components are discussed.

The noise sources from LNAs, BPFs, mixing and ADC circuitries are lumped into a single additive noise term. The effect of filter roll off is neglected as ideal filtering without aliasing losses is assumed. The total RF group delay starting from the antenna to ADC is assumed to be the same for all satellites and therefore it has no effect on the signal propagation. However, this delay needs to be accounted for in timing receivers to generate a precise PTTI pulse output. The amplification scales the signal and noise equally while maintaining the SNR intact and no change in mathematical signal model is necessary. The signal after down-conversion to IF can be modeled as

$$r_{IF}(t) = \sum_{i=1}^{N_{sig}(t)} \sqrt{2P_i(t)} d_i(t - \tau_i) c_i(t - \tau_i) \cos(2\pi f_{IF}t + \theta_{i,IF}(t)) + \eta_{IF}(t) \quad \mathbf{2-6}$$

The parameters that are changed from Eq. 2-2 to 2-6 are as follows: (a) the new centre frequency which is equal to f_{IF} ; (b) the new noise term accounts for added noise until the down-conversion process $\eta_{IF}(t)$; (c) the new composite signal phase process $\theta_{i,IF}(t)$ needs to accommodate for the clock effects in addition to its analog counterpart; (d) the subscript 'a' is replaced by 'IF' to denote the signal at IF. The baseband signal model after the digitization process using complex sampling, neglecting the imperfections of the sampling clock, can be expressed as

$$r(nT_s) = \sum_{i=1}^{N_{sig}(nT_s)} \sqrt{P_i(nT_s)} d_i(nT_s - \tau_i) c_i(nT_s - \tau_i) \exp(j\theta_i(nT_s)) + \eta(nT_s) \quad \mathbf{2-7}$$

In discrete-time notation the Eq. can be written as

$$r[n] = \sum_{i=1}^{N_{sig}[n]} \sqrt{P_i[n]} d_i[n - \tilde{\tau}_i] c_i[n - \tilde{\tau}_i] \exp(j\theta_i[n]) + \eta[n] \quad \mathbf{2-8}$$

The composite phase of the baseband signal can be further expressed, by dropping the discrete time index for simplicity, as

$$\theta_i = \theta_i^{LOS}(\vec{V}) + \theta^g(\vec{A}) + \theta^T(\mathbb{T}) + \theta^{ST} + \theta^{LT} + \theta_i^\eta + \theta_i^0 \quad \mathbf{2-9}$$

where θ_i^{LOS} is the satellite dependent LOS dynamics which dominates the phase process. This component includes the gross phase drift induced by the satellite motion, effecting a Doppler frequency in the range +/- 4 KHz, and the effects of the receiver motion represented by the receiver velocity vector \vec{V} . The θ_i^η represents the stochastic phase disruptions based on the signal propagation channel effects such as ionospheric phase scintillation, θ^g is the oscillator g-sensitivity component dependent on the acceleration \vec{A} experienced by the oscillator which will be described in detail in Chapter 4, θ^T is the clock bias changes due to temperature \mathbb{T} which is usually modeled by a temperature dependent offset not necessarily linear with temperature. The term θ^{ST} captures short term variations of the clock which are characterized by white and various order random walks in phase. It can be measured in terms of Allan or Hadamard variance and can be quantified by a set of PSD parameters. Although this term can be a limiting factor for high sensitivity receivers and a significant source of carrier phase perturbations under certain circumstances, it is generally insignificant for pedestrian receivers when compared to the θ_i^{LOS} term. The term θ^{LT} explains long term changes of the clock which manifests itself as an offset in the carrier frequency of the received signal after demodulation, changes being of the order of parts per billion per year, and it is reasonably constant over the typical observable period of a single satellite. The term θ_i^0 is the satellite-specific arbitrary initial phase of the carrier. The phase process can also be decomposed as

$$\theta_i = 2\pi f_i + \phi_i \quad \mathbf{2-10}$$

where f_i is the instantaneous carrier frequency term and ϕ_i is the instantaneous carrier phase of the signal. The distinction of the carrier Doppler and carrier phase processes facilitate easier incorporation of the drift and bias models of the local oscillator in the tracking process and also permits clarity in the understanding of the phase process. The composite noise term $\eta[n]$ of the baseband signal captures the combined receiver thermal noise introduced by various receiver elements, quantization noise and any aliasing noise due to non-ideal bandpass filters. However, no interference or on-board spurious signals are assumed. Therefore, $\eta[n]$ can be assumed to be a complex AWGN random variable, mathematically expressed as

$$\eta[n] \sim CN \left(\begin{bmatrix} 0 \\ 0 \end{bmatrix}, \begin{bmatrix} \frac{N_0 F_s}{2} & 0 \\ 0 & \frac{N_0 F_s}{2} \end{bmatrix} \right) \quad \mathbf{2-11}$$

where $N_0 = kT$ is the one-sided noise power spectral density, k is the Boltzmann constant which takes the value $1.38 \times 10^{-23} \text{ J K}^{-1}$, T is the ambient temperature which is typically assumed to be about 300 K thus N_0 is about -174 dBm, F_s is the sampling frequency. The Gaussian noise model is used mainly due to the following advantages (Papoulis 1991): (1) Gaussian process is invariant under linear transformation thus the shape of the distribution is preserved upon convolution of distributions; (2) the central limit theorem states that the distribution of the sum of N independent random variables with finite variance follows Gaussian distribution as N becomes large; and more importantly, (3) the Gaussian curve is a natural fit for most real-world observations and therefore it is also known as the *normal* distribution.

2.3.2 Baseband signal processing

The baseband signal processing consists of signal acquisition and tracking. The baseband signal processing begins with signal acquisition which performs two basic tasks: (a) detect the presence of a satellite signal; (b) provide coarse estimates of the signal parameters, namely code phase and carrier Doppler. Signal tracking refines the coarse estimates from acquisition namely Doppler frequency and code phase, also tracks the carrier phase, demodulates navigation data to decode the ephemeris and almanac etc., provides code phase, Doppler and carrier phase observations to estimate navigation solution. The tracking process will be explained in detail later in this chapter.

2.3.2.1 Signal acquisition

The start-up modes of a GNSS receiver can be categorized based on the availability of the following information: previously stored almanac data, previously stored ephemeris data which is still valid, approximate time, approximate previous receiver position. Availability of apriori information determines the ability of the receiver to compute visible satellites list and the corresponding approximate Doppler frequencies which aid the acquisition process. In *cold start* mode, no apriori information is available; therefore no visibility list and consequently all satellites are searched for signal detection. In *warm start* mode, approximate user position, almanac and receiver time are available; the receiver can calculate the visibility list and only attempt to acquire satellites deemed visible. If a receiver is in *warm start* and it also has ephemeris for the visible satellites then the mode is called *hot start*; the receiver can estimate PVT solution as soon as enough satellites are acquired without waiting for ephemeris collection. The acquisition can be formulated as binary hypothesis problem, using baseband signal expression from Eq. 2-8, as

$$H1: \sqrt{P_i[n]}d_i[n-\tilde{\tau}_i]c_i[n-\tilde{\tau}_i]\exp(j\theta_i[n])+\eta[n] \rightarrow \text{signal present} \quad \mathbf{2-12}$$

$$H0: \eta[n] \rightarrow \text{signal absent}$$

Among a total of six unknowns, namely instantaneous signal power, data bit, code phase, carrier Doppler, and carrier frequency and carrier phase offset, it can be shown that signal detection can be performed by jointly estimating only carrier Doppler and code phase (O'Driscoll 2006 and Borio 2008). Hence, the acquisition problem can be formulated as a Generalized Likelihood Ratio Test (GLRT) detection problem (Shanmugam 2008) that consists of an inherent *matched filter* or *correlator*, which is explained in the next section in more detail. However, to implement an optimal GLRT requires infinite matched filters to maximize the post-coherent SNR; in practice, a sub-optimal GLRT is implemented by sampling the search grid by predetermined carrier Doppler and code phase steps as indicated in Figure 2-2.

A reasonable code phase step size is 0.5 chips for GPS L1 C/A signals and Doppler step size is chosen based on the coherent integration period. The step sizes are generally chosen on the basis of allowable correlation losses. The decision statistic, which is the maximum correlation value among all the bins, is compared to a threshold value chosen based on the Neyman-Pearson criterion.

The search space in acquisition depends on the receiver operating mode. For example, in cold start mode, the code phase search space is 1023 chips and Doppler search space is about +/- 9 KHz assuming a clock drift uncertainty of +/- 0.5 ppm and a maximum user velocity of 500 m/s. The duration of coherent integration needed to detect a signal, called the acquisition *dwell time*, depends on the signal power level and the acceptable false-alarm rate. In general, satellite signals with various power levels are incident on the

antenna and the search should be conducted for the highest power level signal to the lowest. If the signal is detected, the Doppler and code phase parameters corresponding to the decision statistic are passed on to tracking for further continuous refinement. The carrier phase is not acquired, but estimated in tracking.

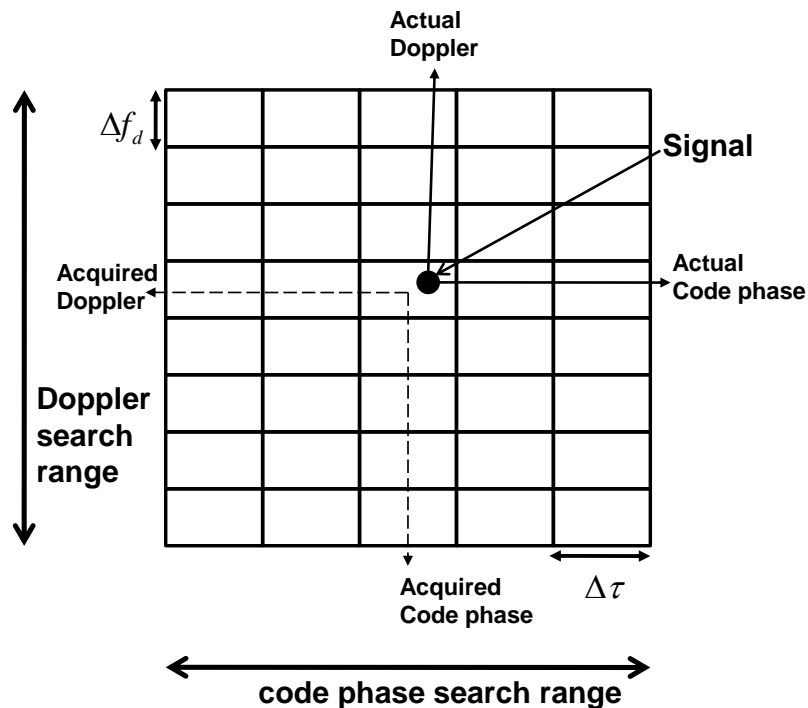


Figure 2-2 Schematic representation of two dimensional acquisition search space

2.3.3 Navigation signal processing

In principle, a GNSS receiver that delivers a traditional code phase based solution needs at least three observations to solve for 3-dimensional user position via trilateration. However, due to the mismatch between satellite and user clocks and various hardware-based delays, an additional fourth unknown, which is the user clock bias, is required. Receivers generally track all satellites in view, thus facilitating an over-determined solution with redundancy which can provide a more accurate and reliable PVT solution. Also, redundant observations are used for Receiver Autonomous Integrity Monitoring

(RAIM) purposes to enhance the integrity of the solution. The carrier phase based navigation solution algorithm used in this thesis is explained in Chapter 6.

2.4 Fundamentals of GNSS signal tracking

The tracking process refines coarse estimates of code phase $\hat{\tau}_i$ and Doppler \hat{f}_{d_i} passed from acquisition and optionally also estimates the carrier phase $\hat{\phi}_i$. Central to GNSS signal processing is the Doppler removal and correlation (DRC) during which the incoming signal is correlated with a local signal replica, as depicted in Figure 2-3.

The goal of the tracking process is to precisely synchronize the local code and carrier signals with the incoming signals using the DRC outputs, a common strategy adopted for CDMA receivers which is also known as the *matched filter* or *correlator*. The duration of integration in DRC depicted by a summation of N samples in Figure 2-3 is known as the *coherent integration period*, $T_{coh} = N / F_s$ and it generally depends on the accuracy of the coarse carrier Doppler estimate \hat{f}_{d_i} and knowledge of the data bit transition instant which is estimated by the *bit synchronization* process in tracking (Dierendonck 1996). For GPS L1 C/A signals, T_{coh} is generally chosen as one code period of 1 ms before bit synchronization and it will be gradually increased to one data bit period of 20 ms after the bit boundary is known.

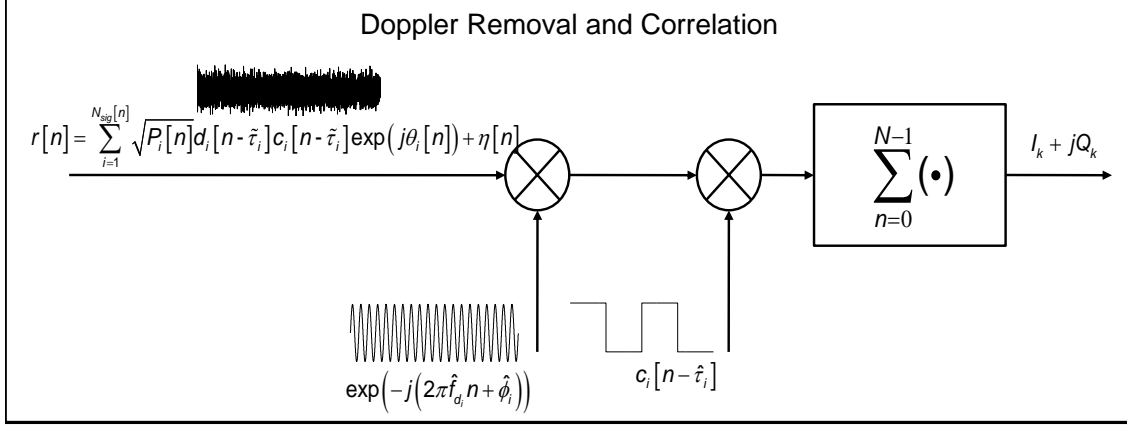


Figure 2-3 DRC process corresponding to i^{th} satellite signal

The mathematical description of the DRC output can be found in Salem et al (2012), which is reproduced below with minor modifications:

$$I_k + jQ_k \approx \sqrt{P_{i,k}} \frac{\sin\left(\frac{\overline{\delta F}_{i,k} T_{coh}}{2}\right)}{\overline{\delta F}_{i,k} T_{coh}} R(\delta\tau_{i,k-1}) \exp(j\overline{\delta\Phi}_{i,k}) + \eta_{coh,i,k} \quad \mathbf{2-13}$$

$$\overline{\delta F}_{i,k} = \delta f_{d_i,k-1} + \frac{\delta a_{i,k-1} T_{coh}}{2}$$

$$\overline{\delta\Phi}_{i,k} = \delta\phi_{i,k-1} + \frac{\delta f_{d_i,k-1} T_{coh}}{2} + \frac{\delta a_{i,k-1} T_{coh}^2}{6}$$

where $P_{i,k}$ is the average satellite signal power, $\overline{\delta F}_{i,k}$ and $\overline{\delta\Phi}_{i,k}$ are average frequency and phase errors over the integration period, $\delta\phi_{i,k-1}$, $\delta f_{d_i,k-1}$ and $\delta a_{i,k-1}$ are the phase [rad], frequency [rad/s] and frequency rate [rad/s²] errors at the beginning of the integration period respectively, $\delta\tau_{i,k-1}$ is the code phase error that is assumed to be a constant over the k^{th} coherent integration, $\eta_{coh,i,k}$ is the white complex normal process expressed as

$$\eta_{coh,i,k} = \eta_{I_{coh,i,k}} + j\eta_{Q_{coh,i,k}}, \text{ with the variance of each component given by } \frac{N_0}{2T_{coh}}. \text{ The average}$$

frequency and phase errors can be computed by assuming constant signal acceleration

over the integration period; more details on the average phase and frequency errors can be found in Psiaki & Jung (2002). In principle, the errors associated with Eq. 2-13 can be estimated using a Maximum Likelihood Estimation (MLE) technique (Kay 1993) by formulating the likelihood function in terms of the probability density of the DRC output. However, in practice the following problems associated with the frequency and phase errors $\overline{\delta F_{i,k}}$ and $\overline{\delta \Phi_{i,k}}$ should be addressed: (1) the errors change with time depending on the incoming signal dynamics and local oscillator effects. Therefore the parameters are recursively estimated using appropriate recursive strategies continuously over time; (2) the effect of noise term, $\eta_{coh,i,k}$, and other error sources such as multipath, interference, etc., needs to be addressed. To this end, the recursive estimation techniques employ filtering of the estimated errors to reduce noise effects. The updated signal parameters are subsequently used as inputs to the numerical controlled oscillators (NCOs), which are used to generate local carrier and PRN code signals, to improve the incoming and local signals synchronization.

To this end, conventional tracking architectures involve the *code lock loop* also known as the *delay lock loop* to estimate code phase error $\delta \tau_{i,k-1}$ and the carrier lock loop to estimate carrier frequency and phase errors $\overline{\delta F_{i,k}}$ and $\overline{\delta \Phi_{i,k}}$. Both code and carrier tracking loops have to be operated simultaneously to refine signal parameter estimates as shown in Figure 2-4.

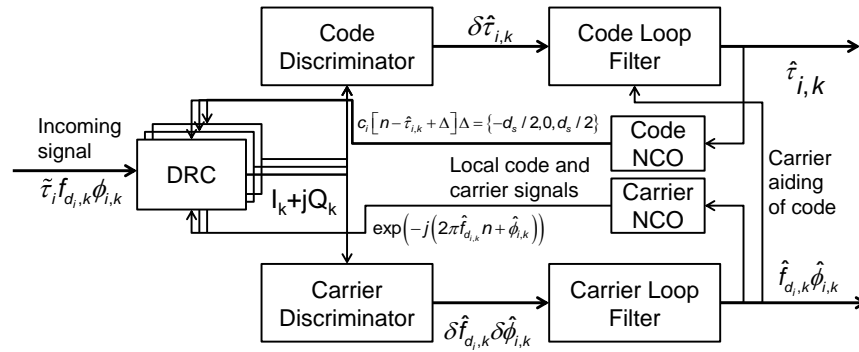


Figure 2-4 Basic components of a GNSS scalar tracking loop architecture

The DRC output correlation values are used to estimate signal parameter errors in Eq. 2-13 by appropriate *discriminators*. The noise in discriminator outputs requires filtering of the estimated errors using a *loop filter* and the outputs of loop filters are used to update signal parameter estimates. The updated signal estimates drive the NCOs thus completing the feedback loop to keep continuous track of the incoming signal variations.

2.4.1 Code lock loop

For GPS L1 C/A signals, traditionally two correlator arms, namely early and late, are used to estimate the code phase $\hat{\tau}_{i,k}$ as shown in Figure 2-5. Consequently, three correlation values are computed using three DRC blocks and the outputs are passed to code discriminator which takes one of the many forms as discussed by Ward et al (2006a) based on the application and receiver operating conditions. The synchronization between code and carrier signals are generally exploited to aid code lock loops with the carrier Doppler estimate. It enables the use of a simple first order code loop filter with relatively narrower bandwidth than otherwise required by a standalone code lock loop without carrier aiding (Dierendonck 1996, Ward et al 2006a).

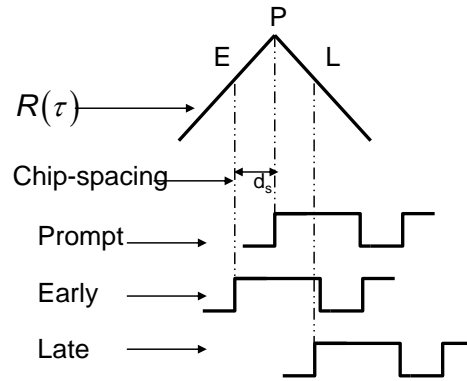


Figure 2-5 Traditional code tracking with early, prompt and late correlator arms

2.4.2 Carrier lock loop

Carrier lock loops are categorized based on the parameters tracked as *frequency lock loop* (FLL) and *phase lock loop* (PLL). The FLL estimates only the carrier frequency $\hat{f}_{d,k}$ allowing signal power to transition between in-phase and quadrature components, while the PLL, which is the focus of this thesis, attempts to keep the signal power in the in-phase component by tracking both carrier frequency $\hat{f}_{d,k}$ and phase $\hat{\phi}_{i,k}$ and, depending on the receiver implementation and application, the rate of change of carrier frequency.

2.4.2.1 Phase lock loop

A number of phase discriminators used in GNSS are given by Dierendonck (1996) and Ward et al (2006a), and explained in detail in Curran (2010). In particular, it is shown in Curran (2010) that a preferred choice of coherent discriminator between quadrature and four-quadrant arctangent discriminators is the latter, due to its comparatively larger linear region, for post-coherent SNR of up to -3 dB. Moreover, the time-varying attenuation of GNSS signals experienced in a pedestrian environment, which will be discussed in more detail in Chapter 3, limits the use of amplitude dependent discriminators. Assuming that

no data bit transition occurs during the coherent integration, the four-quadrant arctangent discriminator provides a good estimate of the phase error given the magnitude of dynamics expected in pedestrian hand held GNSS receivers. It will be explained in the next section that the Kalman filter based tracking architecture do not use explicit discriminators when correlation values from DRC are directly input to the Kalman filter based tracker. Nevertheless, due to the above mentioned reasons the four-quadrant arctangent discriminator, mathematically expressed as follows, is the preferred choice for pedestrian receivers employing discriminator based tracking architectures:

$$\delta\hat{\theta}_{i,k} = \arctan(I_k, Q_k)$$

2-14

The conventional loop filters take the form of proportional-integral (PI) controllers (Ward et al 2006a) which inherently measure various derivatives of the incoming carrier signal phase, namely Doppler, acceleration, jerk, etc. The ability of the PLL to respond to signal dynamics depends on the order of the PI loop filter. Generally, second or third order filters are used in GNSS depending on whether the application demands PLL sensitivity to signal frequency or acceleration respectively. In addition to shaping the dynamic response, the loop filter also reduces the effect of thermal noise on the carrier phase and frequency estimates.

2.4.3 Kalman filter-based tracking

Kalman filters have emerged as potential replacements for traditional PI loop controllers in the communication receivers. Significant work is also done by the GNSS community to exploit Kalman filters for GNSS signal tracking (Psiaki & Jung 2002, Petovello & Lachapelle 2006, O'Driscoll et al 2009, O'Driscoll et al 2011 and Salem et al 2012). The

Kalman filters have the following advantages over traditional PI controllers: (a) the Kalman filter allows dynamic model definition for the signal parameters which eventually contributes in more accurate prediction via additional information; (b) the Kalman filters adapt to changing signal conditions more easily by appropriate modification of process noise and measurement noise matrices; (c) combined tracking of all signal parameters is possible in the same architecture thus avoiding separate DLL-PLL architecture.

The discrete-time Extended Kalman Filter (EKF) formulation takes early, prompt and late correlator measurements as inputs. The error-state vector, measurement vector and design matrix can be expressed as follows:

$$\delta \mathbf{x} = [A \quad \delta\tau \quad \delta\phi \quad \delta f \quad \delta \mathbf{a}]^T \quad \mathbf{2-15}$$

$$\mathbf{z} = [I_k^E \quad Q_k^E \quad I_k^P \quad Q_k^P \quad I_k^L \quad Q_k^L]^T \quad \mathbf{2-16}$$

$$H = \begin{bmatrix} \frac{\partial I_k^E}{\partial A} & \frac{\partial I_k^E}{\partial \delta\tau} & \frac{\partial I_k^E}{\partial \delta\phi} & \frac{\partial I_k^E}{\partial \delta f} & \frac{\partial I_k^E}{\partial \delta \mathbf{a}} \\ \frac{\partial Q_k^E}{\partial A} & \frac{\partial Q_k^E}{\partial \delta\tau} & \frac{\partial Q_k^E}{\partial \delta\phi} & \frac{\partial Q_k^E}{\partial \delta f} & \frac{\partial Q_k^E}{\partial \delta \mathbf{a}} \\ \frac{\partial I_k^P}{\partial A} & \frac{\partial I_k^P}{\partial \delta\tau} & \frac{\partial I_k^P}{\partial \delta\phi} & \frac{\partial I_k^P}{\partial \delta f} & \frac{\partial I_k^P}{\partial \delta \mathbf{a}} \\ \frac{\partial Q_k^P}{\partial A} & \frac{\partial Q_k^P}{\partial \delta\tau} & \frac{\partial Q_k^P}{\partial \delta\phi} & \frac{\partial Q_k^P}{\partial \delta f} & \frac{\partial Q_k^P}{\partial \delta \mathbf{a}} \\ \frac{\partial I_k^L}{\partial A} & \frac{\partial I_k^L}{\partial \delta\tau} & \frac{\partial I_k^L}{\partial \delta\phi} & \frac{\partial I_k^L}{\partial \delta f} & \frac{\partial I_k^L}{\partial \delta \mathbf{a}} \\ \frac{\partial Q_k^L}{\partial A} & \frac{\partial Q_k^L}{\partial \delta\tau} & \frac{\partial Q_k^L}{\partial \delta\phi} & \frac{\partial Q_k^L}{\partial \delta f} & \frac{\partial Q_k^L}{\partial \delta \mathbf{a}} \end{bmatrix} \quad \mathbf{2-17}$$

where $I_k^E, Q_k^E, I_k^P, Q_k^P, I_k^L,$ and Q_k^L are the in-phase and quadrature pairs of early, late and prompt correlation values obtained from three DRC blocks which form the measurement input vector \mathbf{z} . The subscript k denotes the discrete-time index and superscripts E, P and

L denote early, prompt and late. The error-state vector δx consists of the signal amplitude A , code phase error $\delta\tau$, carrier phase error $\delta\phi$, carrier frequency error δf , and carrier frequency rate δa . The notation $\frac{\partial}{\partial \mathbf{s}}$ used in design matrix H is the partial derivative operator with respect to the scalar parameter(s). The measurement noise matrix is expressed as follows:

$$R = \sigma_{coh,k}^2 \begin{bmatrix} 1 & 0 & R(\Delta\tau/2) & 0 & R(\Delta\tau) & 0 \\ 0 & 1 & 0 & R(\Delta\tau/2) & 0 & R(\Delta\tau) \\ R(\Delta\tau/2) & 0 & 1 & 0 & R(\Delta\tau/2) & 0 \\ 0 & R(\Delta\tau/2) & 0 & 1 & 0 & R(\Delta\tau/2) \\ R(\Delta\tau) & 0 & R(\Delta\tau/2) & 0 & 1 & 0 \\ 0 & R(\Delta\tau) & 0 & R(\Delta\tau/2) & 0 & 1 \end{bmatrix} \quad \mathbf{2-18}$$

The variance term $\sigma_{coh,k}^2 = \frac{N_0}{2T_{coh}}$ is equal to the individual variances of the post-coherent noise complex normal noise components, $R(\cdot)$ represents the code autocorrelation function and $\Delta\tau$ is the early-late correlator chip spacing. The EKF system model takes the following form:

$$\frac{d}{dt} \begin{pmatrix} A \\ \delta\tau \\ \delta\phi \\ \delta f \\ \delta a \end{pmatrix} = \overbrace{\begin{bmatrix} 0 & 0 & 0 & 0 & 0 \\ 0 & 0 & 0 & \beta & 0 \\ 0 & 0 & 0 & 1 & 0 \\ 0 & 0 & 0 & 0 & 1 \\ 0 & 0 & 0 & 0 & 0 \end{bmatrix}}^{\text{dynamic model}} \begin{pmatrix} A \\ \delta\tau \\ \delta\phi \\ \delta f \\ \delta a \end{pmatrix} + \overbrace{\begin{bmatrix} 1 & 0 & 0 & 0 & 0 \\ 0 & 1 & \beta & 0 & 0 \\ 0 & 0 & 1 & 0 & 0 \\ 0 & 0 & 0 & 1 & 0 \\ 0 & 0 & 0 & 0 & 1 \end{bmatrix}}^{\text{stochastic model}} \begin{pmatrix} w_A \\ w_\tau \\ w_\phi \\ w_f \\ w_a \end{pmatrix} \quad \mathbf{2-19}$$

where $\frac{d}{dt}$ is the time derivative operator, β is the radians to chips conversion constant, the driving function for the signal amplitude is represented as w_A , the code-multipath and

code-carrier divergence are modeled by w_r , w_ϕ and w_f models the local oscillator drift and bias perturbations due to clock effects, w_a represents the frequency rate perturbations due to LOS dynamics and local oscillator acceleration sensitivities. All driving functions represented by $w_{(\cdot)}$ are assumed to be white noise. Assuming that the dynamic model is time-invariant, the system model can be converted to discrete-time model using the steps discussed by Brown & Hwang (1997). The resulting state transition and process noise matrices are as follows:

$$\Phi = \begin{bmatrix} 1 & 0 & 0 & 0 & 0 \\ 0 & 1 & 0 & \beta\Delta t & \beta\frac{\Delta t^2}{2} \\ 0 & 0 & 1 & \Delta t & \frac{\Delta t^2}{2} \\ 0 & 0 & 0 & 1 & \Delta t \\ 0 & 0 & 0 & 0 & 1 \end{bmatrix} \quad \mathbf{2-20}$$

$$Q = \begin{bmatrix} \Delta tq_A & 0 & 0 & 0 & 0 \\ 0 & \begin{pmatrix} \Delta tq_r + \Delta t\beta^2 q_\phi \\ + \frac{\Delta t^3}{3}\beta^2 q_f + \frac{\Delta t^5}{20}\beta^2 q_a \end{pmatrix} & \beta\left(\Delta tq_\phi + \frac{\Delta t^3}{3}q_f + \frac{\Delta t^5}{20}q_a\right) & \beta\left(\frac{\Delta t^2}{2}q_f + \frac{\Delta t^4}{8}q_a\right) & \left(\frac{\Delta t^3}{6}\beta q_a\right) \\ 0 & \beta\left(\Delta tq_\phi + \frac{\Delta t^3}{3}q_f + \frac{\Delta t^5}{20}q_a\right) & \left(\Delta tq_\phi + \frac{\Delta t^3}{3}q_f + \frac{\Delta t^5}{20}q_a\right) & \left(\frac{\Delta t^2}{2}q_f + \frac{\Delta t^4}{8}q_a\right) & \left(\frac{\Delta t^3}{6}q_a\right) \\ 0 & \beta\left(\frac{\Delta t^2}{2}q_f + \frac{\Delta t^4}{8}q_a\right) & \left(\frac{\Delta t^2}{2}q_f + \frac{\Delta t^4}{8}q_a\right) & \left(\Delta tq_f + \frac{\Delta t^3}{6}q_a\right)q_a & \left(\frac{\Delta t^2}{2}q_a\right) \\ 0 & \left(\frac{\Delta t^3}{6}\beta q_a\right) & \left(\frac{\Delta t^3}{6}q_a\right) & \left(\frac{\Delta t^2}{2}q_a\right) & \Delta tq_a \end{bmatrix} \quad \mathbf{2-21}$$

where Δt is the time difference between the two Kalman filter update instants, the subscripted $q_{(\cdot)}$ terms represent the power spectral densities of the respective $w_{(\cdot)}$ stochastic driving functions.

2.4.3.1 Dynamic performance of Kalman filter

The dynamic performance of the PI loop controller is dictated by the loop bandwidth and therefore it is relatively easy to analyze the dynamic response due to simplicity of the tracking architecture. In contrast, it is difficult to analyse the equivalent bandwidth of the Kalman filter based tracking architecture due to the time-varying Kalman gain and complexity of the system. To this end, Salem et al (2011) developed an empirical methodology to compare the two architectures as follows. In the first step, one obtains the empirical "steady state" noise performance of EKF architecture and sets the bandwidth of the traditional architecture which provides the same noise performance. In the second step, the better tracking architecture is chosen based on which of the two results in better dynamic performance measured by the PLI metric, which is explained in the next section, when the receiver is in motion. It is shown by Salem et al (2011) that the EKF architecture outperforms the traditional architecture in dynamic performance and tracking sensitivity. This provides further justification to use the EKF architecture in this thesis.

2.5 Benefits of carrier phase tracking

Carrier phase tracking is not mandatory in consumer-grade GNSS receivers as the estimation of PVT solutions is possible using only code phase and carrier frequency tracking. However, tracking the carrier phase can provide the following benefits:

1. Navigation data bit decoding sensitivity can be improved by up to 3 dB as the bit error rate (BER) is reduced due to coherent data demodulation which uses only in-phase correlation values. On the contrary, if FLL is used then data bit demodulation should

be performed using both in-phase and quadrature correlation values, thus increasing BER.

2. The use of coherent discriminators results in more accurate code phase and Doppler measurements, can tolerate higher phase dynamics and can reduce the likelihood of cycle slips and loss of phase-lock.
3. Time differencing the carrier phase measurements, assuming no cycle slips, results in accurate change in range, which can be used to smooth code phase based pseudorange to obtain more precise PVT solutions.
4. Enables kinematic applications to enjoy carrier phase-based solution.

2.6 Tracking performance indicators

Three metrics are widely used to quantify GNSS signal tracking performance, namely C/N_0 , frequency lock indicator (FLI) and PLI (Dierendonck 1996). These indicators are obtained through appropriate processing of noisy correlator outputs and therefore caution must be exercised while using these indicators. The C/N_0 and PLI indicators are relevant to this thesis and are briefly discussed in this section.

2.6.1 C/N_0 as a tracking performance indicator

The C/N_0 of a satellite signal is the measure of the satellite signal strength at the input of the antenna and, therefore, it is affected by the signal propagation channel. The C/N_0 for a given satellite signal is defined as

$$C/N_0 = E \left[\frac{P_i}{N_0} \right] \quad \mathbf{2-22}$$

where $E[\bullet]$ is the statistical expectation operator. It is a common practice to take the logarithm on Eq. 2-22 and express C/N_0 in units of dB-Hz. From Section 2.2.1, the effective signal power incident on the receiver antenna varies between -128.5 dBm and -160 dBm for pedestrian applications. The value of N_0 was calculated to be about -174 dBm. Therefore, from Eq. 2-22, the C/N_0 values typically range from 45.5 to 14 dB-Hz for pedestrian receivers. Overall, the C/N_0 parameter dictates the measurements quality of the corresponding satellite signal. One of the early C/N_0 estimators used in GNSS is discussed in Dierendonck (1996), which is still in use today and it is based on the estimation of a monotonic function of C/N_0 . The function is then inverted to obtain the estimate C/N_0 . Under accurate code and carrier tracking operations, by substituting the approximations $\delta\tau_{i,k-1} \approx 0$ and $\overline{\delta F_{i,k}} \approx 0$ in Eq. 2-13, the prompt correlation values can be expressed as

$$I_k + jQ_k = \sqrt{P_{i,k}} \exp(j\overline{\delta\Phi}_{i,k}) + \eta_{coh,i,k} \quad \text{2-23}$$

Assuming that Eq. 2-23 corresponds to 1 ms integration period of GPS L1 C/A signals, and assuming the data bit boundary is also known, the correlation values of Eq. 2-23 can be used to estimate C/N_0 as follows (Dierendonck 1996):

$$\hat{\mu}_i = \frac{\left(\sum_{k=1}^L I_k\right)_i^2 + \left(\sum_{k=1}^L Q_k\right)_i^2}{\left(\sum_{k=1}^L I_k^2 + Q_k^2\right)_i} \quad \text{2-24}$$

$$\frac{C}{N_0} = 10 \log_{10} \left(\frac{1}{T} \frac{\hat{\mu}_i - 1}{20 - \hat{\mu}_i} \right)$$

where $L = 20$, corresponds to the integration of one full GPS L1 C/A data bit period. The ratio term $\hat{\mu}_i$ can be averaged using a moving average (MA) filter to reduce the effect of

noise inherent in the correlation values. It is evident from Eq. 2-24 that C/N_0 estimate do not depend on carrier phase tracking. In contrast, in order to obtain accurate C/N_0 estimate the code phase or carrier frequency errors should not introduce correlation losses. Therefore, it can be concluded that the C/N_0 estimate can be used as a qualitative indicator of the code phase and carrier frequency tracking performance. However, PLI is used for carrier phase tracking performance monitoring, which is discussed next.

2.6.2 Phase Lock Indicator (PLI)

The PLI used in this work measures differential power across in-phase and quadrature components to obtain an estimate of the phase alignment between the incoming and local carrier signal replica (Dierendonck 1996). The PLI can be mathematically represented as

$$\text{PLI}_k = \frac{I_k^2 - Q_k^2}{I_k^2 + Q_k^2} \quad \text{2-25}$$

where PLI_k represents the PLI value computed from prompt correlation values I_k and Q_k corresponding to the k^{th} tracking loop update. In order to obtain a more reliable estimate of the PLI, PLI_k is time-averaged to obtain a more reliable indicator:

$$\text{PLI}_k^{\text{MA}} = \frac{1}{M} \sum_{i=0}^{M-1} \text{PLI}_{k-i} \quad \text{2-26}$$

The number of taps used in the MA filter in this thesis varies from 10 to 100, which correspond to 200 milliseconds to 2 seconds assuming the coherent integration is 20 milliseconds for GPS L1 C/A signals. It can be shown that the PLI metric employed in this work approximately measures $\cos(2\overline{\delta\Phi}_{i,k})$, where $\overline{\delta\Phi}_{i,k}$ is the average phase misalignment as indicated by the arguments of the exponential term in Eq. 2-13. It can also be shown that under high SNR assumption, the PLI in Eq. 2-25 results in the arc-

tangent maximum likelihood estimate (MLE) of the average phase error. However, the correlator values are affected by the thermal noise and hence the PLI is more non-linear and noisy as the SNR degrades and therefore it should be used with caution. The Matlab™ and hardware simulation results shown in Figure 2-6 corroborates the increased non-linearity and standard deviation of the PLI_k^{MA} metric as the C/N_0 and, alternatively the SNR, degrades.

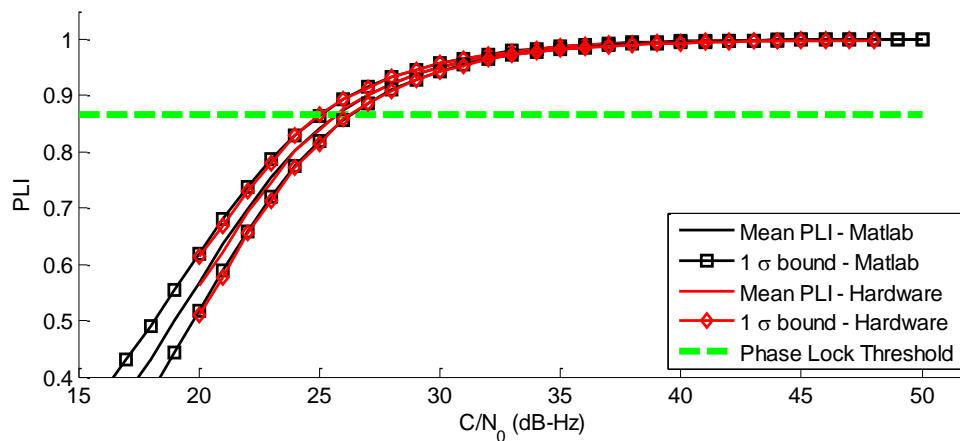


Figure 2-6 PLI simulation results using Matlab™ and a hardware GNSS simulator

A Matlab™ simulation was performed to compute moving average PLI values from simulated in-phase and quadrature samples generated with specific SNRs, without considering the local oscillator and satellite-receiver line-of-sight effects. The GPS dataset for hardware simulation was generated with a Spirent GSS7700 simulator, in which a static receiver scenario was programmed with 12 satellites in view, and the output power was equalized for all satellite signals. The IF data were collected using a 1-bit front-end with 10 MHz complex sampling while gradually lowering the power levels in steps of 1 dB per 10 s. The total duration of the data collection was five minutes. The IF data was post-processed using a modified version of the GNSS software receiver GSNRx™

(Petovello et al 2008), which employed Kalman filter-based tracking architecture explained in the previous section with an acceleration noise spectral density of 0.01 m/s^3 . The acceleration spectral density was lowered to support reliable carrier tracking at lower power levels given the static receiver scenario.

This experiment demonstrated that the satellite motion, the local oscillator stability and phase noise effects, at least for the duration of 5 minutes, can be effectively handled by appropriately designed tracking loops without significantly compromising the carrier phase tracking performance. However, as shown in the plot, the mean PLI value drops below the phase lock threshold of 15 degrees purely due to low SNR, thus demonstrating strong non-linearity of the PLI. The phase lock threshold is chosen as a general rule of thumb that the 1-sigma phase error threshold including all sources of carrier phase disruptions should be less than 15 degrees (Ward et al 2006a). Nevertheless, the PLI can be used as a qualitative measure of carrier phase tracking performance, especially in the current work where the PLI is used as a comparative performance analysis metric across tracking strategies. In addition to the PLI, cycle slip detection and double-difference carrier phase measurements also evaluate carrier phase tracking performance and are commonly used. These two metrics are explained in more detail and used in Chapter 6.

2.6.3 Frequency Lock Indicator

In principle, the FLI is obtained by differentiating the phase error. Therefore, complex correlation values corresponding to two instants are required to estimate FLI. It can be shown that the FLI analogous to the PLI discussed in Section 2.6.2 can be mathematically expressed as

$$FLI_k = \frac{d_{IQ,k}^2 - c_{IQ,k}^2}{d_{IQ,k}^2 + c_{IQ,k}^2} \quad 2-27$$

where $d_{IQ,k}$ and $c_{IQ,k}$ represent dot and cross products of two vectors expressed as

$$\begin{aligned} d_{IQ,k} &= I_k I_{k-1} + Q_k Q_{k-1} \\ c_{IQ,k} &= I_{k-1} Q_k + Q_{k-1} I_k \end{aligned} \quad 2-28$$

The FLI_k can also be refined using a MA filter. In addition to performance evaluation, these indicators are used for decision-based changes in the tracking architecture to be used in the receiver. For example, PLI can be used to transition from the DLL-PLL phase tracking mode to the DLL-FLL frequency tracking mode when loss of phase lock is observed. Conversely, the receiver can switch back to DLL-PLL mode when FLI meets a desirable value.

In this thesis accurate code phase synchronization is assumed and hence C/N_0 and PLI are sufficient for qualitative assessment of carrier frequency and phase tracking performance across tracking architectures, in cases where an absolute phase reference is not available.

2.7 Summary

An introduction to GNSS signal structure was provided in this chapter while focusing on GPS L1 C/A signals. An overview of signal processing operations performed by a GNSS receiver is also provided emphasizing on the baseband signal processing. In particular, an introductory discussion on GNSS carrier phase tracking using Kalman filter based tracking architecture was done. The tracking performance indicators, particularly, the PLI was introduced and its accuracy bounds were empirically derived. The analysis of experimental results in the following chapters is done assuming the signal model and receiver operations discussed in this chapter.

Chapter Three: Pedestrian Environment Characterization

3.1 Introduction

The objective of this chapter is to understand the effects of pedestrian dynamics and human attenuation of GNSS signals on carrier phase tracking. The dynamic characterization is done using MEMS based accelerometers as they are suitable for pedestrian applications. The accelerometers data is processed and converted into PSD by non-parametric spectrum estimation techniques which are based on Fourier signal analysis as discussed in Section 3.2. The effect of human attenuation on carrier phase tracking is analyzed in Section 3.3.

3.2 Dynamics Characterization

The MEMS based accelerometers are finding uses in myriad of applications including navigation due to their low cost, size, and power consumption. In connection with the pedestrian navigation the accelerometers are extensively used in gait analysis as discussed in Chapter 1. On similar lines, accelerometers are used in this thesis for pedestrian dynamics characterization to study pedestrian motion patterns. Particularly, motion patterns analysis of pedestrian velocity and position processes are conducted in the frequency domain in terms of PSD. The relationship between pedestrian motion patterns and GNSS signal carrier frequency and phase are explored. The dynamics characterization provides vital information which will be used in chapters 4 and 5 to customize tracking architectures for enhanced carrier tracking performance.

3.2.1 Accelerometer model

The measurement from a three-axis accelerometer can be modeled as follows:

$$\begin{bmatrix} a_x \\ a_y \\ a_z \end{bmatrix} = \begin{bmatrix} f_{a,x} \\ f_{a,y} \\ f_{a,z} \end{bmatrix} + \begin{bmatrix} b_{a,x} \\ b_{a,y} \\ b_{a,z} \end{bmatrix} + \begin{bmatrix} S_x & N_{xy} & N_{xz} \\ N_{yx} & S_y & N_{yz} \\ N_{zx} & N_{zy} & S_z \end{bmatrix} \begin{bmatrix} f_{a,x} \\ f_{a,y} \\ f_{a,z} \end{bmatrix} + \begin{bmatrix} \eta_{a,x} \\ \eta_{a,y} \\ \eta_{a,z} \end{bmatrix} \quad 3-1$$

where $a_{(\bullet)}$ represents acceleration measurements, the subscripts x , y and z represent the values measured along the corresponding axis, $f_{a,(\bullet)}$ is the true acceleration also known as the specific force, $b_{a,(\bullet)}$ is the measurement bias, $S_{(\bullet)}$ is the scale factor error, N_{xy} is the non-orthogonality component between x and y axes, and $\eta_{a,(\bullet)}$ is the white measurement noise.

The measurement bias $b_{a,(\bullet)}$ can be modeled using the three following components (Groves 2008): (1) systematic bias that is usually determined during the factory calibration; (2) turn-on bias which remains constant only until the next device power-on; and (3) the time-varying "bias" which changes its value during the device operation primarily due to temperature variations. In general, the scale factor errors also contain systematic and time-varying components. The systematic components of bias and scale factor, along with non-orthogonality errors are factory-calibrated and hence easily removed from measurements. In addition to those mentioned in Eq. 3-1, there are other errors such as non-linearity between the input and output, bias and scale factor asymmetries, dead-zone output region for which no output is observed despite the input, and quantization errors due to ADC. However, these errors are generally negligible and can be ignored. The time-varying biases are generally modeled as Gauss-Markov random processes and estimated along with the navigation states (Groves 2008). The time-

varying scale factors are also estimated in case of high dynamic range applications. However, such error estimation techniques are not relevant to this chapter, and hence not discussed.

Table 3-1 Accelerometer Specifications

Specification	Value
Dynamic range	+/- 24 g
Noise spectral density	650 $\mu\text{g}/\sqrt{\text{Hz}}$
Nominal Bandwidth	433 Hz
Nominal Measurement rate	866 Hz
Resolution	14 bit
Sensitivity	12 mg/bit

The specifications of three-axis portable accelerometers hosted by the 3-space sensor IMU data logger (TSS-DL-HH-S 2012) used in this thesis are listed in Table 3-1. The IMU data logger captures the three-axis acceleration data along with data from other sensors into micro SD card thus being the convenient setup for pedestrian applications.

3.2.2 Time series analysis

One of the simplest signal analysis methods is to analyze the signal variation over time. The visual analysis of signal variations over time provides insight into the nature of the underlying system. To this end, time-variation of accelerations recorded during a series of pedestrian movements on a flat terrain, namely regular walking, running and biking along with a few short static instants in between the modes. Two IMU locations on subject are studied, namely strapping on the wrist and the lower pocket of cargo shorts such that the IMU was up to subject's knee-level. The variation of accelerations over time corresponding to the shorts pocket dataset is shown in Figure 3-1.

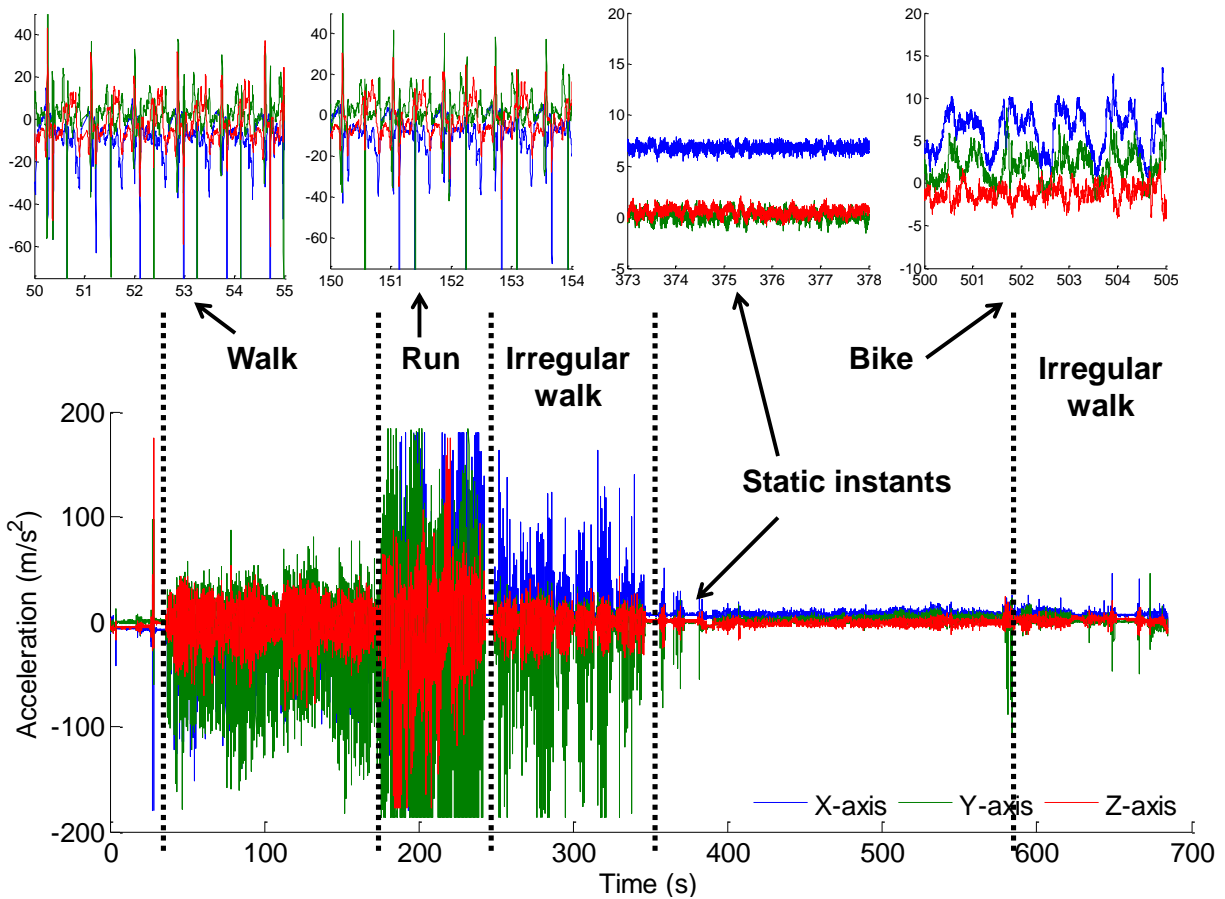


Figure 3-1 Acceleration patterns based on the pedestrian motion mode for pocket data

The subplots on top of Figure 3-1 shows magnified acceleration variations to distinguish motion patterns. The following attributes of acceleration signals can be seen from Figure 3-1: (1) the pedestrian dynamics in general is *non-stationary* as the acceleration patterns and magnitudes change based on the motion mode, for example, running to biking; (2) the pedestrian motion appears to exhibit *quasi-periodicity* during a specific motion mode. For example, the top-left subplot of Figure 3-1 corresponding to regular walking, exhibits repeating patterns at almost regular intervals. A similar analysis for the IMU strapped on the pedestrian's right wrist is shown in Figure 3-2.

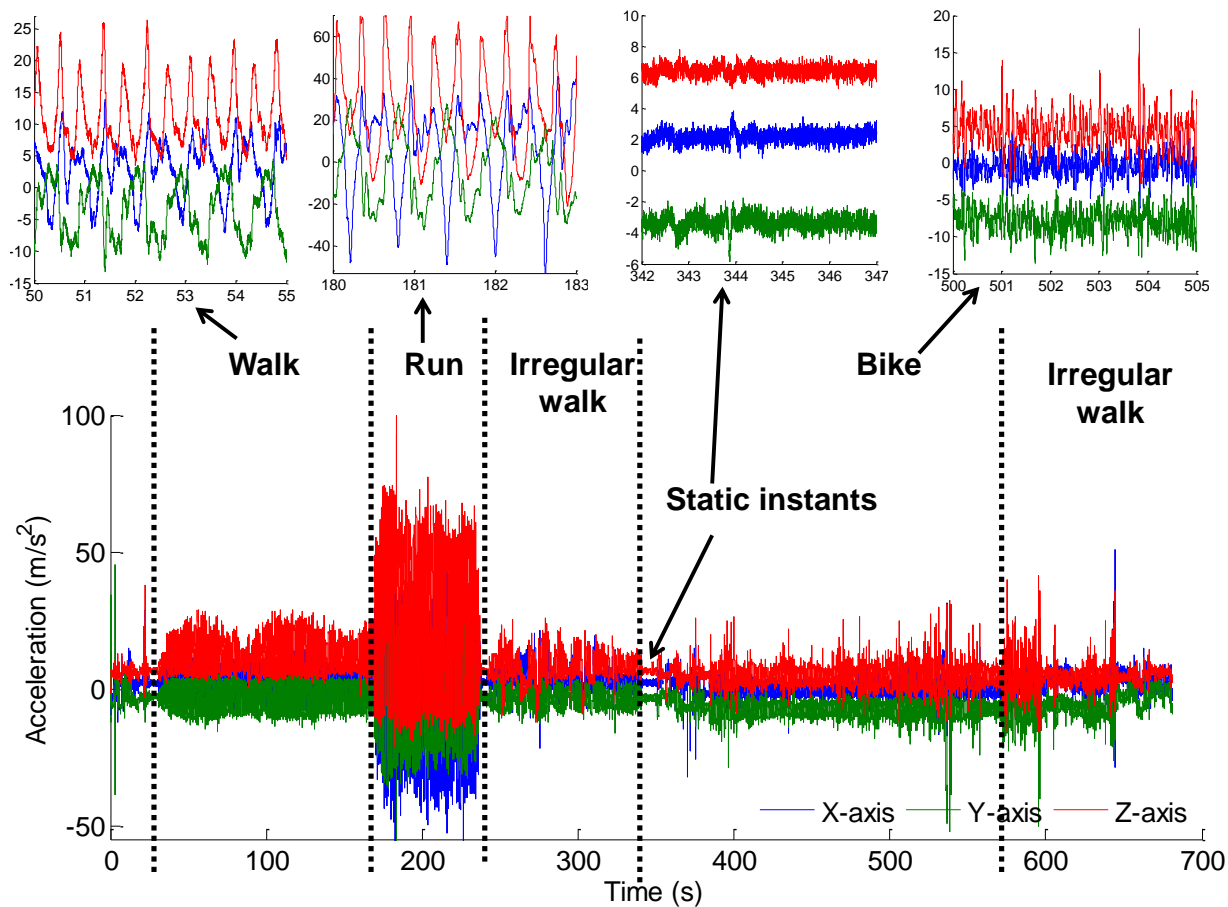


Figure 3-2 Acceleration patterns based on the pedestrian motion mode for wrist dataset

The subplots in Figure 3-2 corroborate the general non-stationary and mode-specific quasi-periodicity of pedestrian dynamics, which are also evident in the pocket dataset. In addition, the magnitude and pattern of acceleration variations are significantly different from Figure 3-1 to Figure 3-2, which indicates that the pedestrian dynamics is a function of sensor location.

3.2.3 Interpolation to get uniformly sampled data

The sampling duration of 3-space sensors over time is not constant as shown in Figure 3-3 (a) for the pocket dataset discussed in the previous section. Therefore, linear

interpolation is used to convert the logged data into uniform data rate of $F_{S,IMU}$ which is 1 KHz. The effect of interpolation on the data is shown in Figure 3-3 (b). The up-sampling introduces correlation in the acceleration measurements, converting the white noise process $\eta_{a,(*)}$ into time-correlated process. However, the effect is assumed to be insignificant for the purposes of this work.

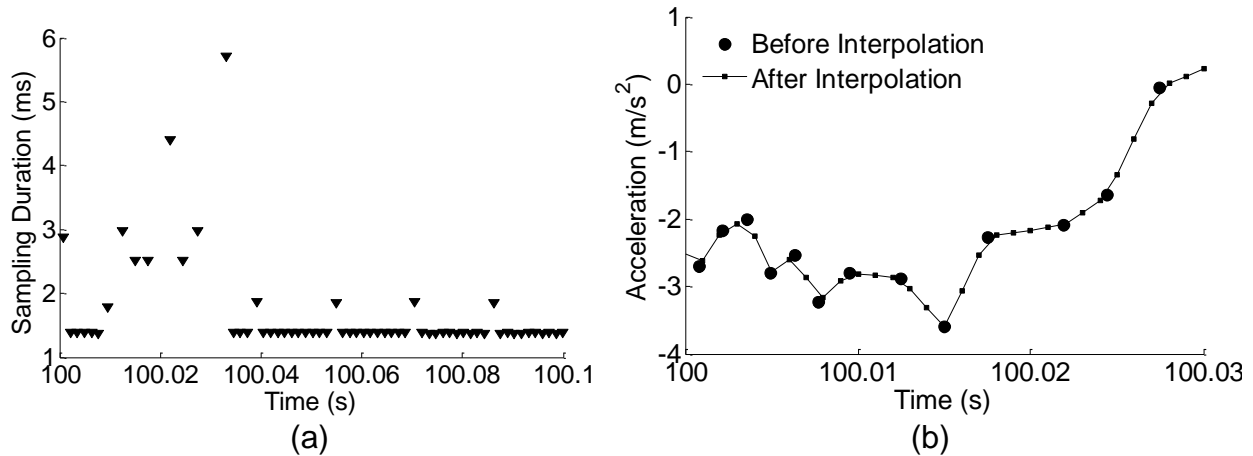


Figure 3-3 (a) The plot shows that the durations between successive samples are non-uniform; (b) the effect of interpolation on acceleration measurements is shown for a portion of the pocket dataset - interpolation is used to obtain uniformly sampled signal

3.2.4 Double integration of acceleration

The characterization needs to be performed in terms of the velocity and position as they are related to the LOS carrier frequency and phase respectively, which necessitates conversion of the *acceleration process* to *velocity and position processes* via successive integrations. A constant acceleration only results in linear change in velocity and quadratic change in position, which is effectively handled by PLL with a third order loop filter. However, the actual dynamics exhibited by pedestrian receivers contain time-varying accelerations with significant magnitudes as shown in Section 3.2.2, thus forcing even a

third order PLL into sub-optimal operating mode due to prevailing tracking errors in *steady state*. The steady state errors can be reduced by increasing the loop bandwidth, which also increases thermal noise effects. Therefore, it is of interest to characterize the variations in accelerations, which is termed herein as *the acceleration process*, and resulting *velocity* and *position processes*. The acceleration and velocity mean values in all the three axes are removed before the first and second integrations respectively. The dataset is segmented into overlapping blocks and the integration is performed block-wise as

$$\begin{aligned} \mathbf{v}[n] &= T_s \sum_{i=n}^{(n+N-1)} (\mathbf{a}[i] - \bar{\mathbf{a}}) \\ \mathbf{p}[n] &= T_s \sum_{i=n}^{(n+N-1)} (\mathbf{v}[i] - \bar{\mathbf{v}}) \end{aligned} \quad \mathbf{3-2}$$

where the bold symbols $\mathbf{a} = [a_x \ a_y \ a_z]^T$, $\mathbf{v} = [v_x \ v_y \ v_z]^T$ and $\mathbf{p} = [p_x \ p_y \ p_z]^T$ are three-dimensional acceleration, velocity and position vectors respectively, $T_s = 1/F_{s,IMU}$ is the sampling frequency after interpolation, N is the number of samples per block of data, and the bar on a vector $\bar{\mathbf{q}}$ represents the sample mean of the vector over the current block

$$\text{expressed as } \bar{\mathbf{q}} = \frac{T_s}{N} \sum_{i=n}^{(n+N-1)} \mathbf{q}[i].$$

3.2.5 Estimation of power spectral density

A brief time-domain analysis reveals that pedestrian processes are, in general, non-stationary, but exhibit quasi-periodic patterns over a short duration specific to the pedestrian motion mode. Therefore, the parametric spectrum estimation techniques are

difficult to apply for spectrum analysis of pedestrian dynamics. A non-parametric technique is used in this work, namely Welch's method (Welch 1967), which is based on the Fourier signal analysis and it is schematically represented in Figure 3-4.

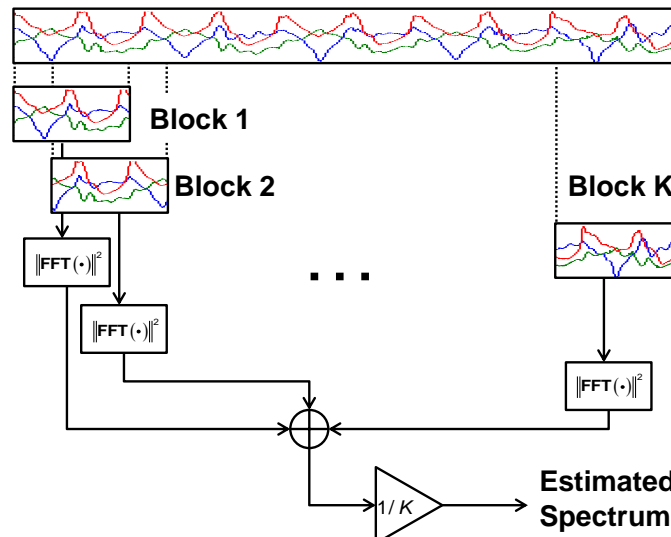


Figure 3-4 Welch's method of spectrum estimation of a random process

The Welch's method of spectrum estimation consists of the following steps (Proakis & Manolakis 2001): (a) segmentation of data into overlapping blocks; (b) Fourier transform of the segmented data using FFT and conversion of FFT output into spectral density estimates by squaring; and (c) averaging the estimated spectra across data segments in order to reduce the variance. This method inherently assumes that the underlying process is stationary. Although this assumption is strictly not true for the pedestrian dynamics in general, this assumption holds well over a short period of time when the pedestrian motion mode does not involve abrupt changes. The spectrum estimation corresponding to a single block of data can be mathematically represented as (Proakis & Manolakis 2001)

$$\widehat{S}_{p_x p_x}^n(f) = \frac{1}{NU} \left| \sum_{i=n}^{n+N-1} p_x[i] w[i] e^{-j2\pi f i} \right|^2 \quad 3-3$$

where $S_{p_x p_x}^n$ is the estimated spectrum of the data segment p , N is the number of samples in a block, the data segment is multiplied by a window function w for the purposes discussed later in this section, f is the Discrete-Time Fourier Transform (DTFT) frequency variable, $U = \frac{1}{N} \sum_{i=0}^{N-1} w^2[i]$ is required to normalize the power in the window function w . The

average spectrum estimate is given by

$$\widehat{S}_{p_x p_x}(f) = \frac{1}{K} \sum_{n=1}^K \widehat{S}_{p_x p_x}^n(f) \quad 3-4$$

Although the mathematical models described in this section represent the DTFT which consists of continuous frequency variable, in practice the FFT is used to implement spectrum estimation algorithms, which samples the spectrum at discrete frequencies.

3.2.6 Resolution versus spectral dynamic range trade-off

When a rectangular window is used in Eq. 3-3, the spectrum estimator reduces to a *periodogram*. It is shown that the periodogram is a *consistent* estimator, meaning the estimated spectrum approaches the true value when the number of samples considered approaches infinity. However, the data segment is restricted in this work due to the following reasons: (a) only a finite length of data is available in practice, which can be mathematically represented by multiplying the data by a finite duration window with unit amplitude; (b) more importantly, due to variations within the pedestrian motion mode itself, the data segment duration is restricted to one gait cycle corresponding to the motion mode. It can be shown that the expected value of the Welch spectrum estimate in Eq. 3-3

is the convolution of the Fourier transform of the window function with the Fourier transform of the signal which can be expressed mathematically as follows:

$$\widehat{S}_{p_x p_x}^n(f) = \int_{-1/2}^{1/2} \Gamma_{p_x p_x}^n(\alpha) W(f - \alpha) d\alpha \quad 3-5$$

where $\Gamma_{p_x p_x}^n$ is the actual spectrum of the data segment and W is the spectrum of the window function. The presence of the window distorts the signal spectrum in the two following ways (Proakis & Manolakis 2001): (1) loss of frequency resolution of the signal due to finite window width; and (2) unwanted side-lobes of the window function W results in bias in the estimated signal spectrum. These effects are illustrated with rectangular and Hamming windows in Figure 3-5(b) on a composite signal which consists of three sinusoids at 1.5, 3 and 5 Hz with corresponding spectral density values of -6, -6 and -20 dB. The sampling frequency and data segment duration were chosen arbitrarily at 1 KHz and 1.28 s. The spectral properties of rectangular and Hamming windows are in Figure 3-5(a).

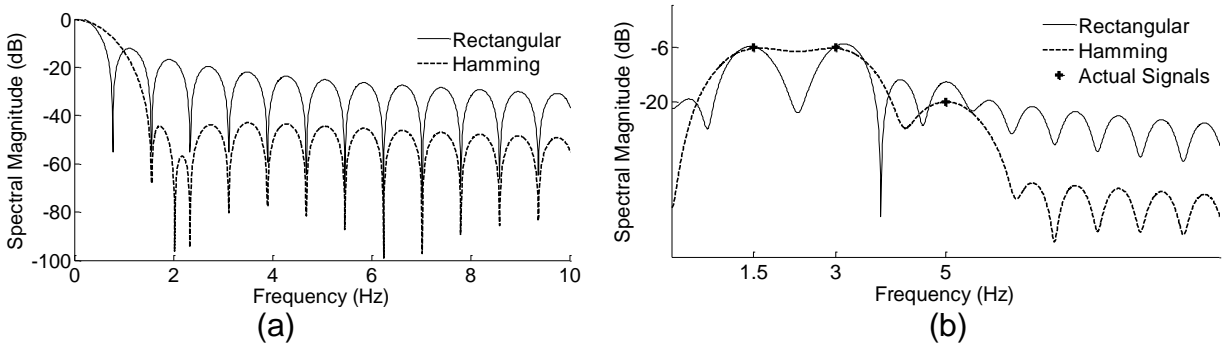


Figure 3-5 (a) spectral properties of window functions (b) Effect of windows on spectral estimation

The analysis of Figure 3-5(b) indicates the following:

- In order to resolve signal components which are closely spaced in frequency, the window function needs to have small main lobe width. For example, the signal

components 1.5 Hz and 3 Hz can be easily resolved by rectangular window, whereas by using the Hamming window the peaks are barely distinguished.

- Side lobes of the rectangular window contain significant power that affect the spectral identification of the third signal component at 5 Hz, whereas this weak signal peak can be clearly recognized in the spectral estimate with Hamming window.

These contradicting effects of windowing result in spectral resolution versus dynamic range trade-off. In this work, a Hamming window is used for the estimation of cumulative power distribution so that the false peaks at high frequencies are reduced.

3.2.7 Spectrum analysis of pedestrian dynamics

An overview of the time-varying nature of pedestrian dynamics in the frequency domain can be obtained from STFT based acceleration spectrograms corresponding to wrist-mounted and pant pocket datasets, which were used in Section 3.2.2, are shown in Figure 3-6. The walking and running modes exhibit harmonics characterized by horizontal shades of high spectral intensity for both datasets. When cycling, harmonics are observed by the sensor placed in the pocket which measures pedaling, which is noticeable in Figure 3-6 (b), whereas the wrist-strapped IMU experiences high frequency vibrations due to the terrain variations as the hands were placed on the bicycle handlebar.

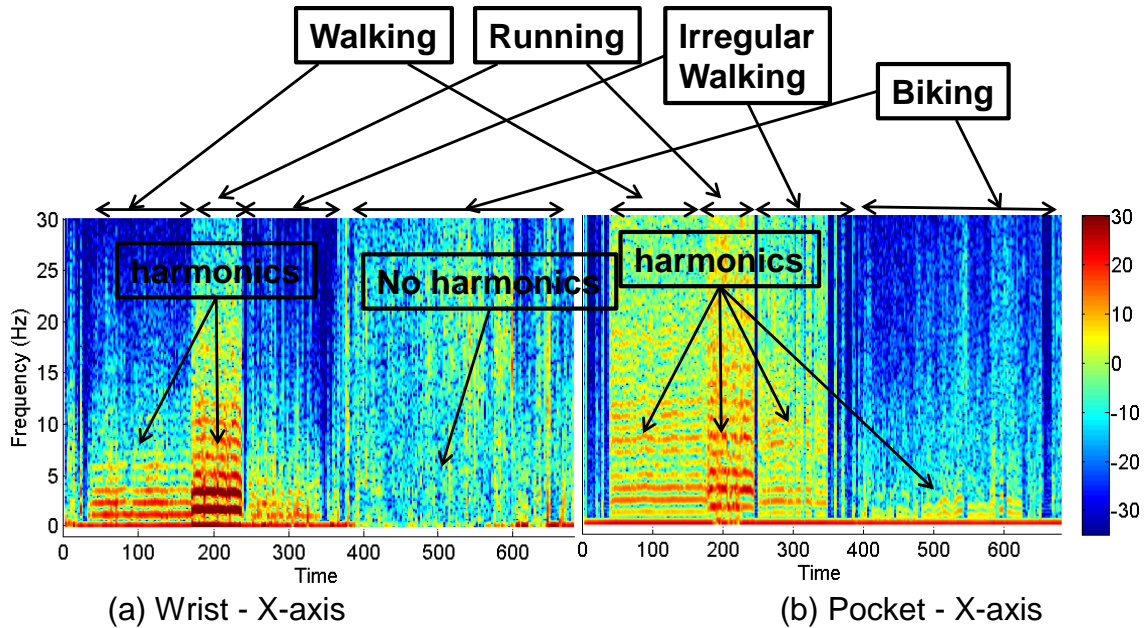


Figure 3-6 Spectrogram corresponding to datasets containing several motion modes

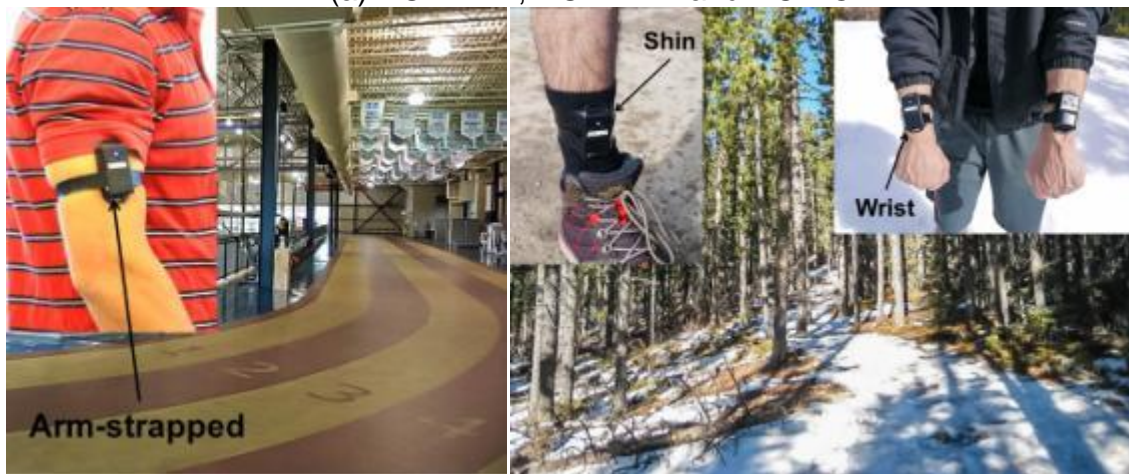
A series of datasets were collected at various sensor locations on the subject as listed in Table 3-2 to enable detailed dynamics characterization. The datasets are processed according to the method described in Section 3.2.5. The number of FFT points for the computation of PSD was chosen to obtain a smooth frequency resolution of 0.1 Hz.

Table 3-2 Datasets corresponding to dynamics characterization

Dataset name	Location on Subject	Dynamics Involved	Duration (min)
DC-BP-W	Backpack	Walking on a flat terrain	20
DC-HH-W	Hand held	Walking on a flat terrain	10
DC-PO-W	Trouser pocket	Walking on a flat terrain	20
DC-AR-R	Strapped on Arm	Running on indoor track	15
DC-WR-HK	Strapped on wrist	Running down a mountain (Prairie Mountain)	5
DC-FT-HK	Strapped on shin	Running down a mountain	5



(a) DC-BP-W, DC-HH-W and DC-PO-W



(b) DC-AR-R

(c) DC-WR-HK and DC-FT-HK

Figure 3-7 Data collection setup showing sensor locations and data collection scenarios

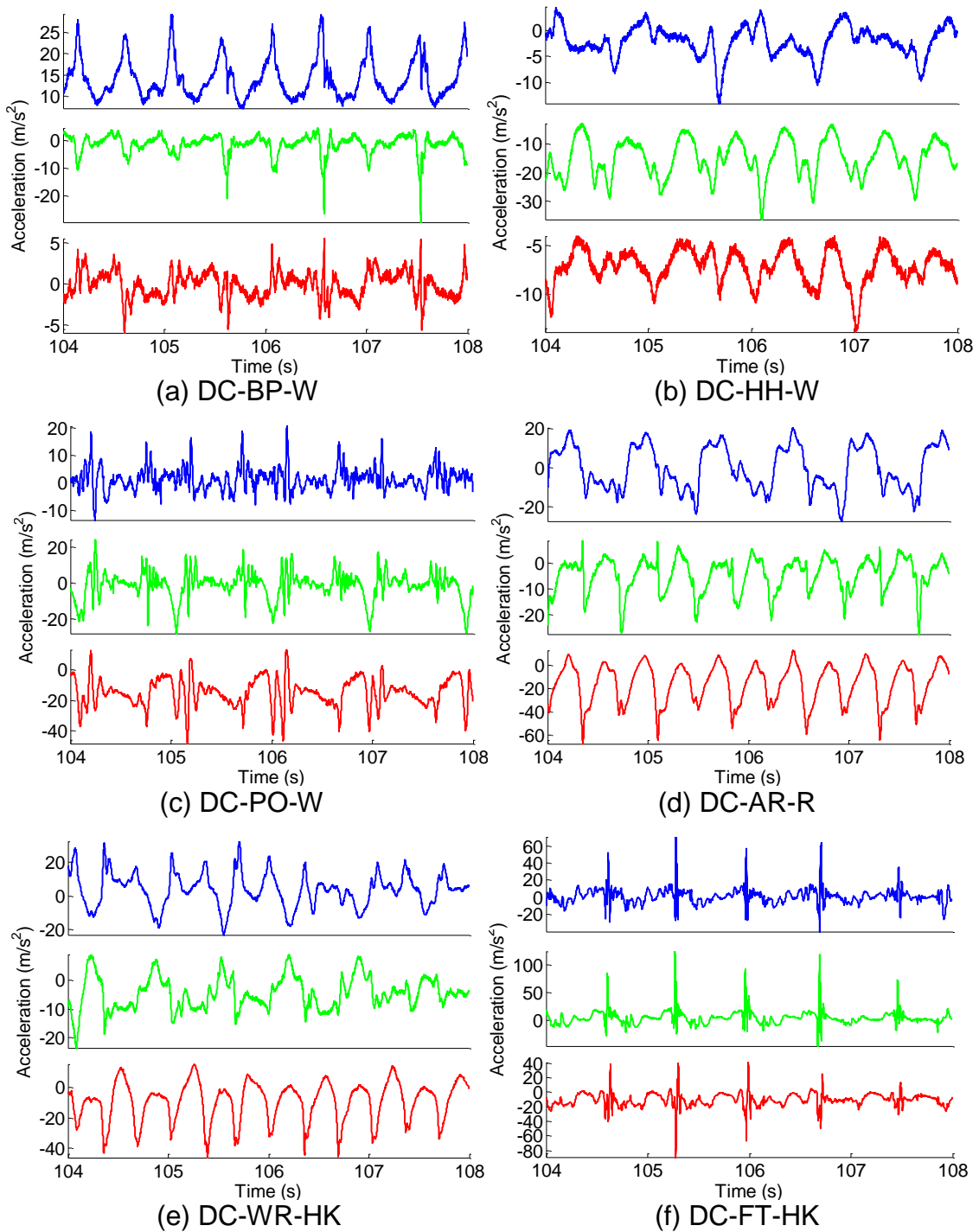


Figure 3-8 Acceleration process over time corresponding to all datasets; the colors blue, green and red represent X, Y and Z-axis respectively

The data collection locations and sensor placements on the subject are shown in Figure 3-7 for the datasets listed in Table 3-2. The first three datasets, namely DC-BP-W, DC-HH-W and DC-PO-W correspond to regular walking mode of the subject on outdoor flat terrain on The University of Calgary campus. The dataset DC-AR-R corresponds to running on a 200m track while the sensor was strapped to subject's arm shown in Figure 3-7 (b). The datasets DC-WR-HK and DC-FT-HK correspond to winter downhill hiking on a mountain that has a height ascent/descent of 700 m over 3.5 km each way, and the sensor locations were wrist and shin. As the subject was hiking down the trail covered with snow, the magnitude of acceleration experienced could be reduced due to its damping effect. Although there were a few intermittent pauses in motion such as the duration of these datasets chosen for processing consists of uninterrupted exhibition of the corresponding motion modes.

The accelerations over time from all the datasets are shown in Figure 3-8. The analysis of the subplots is consistent with the discussion of Section 3.2.2 on time series analysis of wrist-strapped and pocket datasets with various motion modes. The maximum peak-to-peak accelerations range from about 30 m/s^2 for regular walking dataset with sensor on the backpack to about 150 m/s^2 when hiking downhill with sensor mounted on the shin. Three types of pattern can be recognized: (1) sharp impulse-like acceleration peaks occurs in subplots (c) and (f) when sensors are located in the pocket and on the shin - similar spikes are noticeable in Figure 3-1 for the running portion of the dataset when the sensor is in the pant's lower pocket; (2) relatively smooth acceleration changes noticeable in subplots (b), (d) and (e) with hand-held, arm-strapped and wrist-strapped datasets; and

finally, (3) intermediate pattern between sharp spikes and smooth curves such as in subplot (a) for the backpack dataset.

The sharp impulsive spikes can be attributed to the initial portion of the stance phase of the gait cycle when the foot makes a contact with the ground at which time the accelerometer suddenly comes to a halt, thus inducing a spike in measured acceleration.

The spikes are prominent when the sensor is mounted on the foot and less noticeable for other sensor locations on the upper body. In contrast, the smooth curves that are noticeable with sensor locations such as arm, wrist and hand can be attributed to the back and forth hand motion in a gait cycle. In these locations the sensor measures accelerations during both forward and backward hand movements unlike the heel strike during the stance phase.

The subject has six degrees of freedom which allows motion in three dimensions. As a consequence, it may be possible that the three axes measure accelerations differently. The feet usually move in a more restricted and predictable pattern compared to hands. Therefore, the subplots (c) and (f) corresponding to pocket and foot locations comparatively exhibit more similarity across three axes than (b), (d) and (e).

The PSDs of acceleration, velocity and position corresponding to the datasets are shown in Figure 3-9. It is evident from the subplots (a) to (f) that all six pedestrian motion modes exhibit harmonics with their fundamental frequency located within 5 Hz. However, the differences between the datasets which are affected by the stance phase and motion of the hand can also be noticed in the frequency domain. The acceleration processes corresponding to subplots (c) and (f) have their power shared across larger frequencies

compared to the acceleration processes corresponding to arm, wrist and hand held cases in subplots (b), (d) and (e).

This behavior is more evident in cumulative spectral distribution (CSD) plots, which are the integration of PSD, analogous to cumulative distribution functions and probability density functions. The normalized CSD plots corresponding to the PSDs are shown in Figure 3-10. Notice the stark contrast in power distribution between subplots (c) & (f) and subplots (b), (d) & (e). Therefore, it can be concluded that the acceleration processes corresponding to foot mounted and pocket datasets have a wider power spreading across higher frequencies compared to those of hand held datasets.

The conversion of acceleration process into velocity and position processes via double integration can be represented in the frequency domain as

$$\widehat{S}_{v_x, v_x}^n(f) = \frac{1}{(2\pi f)^2} \widehat{S}_{a_x, a_x}^n(f) \quad , \quad \widehat{S}_{p_x, p_x}^n(f) = \frac{1}{(2\pi f)^2} \widehat{S}_{v_x, v_x}^n(f) \quad \text{3-6}$$

where $\widehat{S}_{a_x, a_x}^n(f)$, $\widehat{S}_{v_x, v_x}^n(f)$ and $\widehat{S}_{p_x, p_x}^n(f)$ are the x-axis acceleration, velocity and position processes respectively. The expression follows from the fact that the integration operator in the time domain is the frequency scaling operator in frequency domain. The effect of such scaling is progressively higher attenuation of high frequency components. The conversion of the velocity process into the position process further attenuates high frequency components. This effect can be noticed in all PSD plots of Figure 3-9 by the disappearance of high frequency harmonics as the acceleration process is converted to position process. The position processes are still characterized by a few harmonics, but the power of the process is distributed over a much narrower frequency range, as evident in cumulative power distribution plots in Figure 3-10.

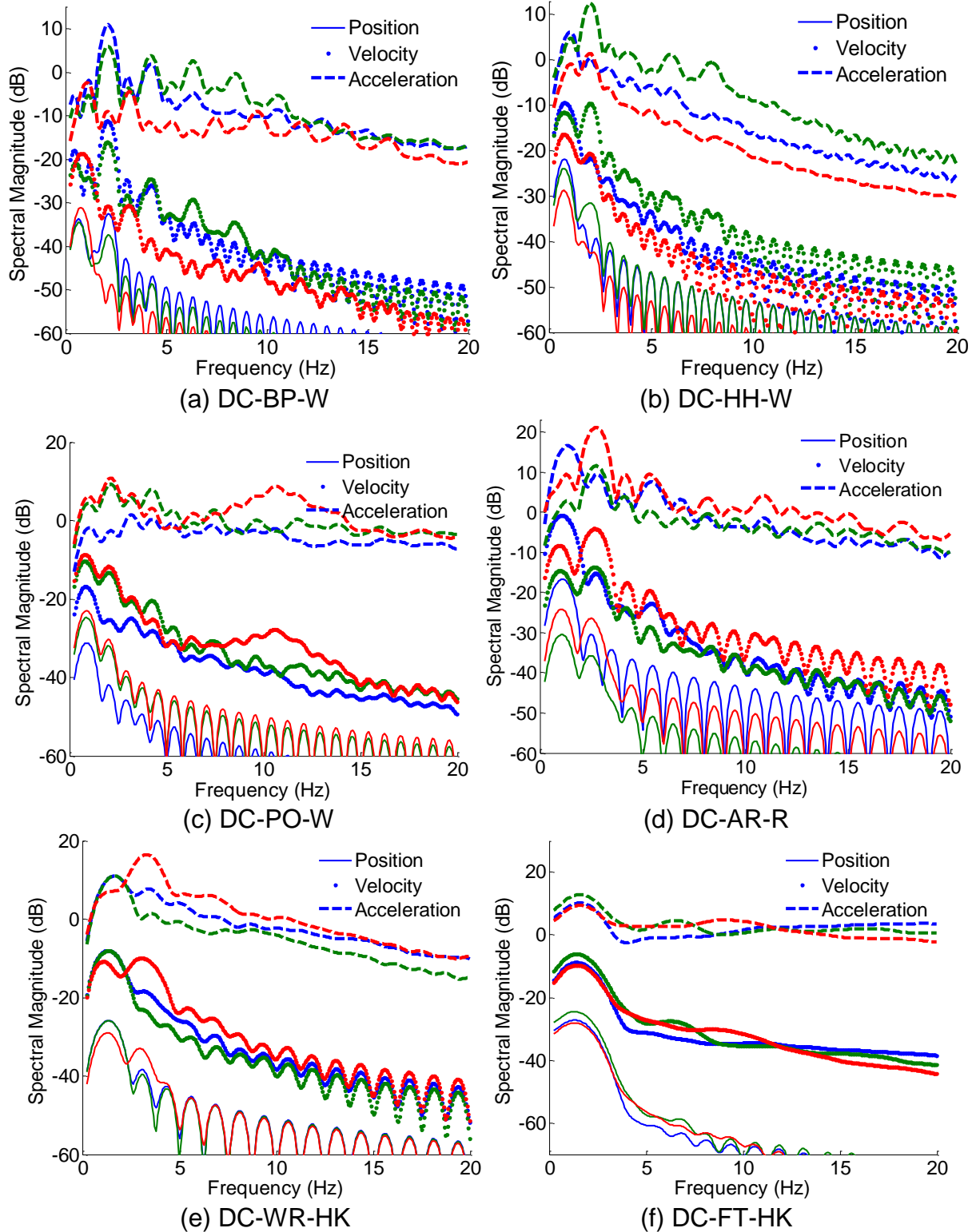


Figure 3-9 PSDs of position, velocity and acceleration corresponding to all datasets; blue, green and red represent the X, Y and Z-axis

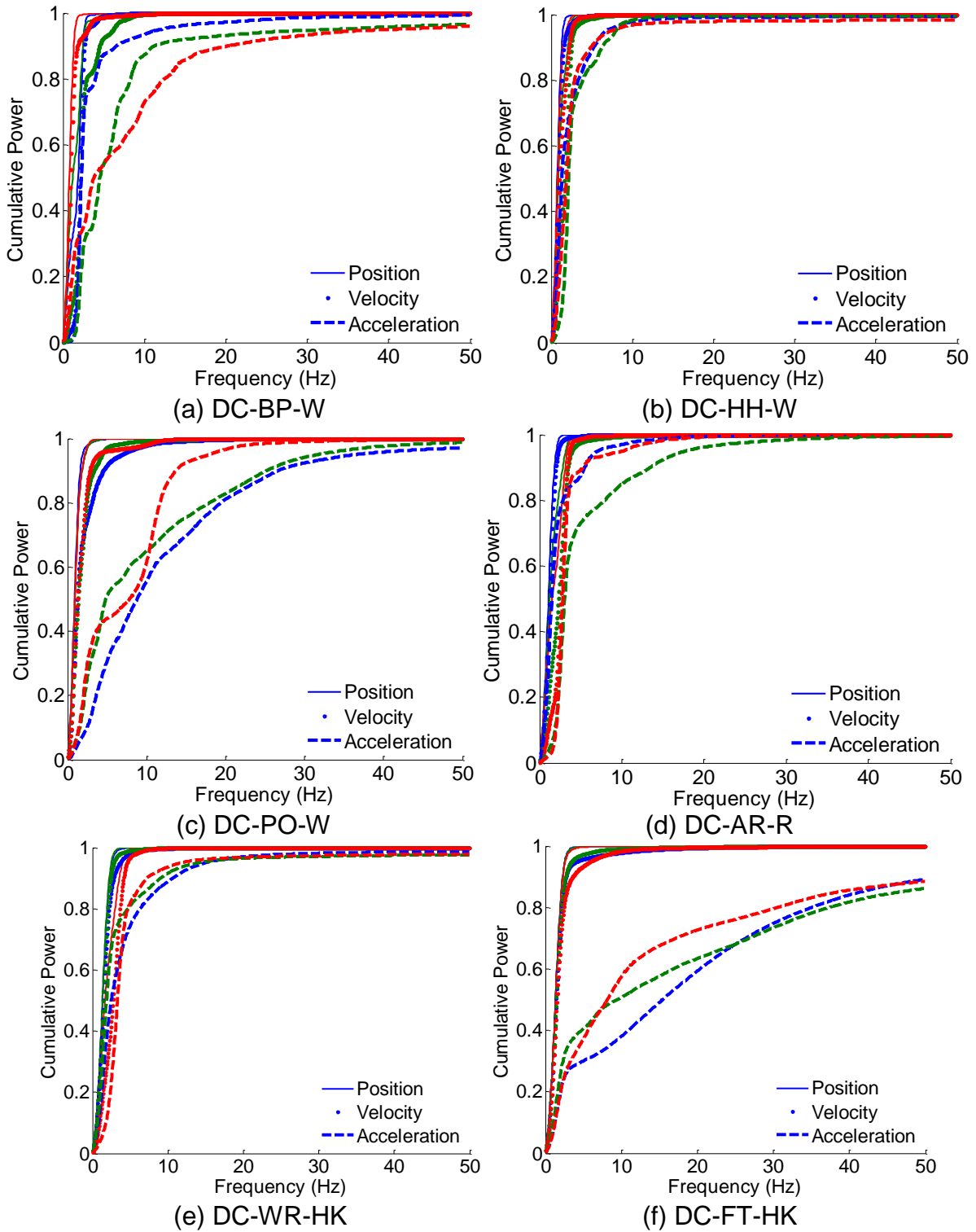


Figure 3-10 Cumulative power distributions of position, velocity and acceleration corresponding to all datasets; blue, green and red represent the X, Y and Z-axis

It is evident from the PSD plots of acceleration, velocity and position processes that the power is concentrated at lower frequencies. Therefore, by treating pedestrian dynamics as a low-pass process, the one-sided bandwidth of the process can be defined. In this work process bandwidth is defined as the frequency that contains 95 % of the process power. The empirical process bandwidth analysis can be readily conducted using cumulative power distribution and the resulting bandwidths for position, velocity and acceleration processes are shown in Figure 3-11.

The acceleration process in Figure 3-11 (c) shows that the stance phase dominated datasets, namely backpack, pocket and shin-mounted datasets have higher bandwidths compared to the hand held, wrist and arm-strapped datasets. In particular, the shin-mounted dataset exhibits about 115 Hz of bandwidth, which is one order of magnitude larger than the arm-mounted datasets. The conversion of acceleration to velocity and subsequently to the position process not only progressively reduces the process bandwidth for a particular dataset, but it also drastically reduces the bandwidth differences across the sensor locations. Overall, it can be concluded that the process bandwidth depend more on the sensor location and then the pedestrian motion mode. Figure 3-11 also shows the total power of position, velocity and acceleration processes for all datasets. It can be noticed that the last three datasets, namely downhill hiking and running datasets, contain more power compared to the first three walking datasets, which is intuitive as the subject has to spend more energy while running then walking. Therefore, unlike the process bandwidth, process power depends more on the pedestrian motion mode and less on the sensor location.

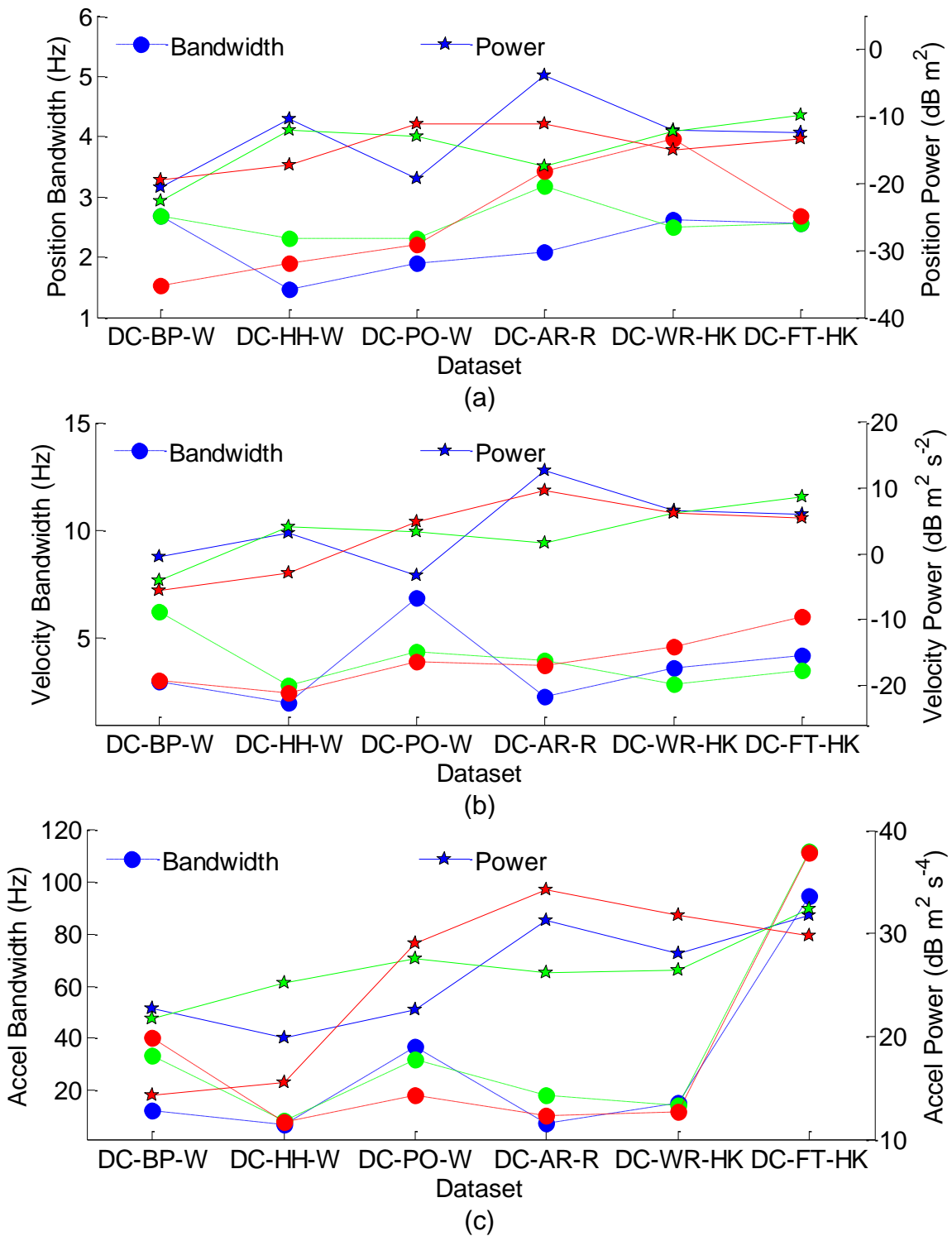


Figure 3-11 (a) position, (b) velocity and (c) acceleration bandwidths and total measured power for all datasets; blue, green and red represent the X, Y and Z-axis

3.2.8 Pedestrian dynamics and GNSS signal parameters

The position, velocity and acceleration processes characterized in previous sections are derived from appropriately processed data from inertial sensors assuming that the derived processes represent the GNSS signal parameters, namely carrier phase and frequency. In this section the relationship between derived processes and GNSS signal parameters is established theoretically and verified empirically by comparing the characterization results from inertial sensors and the GNSS signal parameters estimated by carrier tracking loops. The carrier phase corresponding to a satellite signal after down-conversion and ADC operations is given in Eq. 2-9. On similar lines the carrier frequency of the incoming signal after ADC operation can be written as

$$f_i = f_{IF} + f_i^{LOS} + f^g(\vec{A}) + f^T(\mathbb{T}) + f^{ST} + f^{LT} + f_i^\eta \quad \mathbf{3-7}$$

where f_i^{LOS} is the LOS component of carrier frequency, f_i^η is the stochastic frequency disruptions based on the signal propagation channel effects such as ionospheric phase scintillation, f^g is the oscillator g -sensitivity induced frequency disruptions that depends on the acceleration \vec{A} in the oscillator frame, f^T is the clock drift variations due to temperature \mathbb{T} , f^{ST} and f^{LT} capture short and long term variations of the clock, and f_{IF} is the carrier IF. The carrier frequency in Eq. 3-7 can be re-written by retaining the components that depend on receiver dynamics, namely LOS dynamics component $f_i^{LOS,rx}$ and oscillator g -sensitivity component f^g , as

$$f_i^{rx} = \overbrace{DCM_{NEU} \cdot v_{rx,NEU}}^{f_i^{LOS,rx}} + \overbrace{f_c(\vec{\Gamma} \cdot \vec{A}(t))}^{f^g[\vec{A}]} \quad \mathbf{3-8}$$

where f_i^{Rx} denotes the total receiver dynamics dependent carrier frequency disruptions on the i^{th} satellite in m/s, $DCM_{NEU} = [\cos(\varepsilon_i)\cos(\alpha_i) \quad \cos(\varepsilon_i)\sin(\alpha_i) \quad \sin(\alpha_i)]$ is the direction cosine matrix with ε_i and α_i being the elevation and azimuth angles, the receiver velocity vector is given by $v_{rx,NEU} = [v_{n,rx} \quad v_{e,rx} \quad v_{u,rx}]^T$ in the North East Up (NEU) local-level frame where subscripts n , e , and u are used to represent the individual axis, the operator \bullet denotes the inner product of two vectors, $\vec{\Gamma}$ is the local oscillator g -sensitivity vector expressed in ppb/ g , \vec{A} is the acceleration vector in the local oscillator frame with units in g , f_c is the centre frequency of the GNSS signal which is 1575.42 MHz for GPS L1. The LOS and local oscillator components of the carrier phase can be obtained by integrating Eq. 3-8, which leads to an additional constant of integration corresponding to the initial arbitrary phase offset.

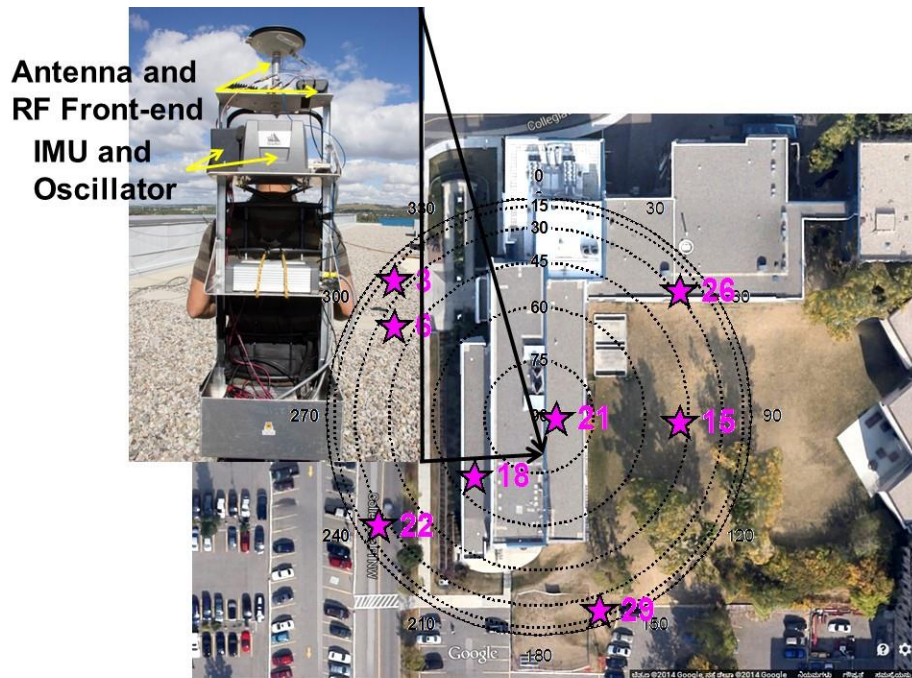


Figure 3-12 Data collection setup, location and skyplot used to establish relationship between processed inertial sensors data and GNSS carrier signal

The theoretical formulation in Eq. 3-8 is validated by conducting an experiment using the equipment shown in Figure 3-12 which consists of a NovAtel 702 GG antenna, a tactical grade IMU (LCI 2014), an OCXO (MORION 2012), an RF front-end hosting an 1-bit ADC which provides complex IF samples at 10 MHz rate. The data were processed using the software receiver GSNRx-UT™ capable of performing ultra-tight GNSS/INS integration. The g -sensitivity vector of the oscillator was $\vec{\Gamma} = [1.148 \ 0.095 \ 1.818]^T$ ppb/ g . The measurement of oscillator g -sensitivity will be discussed in detail in Chapter 4. The goal of this experiment is to analyze the similarity between the carrier frequency disruptions due to receiver dynamics as per Eq. 3-8 and the carrier frequency estimate from the tracking loops. The PSDs of carrier frequency disruptions corresponding to inertial sensors and tracking loops data are computed using Welch's method discussed in

Section 3.2.5. The data segment duration in this case was one second which contains about two fundamental harmonic cycles. The mean value of the carrier frequency was removed before computing PSD and the remaining effects other than the receiver dynamics are assumed to be negligible over the duration of one second. A similar analysis is performed on carrier phase disruptions corresponding to inertial sensors and tracking loops output data.

In order to compare the characterized receiver dynamics with carrier signal parameters, the inertial measurements need to be converted to the local-level frame, which is accomplished by multiplication of the acceleration vector by a rotation matrix from XYZ or body frame to NEU frame, which can be mathematically expressed as

$$\vec{a}_{NEU} = R_{XYZ}^{NEU} \vec{a}_{XYZ} \quad \mathbf{3-9}$$

where $\vec{a}_{XYZ} = [a_x \ a_y \ a_z]^T$ is the acceleration vector in the body frame that is used in the characterization discussed in previous sections, $\vec{a}_{NEU} = [a_n \ a_e \ a_u]^T$ is the acceleration vector in the NEU frame, R_{XYZ}^{NEU} is the rotation matrix to convert from body frame to local-level frame that depends on the receiver attitude (Groves 2008), which is obtained from the output of GSNRx-UT™. The oscillator frame and body frame are assumed to coincide as the oscillator was mounted in close proximity to the IMU which completely measures the accelerations experienced by the oscillator. Would the two units have been separated by a significant distance, the gyroscope may have been utilized to estimate the relative change in acceleration during rotations.

The carrier frequency and phase process PSDs obtained from processed IMU data and tracking output are shown in Figure 3-13 for PRNs 21, 18 and 26 at about 85, 65 and 29 degrees of elevation. The IMU and tracking loop output PSDs are not identical throughout all side-lobes. However, the main-lobe dominates other harmonics in power and main-lobes from the IMU data and tracking loop outputs are in good agreement; therefore, the characterization of carrier frequency and phase processes due to pedestrian dynamics using processed inertial sensor data are deemed to be correct. From the analysis of the cumulative power distribution plot for carrier frequency process shown in Figure 3-13 (c), it appears that the process bandwidth is marginally higher than that of results shown in Figure 3-11 (b) from the previous section for the backpack dataset. The cause of such a marginal increase in bandwidth is attributed to the oscillator g -sensitivity effect which was ignored in the previous section. The receiver dynamics affects the carrier frequency process in two ways as per Eq. 3-8: firstly, the LOS Doppler variations that is proportional to the receiver velocity; secondly, apparent frequency variations due to the oscillator g -sensitivity that is proportional to the receiver acceleration. The oscillator g -sensitivity induces frequency disruptions that are proportional to the oscillator accelerations which increase the process bandwidth.

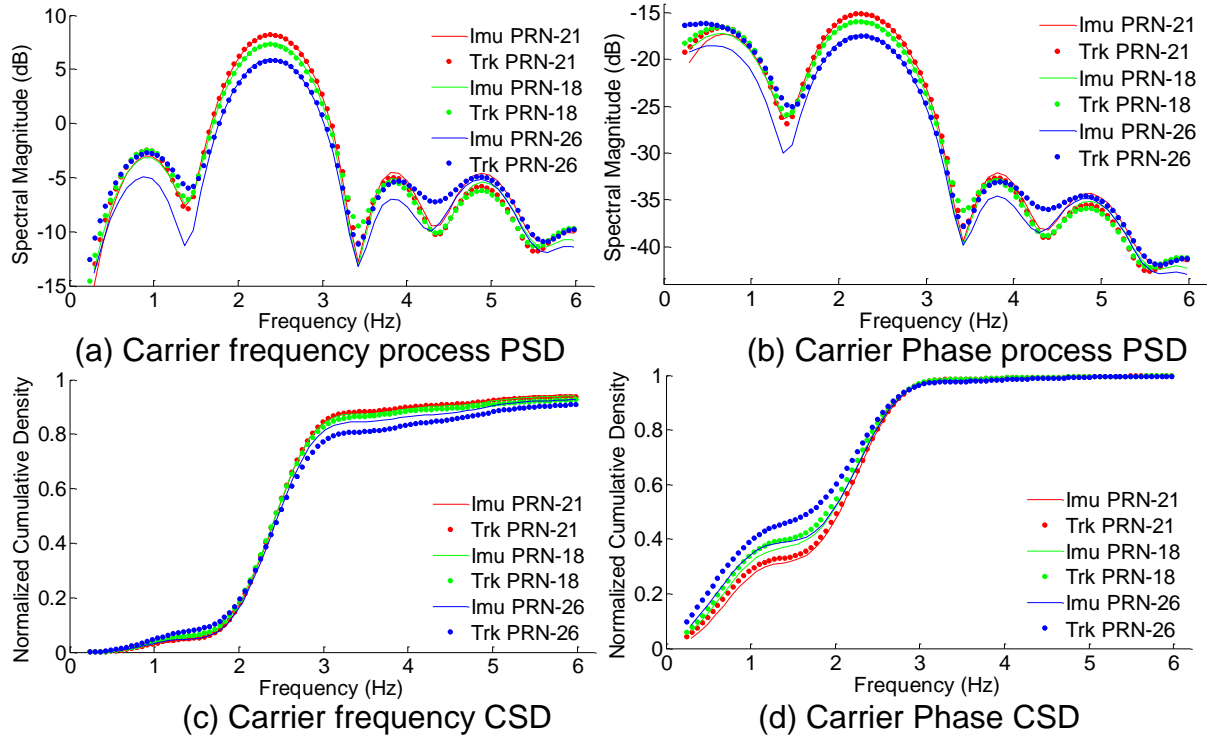


Figure 3-13 PSDs and CSDs of carrier frequency and phase processes due to receiver dynamics

The contribution from the oscillator g -sensitivity and LOS receiver dynamics is shown in Figure 3-14 for bandwidth and power as a function of satellites elevation angle. Specifically, it depends on the receiver dynamics and the oscillator g -sensitivity, but not on satellites' locations or dynamics; therefore the bandwidth and process power of the g -sensitivity component is constant for all satellite elevations. However, the bandwidth and process power of the receiver dynamics component, when projected onto LOS, change with satellite elevation as expected. The bandwidth and process power estimated from the tracking loop output is higher than their corresponding IMU-derived values due to the following reasons: (a) only receiver dynamics components of the carrier frequency disruptions are considered in the IMU data, whereas in tracking loop outputs all sources

of disruptions present in Eq. 3-7 are present; (b) the noise processes in IMU measurements and tracking loop outputs are different. Despite the magnitude differences, the IMU and tracking loop data follow the same trend across different satellite elevations. It can be observed that the total process bandwidth in Figure 3-14 (a) for the satellite at 85 degrees elevation is less than the g -sensitivity induced process bandwidth. This is due to the fact that the total process is dominated by LOS dynamics; therefore, the process bandwidth, due to its definition, is dictated by the dominating component. Comparing the process power across IMU and tracking loop data, it is concluded that the dominant sources of carrier disruptions in the current experiment are the oscillator g -sensitivity and receiver dynamics projected on LOS.

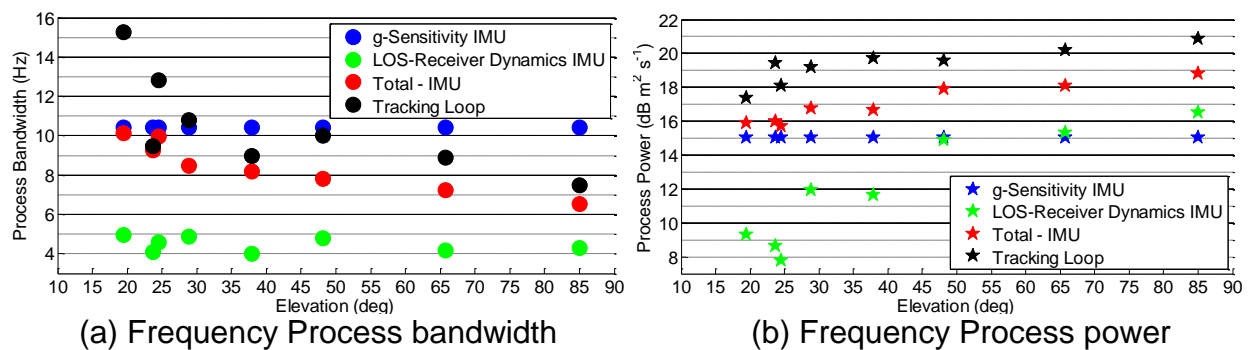


Figure 3-14 Individual contribution of g -sensitivity and LOS receiver dynamics

3.3 Effect of human attenuation of GNSS signals on carrier phase tracking

The effect of human attenuation as a function of antenna placement is assessed by conducting an experiment with a static user antenna. The analysis is aimed at understanding the effects of human attenuation on the effective C/N_0 and the achievable carrier phase tracking performance measured in terms of PLI.

3.3.1 Data collection setup

The data collection setup includes a NovAtel 701 GG omnidirectional antenna mounted on a stable platform under open-sky conditions as shown in

Figure 3-15. The RF front-end and oscillator used in Section 3.2.8 are also used here.

Several datasets were collected by adjusting the antenna height from the ground to various levels relative to the subject's height as shown in

Figure 3-15.

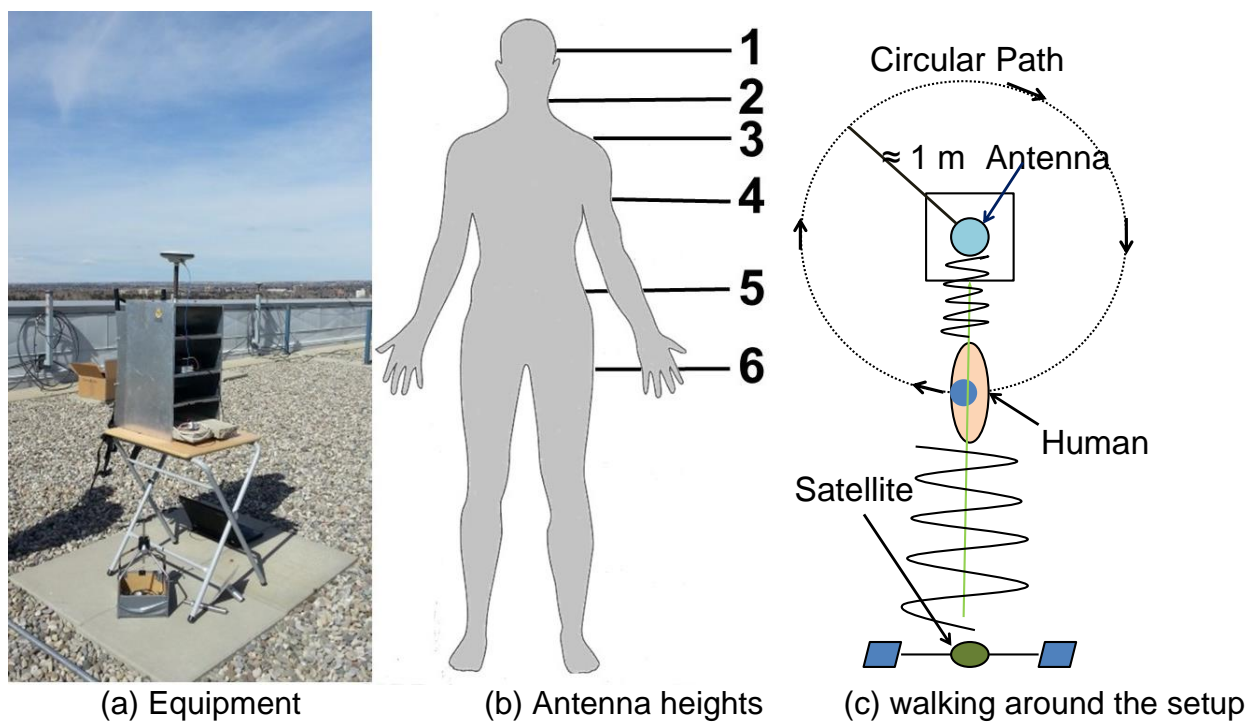


Figure 3-15 Data collection setup used for human attenuation characterization

The data collection duration was approximately 200 s for each dataset. The subject walked around the antenna setup at various speeds keeping a radial distance of approximately 1 m from the antenna as shown in the figure. This enables the analysis of the time-varying attenuation of satellite signals spanning all elevation and azimuth ranges.

The collected data were processed using the standard version of GSNRx™ that employs the Kalman filter based tracking algorithm discussed in Chapter 2.

3.3.2 Signal attenuation analysis

The maximum and minimum recorded C/N_0 values while the pedestrian was in motion around the antenna are shown in Figure 3-16 (a). The difference between the maximum and minimum C/N_0 and phase misalignment will be referred to, herein, as "*variation*". It is evident that the C/N_0 variation is generally large for low elevation satellites. The variation further increases when lowering the antenna height from location 1 to 6 corresponding to the levels marked with the subject's height in

Figure 3-15 (b).

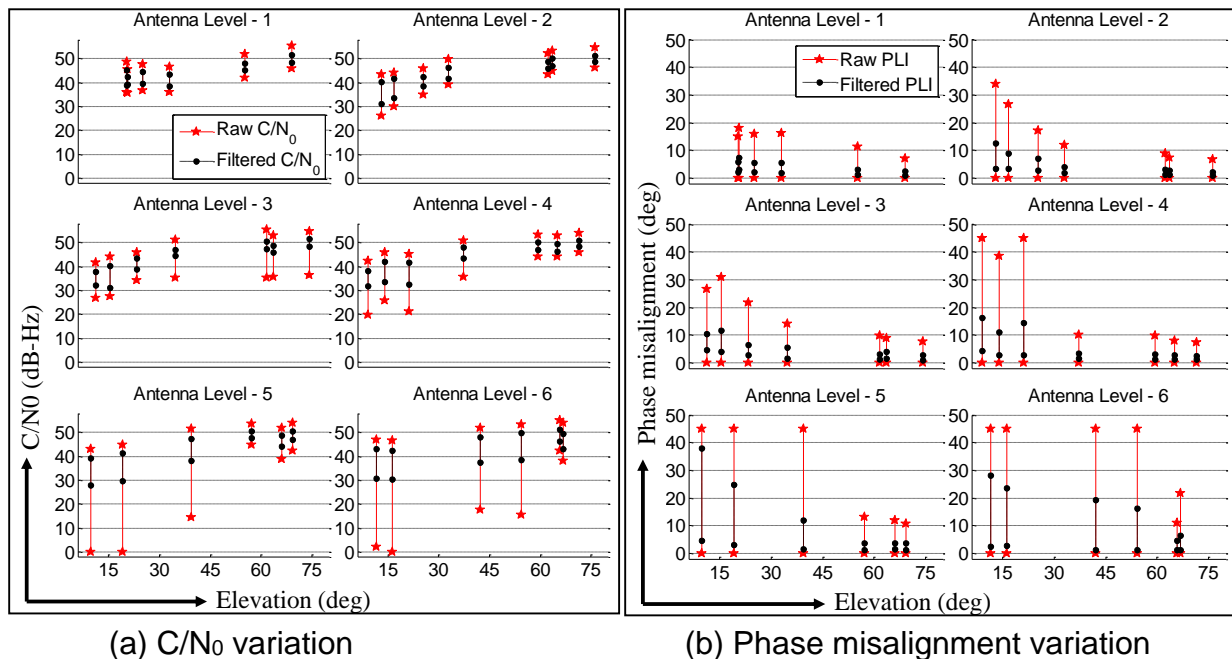


Figure 3-16 Variations in C/N_0 and carrier phase misalignments for selected antenna levels

This observation is in agreement with the intuition that lowering the antenna level will increase the portion of the human body blocking the antenna signal. Consequently, variations in the carrier phase misalignment $\phi \approx 0.5 \cos^{-1}(\text{PLI})$ shown in Figure 3-16 (b) also increase for lower antenna heights. From Figure 3-16 (b), especially for antenna levels 4 to 6, the carrier phase misalignment is more than the phase lock threshold of 15 degrees. If the dynamics is not significant, for example when the pedestrian is standing while holding the device in hand, human attenuation can be addressed through post coherent SNR enhancement by increasing the coherent integration period. This would require data bit assistance in the case of GPS L1 C/A code for integration periods beyond 20 ms. However, when the pedestrian is either walking or running, coherent integration cannot be increased, but dynamics aiding by external means, such as through inertial sensors integration, is necessary. Furthermore, even if external dynamics aiding is available, given the non-linear behavior of PLI at low SNR conditions it is difficult to distinguish the true loss of phase lock from an apparent reduction in PLI due to signal attenuation only, as discussed in Section 2.6.2. Also, as discussed in Chapter 1, human proximity affects the signal propagation in the following ways: (1) signal attenuation due to absorption by body tissues; (2) increased multipath due to skin reflections; (3) variation of antenna parameters such as radiation pattern, resonant frequency etc. Although, isolation of such propagation effects is beyond the scope of the current work, the combined effects are measured using the C/N_0 and PLI indicators used herein.

The raw C/N_0 and phase misalignment variations shown in Figure 3-16 are computed from correlation values obtained after 20 ms of coherent integration and therefore the indicators are noisy. Therefore, the C/N_0 and phase misalignment need to be filtered to

obtain smooth indicators. To this end, a moving average filter with one second window is utilized to reduce the raw indicator variance due to noise as discussed in Chapter 2 and the resulting indicators are also shown in Figure 3-16.

A sample of filtered C/N_0 indicator over time along with the raw indicator is shown in Figure 3-17 for PRN 1 at an elevation of about 16 deg. The moving average filter is effective in noise reduction for stationary *signals* that consist of no abrupt changes - the term '*signals*' in this context is the actual C/N_0 . Unfortunately, for pedestrian GNSS receivers, given the tendency of the pedestrian to induce rapid time-varying power-levels, the tracking performance indicators are highly non-stationary. The application of a moving average filter on such non-stationary performance indicator causes the following problems noticeable in Figure 3-17: (1) low pass filtering introduces a delay in signal variation and causes immediate detection of signal outages due to human attenuation, which is a challenge; (2) the low pass filter wrongly interprets momentary signal outages as high frequency noise and smooths the signal. Therefore, the usefulness of C/N_0 and PLI are limited to qualitative indication of the power level and carrier phase alignment. These effects must be borne in mind when the indicators are used for decision making purposes in the receiver, such as for tracking status monitoring and measurement weighting during position estimation. Accurate indication of carrier phase tracking is possible via differential GNSS techniques, as will be discussed in later chapters.

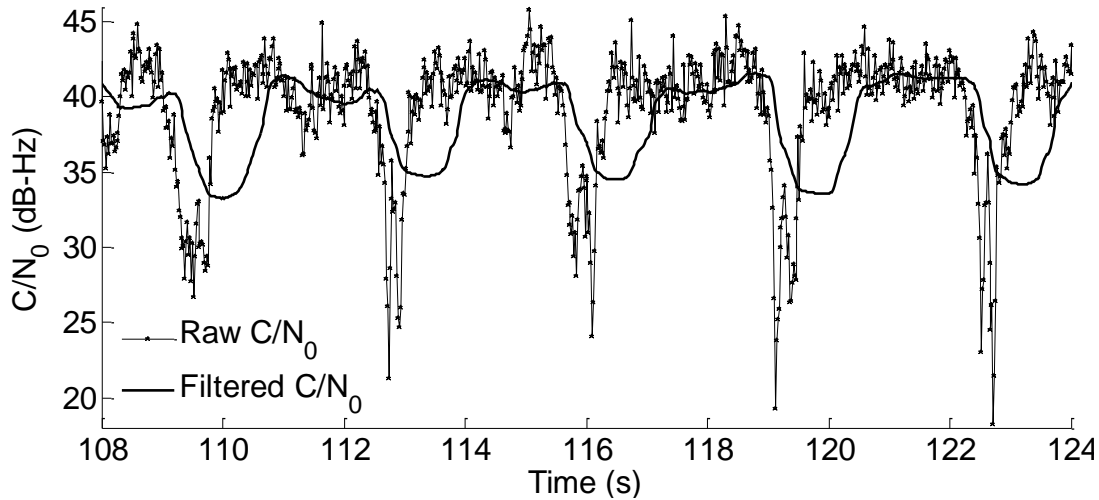


Figure 3-17 Trade-off between dynamic response of signal variations versus smoothness

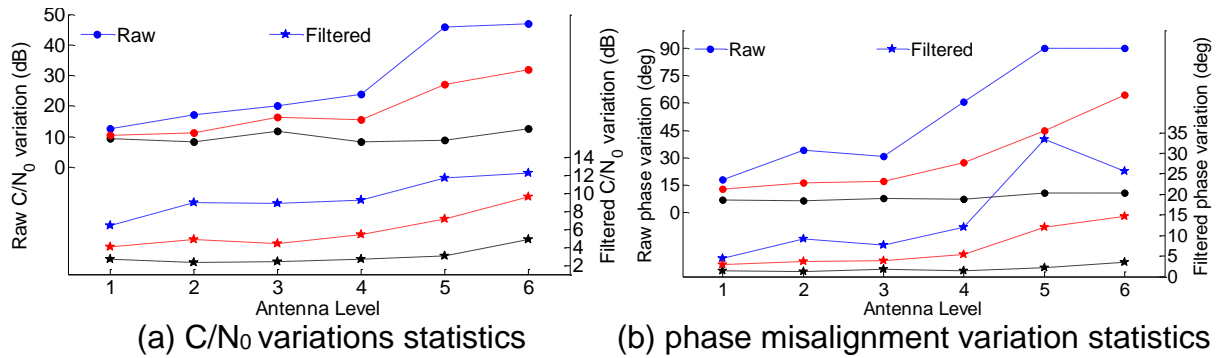


Figure 3-18 The *maximum (blue), mean (red) and minimum (black)* values of C/N_0 and phase misalignment variations. The statistics are computed across 6-7 available satellites for the corresponding antenna level as per Figure 3-15.

Nonetheless, the qualitative analysis conducted in this section indicates that human attenuation of GNSS signals can cause a significant C/N_0 and phase tracking performance reduction. The statistics of *variation*, that is the statistics of the *difference between maximum and minimum C/N_0 and carrier phase misalignment*, computed across the available satellites for all antenna levels, are summarized in Figure 3-18. The general

tendency when lowering the antenna height is increased variations in signal attenuation and carrier phase misalignments.

The propagation of a satellite signal through a human body is a complex function of the body type, the distance from the subject to the antenna, and the antenna type.

3.4 Summary

This chapter introduced the pedestrian operating environment. Although non-stationary in general, the PSD analysis exhibited strong quasi-periodicities. A relationship was derived and verified between the characterized pedestrian dynamics in terms of acceleration, velocity and position and signal parameters, namely carrier frequency and phase, using GPS data. It was shown that the oscillator g-sensitivity and receiver component of LOS dynamics are the two major sources of carrier variations. It is deemed that these two factors can significantly affect the carrier tracking performance. It was also shown that the *process bandwidth*, in general, depends on the pedestrian motion mode and sensor location. Also, it was shown that the process bandwidth is generally high when the inertial sensor is placed such that it is affected by the stance phase of the human gait cycle due to the heel strike.

An experiment was conducted to understand the effect of human proximity of about 1 m on GNSS signal attenuation and carrier phase tracking. It was shown that the placement of the antenna with respect to human subjects strongly affects the incurred attenuation using qualitative C/N_0 and PLI indicators. It was also shown that the indicators suffer from trade-off between prompt and accurate signal attenuation indication versus thermal noise

variance. The understanding obtained in this chapter will be used in chapters 4 and 5 to improve receiver carrier phase tracking performance.

Chapter Four: Oscillator g -sensitivity effects on GNSS carrier phase tracking

4.1 Introduction

The acceleration sensitivity of a crystal oscillator, known as g -sensitivity, can induce variations in the local replica of the GNSS carrier signal, degrading the synchronization in tracking in the process. As illustrated in Section 3.2.8, oscillator g -sensitivity has a significant effect on carrier disruptions that is comparable to LOS dynamics. A method to compensate for the oscillator g -sensitivity using information from an IMU is proposed and tested in this chapter. A simple 2- g tip-over test is used for oscillator g -sensitivity calibration, as discussed in Section 4.2. The method of compensation using an IMU is proposed in Section 4.3. The performance evaluation of the proposed method under various operating environments from pedestrian to automobile navigation is discussed in Section 4.4. The design choices such as IMU quality, IMU data rate and IMU and oscillator calibration are discussed in Section 4.5.

4.2 Laboratory calibration of oscillator g -sensitivity

The quality of a GNSS receiver's local frequency reference is integral to its performance, influencing everything from signal acquisition and data demodulation to velocity estimation and carrier-phase based positioning. In this regard, the quality of the local oscillator is crucial to receiver performance. The total observed carrier phase for a given satellite signal, after down-conversion from the nominal center frequency, which is 1575.42 MHz for the GPS L1 C/A signal, to baseband is given by Eq. 2-9 and reproduced below for convenience:

$$\theta_i = \theta_i^{LOS}(\vec{V}) + \theta^g(\vec{A}) + \theta^T(\Upsilon) + \theta^{ST} + \theta^{LT} + \theta_i^\eta + \theta_i^0 \quad 4-1$$

The sensitivity of the local oscillator to applied acceleration is represented by the $\theta^g(\vec{A})$ term and is the focus of this chapter. Quartz crystal oscillators are mechanical devices which operate on the principle of resonance (Marrison 1930, Cady 1955). Any external force on the oscillator can therefore deform the crystal and influence the resonant frequency of the crystal. By employing a simple, linear model, the frequency output of an oscillator, denoted by f_{OSC} , experiencing acceleration \vec{A} can be expressed as (Filler 1988)

$$f_{OSC}(\vec{A}) = f_0(1 + \langle \vec{\Gamma} \cdot \vec{A} \rangle) \quad 4-2$$

where f_0 represents the nominal frequency of the oscillator, $\vec{\Gamma}$ is the acceleration sensitivity vector of the oscillator in units of g^{-1} , g is the gravitational acceleration, and the operator $\langle \cdot \rangle$ is the scalar or dot product between the two input vectors. If a frequency synthesizer or multiplier is used, the term f_0 should represent the final up-converted frequency. The g -sensitivity is scaled in a linear fashion with frequency.

Although an indication of the g -sensitivity of a particular production oscillator is often provided in a product datasheet, the exact three-dimensional characterizations are rarely available. These values can be readily estimated by means of a simple test, known as a 2- g tip-over test (Filler 1998, Besson et al 1996). In the case of a GNSS receiver, it is possible to estimate the g -sensitivity of an oscillator by measuring the change in carrier frequency observed on a receiver channel as the physical orientation of the oscillator is

varied with respect to gravity. The exact g-sensitivity exhibited by an oscillator, in general, is a function of the ambient temperature. For quartz oscillators it appears to be reasonably constant in the range 0-80° C (Hanson & Wickard 1989).

To measure the three dimensional acceleration sensitivity vector, the RF signal from a Spirent GPS/SBAS simulator was connected to the digitizing receiver front-end which employed the oscillator under test as its frequency reference. The single channel utility in the GPS simulator was selected and programmed to broadcast a GPS L1 C/A signal with constant Doppler during the calibration test. IF samples were recorded and processed using the standard version of GSNRx™ software receiver. As such, any change in the observed carrier frequency is due to the acceleration sensitivity of the oscillator alone, assuming negligible oscillator phase noise. The oscillator was mounted inside a rectangular parallelepiped enclosure, and three axes were marked arbitrarily. IF samples were recorded for approximately 120 s for each of the three axes, during which time the axis under test was aligned with the vertical, rotated through 180 degrees and, once again, aligned with the vertical. This results in a total change of acceleration of 2 g on each axis. It is assumed that the sensitivity of the axis is similar for both positive and negative accelerations and also that the oscillator response is linear with accelerations in the range of 50 g (Besson et al 1996).

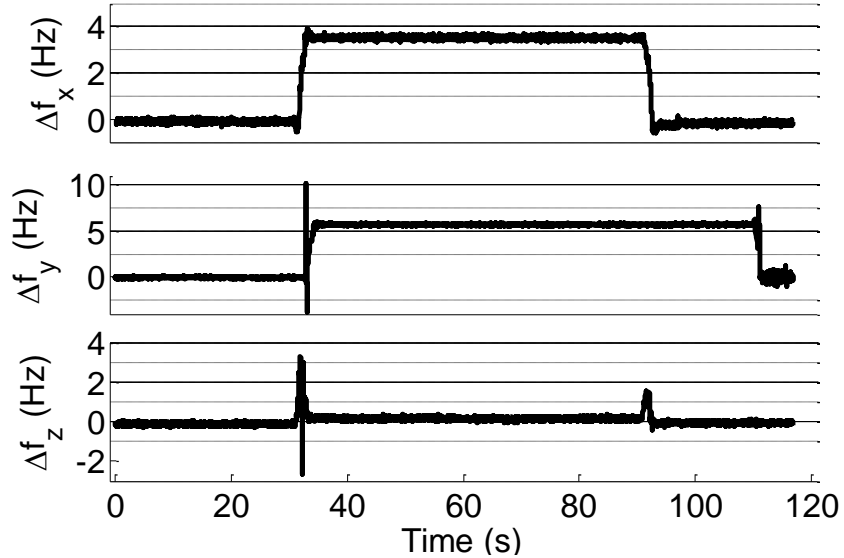


Figure 4-1 Observed GPS L1 frequency change corresponding to the 2-g tip-over test conducted for each axis of the Morion MV89A OCXO

The results of the test are shown in Figure 4-1, for the Morion MV89A OCXO (Morion 2012), where Δf represents the change in the observed carrier frequency. The sensitivities in both x- and y-axes are clear with each exhibiting a frequency deviation of approximately 4 Hz and 6 Hz, while the z-axis appears to be virtually insensitive to acceleration. This behavior is due to the variation in the g -sensitivity of the corresponding axis and it is specific to the oscillator unit used. There are frequency perturbations in the z-axis at 30 s and 90 s; the oscillator was physically flipped to change the orientation of the axis under test by 180 degrees thereby changing the acceleration along the axis by 2 g . While flipping the oscillator to negate the z-axis orientation, momentarily the y-axis becomes normal to the ground thereby inducing a spike in the measured Doppler frequency. A similar behaviour is also observed in the frequency perturbation plot in the y-axis test when the x-axis passes through the vertical during the flip.

The scalar g -sensitivity corresponding to each axis can be estimated as follows:

$$\Gamma_{axis} = \frac{\Delta f_{2g}}{2f_{L1}}$$

4-3

where Δf_{2g} represents the observed change in carrier frequency between acceleration due to gravity being aligned with positive and negative directions of the axis under test and f_{L1} is the GPS L1 centre frequency. The estimated g -sensitivity values for various oscillators, including the Morion OCXO and two TCXOs, are shown in Table 4-1, where the notation $\|\vec{\Gamma}\|$ denotes the norm of the vector $\vec{\Gamma}$. It is clear that these quartz-based oscillators exhibit g -sensitivity in the range of 2 ppb/ g along the vector norm $\|\vec{\Gamma}\|$. The implications of this sensitivity will be discussed in Section 4.4.

Table 4-1 Measured g -sensitivity for a selection of oscillators

g -Sensitivity (ppb/ g)→ Oscillator↓	Γ_x	Γ_y	Γ_z	$\ \vec{\Gamma}\ $
Morion OCXO (Morion 2012)	1.17	1.84	0.05	2.18
Fordahl 0727 TCXO	-1.27	-0.48	-0.35	1.4
Rakon TCXO (IT3200C 2014)	-1.49	-0.95	2.22	2.84

4.3 Proposed compensation technique

When the local oscillator experiences acceleration, the change in observed carrier frequency is common to all the satellite signals. In a noiseless scenario, this frequency change will manifest itself in the navigation solution as an incremental local clock drift. Unfortunately, due to the inevitable presence of noise, variable signal power levels and variable loop settings, individual tracking loops estimate and compensate for the change

in carrier frequency independently. Also, since the GNSS signal tracking loop is a feedback control system, which takes a finite time to respond, acceleration-induced carrier frequency errors can induce cycle slips or drive the tracking channels out of phase-lock. Even though g -sensitivity compensated oscillators are available (Bloch et al 2009), they are expensive and often quite large and are more suited to other applications than for pedestrian receivers.

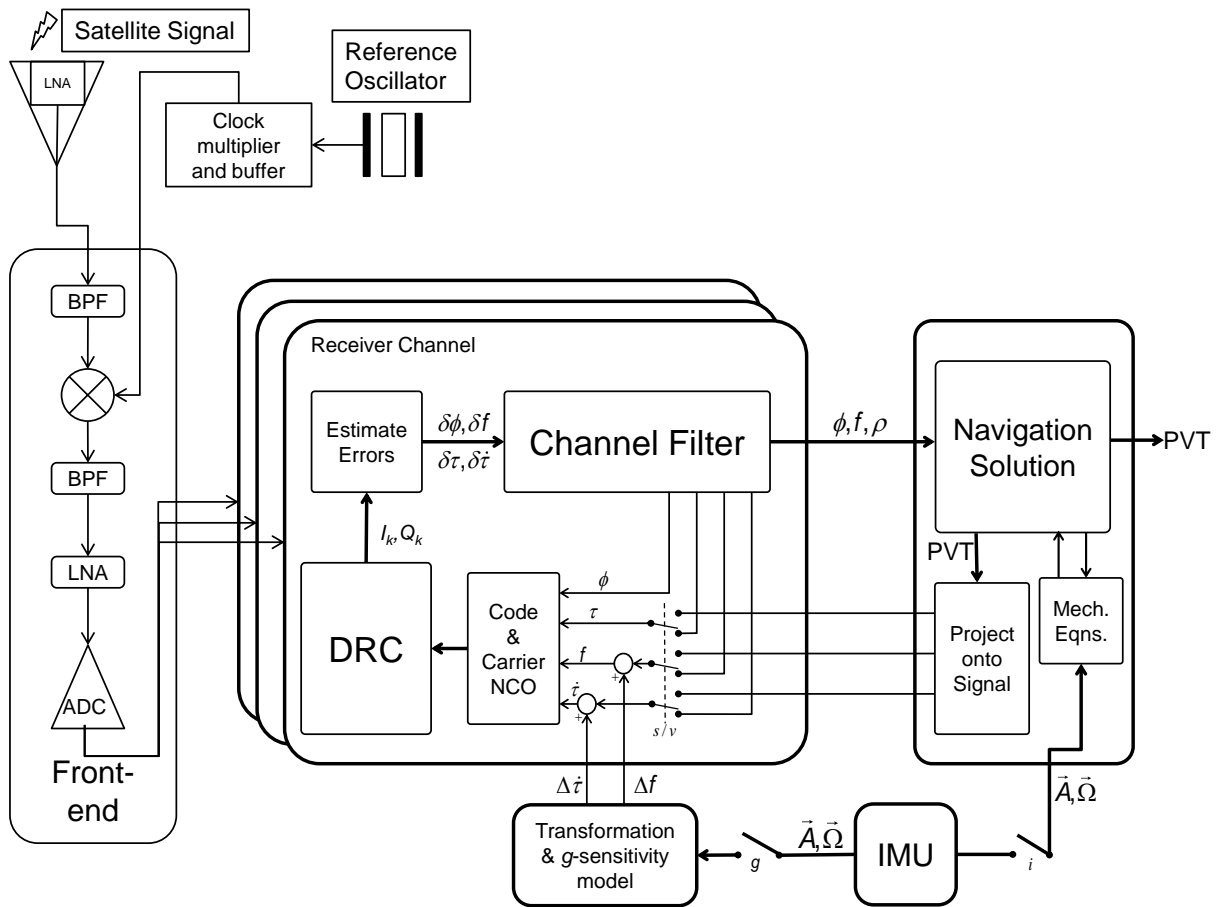


Figure 4-2 Generic block diagram of a GNSS receiver supporting scalar-based, vector-based or ultra-tight architecture with optional g -sensitivity compensation

The principle behind this work is that, in an IMU-equipped system, the acceleration impingement upon the oscillator can be readily estimated. Given appropriate

characterization of the oscillator's g -sensitivity, the frequency perturbation can be forecast and the tracking loops can be appropriately aided. Moreover, given the presence of the IMU in the ultra-tight system, and even in some non-ultra-tight systems such as a modern cellular handset, it seems prudent to employ it to the extent of its ability. It will be shown herein that it is possible to perform g -sensitivity compensation, without incurring extra weight, cost or power consumption in the system.

The receiver architecture employed in this work is shown in Figure 4-2, which is a generalized version of the scalar-based receiver architecture discussed in Section 2.3 supporting scalar-based, vector-based or ultra-tight operating modes. The generalization was accomplished by the addition of the following components: (a) IMU providing three-dimensional accelerations \vec{A} and angular rates $\vec{\Omega}$; (b) a set of mechanization equations, denoted Mech. Eqns; in Figure 4-2, produces estimates of the changes in velocity and attitude in the body frame using \vec{A} and $\vec{\Omega}$ from the IMU; (c) a block that interprets the satellite ephemeris and current PVT solution to provide estimates of the current received signal parameters for each tracked satellite signal, thus facilitating vector operation; (d) the switches ' s/v ', ' i ' and ' g ' that dictate receiver operating modes; (e) finally, a block which interprets \vec{A} and $\vec{\Omega}$ provides g -sensitivity corrections to tracking loop NCOs given the oscillator's g -sensitivity.

The bank of switches denoted ' s/v ' relays signal parameter estimates from either the channel filter or the navigation processor to the code and carrier NCO, to affect either

scalar- or vector-mode operation. When operating in scalar mode, each receiver channel performs signal tracking operations independently. To provide vector-based tracking, the receiver channels relinquish control of some of the signal parameters to the navigation solution. Specifically, carrier frequency and pseudorange values are estimated by the navigation solution by projecting the estimated PVT into the signal parameter space. Generally, the receiver's ability to estimate PVT and other propagation effects limits vector operation to these two signal parameters and carrier phase must be tracked on a channel-by-channel basis. Inclusion of the inertial measurement unit is controlled via the switch 'i', transforming the vector-based receiver to an ultra-tight receiver. Compensation techniques for the local oscillator g -sensitivity are enabled via the switch labelled 'g'.

In the proposed system, the raw IMU measurements \vec{A} and $\vec{\Omega}$ are recorded and transformed into an acceleration vector in the frame of the oscillator. They are then multiplied by the g -sensitivity vector of the oscillator and directly applied to the DRC NCO values, as shown in Figure 4-2. The oscillator-induced changes in carrier frequency and code rate are respectively given by

$$\begin{aligned}\Delta f &= -f_0 \langle \vec{\Gamma} \cdot \vec{A}_{osc} \rangle \\ \Delta \dot{\tau} &= -\dot{\tau}_0 \langle \vec{\Gamma} \cdot \vec{A}_{osc} \rangle\end{aligned}\tag{4-4}$$

where \vec{A}_{osc} denotes the 3-axis acceleration in the oscillator frame and $\dot{\tau}_0$ denotes the nominal chipping rate of the GNSS signal. An increase in the oscillator frequency induces an apparent reduction in the observed carrier frequency and code rate. By utilizing the available IMU measurements and the known oscillator g -sensitivity, the Δf and $\Delta \dot{\tau}$

variations can be compensated for directly. Examining the relative magnitudes of the coefficients f_0 and $\dot{\tau}_0$, it is clear that, although compensation of the carrier loop may be quite beneficial, the code tracking loop is relatively insensitive to oscillator effects. The physical reason for this is that variations in the oscillator frequency manifest themselves as a time-dilation in the code loop, whereas in the carrier loop, this dilation is scaled by the carrier center frequency which, in the case of GPS L1 C/A, is 1575.42 MHz.

4.4 Experimental validation

To investigate the effects of oscillator g -sensitivity and the benefits of oscillator compensation a number of sets of IF GNSS data were collected. A one-bit digitizing front-end was used employing the Morion OCXO as a frequency reference and was fed by an external NovAtel GPS-702-GG antenna via an external LNA. Complex samples were collected at a rate of 10 MHz. A reference trajectory was obtained from a NovAtel SPAN™ LCI IMU and SPAN™ SE receiver, providing IMU data at 200 Hz. For the purposes of IMU aiding of the oscillator, a selection of inertial sensors were attached to the data collection setup including a 3-Space Sensor (TSS-DL-HH-S 2012), HTC Wildfire smartphone, and Nexus 7 tablet. The three devices containing inertial sensors were strapped-down in close proximity to the oscillator, such that it is reasonable to assume that the acceleration experienced by the oscillator during dynamics was captured entirely by the various IMUs. Were the two units separated by a significant distance, the gyroscope may have been utilized to estimate the relative change in acceleration during rotations.

Datasets of five minute duration were collected under static and various dynamic scenarios and the data was post-processed by various versions of GSNRx™ wherein the receiver channels employed a Kalman filter based tracking strategy. These versions included the standard scalar-based receiver, the ultra-tight receiver and a modification of each of these, including *g*-sensitivity compensation, as depicted in Figure 4-2. As discussed in Chapter 2, a PLI is used as a qualitative measure of the carrier phase tracking performance across receiver architectures.

Table 4-2 Data collection scenarios

Scenario	Notes
A	Pedestrian mounted antenna, oscillator, IMUs and front-end under open-sky conditions
B	Pedestrian mounted oscillator, IMUs and front-end connected to a static antenna under open-sky conditions
C	Automobile mounted antenna, oscillator, IMUs with moderate speeds on gravel roads and mild off-track roads

A selection of operating environments was considered, including pedestrian navigation under both open and obstructed sky conditions and an automotive environment. These are briefly summarized in Table 4-2. In scenarios A and B the pedestrian was initially stationary to allow the receiver to collect ephemeris and executed a series of movements such as gentle walking on level-ground, walking and slow running on a staircase for the rest of the dataset. There were sporadic pauses of approximately 5 to 10 second duration in between movements during which the pedestrian was at rest. On some occasions the halting time is as large as about 20 seconds. The implications of these dynamics on the oscillator's *g*-sensitivity, and hence on the carrier phase tracking, will be discussed further in Section 4.4.1. In scenario C, the equipment was mounted on a vehicle and tested on

gravel and unpaved roads. The vehicle on the gravel road experienced mild high-frequency vibrations throughout the drive, whereas the vehicle encountered sudden bumps on another unpaved road, as will be discussed in detail in Section 4.4.3.

As mentioned in Section 4.2, variations in the acceleration impinging upon the oscillator will induce variations in the observed carrier frequency. If the frequency variation is perfectly tracked in all channels, the instantaneous frequency will appear as a clock drift term within the navigation solution. If one or more channels fail to adequately track these frequency variations, however, the navigation solution will observe an apparent LOS velocity for the corresponding satellite, which, in turn, will induce errors in the velocity solution. These apparent LOS velocities are expected to be eliminated by explicitly compensating for the oscillator g -sensitivity effects in all tracking channels.

4.4.1 Demonstrating g -sensitivity compensation

A five minute dataset was collected in test scenario A, wherein a pedestrian was equipped with a rigid backpack on which was mounted the oscillator, the front-end, the antenna, and the NovAtel LCI IMU, as depicted in Figure 4-3. The pedestrian remained stationary for the first 40 seconds, to allow the receiver to extract ephemeris on all satellites in view after which point the pedestrian executed a series of movements.

This dataset was post-processed using both the standard and ultra-tight variations of GSNRx™, without applying any oscillator compensation and the resultant PLI metric corresponding to one particular satellite, PRN 8, which was located at an elevation of approximately 78 degrees, was recorded and plotted in Figure 4-4. Degradation in carrier tracking performance can be observed for all receiver configurations from approximately

40 to 275 seconds during which time the pedestrian was moving. There are two primary contributing factors to this carrier phase tracking error: the physical dynamics of the antenna relative to the satellite and the g -sensitivity of the oscillator. In Figure 4-4 (a) it can be seen that the performance of the uncompensated scalar receiver is considerably improved by applying oscillator compensation. Comparing the uncompensated curves in Figure 4-4, enabling ultra-tight mode also induces a significant performance improvement. However, neither the compensated scalar receiver, nor the uncompensated ultra-tight receiver can effectively track the carrier phase. To achieve this, oscillator compensation must be activated on the ultra-tight receiver. Figure 4-4 demonstrates the resultant PLI performance wherein it can be seen that almost all of the tracking error has been removed. The mean PLI value for all satellites in view is presented in Figure 4-5 (a), again demonstrating the benefit of oscillator compensation both for the scalar and ultra-tight receivers. It is interesting to note the spikes in the PLI when the pedestrian halted temporarily in between the movements, for example between 165 to 180 s in Figure 4-4 (a). When the pedestrian halts the dynamic stress on the tracking loop significantly reduces, due to the reduction of satellite-receiver LOS dynamics as well as elimination of oscillator's g -sensitivity effects, leading to improved phase tracking performance.

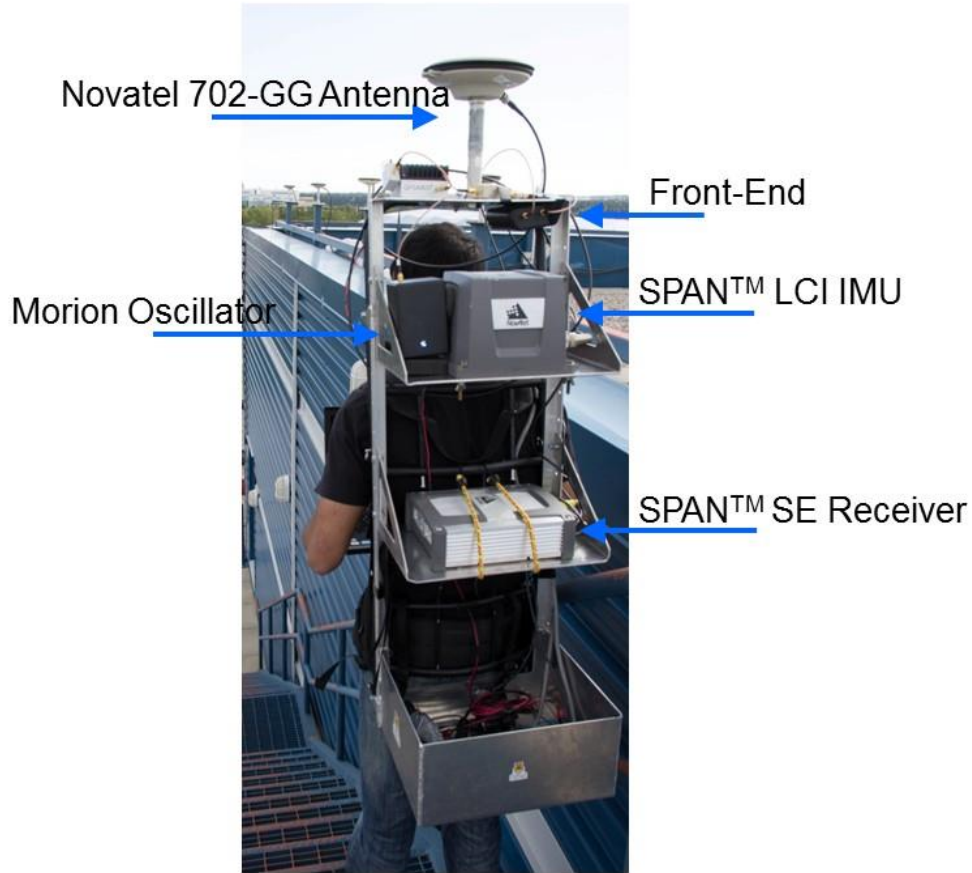


Figure 4-3 Equipment configuration for pedestrian data collection in Scenarios A and B

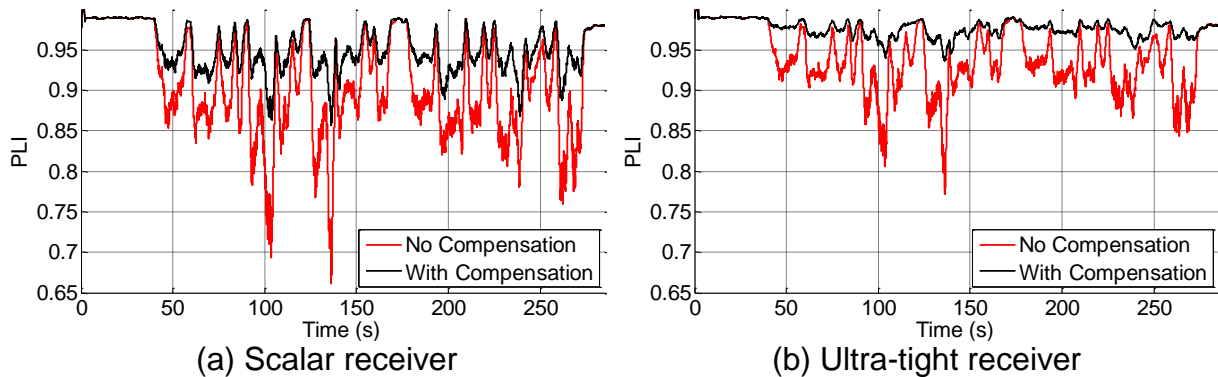
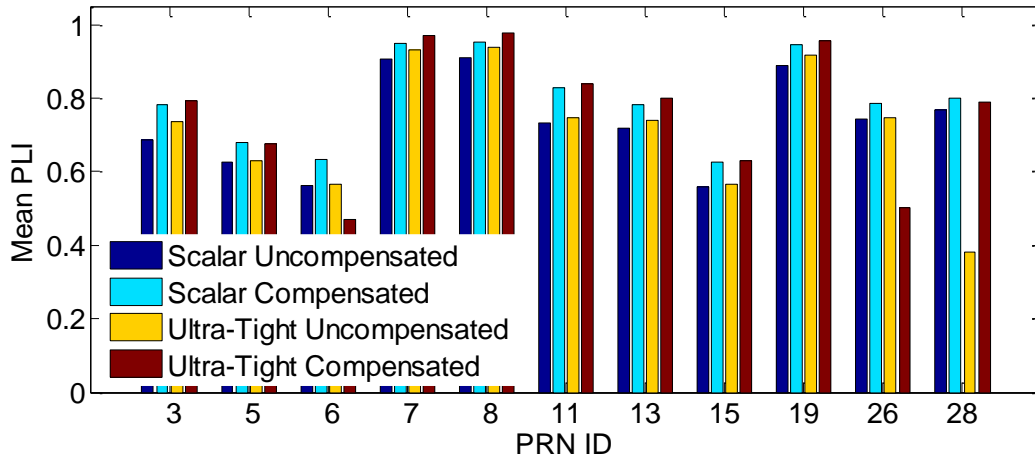
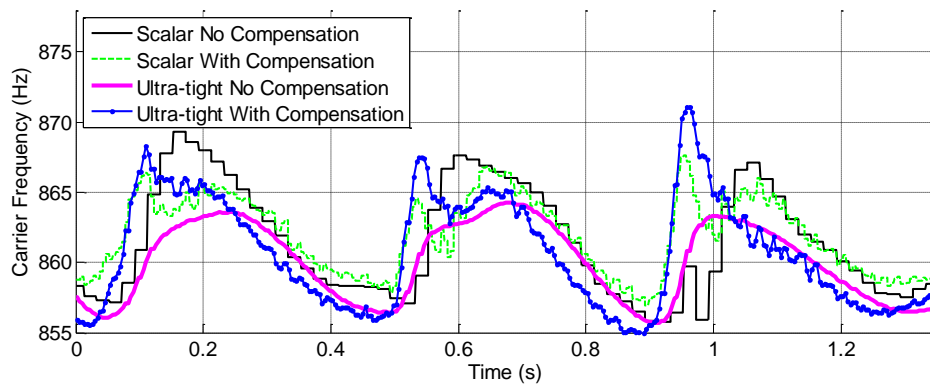


Figure 4-4 Carrier phase tracking performance of the scalar and ultra-tight receivers with and without oscillator compensation for scenario A for PRN 8



(a) Mean PLI for Scenario A



(b) Carrier frequency trajectories for various receiver configurations

Figure 4-5 (a) Mean PLI values for all satellites in view for various receiver configurations in Scenario A (b) Estimated carrier frequency for various receiver configurations in the same scenario

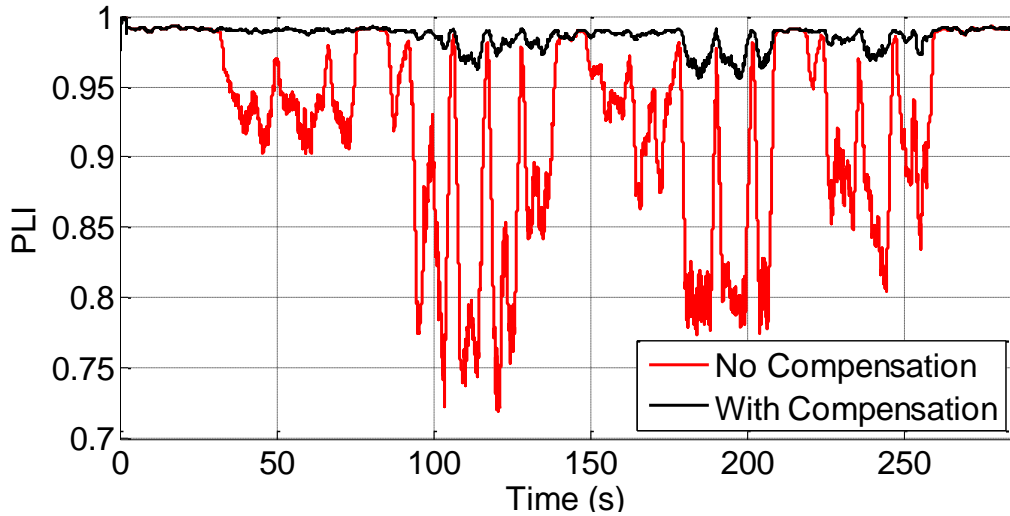
Figure 4-5 (b) compares the carrier frequency estimates of both the scalar and ultra-tight receivers both with and without g -sensitivity compensation over the period of three consecutive pedestrian strides. The fundamental difference in behavior between compensated and uncompensated receivers is evident. The g -sensitivity compensation mechanism is a feed-forward technique whereas standard tracking in a scalar receiver is feed-back only. Therefore, in general, compensating receivers will react more accurately and more readily to oscillator induced frequency disruptions than a non-compensating

receiver. As is clear in the figure, the compensating receivers respond earlier to changes in carrier frequency which results in a lower phase tracking error and, thus, a higher observed PLI value.

The carrier phase tracking performance, for the dataset discussed in this section, depends on two major sources of dynamic stress, namely LOS dynamics and oscillator-induced dynamics. However, it is of interest to quantify the oscillator related errors, which is investigated by collecting another dataset aimed to isolate the two error sources; this is described next.

4.4.2 Isolating oscillator induced carrier disruptions

A five minute dataset was collected in Scenario B, wherein the experimental setup and pedestrian motion were similar to that of Scenario A, except that the antenna was mounted on a stationary pillar and connected via a low noise amplifier and a 30 m coaxial cable to the pedestrian mounted front-end. In this way, the pedestrian motion is experienced by the oscillator, but not the antenna and the observed carrier frequency variations are therefore only due to satellite motion and the oscillator. As the satellite induced Doppler drift is relatively low and effectively constant over a five minute duration, the observed carrier tracking error can almost entirely be attributed to the oscillator's g -sensitivity. This dataset was processed with the scalar version of the receiver both with and without g -sensitivity compensation enabled.



4-6 Carrier phase tracking performance of the scalar receiver with and without oscillator *g*-sensitivity compensation for scenario B for PRN 8

The resultant PLI measurements are shown in Figure 4-6. It is evident that the oscillator is a significant error source and that these errors can be effectively mitigated by a simple feed-forward compensation technique. The tracking errors are almost completely removed, resulting in tracking performance during pedestrian motion comparable to the initial 30 s, where the pedestrian was stationary. It is interesting to note momentary spikes in PLI when the pedestrian halts momentarily.

4.4.3 Vehicular navigation

The effectiveness of oscillator *g*-sensitivity compensation for vehicular navigation is examined in this section. A dataset was recorded in Scenario C where the antenna, IMU, oscillator, and front-end were mounted on the roof of a typical urban vehicle, as depicted in Figure 4-7 (a). The vehicle was driven at moderate speeds on both a gravel road and on unpaved trails for a period of five minutes each.

The two datasets differed in terms of the acceleration experienced by the receiver. In the case of the gravel road, the accelerations were typically of small amplitude but of very high frequency, whereas the off-road dataset exhibited sporadic large accelerations. It is emphasized here that the g -sensitivity issue becomes prominent when the oscillator is exposed to rapid acceleration changes. Constant velocities or accelerations, however, have little effect on the carrier phase tracking performance.

Examining Figure 4-8 (a), it is clear that the gravel road environment does not generally pose a significant challenge to the phase tracking process. This is not surprising as these vibration-induced accelerations are of such a high frequency that they result only in small amplitude, high-frequency phase jitter. What is significant is that the better performing implementations are the two employing oscillator compensation. Specifically, in this case, the standard scalar receiver with the addition of oscillator compensation outperforms the uncompensated ultra-tight receiver in terms of phase tracking. Also noteworthy is the phase perturbation at approximately 25 and 65 seconds, where both uncompensated receivers exhibit a sustained phase error while the compensated varieties do not. This is the characteristic of the behavior of receivers under the influence of large constant or low frequency accelerations. This effect can be observed to a much higher degree in Figure 4-8 (b), for the unpaved road dataset where the difference between receivers which employ oscillator compensation and those that do not is much more significant. In this case, the vehicle traveling on a straight path encountered significant bumps on the road inducing disruptions due to oscillator g -sensitivity. Again, it is clear that the two compensating receivers offer better phase tracking performance. The compensating

ultra-tight receiver does, however, distinguish itself as providing the best performance in terms of highest mean PLI value and highest minimum PLI value across the dataset.

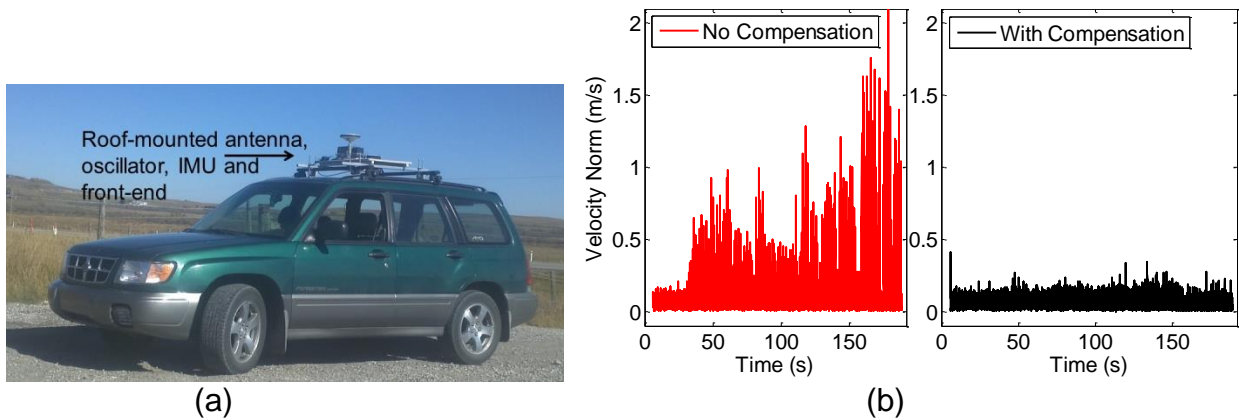


Figure 4-7 (a) Equipment configuration for vehicular navigation data collection, (b) Norm of three-dimensional velocity errors for the g -sensitivity isolated dataset

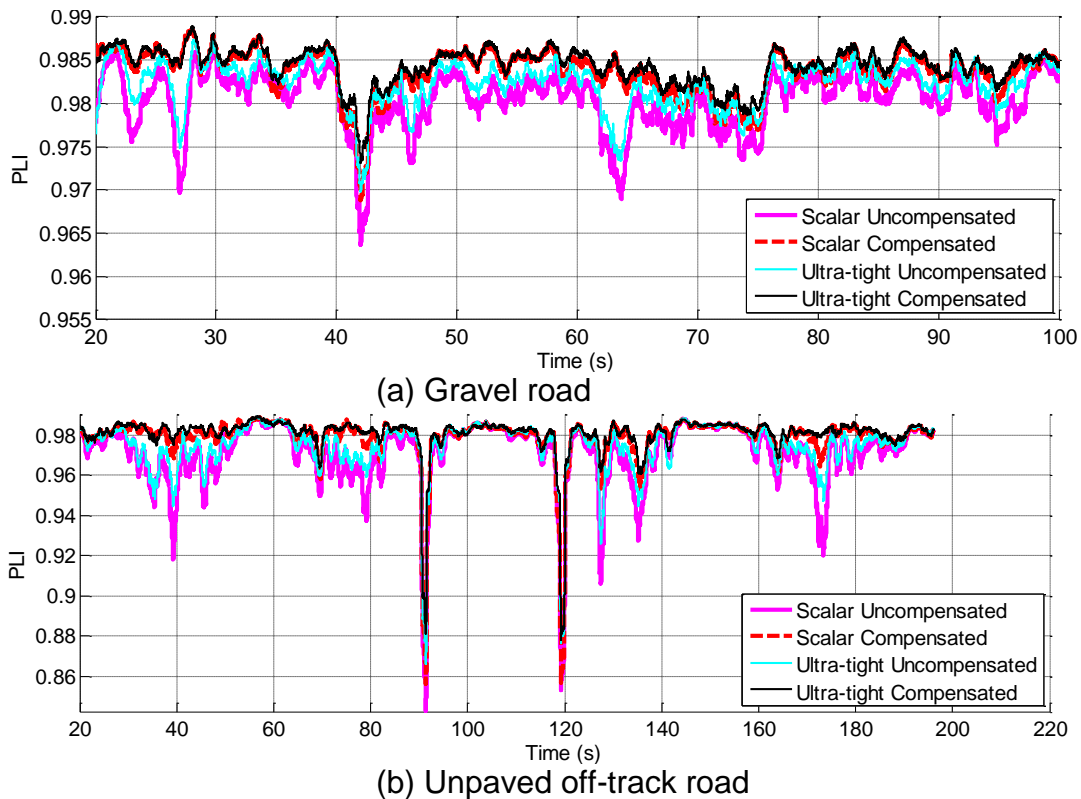


Figure 4-8 Phase tracking performance of the scalar and ultra-tight receivers with and without oscillator compensation for scenario C

4.4.4 Navigation domain performance analysis

Oscillator g-sensitivity compensation not only improves carrier phase alignment and frequency tracking, it also has a pronounced effect in the navigation domain. To illustrate this, the dataset collected in Scenario B was processed for both the non-compensating and compensating receiver configurations using a least-squares navigation solution at a rate of 200 Hz, synchronous with that of the IMU data. The least-squares algorithm was preferred to a Kalman filter to eliminate the influence of system model and to enable a focused analysis on the accuracy of estimated velocities as a function of the measurements only. As the antenna was stationary for the duration of the dataset, the velocity estimates produced by the navigation solution can be directly interpreted as velocity errors.

Figure 4-7 (b) shows norm of the three-dimensional velocity errors for both the compensated and uncompensated receiver. It is clear that once the pedestrian begins to move the velocity errors in the uncompensated receiver begin to grow rapidly. The oscillator induced frequency changes are common to all tracked satellite signals and should, ideally, result only in a change in the estimated clock drift. Unfortunately, however, not all receiver channels will accurately track these frequency changes and the residual errors will manifest themselves as errors in the estimated LOS velocity to each satellite. Moreover, as the phases of the received spreading code on each satellite signal are different, the tracking channels are updated asynchronously. Thus, when the oscillator is experiencing high dynamics, the Doppler observations from each channel will reflect the average oscillator frequency over different, albeit overlapping, periods.

Table 4-3 Velocity component standard deviations for scenario B

$\sigma_{\vec{v}}$ (m/s)	North	East	Vertical	$\ \vec{v}\ $
No Compensation	0.04	0.03	0.16	0.17
With Compensation	0.02	0.02	0.05	0.06
Mean DOP values	NDOP - 0.57	EDOP - 0.54	VDOP - 1.21	GDOP - 1.59

By compensating for the oscillator g-sensitivity centrally, this problem is significantly reduced, as evidenced by the stark reduction in velocity errors for the compensating receiver, as shown in Figure 4-7 (b). Indeed, the velocity errors corresponding to the period of time when the pedestrian was in motion are comparable to those when the pedestrian was stationary, suggesting that little more than the effects of thermal noise remain. The north, east and vertical velocity standard deviations for both receiver configurations are presented in Table 4-3. It is interesting to note that the performance improvements appear to be concentrated in the vertical direction. In GNSS positioning the height in the geodetic coordinate system is highly correlated with the user clock bias due to satellite geometry. A satellite is visible to the receiver only if it is above the receiver's local horizon. This one-sided placement of satellites with respect to the receiver's local-level position results in a correlated vertical position and clock bias, as a part of the altitude correction in the navigation solution will be interpreted as a correction to clock bias. This leaves the user height and the clock bias correlated; the same reasoning applies to the correlation between the vertical velocity and clock drift. In the current work the estimate of the user clock drift is improved due to improved Doppler

measurements. Therefore, given the high correlation between clock drift and vertical velocity, significant improvements in the latter are expected. Improved velocity accuracy can also yield improved position accuracy when velocity models are used in navigation filter.

4.4.5 Phase tracking sensitivity and cycle slips

The usefulness of the proposed algorithm was gauged by PLI. However, it is also useful to understand the effectiveness of the proposed method in lowering the effective noise equivalent bandwidth. This section demonstrates how g -sensitivity compensation can lower the tracking loop bandwidth by measuring the lowest bandwidth that can be used without incurring cycle slips. The occurrence of cycle slipping is a non-linear complicated function of dynamics, signal-to-noise ratio, and loop parameters. The cycle slips analyzed in this paper are restricted to scenario B where the dynamics experienced by carrier tracking loops are only due to the oscillator. A cycle slip is declared when the carrier phase measurement from the test receiver deviates from the reference by a preset threshold, which is generally half a cycle for GPS L1 C/A signals. The reference carrier phase was generated by a compensated receiver with a sufficiently large bandwidth under the assumption that no cycle slips have occurred. The reduction of noise-equivalent bandwidth in traditional tracking architectures is similar to reducing power spectral density values in Kalman filter-based tracking architectures. The analysis conducted in this section, therefore, is through reduction of power spectral density values for the acceleration state of the five-state Kalman filter discussed in Chapter 2. It should also be noted that the oscillator phase and frequency spectral densities are set to zero, thus the

stochastic model for the Kalman filter reduces to a random walk model in signal acceleration. This modification permits comparative analysis of the limit of LOS spectral density with and without compensation.

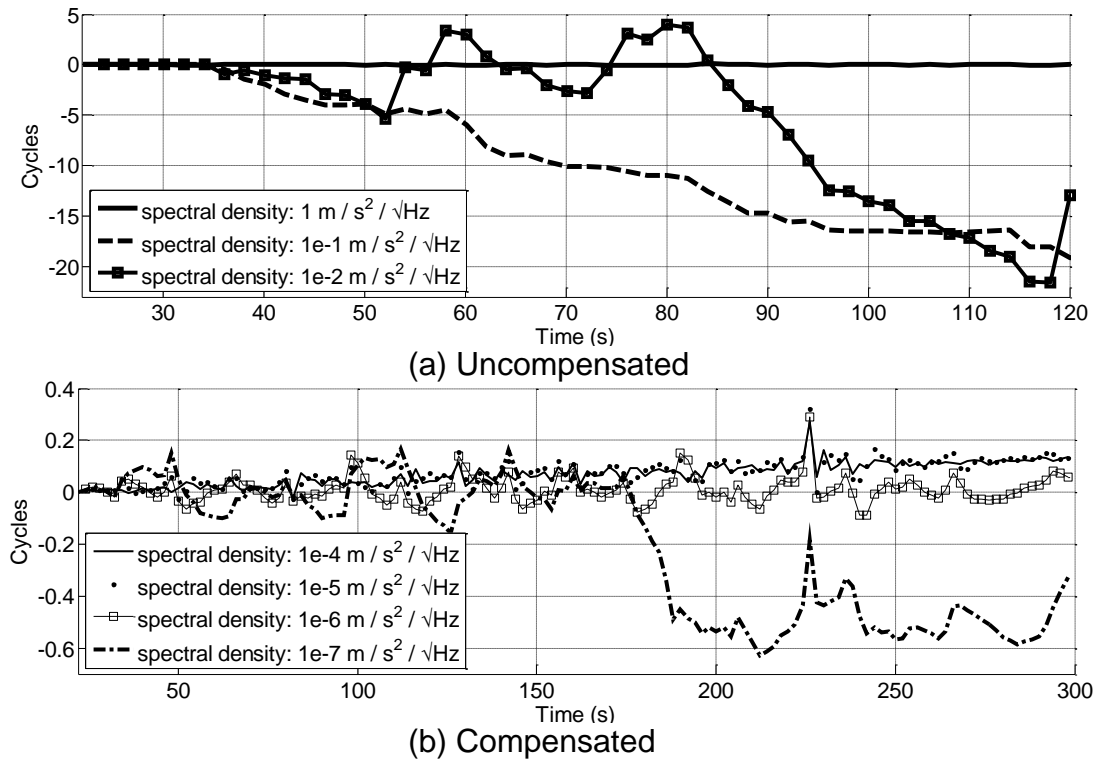


Figure 4-9 Carrier phase cycle-slip test statistics for selection of spectral density values for compensated and uncompensated receivers in Scenario B

Figure 4-9 compares cycle slip test statistics for PRN 7, with approximately 72 degrees of elevation and with a C/N_0 value of about 48 dB-Hz for both compensated and uncompensated receivers. It can be observed that the compensated version allows lower spectral densities without incurring cycle slips thereby improving carrier phase tracking noise performance. It is interesting to note that in this particular operating scenario there is no significant LOS dynamics, and hence no discernible cycle slips after compensation due to reduced bandwidth. However, the PLI metric shown in Figure 4-10 indicates that

lower tracking loop bandwidth leads to loss of phase alignment. Therefore, under these conditions, the tracking loop declares loss of phase lock before a cycle slip occurs and the limiting spectral density in this case is determined to be $10^{-4} \text{ m/s}^2/\sqrt{\text{Hz}}$ (Figure 4-10), where PLI remained well above the phase lock threshold of 0.866. The phase lock threshold is obtained from the relation $\text{PLI} \approx \cos(2\overline{\delta\Phi})$, where $\overline{\delta\Phi}$ is the tolerable 1-sigma phase jitter equal to 15 degrees (Ward et al 2006a). The limit obtained in compensated receivers is predominantly a trade-off between thermal and accelerometer measurement noise vs. oscillator phase noise and satellite dynamics.

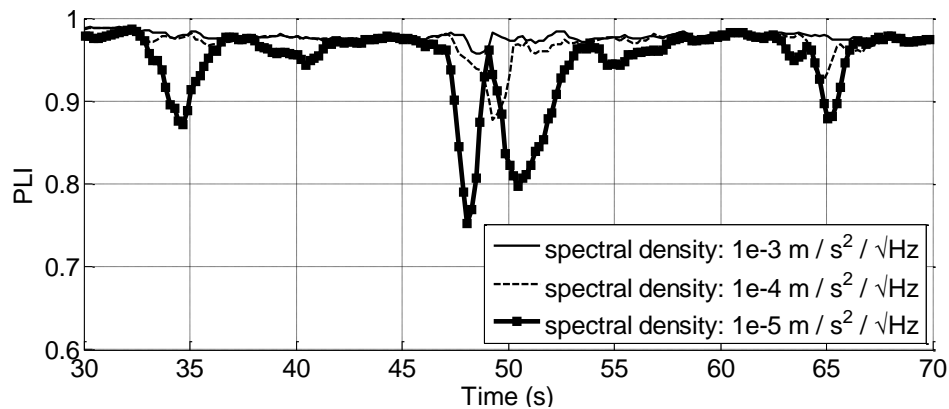


Figure 4-10 PLI for selection of spectral densities depicting phase misalignment below the phase-lock threshold for compensated receiver in scenario B

4.5 Design considerations

A number of key design choices and IMU features which influence the effectiveness of oscillator g-sensitivity compensation and overall carrier phase tracking performance are examined here, including accelerometer linear range, IMU data rate and accelerometer calibration.

4.5.1 Accelerometer quality

The quality of the IMU used for g -sensitivity compensation is critical and poor quality acceleration measurements can not only fail to improve tracking performance but can, in fact, degrade it. Moreover, it is evident that the use of higher quality acceleration measurements results in improved carrier tracking performance. To explore this notion, the relative performance of the LCI and HTC IMUs are compared via a dataset collected in Scenario A where the receiver antenna and the oscillator and IMU were subject to pedestrian dynamics. The resultant PLI is presented in Figure 4-11 (a). The difference in performance between the receiver that uses the LCI IMU and that which uses the HTC IMU is a result of reduced noise in each measurement, less coarse acceleration decimation and less saturation of the accelerometers. The effect of sensor saturation is particularly evident at approximately 95 s, at which point the equipment experienced a sudden sharp acceleration resulting from knocking the receiver against the wall.

Pedestrian motion, in particular, can induce quite large accelerations and can often saturate low quality MEMS sensors. A short dataset collected in Scenario A and shown in Figure 4-11 (b) illustrates the difference between measured accelerations using different quality IMUs. The HTC sensor limited linear range of about 2 g is exceeded in the pedestrian receiver during most walking and running manoeuvres. The IMU should therefore be chosen carefully to ensure that it can adequately measure the full range of the receiver dynamics.

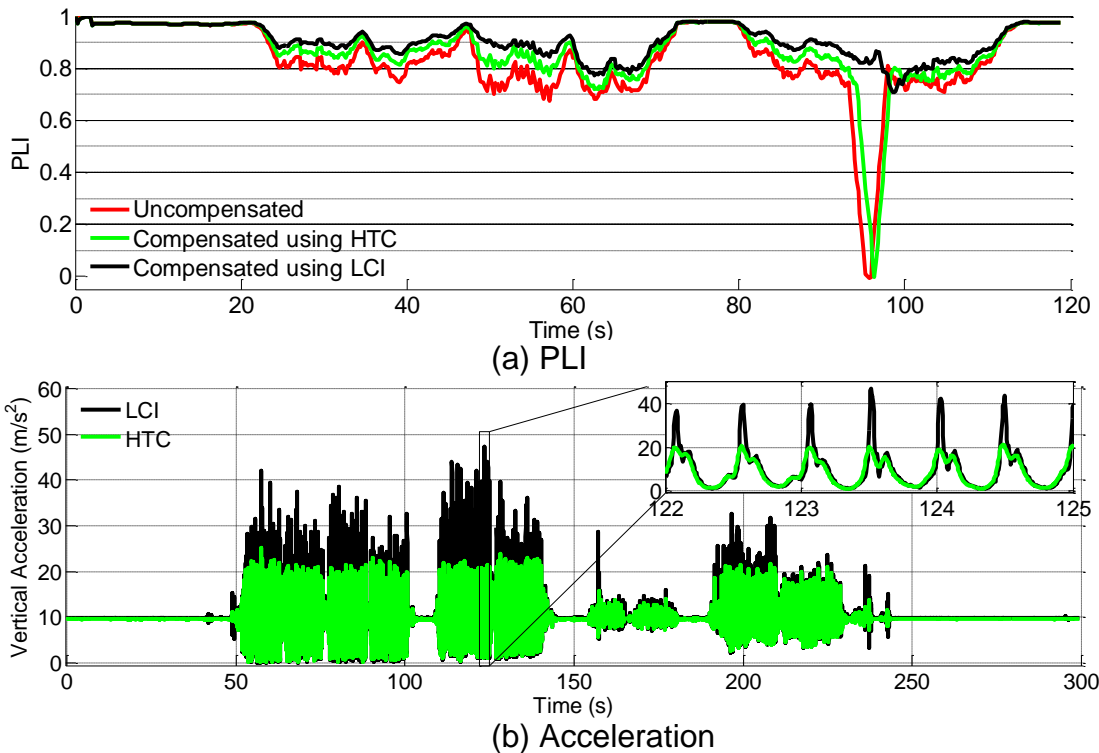


Figure 4-11 (a) PLI values for scenario A with no compensation and with compensation using HTC and LCI IMUs (b) Corresponding pedestrian accelerations recorded by LCI and HTC IMUs

4.5.2 IMU data rate

Carrier frequency and code-rate corrections provided by the g -sensitivity compensation algorithm are provided to the code and carrier NCOs synchronously across all receiver channels at a fixed rate, dictated by the IMU. The choice of update rate can have a significant impact on the effectiveness of the g -sensitivity compensation depending on the temporal characteristics of the user dynamics. The effect of the IMU data rate on the observed PLI for receivers operating in Scenario A and C were examined for a selection of IMUs. The results are presented in Figure 4-12 for a selection of data rates between 6.25 and 800 Hz.

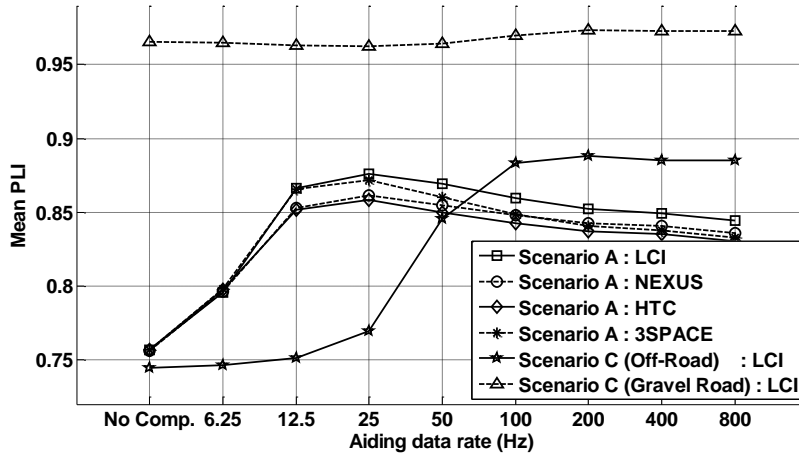


Figure 4-12 Mean PLI value versus IMU data rate for a selection of IMUs examined in both Scenario A and B

Examining the curves corresponding to Scenario A it is clear that PLI performance is maximized for an update rate of approximately 25 Hz while it falls sharply for lower rates. This implies that the pedestrian dynamics are concentrated between 0 and 12 Hz, observing Nyquist. Interestingly, the trend is consistent across all four IMUs, even though they vary significantly in quality. This implies that the choice of data rate should be conditioned by the desired application and not by the quality of the IMU measurements. For the curves corresponding to Scenario C it appears that the rate should be chosen to be above approximately 150 Hz, although it is evident that the *g*-sensitivity effects are significantly less pronounced for the gravel road case.

4.5.3 IMU and oscillator *g*-sensitivity calibration

Generally before measurements from an IMU can be employed for the purpose of navigation, the device must be calibrated. The calibration parameters, namely bias and scale-factor are often obtained either via an offline calibration procedure or via on-line recursive estimation. Assuming a set of biased acceleration measurements and

examining Eq. 4-4, it is clear that when implementing g -sensitivity compensation, IMU bias results in a biased frequency estimate within the receiver. This bias, however, manifests itself in exactly the same manner as the inherent clock drift. It will have no impact on the overall receiver performance provided the bias is small enough and varies sufficiently slowly over time. Receivers are generally designed to tolerate clock drift in the region of 200 m/s or more and taking the worst case values from Table 4-1, it is clear that even a bias of 1 m/s^2 on each axis would have a negligible effect on receiver performance. The accelerometer scale factor, in contrast, can be more problematic as a non-unity gain will result in a frequency correction that is not proportional to the induced frequency change. The oscillator g -sensitivity calibration errors also result in non-unity gain in the frequency correction computed by the proposed algorithm. To explore this effect, the data corresponding to Scenario B was processed using a compensating scalar receiver within which the accelerometer scale-factor, or alternatively the oscillator g -sensitivity, was intentionally miscalculated by a certain percentage. Figure 4-13 illustrates the maximum observed phase error during the test versus calibration error where an error of -100 % is equivalent to no compensation and an error of +100 % is equivalent to over-compensation by a factor of two. The phase error was estimated by inverting the PLI metric. It appears that calibration errors of up to 10% have little effect on the overall performance whereas larger errors degrade the carrier phase tracking performance linearly.

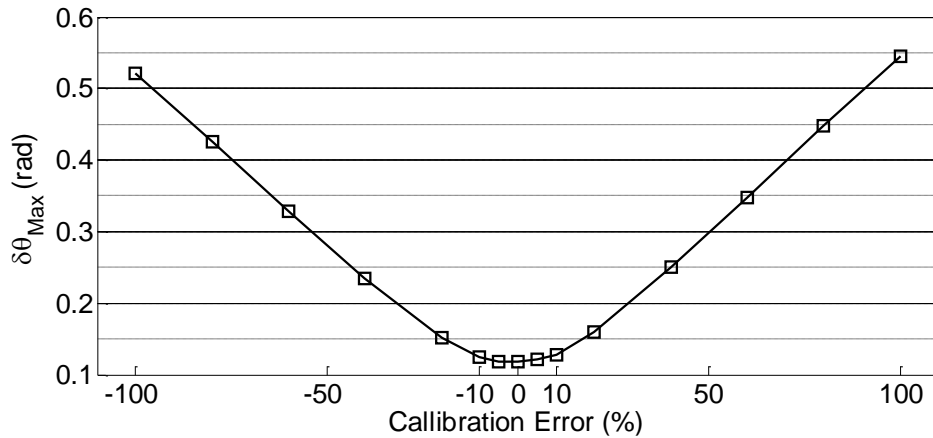


Figure 4-13 Maximum observed phase errors for a receiver operating in Scenario B for a range of scale factor calibration errors

4.6 Summary

It is evident that the acceleration sensitivity exhibited by typical TCXOs and OCXOs can be problematic when tracking carrier phase in GNSS receivers. By utilizing a receiver borne IMU, these oscillator induced tracking errors can be compensated for, which can result in a significantly improved tracking performance. The tracking improvement gained by employing this technique has been demonstrated in both a pedestrian and vehicular scenario using both a scalar and ultra-tight receiver and it has been shown that both receiver architectures can benefit. Results show that the compensation technique is relatively insensitive to IMU quality and low-cost MEMS grade sensors are adequate although performance can be improved through the use of a better IMU.

Chapter Five: Pedestrian dynamics prediction exploiting quasi-periodicity

5.1 Introduction

Pedestrian dynamics affect tracking loop dynamics stress in two ways, namely the apparent dynamics due to the local oscillator g-sensitivity and LOS Doppler variations. It was demonstrated in Chapter 3 that even though oscillator's g-sensitivity is compensated for using accelerometers, the LOS dynamic stress has to be addressed for effective carrier phase tracking. It was shown in Chapter 4 that by activating oscillator g-sensitivity compensation on an ultra-tight receiver, dynamic stress due to both g-sensitivity and LOS frequency variations can be addressed. An alternative dynamic compensation technique is proposed in this chapter, which is explained in Section 5.2 that involves dynamics prediction using quasi-periodicity inherent in pedestrian dynamics, thus attempting to obviate IMUs to measure dynamics. The experimental validation of the proposed method with pedestrian dynamics in a controlled environment is discussed in Section 5.3. Section 5.4 presents a detailed description of the details of the prediction algorithm. Additional results with regular pedestrian dynamics, along with oscillator g-sensitivity effects across pedestrian subjects, are discussed in Section 5.6.

5.2 Proposed dynamics compensation technique

Strong quasi-periodicities in pedestrian dynamics that manifest as harmonics in the frequency domain were demonstrated in Chapter 3. The amplitudes and frequencies of harmonics depend on the sensor location and motion pattern such as walking or running. It was also demonstrated through experiments in Chapter 4 that the pedestrian motion

causes significant dynamic stress on tracking loops. The traditional tracking loop architectures, being feedback systems, are often slow to respond to changing signal conditions. The method proposed in this chapter attempts to bridge the intrinsic response time delay by predicting dynamics ahead of time by exploiting the quasi-periodicity inherent in pedestrian dynamics to the extent possible. The predicted dynamics is used to generate a feed-forward carrier frequency correction to enhance carrier synchronization.

The composite carrier phase process model of the baseband signal is described in Chapter 2, Eq. 2-9, and is reproduced below for convenience:

$$\theta_i = \theta_i^{LOS}(\vec{V}) + \theta^g(\vec{A}) + \theta^T(\mathbb{T}) + \theta^{ST} + \theta^{LT} + \theta_i^\eta + \theta_i^0 \quad \mathbf{5-1}$$

The LOS dynamics and oscillator g -sensitivity contributions to the incoming signal carrier phase can be further split into quasi-periodic and aperiodic components as

$$\begin{aligned} \theta_i^{LOS}(\vec{V}) &= \theta_{qp}^{rx}(\vec{V}) + \theta_{ap}^{rx}(\vec{V}) + \theta^{sat,i} \\ \theta^g(\vec{A}) &= \theta_{qp}^g(\vec{A}) + \theta_{ap}^g \end{aligned} \quad \mathbf{5-2}$$

where the quasi-periodic component due to LOS pedestrian dynamics is represented by θ_{qp}^{rx} and the oscillator g -sensitivity induced phase variations is θ_{qp}^g . The terms θ_{ap}^{rx} and θ_{ap}^g represent the respective aperiodic counterparts. The LOS dynamics due to satellite motion is denoted by $\theta^{sat,i}$. The composite phase process in Eq. 5-1 can be categorized into quasi-periodic and aperiodic components as

$$\theta_i = \theta_{qp}^{rx,g}(\vec{V}, \vec{A}) + \theta_{ap}^{rx,g,T,ST,LT,\eta}(\vec{V}, \vec{A}) + \theta_i^0 \quad \mathbf{5-3}$$

where quasi-periodic components θ_{qp}^{rx} and θ_{qp}^g are combined into the term $\theta_{qp}^{rx,g}$, all the other aperiodic components are lumped into $\theta_{ap}^{rx,g,T,ST,LT,\eta}$ except for the arbitrary initial

phase offset θ_i^0 . The carrier phase process can be recast into a carrier frequency process without loss of generality, except for the constant of integration, which is the arbitrary initial phase, as

$$f_i = f_{qp}^{rx,g}(\vec{V}, \vec{A}) + f_{ap}^{rx,g,\mathbb{T},ST,LT,\eta}(\vec{V}, \vec{A}) \quad 5-4$$

where the frequency terms $f_{qp}^{rx,g}$ and $f_{ap}^{rx,g,\mathbb{T},ST,LT,\eta}$ are the quasi-periodic and aperiodic counterparts of the phase terms $\theta_{qp}^{rx,g}$ and $\theta_{ap}^{rx,g,\mathbb{T},ST,LT,\eta}$.

The proposed method aims to predict the component $f_{qp}^{rx,g}$ that dominates the carrier phase process and, subsequently, to aid the tracking loop with changes in dynamics to enhance carrier synchronization. The dynamics prediction algorithm is combined with the Kalman filter based architecture discussed in Chapter 2, as shown in Figure 5-1. The component $f_{qp}^{rx,g}$ is assumed to be fully represented by a set of sinusoidal basis functions over a short duration. The prediction algorithm attempts to separate $f_{qp}^{rx,g}$ using the carrier frequency estimate \hat{f}_i obtained from the Kalman filter based tracking loop and subsequently applies feed-forward correction to the carrier NCO. The carrier frequency estimate \hat{f}_i is affected by thermal noise in addition to the carrier frequency process parameters mentioned in Eq. 5-4, which can be expressed as

$$\hat{f}_i[k] = \overbrace{f_{qp}^{rx,g}(\vec{V}, \vec{A}, k)}^{\text{quasi-periodic}} + \overbrace{f_{ap}^{rx,g,\mathbb{T},ST,LT,\eta}(\vec{V}, \vec{A}, k)}^{\text{aperiodic}} + \overbrace{\eta_{\hat{f}_i}[k]}^{\text{thermal noise}} \quad 5-5$$

where the term $\eta_{\hat{f}_i}$ denotes the error due to thermal noise effects in the estimated carrier frequency. The discrete-time index k is introduced to indicate that the underlying process evolves over time.

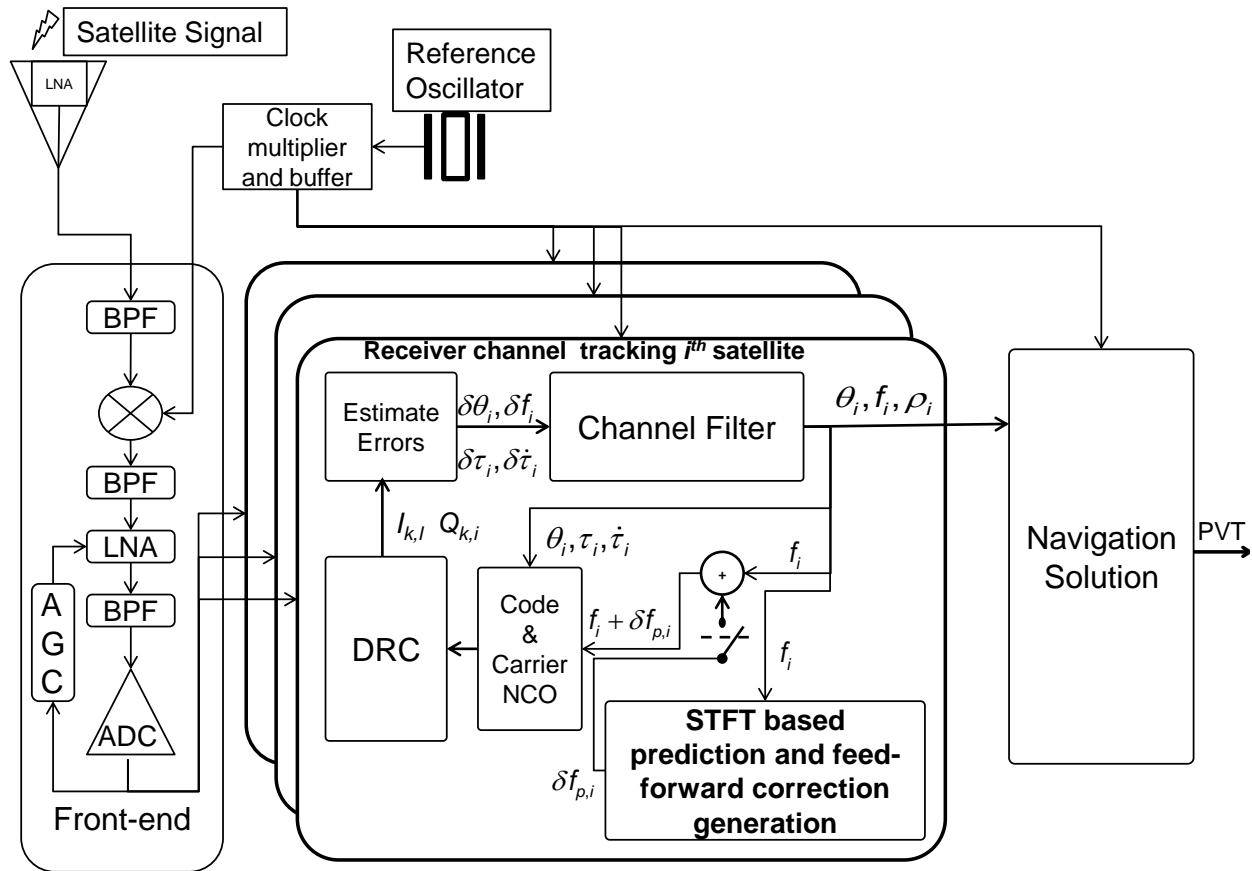


Figure 5-1 Proposed tracking architecture illustrated as an augmentation to the traditional tracking architecture

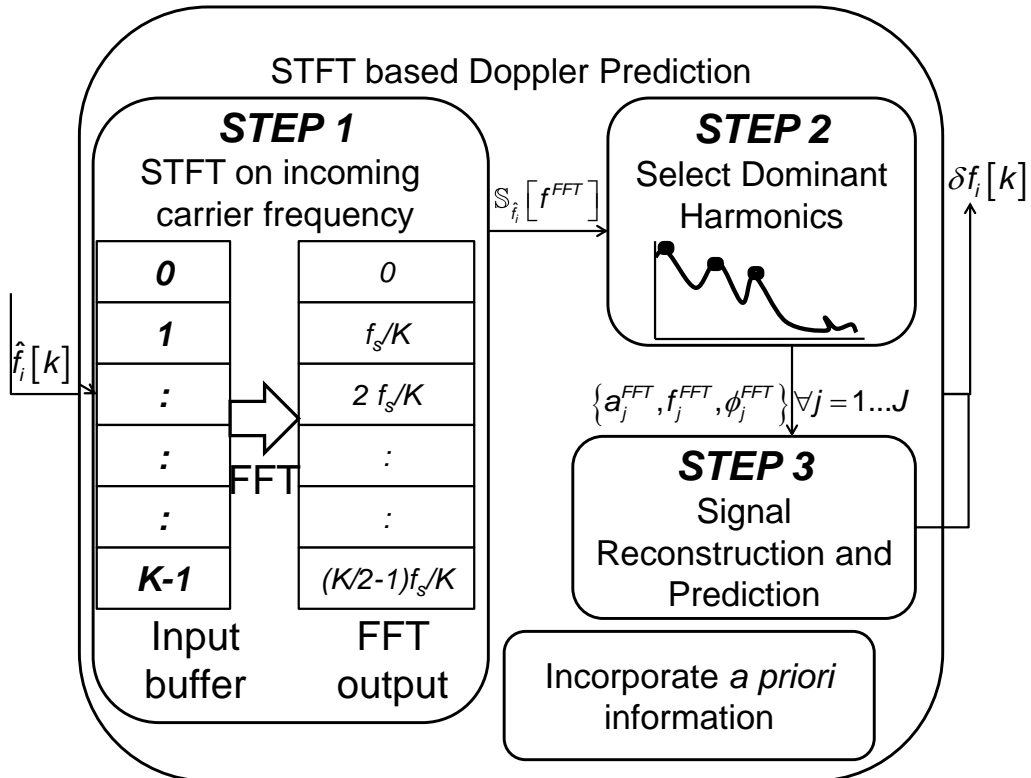


Figure 5-2 Details of STFT-based feed-forward compensation algorithm

The algorithm is schematically represented in Figure 5-2 and explained step-by-step in the following sections.

Step 1: Short-term Fourier transform

The carrier frequency estimates from the tracking loop filter are collected into a buffer with a predefined length. The algorithm begins to operate once the buffer is filled. The carrier frequency process is converted into the frequency domain by performing an FFT operation on the input buffer resulting in Discrete Fourier Transform (DFT) coefficients, mathematically expressed as

$$\widehat{F}_{i,k}[l] = \sum_{m=0}^{m=K-1} \widehat{f}_i[m-k] e^{-\frac{j2\pi lm}{K}} \quad 5-6$$

where $\widehat{F}_{i,k}[l]$ is the sequence of DFT coefficients defined for $\forall l = 0 \dots K-1$, where l is the frequency domain index and K is the length of the input array. The discrete-time index k is used to reference the incoming carrier frequency samples corresponding to i^{th} satellite. The buffer is synchronously updated with the tracking loop update at 20 ms; the sampling frequency $F_{S,STFT}$ of the carrier frequency process is therefore 50 Hz, which is well above the Nyquist rate, considering the frequency process bandwidth discussed in Chapter 3.

Although it is preferable to improve the spectral separation of harmonics by increasing the input buffer length, the pedestrian dynamic variations, due to its quasi-periodic nature, limits the buffer length. The observation window length K varies from 32 to 128 respectively corresponding to 0.64 and 2.56 seconds. The length of the input buffer should accommodate one full period of fundamental frequency in pedestrian dynamics that corresponds to the time taken for one pedestrian step, which changes across pedestrian motion modes, sensor location and subjects. Therefore, this parameter is subject to tuning based on the knowledge of the pedestrian motion. The frequency resolution of an FFT is given by $F_{S,STFT}/K$, which corresponds to 1.56 Hz for $K = 32$. The input samples are zero-padded to use a 512 point FFT algorithm, which increases the frequency resolution to approximately 0.1 Hz; the increase in FFT buffer length can be represented in Eq. 5-6 by replacing the old buffer length K by a new variable L where $L = K + P = 512$.

Step 2: Selection of dominant harmonics

This step operates on the PSD of the frequency process computed by squaring the FFT results obtained from *Step 1*, mathematically represented as

$$S_{i,k} [l] = |F_{i,k} [l]|^2 \quad \forall l = 1 \dots L \quad \mathbf{5-7}$$

Due to FFT spectral leakage, a harmonic, which is ideally a line spectrum, becomes a smooth curve in a PSD. The curves become smoother with zero-padding. Therefore, the local maxima of such curves should be identified for dominant harmonics selection. A harmonic is identified by a simple test on the PSD value against its nearest adjacent local minimum. If the PSD of a local maximum is more than 3 dB higher than its adjacent local minima, then it is identified as a dominant harmonic. After the local maxima are identified, the harmonics that fully represents the quasi-periodic components $f_{qp}^{rx,g}$ should be selected. However, it is challenging to separate the side-lobes that result due to the windowing effect from the actual harmonics, given the trade-off between spectral resolution and dynamic range of the PSD estimate as discussed in Section 3.2.6. To this end, the harmonics are sorted based on the PSD value and a fixed number of harmonics with the highest PSD values are selected, as the process power is concentrated in a first few dominant harmonics which is evident from the PSD characterization results in Chapter 3. The maximum number of such harmonics, which is also a design parameter, is restricted to 4. The choices of design parameters, namely peak selection threshold and maximum number of harmonics, are verified based on an empirical evaluation of carrier tracking performance in this work.

The mean value of input samples for STFT should be removed from the input samples as the DC component has no value addition for dynamics prediction. Moreover, the zero padding of input data requires zero mean in the input samples in order to avoid distortions in the estimated PSD. In addition to DC any linear trend over time in carrier frequency, which is mainly due to slow time-varying satellite motion and the linear rate of change of the local clock drift, can also be removed from the input samples. The aim of the algorithm is to predict the quasi-periodic components of the receiver dynamics only. Therefore, any known aperiodic pattern in the carrier frequency process should be removed. The linear trend is estimated using a simple line fitting using least-squares.

The number of selected harmonics, J , at any specific instant, can be either less than or equal to the maximum number of harmonics. The output harmonics are represented by their amplitude, frequency and phase, denoted as $\{a_j^{FFT}, f_j^{FFT}, \phi_j^{FFT}\} \forall j = 1 \dots J$.

Step 3: Doppler reconstruction, prediction and correction data generation

The signal components corresponding to the harmonics selected in step 2 can be reconstructed by applying a simple Inverse Discrete Fourier Transform (IDFT). The signal reconstruction is mathematically depicted as

$$\tilde{f}_i[k] = \sum_{j=1}^J 2a_{j,k}^{FFT} \cos(2\pi f_{j,k}^{FFT} n + \phi_{j,k}^{FFT}) \quad 5-8$$

where k is the discrete time index that refers the carrier frequency process, $\tilde{f}_i[k]$ is the reconstructed carrier frequency process, $a_{j,k}^{FFT}$, $f_{j,k}^{FFT}$ and $\phi_{j,k}^{FFT}$ are the amplitude, frequency and phase of the j^{th} harmonic respectively, estimated at the time index k , and J is the number of selected harmonics. The amplitude, frequency and phase of the dominant

components are time-dependent, which indicates that the underlying carrier frequency process is only short-term stationary. Therefore, continuous estimation of the process is necessary to accommodate and measure time-varying process attributes.

The signal reconstruction technique described in this section is not exactly the same as IDFT, as all the Fourier coefficients are not considered for reconstruction. However, this is necessary to separate aperiodic and noise components and use only quasi-periodic components for reconstruction.

As the selected harmonics are deemed to represent a quasi-periodic portion of the underlying process, the process can be predicted ahead of the current time window. The proposed method attempts to prove the usefulness of prediction to improve carrier tracking performance. The prediction is performed for the sample immediately following the current window and the difference between the last sample in the current window and the next sample is applied to the carrier NCO as a feed-forward correction. The application of feed-forward correction operates continuously synchronous with the tracking loop update. The tracking loops can be relatively slow to respond to changing dynamics and therefore one-sample feed-forward correction, provided that the dynamics are estimated correctly, should improve carrier synchronization. The correction factor can be mathematically written as

$$\widehat{\delta f}_i[k] = \alpha (\tilde{f}_i[k+1] - \tilde{f}_i[k]) \quad \mathbf{5-9}$$

where α is the feed-forward gain which is also a design parameter and normally takes values in the range 0 to 1. When $\alpha = 0$, no feed-forward correction is applied and the tracking loop reduces to traditional architecture.

Incorporation of additional information

It is desirable to incorporate any additional information that is known *a priori* to improve the estimation of the feed-forward correction factor. The additional information can be information about the receiver dynamics pertaining to the application or information available through other algorithms in the receiver such as context awareness. In this work, the additional information in the form of an upper frequency limit to the harmonics search in the estimated PSD is incorporated. The pedestrian dynamics is shown to contain much of its energy concentrated within 15 Hz (Antonsson & Mann 1985), which is also consistent with the characterization results discussed in Chapter 3. Therefore, it is reasonable to select dominant harmonics within 15 Hz. There is also a lower frequency limit to the usefulness of the estimated PSD. The lower limit is due to the observation window length used for the FFT. For example, if the window length is 0.64 seconds, no harmonics below the fundamental frequency of 1.56 Hz can be resolved due to insufficient data length. In the current work, this information is readily incorporated as additional constraints in *Step 2* during the dominant harmonics selection.

5.2.1 A few possible alternatives to STFT

The Kalman filter based tracking architecture already contains prediction and stochastic models of the signal parameters to be estimated, as discussed in Chapter 2. However, only linear models are used in the dynamic model that fails to incorporate the quasi-periodic nature of the states. Even though it is possible to define dynamic models for quasi-periodic processes, the process is quite complex and often requires precise knowledge of the amplitude and frequency of the harmonics responsible for quasi-

periodicity, which requires online characterization of pedestrian dynamics using inertial sensors. No attempt is made in that direction herein. Also, the augmentation architecture proposed in this work is generic and can be applied, at least in principle, to other tracking architectures such as PI controllers.

There are other parametric models available for quasi-periodic signal analysis and prediction, such as wavelet transforms, Linear Predictive Coding (LPC), etc. However, their performance primarily depend on the correct choice of parameters, for example the wavelet shape. Unfortunately, as shown in Chapter 3, the pedestrian dynamics changes over time and the parameters need to be readjusted if parametric models are employed. However, STFT is one of the simplest and convenient non-parametric models for signal analysis. In addition, numerous studies on gait analysis mentioned by Voutsis et al (2014) indicate that the pedestrian motion consists of sinusoidal variations and STFT uses sinusoidal basis for signal analysis. Furthermore, STFTs can be readily implemented in software or dedicated hardware in modern Digital Signal Processor (DSP) chips as FFT.

5.3 Experimental validation with LOS dynamics only

The effectiveness of the proposed method in delivering improved carrier phase tracking performance is demonstrated in this section through experiments using live GPS signals.

5.3.1 Experimental setup and data processing

Even though the oscillator g -sensitivity is addressed, using the method proposed in Chapter 4 for example, the LOS dynamics can be a significant source of carrier disruptions that needs to be compensated for in order to obtain effective carrier tracking performance. To this end, the oscillator and front-end are kept stationary through the data

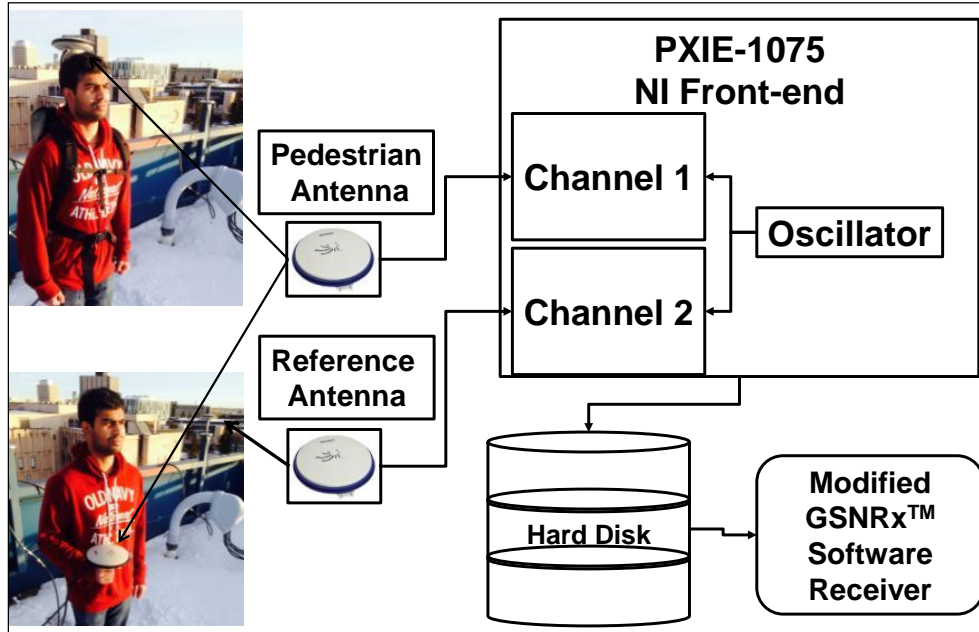
collection to eliminate oscillator g-sensitivity effects. The differential GNSS setup with two antennas is shown in Figure 5-3 (a), where live GPS IF data was collected under open sky conditions from two NovAtel 702 GG antennas separated by 5.19 m using an NI PXIE-1075 two-channel front-end. The two channels are synchronized with a common OCXO. The details of the datasets collected with this setup are available in Table 5-1. The datasets will be referred to herein according to the naming convention stated in Table 5-1.

Table 5-1: Datasets collected with various pedestrian motions

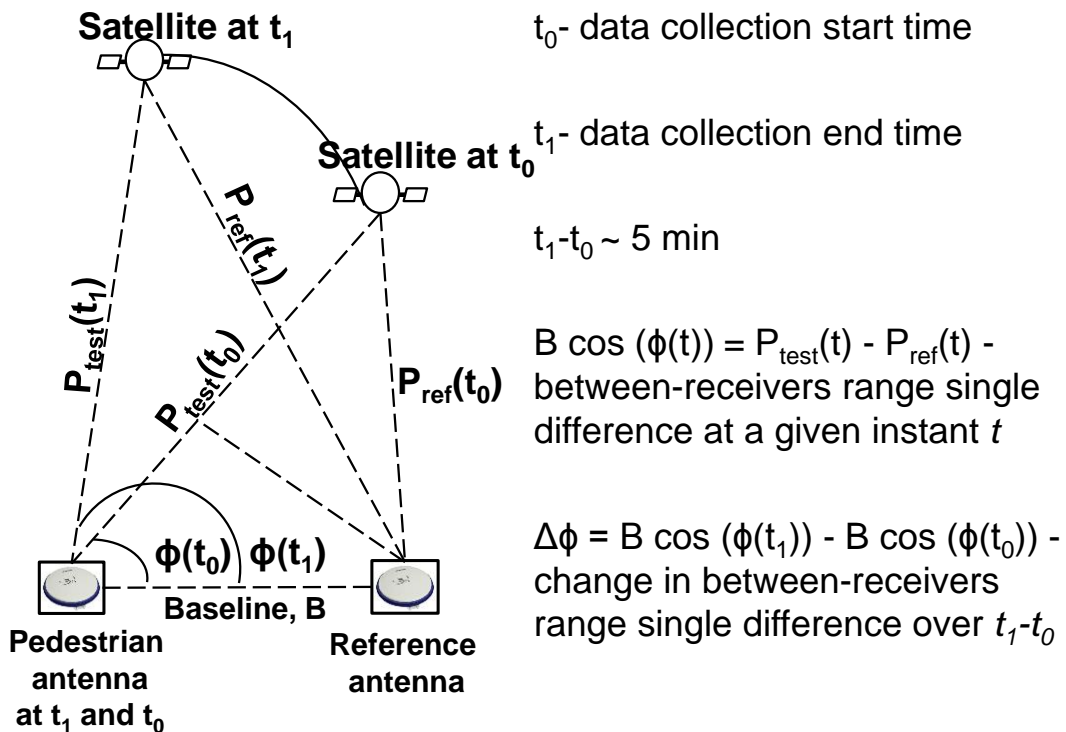
Name	Antenna Location	Pedestrian motion
Scenario-A	Backpack, overhead	Jogging
Scenario-B	Hand-held	Jogging
Scenario-C	Hand-held	Running, sway, jogging, walking

One of the antennas was kept stationary and served as reference, while the other pedestrian borne antenna was subject to the various manoeuvres described in Table 5-1. This DGPS data collection setup enables the removal of most satellite dynamic effects on the observed carrier frequency and phase through between-receivers single differences of carrier phase and frequency measurements due to the short baseline and small data collection duration such that differential satellite motion can be ignored. However, a more comprehensive method of cycle slip detection will be discussed in Chapter 6 by extending the technique adopted in this section. The maximum differential change in range due to satellite motion over five minutes for the baseline length of 5.19 m was calculated as shown in Figure 5-3 (b) and is approximately equal to one GPS L1 cycle. The clock effects are cancelled via differencing as the same clock is used for two receivers. The differencing was performed only for the analysis purposes and no changes

in the algorithm were necessary. The datasets were processed using the modified version of GSNRxTM that implements the proposed algorithm.



(a)



(b)

Figure 5-3 (a) Test setup to isolate the effect of pedestrian dynamics on carrier signal from other sources (b) Computation of differential residual ranges due to satellite motion for the given baseline

5.3.2 Performance demonstration

The performance of the proposed method can be evaluated from the PLI plots shown in Figure 5-4 for PRN 14 with about 51 degrees of elevation corresponding to Scenario-A and Scenario-B datasets, for compensated and uncompensated receivers. The receiver that employs the proposed tracking strategy with the STFT based feed-forward correction is named the *compensated receiver* whereas the *uncompensated receiver* is identical to the compensated receiver except for the feed-forward correction. The compensation in this chapter refers to STFT-based feed-forward compensation only, but not the g-sensitivity compensation. The PLI plots shown in Figure 5-4 contain intervals of data while the pedestrian was stationary; the time intervals during which the pedestrian was in motion vary from 63.5 to 191 seconds and 198 to 213 seconds in the Scenario-A dataset, and from 54 to 170 seconds and 176 to 197 seconds in the Scenario-B dataset. It appears that the carrier phase tracking performance substantially improves in the compensated receivers, as shown in Figure 5-4. The C/N_0 plots corresponding to PRN 14 are shown in Figure 5-5. It can be inferred that the increase in C/N_0 in the compensating receiver is due to improved carrier frequency synchronization. Of particular relevance is the difference in C/N_0 patterns between the two datasets. The antenna corresponding to Scenario-A dataset was over the head of the pedestrian, as shown in Figure 5-3 (a), and, therefore, experienced no attenuation due to human proximity, but mild attitude changes due to pedestrian motion that induced changes in the antenna gain. In contrast, the antenna in Scenario-B experienced significant signal attenuation due to human proximity and comparatively more changes in the attitude due to hand motion, resulting in higher attenuation, evident in Figure 5-5 (b).

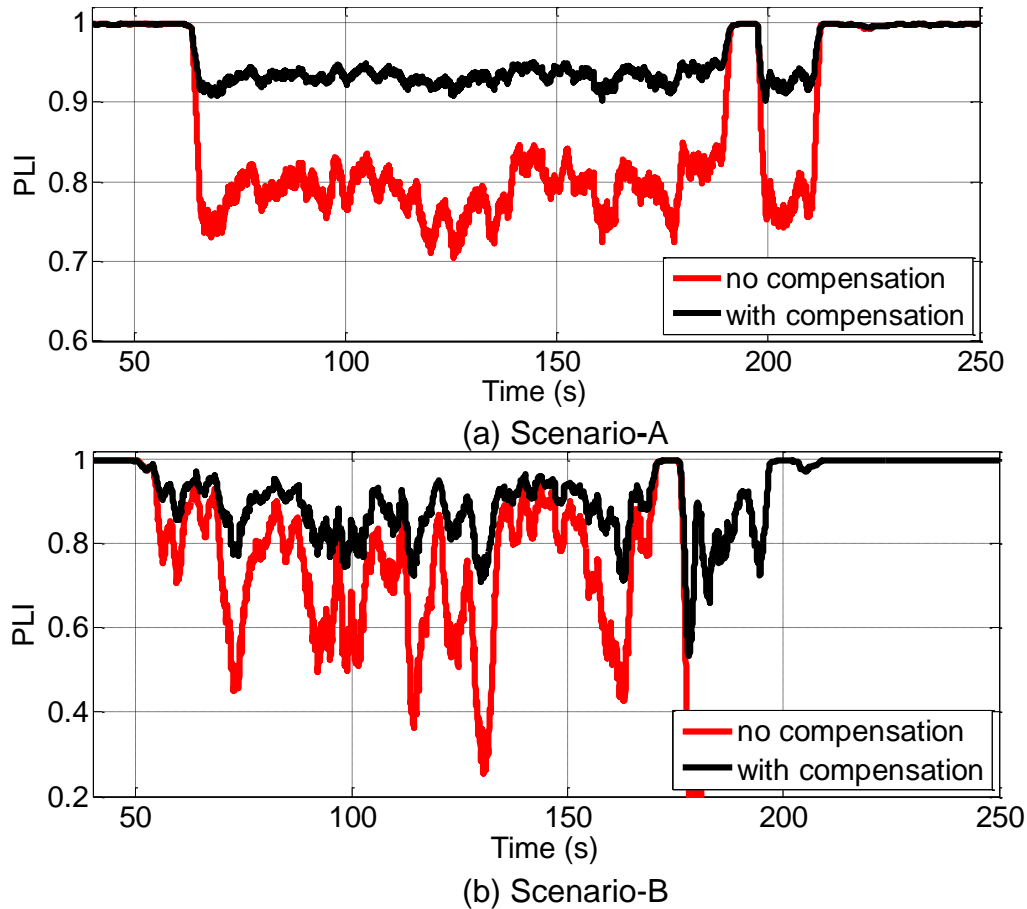


Figure 5-4 PLI corresponding to PRN 14 for Scenario-A and Scenario-B datasets

Figure 5-6 shows the carrier frequency estimates due to pedestrian motion in the compensated and uncompensated receivers for the Scenario-A. In particular, PRN 14 exhibited noticeable changes in the carrier frequency. The satellite motion and local oscillator effects on the estimated carrier frequencies were removed through between-receivers differencing to focus the analysis on pedestrian motion. The uncompensated version necessitates a longer response time to changing dynamics as shown in Figure 5-6, whereas the compensated receiver responds quickly, thus improving the carrier tracking performance. On a similar note, a loss-of-lock can be noticed in the

uncompensated receiver in the Scenario-B dataset, in Figure 5-4 (b) and Figure 5-5 (b), at about 175 s, whereas the compensated receiver continues to track the signal.

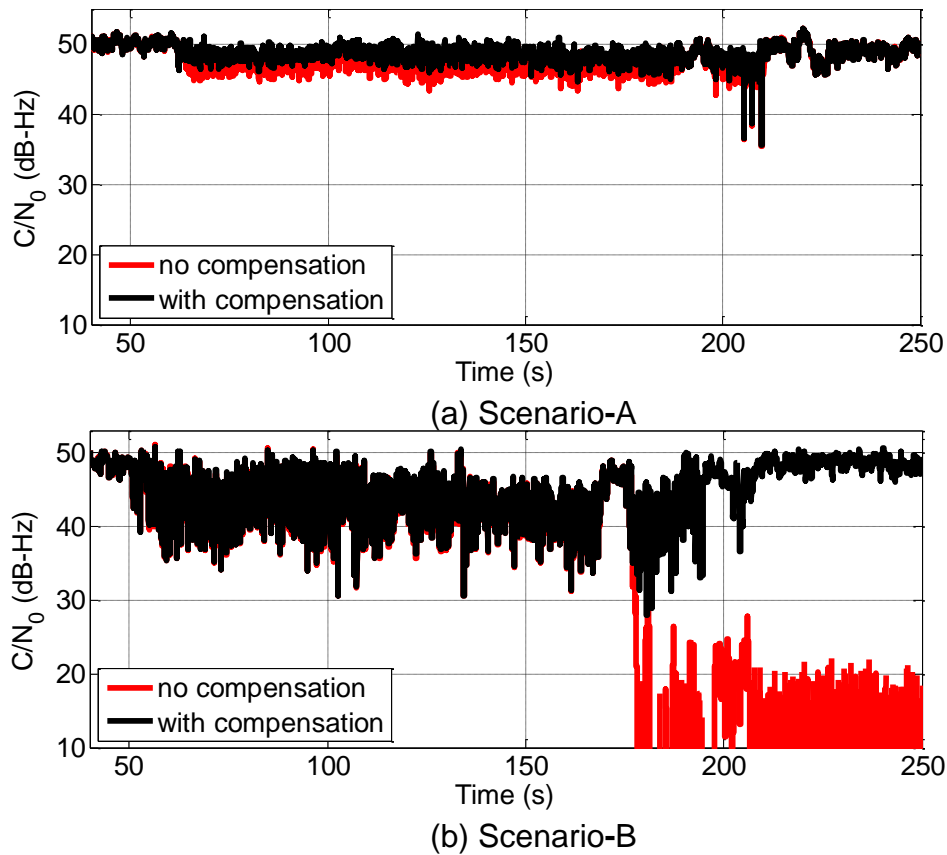


Figure 5-5 C/N₀ corresponding to PRN 14 for Scenario-A and Scenario-B datasets

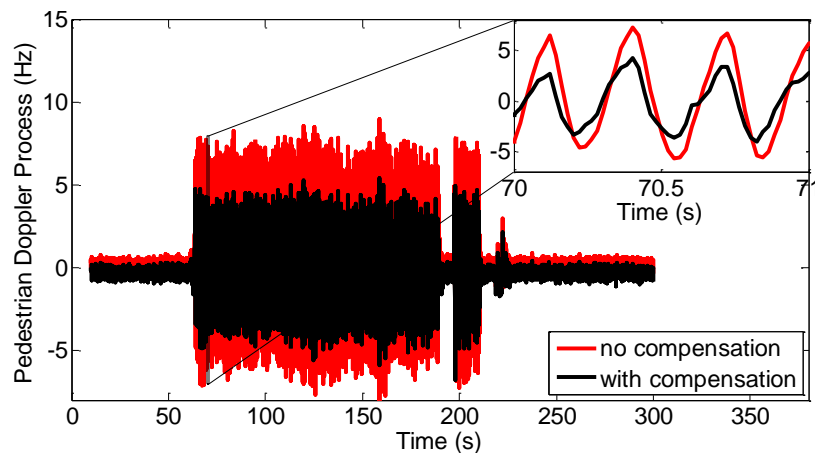


Figure 5-6 Between-receivers difference Doppler corresponding to PRN 14 Scenario-A dataset for the compensated and uncompensated receivers

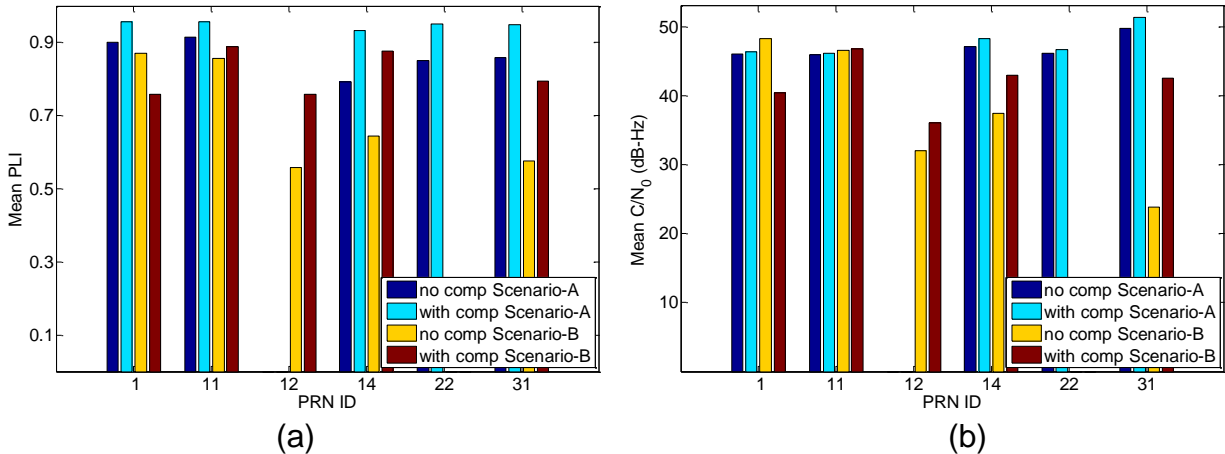


Figure 5-7 (a) Mean PLI and (b) Mean C/N₀ for all satellites in view for Scenario-A and Scenario-B datasets

The mean PLI and mean C/N₀ values for all satellites in view, excluding the intervals during which the subject was stationary, are shown in Figure 5-7 for Scenario-A and Scenario-B. Performance differences with and without compensation were insignificant for stationary intervals, and therefore omitted. It can be seen that the proposed method delivers improved carrier tracking performance over the traditional Kalman filter based tracking architecture. The performance improvement obtained from the proposed method depends on the magnitude of quasi-periodic carrier disruptions of a particular satellite. For example, for the dataset Scenario-B the improvements in PLI for PRN 11 are practically insignificant, whereas it is significant for PRN 12, 14 and 31. Deterioration in performance, in terms of lower PLI and C/N₀ values, is noticeable for PRN1 in the compensated receiver for Scenario-B dataset in Figure 5-7. A detailed inspection of the carrier frequency revealed that the compensated receiver exhibited a false carrier frequency lock on the side-band followed by a loss-of-lock while the uncompensated receiver exhibited continuous tracking. Nevertheless, this was the only instance where contrary results were noticed.

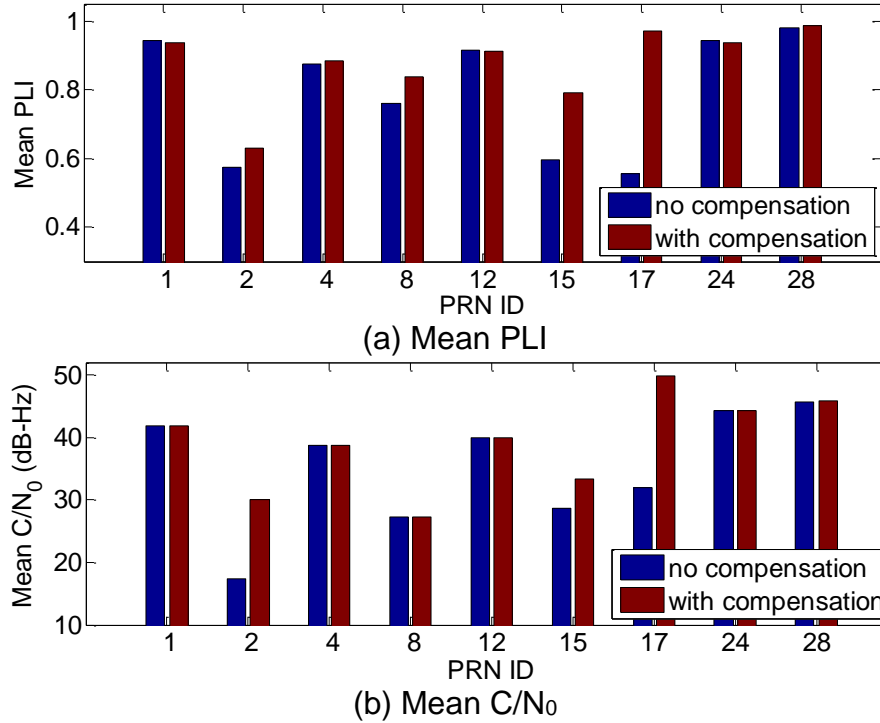


Figure 5-8 Mean PLI and C/N₀ for all satellites in view corresponding to the Scenario-C dataset

In Scenario-A and Scenario-B datasets, the pedestrian exhibited only one motion pattern, namely jogging. Another dataset, named Scenario-C, was collected with various other motion patterns such as running, swaying and walking. The results are shown in Figure 5-8 where it is evident that the compensated receiver delivers improved carrier tracking performance, thereby demonstrating the usefulness of the proposed method. The performance improvements are attributed to the incorporation of additional information into the system, which is the quasi-periodic nature of pedestrian dynamics. The improved results demonstrate successful prediction of quasi-periodic receiver dynamics observable in the carrier frequency process, resulting in the effective reduction of the tracking loop dynamic stress and improved synchronization.

5.3.3 Heuristic cycle slip detection

The performance of receivers employed in RTK applications are fundamentally dependant on continuous and reliable carrier phase tracking. To this end, it is necessary to improve the ability of the tracking algorithm to deliver sustained carrier phase tracking with no or a minimal number of cycle slips. In the current work, although a direct measurement of cycle slips in the pedestrian test receiver is not possible, a qualitative measure can be obtained from between-receivers single difference carrier phase analysis, performed between the pedestrian test antenna and the stationary reference antenna. In order to further simplify the analysis of differential carrier phase measurements, the pedestrian was instructed to begin and end the data collection in the same position while collecting live GNSS data. The initial phase offsets in the single-difference carrier phases are removed. Therefore, the carrier phase differences begin at zero and are expected to end at a predicted value which can be calculated according to Figure 5-3 (b), which is the residual satellite motion explained in Section 5.3.1. Although this method is rather heuristic, it is deemed useful for a comparative analysis of differential carrier phases. The differential carrier phase plots are shown in Figure 5-9 for Scenario-A and Scenario-B datasets.

According to the subplots corresponding to Scenario-A in Figure 5-9, it appears that the compensated and uncompensated receivers behaved almost identically, with no noticeable cycle slips. The relative performance improvement of the proposed method was however noticeable in the improved PLI and C/N_0 values shown in Figure 5-7. However, the uncompensated receiver operating in Scenario-B incurs more losses of

lock, which are identified by discontinuities in carrier phase differences characterized by vertical lines in the y-axis, compared to compensated versions.

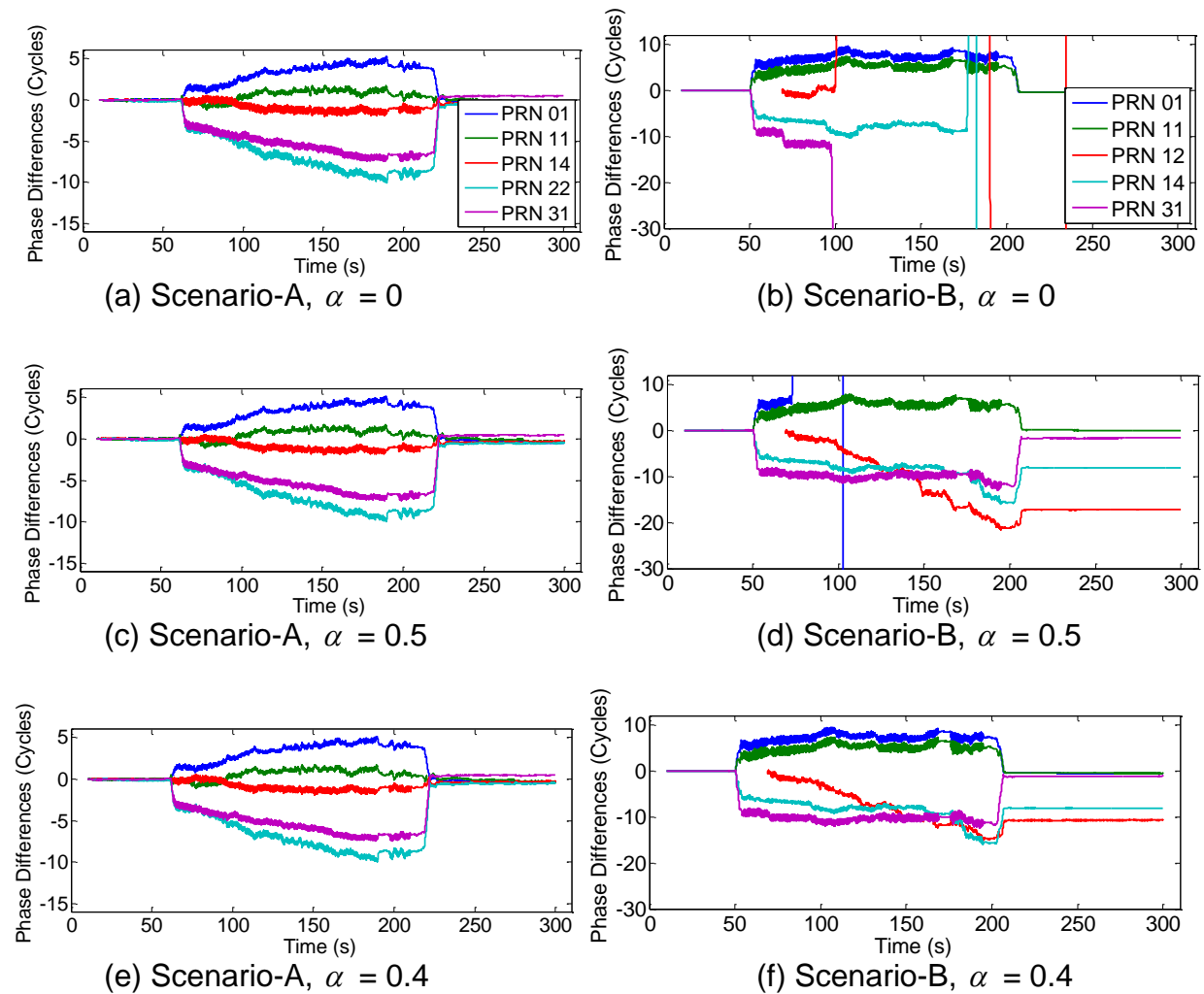


Figure 5-9 Carrier phase between-receivers single difference plots for all satellites in view corresponding to Scenario-A dataset for various feed-forward gains

The carrier phase tracking performance also depends on the feed-forward correction gain, α , described in Eq. 5-9. Notice the carrier phase difference for PRN 1 in Figure 5-9 (d) that corresponds to the compensated receiver with a gain of 0.5 resulted in a loss of lock while the receiver with a lesser gain of 0.4 delivered lossless tracking of PRN 1.

However, it was observed that the tracking performance measured in terms of PLI was slightly degraded when the gain was reduced from 0.5 to 0.4. The dataset Scenario-A exhibited identical performance across 0.5 and 0.4 gains in terms of the PLI. Therefore, the feed-forward is subject to tuning based on the operating scenario. Overall, the proposed method delivers improved carrier phase tracking performance and comparatively more immune to cycle slips. The rest of the results presented herein correspond to a 0.5 correction gain. Unity feed-forward gain is not preferred due to the following reasons: (a) noise prevalent in the estimated pedestrian dynamics might cause instability of the tracking loops, when feed-forward is applied fully; (b) changes in pedestrian motion pattern, for example from walking to a sudden stop, pose challenges to dynamics prediction. Therefore, it is safer to reduce feed-forward gain not to cause loop instabilities. Furthermore, the traditional feed-back tracking loop architecture, by design, also responds to changing dynamics. Therefore, when applying the feed-forward gain, it is also necessary for this gain to be reduced by controlling the loop bandwidth to avoid overcompensation of measured dynamics. The effect of feed-forward gain choices on the achievable carrier phase tracking performance is further explored in Section 5.5. The effect of bandwidth with and without compensation is explored in the next section. The relative difference in performance between the two datasets can be attributed to increased human body attenuation in the Scenario-B dataset, corroborated by the C/N_0 plots shown in Figure 5-7.

5.3.4 Effect of dynamic compensation on the noise equivalent bandwidth

It is desirable to reduce tracking loop bandwidth to keep thermal noise from corrupting the carrier phase measurements. The optimal bandwidth, unfortunately, is a compromise between rapid dynamic response and thermal noise effects. The proposed method is expected to lower the effective noise equivalent bandwidth by compensating for the predictable component of the receiver dynamics. The noise prevalent in the feed-forward path is assumed not to deteriorate the effective noise performance of the loop, as the reduction in feed-forward gain acts as a first order filter on the feed-forward correction. The performance of the tracking loops is assessed in term of the ability of the receiver to track the signal while gradually lowering the bandwidth.

The dataset Scenario-A was processed, with and without compensation for a selection of noise equivalent bandwidths, which is applied in the current Kalman filter-based architecture via a selection of signal acceleration spectral densities. A similar analysis discussed in Section 4.4.5 is repeated in this section. The results are presented in the form of carrier phase difference plots where the differencing is performed between the carrier phase output from a high bandwidth reference version and a selection of test versions. The reference version was chosen as the compensated receiver with a spectral density of $128 \text{ m/s}^3/\sqrt{\text{Hz}}$, thereby assuring that the noise equivalent bandwidth is sufficiently high such that no cycle slips were incurred by visual inspection, which is analogous to the analysis conducted in Section 4.4.5. As the receiver was operating in open sky environments during this test, no significant thermal noise effects occurred by increasing the spectral density value. A cycle slip is declared when a differential carrier phase measurement exceeds one half of the L1 signal.

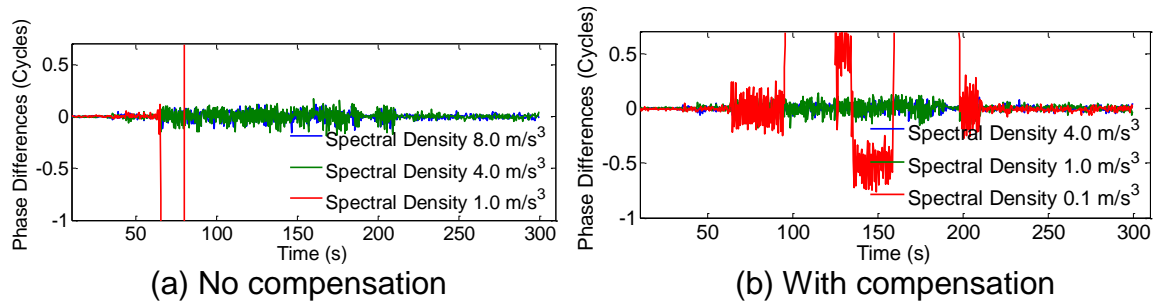


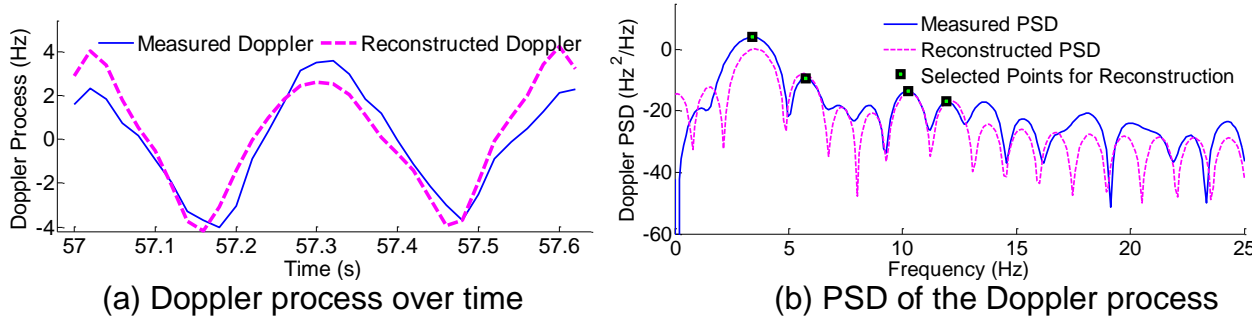
Figure 5-10 Carrier phase between-receivers single differences for PRN 14 serving as qualitative cycle slip test statistics

The results are shown for PRN 14 in Figure 5-10. It is noticed that the compensated receiver does not incur cycle slips until the spectral density is reduced to $0.1 \text{ m/s}^3/\sqrt{\text{Hz}}$ whereas cycle slips are noticeable in the uncompensated version for spectral density of $1 \text{ m/s}^3/\sqrt{\text{Hz}}$. The same behavior is observed for all other visible satellites.

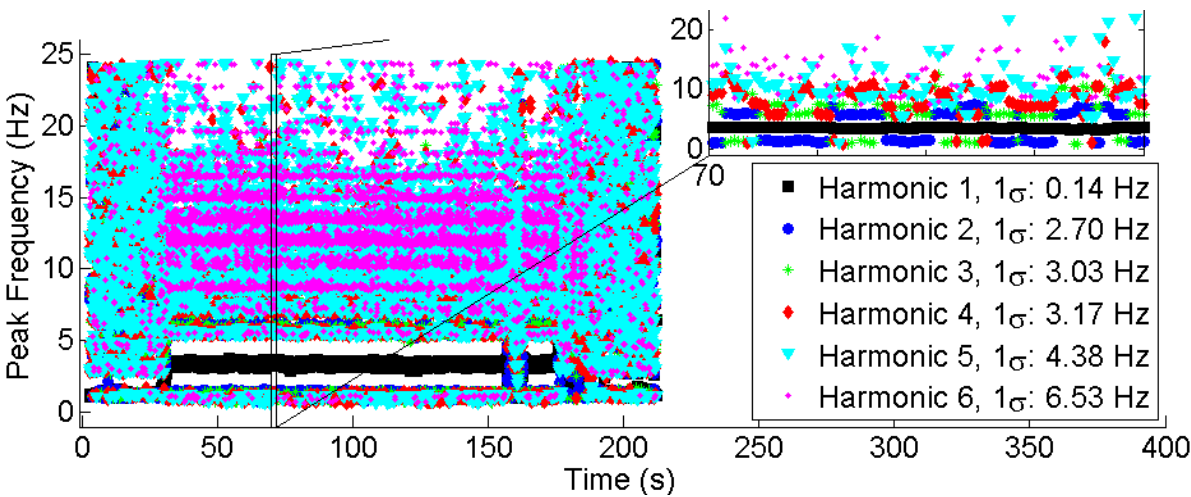
5.4 Details of the prediction algorithm

This section explores the dynamics prediction algorithm by examining the outputs of each section of the algorithm for the Scenario-A dataset. This section is intended to explore the components of the algorithm in detail from a signal processing perspective and also an attempt is made, wherever applicable, to provide empirical justifications of the design parameter choices such as number of harmonics used for reconstruction.

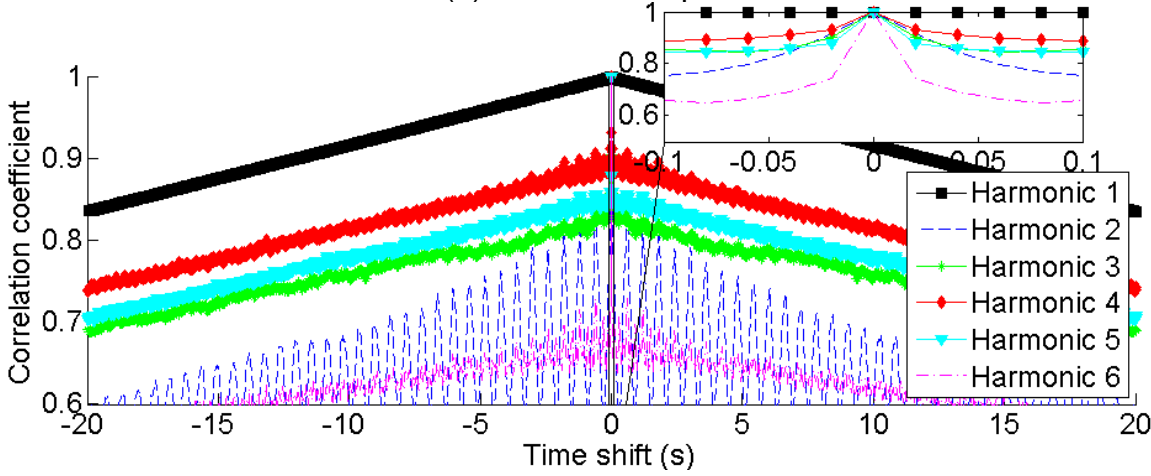
The selection of design parameters inherently depends on the pedestrian dynamics. It is possible to design a more sophisticated prediction algorithm which enables adaptive selection of the design parameters in real-time. However, in order to simplify the design and implementation, the maximum number of dominant harmonics and the threshold for harmonic detection were fixed.



(a) Doppler process over time (b) PSD of the Doppler process
Figure 5-11 Time variation of the Doppler process and its corresponding PSD for a portion of Scenario-A dataset for PRN 14



(a) dominant frequencies



(b) time-correlation of dominant frequencies

Figure 5-12 (a) Time-variation and (b) Time-correlation of dominant frequency components for PRN 14 corresponding to Scenario-A dataset

The variation of the carrier frequency process over the duration of one observation window, having a duration of 0.64 seconds, corresponding to a portion of Scenario-A dataset is shown in Figure 5-11 (a). Also shown is the measured PSD of the Doppler process in Figure 5-11 (b). It can be noticed that the Doppler process is dominated by a set of key frequency components, which constitute a major portion of the signal power. Accordingly, such harmonics are selected for reconstruction, which are highlighted in Figure 5-11 (b) and the reconstructed signal is aimed to reproduce the selected frequency components only.

Table 5-2 Comparison of the mean power in the Doppler process, when the pedestrian is in motion, with mean powers in individual harmonics for PRN 14, normalized for the dominant harmonic.

Signal	Mean power (dB-Hz)
Harmonic 1	0
Harmonic 2	-9.24
Harmonic 3	-12.87
Harmonic 4	-16.07
Sum of 4 harmonics	0.77
Total Doppler process	3.46

Note: The unit dB-Hz is not to be confused with the spectral density; the quantity being measured itself is the carrier frequency process.

The rationale behind the choice of the number of harmonics can be understood by analyzing the time-variation of the dominant frequency components shown in Figure 5-12 (a). The harmonics 1 through 6 are named in the descending order of their spectral density magnitudes. The first dominant frequency, when the pedestrian subject is in

motion during the intervals 40 s to 150 s, exhibits almost no variation. As the dominant harmonic number increases, the variation also increases due to two reasons: (1) this could be due to the dynamic range limitation in STFT as discussed in Section 3.2.6; (2) it could also be due to the variations in pedestrian motion, especially the step duration, which in turn manifest as variations in the location of harmonics on the frequency scale of the PSD. Nevertheless, this behavior has an interesting and important implication on the performance of the proposed algorithm. The larger variations in the dominant frequency components over time imply low quasi-periodicity and hence low predictability. Figure 5-12 (b) shows the normalized time-correlation plot to indicate the change of harmonic frequencies over time for Scenario-A dataset. It is evident that the harmonic 1 is highly time correlated, at least in the range of about 100 milliseconds, which is a defining feature of quasi-periodic components. In contrast, harmonics 5 and 6 are less time-correlated but have a larger variance, as shown in the enlarged window of Figure 5-12 (b), which can pose a significant challenge to the prediction of the effect of these harmonics on the underlying carrier frequency process. Furthermore, harmonics 5 and 6 appear a number of times beyond 15 Hz, which is the a priori upper limit for peak detection for pedestrian dynamics as discussed in Section 5.2. This behavior has a profound influence on the number of dominant components to consider for signal reconstruction. This analysis provides an overview of the difficulty in separating the frequency components associated with carrier frequency process PSD into quasi-periodic and aperiodic components. The analysis conducted in this section reveals that the distinction is not sharp and requires a compromise.

It is also useful to analyze the power contained in the corresponding harmonics. It is noticed in Table 5-2 that the first dominant harmonic constitutes a major portion of the overall process power and contributions from other harmonics are not significant. Although this analysis reasonably supports the idea of limiting the number of dominant frequency components, it does not necessarily support the choice of four dominant components used in the current work. The final choice, however, should be based on the performance evaluation of the proposed algorithm with various numbers of harmonics ranging from 1 to 6. It was observed on the average across all satellites that the phase tracking performance was not significantly different for a selection of maximum number of harmonics, as evaluated by the PLI. A similar analysis was performed on the threshold for peak detection. The receiver performance was evaluated on the Scenario-A dataset with a series of values for the threshold. If the values are too large, the harmonics were not identified and hence there was no prediction; if the values were too low, unwanted noise near the low frequency region, although aperiodic, was selected. The threshold of 3 dB was found to deliver the best performance. However, the maximum number of harmonics and threshold are design parameters and should be tuned according to the receiver dynamics for improved performance; failure to modify these design parameters based on dynamics could amount to improper constraints imposed on the prediction algorithm and therefore could render the proposed algorithm less effective.

5.5 Influence of observation data length and feed-forward gain

The key design choices that influence the effectiveness of the dynamic prediction algorithm, namely the feed-forward correction gain, α , and the carrier frequency process

input data observation window for STFT, denoted T_{STFT} , are examined in this section. To understand the effect of these design parameters on carrier phase tracking performance, a selection of T_{STFT} from 0.5 seconds to 1.5 seconds and α from 0.2 to 0.8 were considered for a receiver operating in Scenario-A. The corresponding mean phase errors, $\delta\theta_{mean}$, obtained by inverting the PLI metric as $\delta\theta_{mean} \approx 0.5 \cos^{-1}(\overline{\text{PLI}})$, are shown in Figure 5-13 for all visible satellites. The spectral density for signal acceleration state was 3 m/s³/√Hz throughout the analysis.

By examining Figure 5-13, it appears that the carrier phase tracking performance depends on both T_{STFT} and α . When α is increased from 0.2 to 0.6, $\delta\theta_{mean}$ decreases for all satellites. However, a further increase in α to 0.8 results in losses-of-lock, due to overcompensation of dynamics (The corresponding plots are not shown as $\delta\theta_{mean}$ was around 45 degrees for all satellites indicating a total loss of phase lock). Therefore, there is an optimal choice of α , somewhere in the region of 0.4 to 0.6. Furthermore, it is shown in Section 5.3.3 that increasing α from 0.4 to 0.5 itself results in cycle slips and loss-of-lock for PRN 1. However, for the same dataset, no loss-of-lock for PRN 1 was observed even with $\alpha = 0.6$, when the tracking loop bandwidth is reduced. For the cycle slips analysis in Section 5.3.3, the LOS spectral density of signal acceleration state was 4 m/s³/√Hz, which was reduced to 3 m/s³/√Hz for the analysis in this section. This demonstrates that to maintain loop stability and avoid losses-of-lock in the process, the feed-back and feed-forward gains have to be adjusted to avoid overcompensation of dynamics. Furthermore, the design choice α , in principle, also depends on the thermal noise prevalent in the feed-forward path, as discussed in Section 5.3.3. However, the

effect of this noise can be assumed to be insignificant for the receiver operating in Scenario-A, as the antenna was mounted over the head of the pedestrian without any significant attenuation.

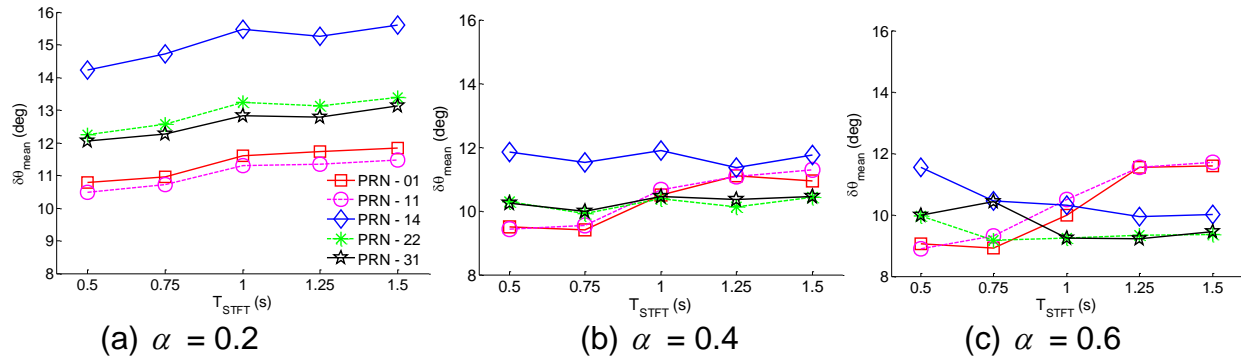


Figure 5-13 Variation of mean phase error over various input data lengths for feed-forward gains namely (a) 0.2, (b) 0.4 and (c) 0.6 for dataset Scenario-A. Losses-of-lock were observed for a feed-forward gain of 0.8.

The effect of another design parameter, T_{STFT} , can be examined by fixing α to near its appropriate value, which is about 0.4 following the discussion above. Examining Figure 5-13 (b) that corresponds to $\alpha = 0.4$, two trends in the variation of $\delta\theta_{mean}$ over various T_{STFT} values can be noticed. The $\delta\theta_{mean}$ values for PRNs 1 and 11 appear to increase with an increase in T_{STFT} from 0.75 seconds to 1.25 seconds. A second trend is observable in the plots that correspond to PRNs 14, 22 and 31, where the mean phase error $\delta\theta_{mean}$ appears to be relatively insensitive to T_{STFT} compared to PRNs 1 and 11. The cause of these two trends can be explained by observing the influence of satellite locations on LOS Doppler variations, as shown in Figure 5-14.

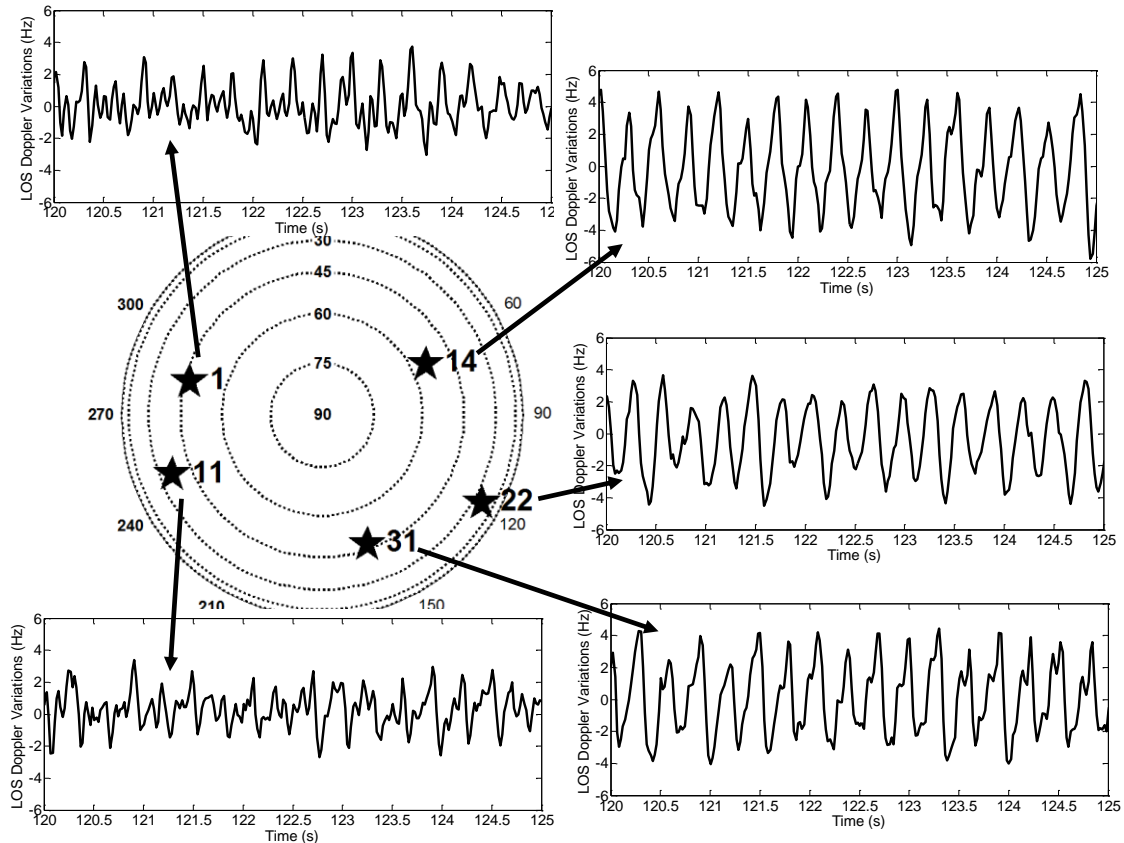


Figure 5-14 LOS Doppler variation patterns across satellites as a function of satellite locations

PRN 1 and 11 were located to the west, whereas other satellites were located to the east with respect to the data collection location. When pedestrian exhibits dynamics, the effective LOS variations are therefore different. The LOS variations for PRN 1 and 11 were comparatively of higher frequencies, involving comparatively quick changes in variation patterns. Therefore, this requires a shorter observation window. In contrast, PRN 14, 22 and 31 exhibit LOS variations with comparatively more stable patterns, and hence, comparatively longer observation windows are necessary. However, PRN 1 and 11 exhibit lower LOS Doppler variation magnitudes. Therefore, as such, carrier phase tracking enhancement can be focussed towards the other satellites for which LOS

Doppler variations are significant. To this end, the design parameter T_{STFT} can be chosen such that the relative performance across all visible satellites is on an average the same. For the dataset under consideration, choosing $T_{STFT} = 1$ second delivers similar performance in terms of $\delta\theta_{mean}$, which can be noticed by overlapping points in Figure 5-13 (b), for all satellites except PRN 14, which suffered sharper LOS Doppler variations that resulted in a comparatively poor performance.

Overall, it can be concluded that the design parameter T_{STFT} should be chosen based on the knowledge of LOS Doppler variations and not just based on the pedestrian dynamics in the body-frame. The choice of α , in contrast, is more complicated, and depends on the feed-back gain, the magnitude of LOS Doppler variations and the accuracy of dynamics prediction.

5.6 Performance evaluation in regular pedestrian environments

The datasets used in previous sections were collected while the pedestrian executed moves within a confined space while carrying only the antenna, but keeping the oscillator and the front-end stationary. Such experiments enabled the performance analysis of the proposed algorithm with LOS dynamics only, but no effect of oscillator g -sensitivity on the carrier tracking performance. It is more realistic to analyze the effect of pedestrian dynamics, in terms of LOS dynamics and oscillator g -sensitivity. Although the oscillator g -sensitivity compensation was demonstrated effectively using IMUs in Chapter 4, only quasi-periodic dynamics are addressed in this chapter using the STFT-based method without aiding from IMUs. It is also of interest to evaluate the performance of the proposed

algorithm with low-cost equipment suitable for pedestrian applications such as cell phones. These situations are explored in this section.

5.6.1 Experimental validation with LOS dynamics and oscillator g-sensitivity

A series of datasets, presented in Table 5-3, were collected using a GPS front-end with 1-bit quantization, which suits low-cost and low-form-factor requirements of pedestrian GNSS receivers, a Morion MV89A OCXO (MORION 2012), a NovAtel 702-GG antenna and a Low-Noise Amplifier (LNA). The data collection setup was similar to the one discussed in Figure 4-3.

Table 5-3: Datasets with regular pedestrian motion with various patterns and antenna placements

Name	Antenna location on the pedestrian subject	Data collection scenario	Pedestrian motion (In the order of execution)
Ped-A	Backpack, overhead	Paved walkway, 37 th Street, 32 Ave, Calgary	Running, marching, gentle walking
Ped-B	Hand-held, shoulder-level	Paved walkway, 37 th Street, 32 Ave, Calgary	Running, marching, gentle walking
Ped-C	Backpack, overhead	Turf soccer field, University of Calgary	Gentle walking, light marching, running

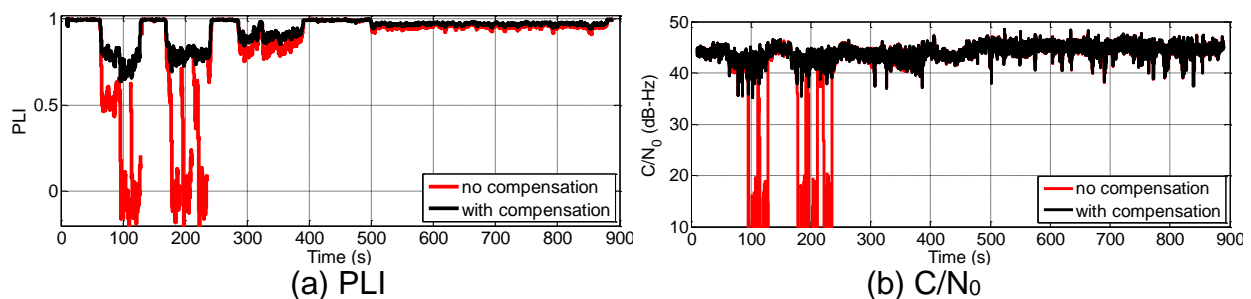
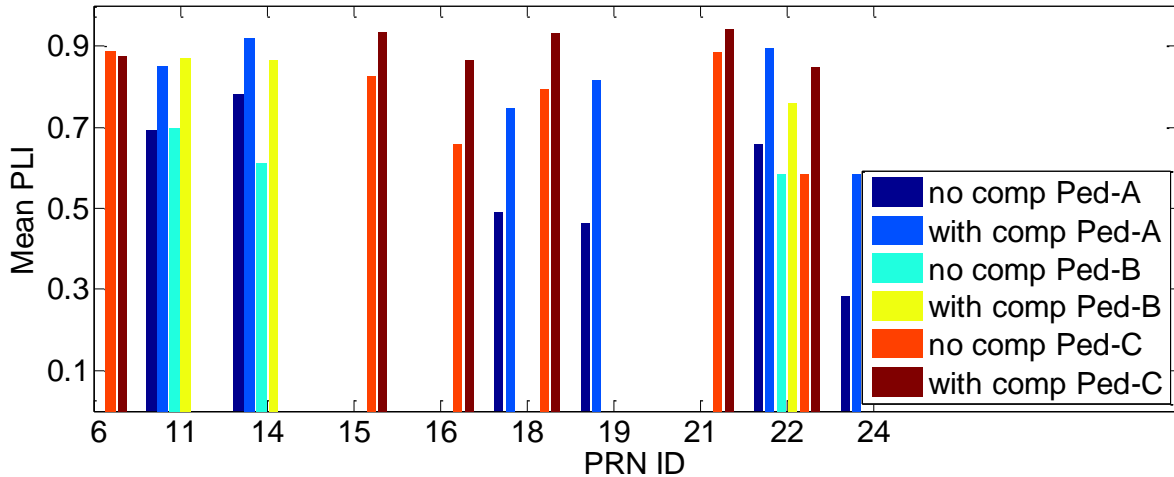
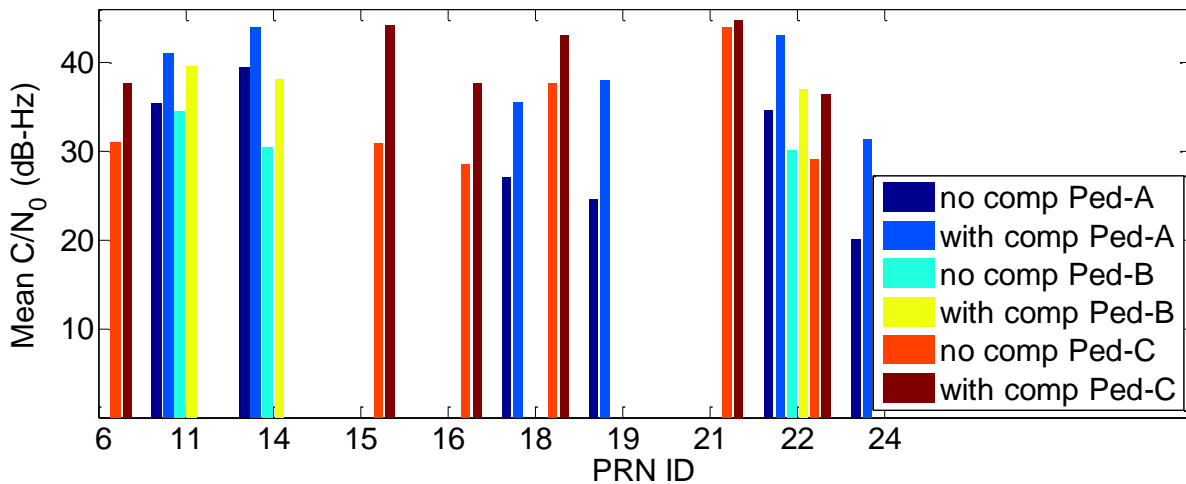


Figure 5-15 PLI and C/N₀ plots corresponding to Ped-A dataset for PRN 14

The datasets Ped-A and Ped-B were collected while the pedestrian exhibited the manoeuvres on a straight path over a paved flat terrain. The dataset Ped-C was collected in a turf soccer field in a square walking trace. In both Ped-A and Ped-C datasets the antenna was mounted on a backpack protruding above the pedestrian's head in order to minimize human attenuation. In Ped-B dataset, the antenna was hand-held at the shoulder level. The data collection in all the datasets lasted 20 minutes. The carrier phase tracking performance achievable by the proposed algorithm is shown in Figure 5-15, corresponding to Ped-A dataset, for PRN 14 at about 75 degrees of elevation. It is evident through improved PLI and C/N_0 and no apparent instances of loss-of-lock that the compensated receiver outperforms the uncompensated receiver. The pedestrian dynamics correspond to the periods from 63 to 131 s, 168 to 243 s, 284 to 391 s and 498 to 881 s in the Ped-A dataset; the pedestrian remained static otherwise. The mean values of PLI and C/N_0 across all visible satellites, computed only for the portion of datasets while the pedestrian was in motion, are shown in Figure 5-16 for the datasets stated in Table 5-3.



(a) Mean PLI



(b) Mean C/N₀

Figure 5-16 Mean PLI and C/N₀ values computed across all visible satellites for regular pedestrian motion datasets

The overall relative performance deterioration in the Ped-A dataset compared to Scenario-A dataset, despite both datasets used overhead antenna imposing no human attenuation, is due to the oscillator g -sensitivity, which is an additional source of dynamics stress on the tracking loops in Ped-A dataset. The Morion MV89A OCXO oscillator measures a g -sensitivity norm of about 2.18 ppb/ g , as discussed in Section 4.2, which results in carrier frequency change of about 3.4 Hz for the GPS L1 C/A signal when the oscillator is subject to a change in acceleration of 1 g in the direction of its g -sensitivity

vector norm. Unlike the technique discussed in Chapter 4, the combined variations in the carrier frequency process due to changes in LOS dynamics and the oscillator g -sensitivity effects are estimated and compensated. Therefore, the need for inertial sensors to measure oscillator accelerations are obviated to some extent. However, the method proposed here only accounts for the quasi-periodic components. When the receiver is subject to significant aperiodic motion, the compensation method based on inertial sensor data, discussed in detail in Chapter 4, outperforms the current method.

The deterioration in C/N_0 values and number of satellites from Ped-A to Ped-B dataset, noticeable in Figure 5-16, is attributable to human attenuation in addition to LOS dynamics and oscillator g -sensitivity. However, the compensated receiver still proves beneficial in delivering higher PLI and C/N_0 values. The turf field dataset Ped-C also provides a striking demonstration of carrier tracking performance enhancement with dynamic compensation.

5.6.2 Compensation with low-cost equipment across pedestrian subjects

This section extends the performance evaluation of the method conducted in the previous sections to relatively low-cost equipment consisting of a consumer-grade u-blox ANN-MS-005 active patch antenna and a Fordahl 0727 TCXO with a g -sensitivity norm of 1.4 ppb/ g and a 1-bit front-end which logs complex GPS IF data at 10 MHz.

Additional datasets were collected on a paved walkway similar to the scenario in Ped-A, referred to as Ped-D. Three pedestrian subjects exhibited walking and running while holding the antenna in hand for about eight to ten minutes of data collection duration. The

antenna location was lowered from overhead to shoulder-level to the waistline during the data collection to include various human attenuation patterns. The pedestrians exhibited mild hand swings while the antenna was at the waistline-level to induce additional dynamics. The carrier tracking enhancements obtained by incorporating the proposed method for Ped-D datasets collected with comparatively low-cost equipment is evident in the mean PLI and C/N_0 plots shown in Figure 5-17.

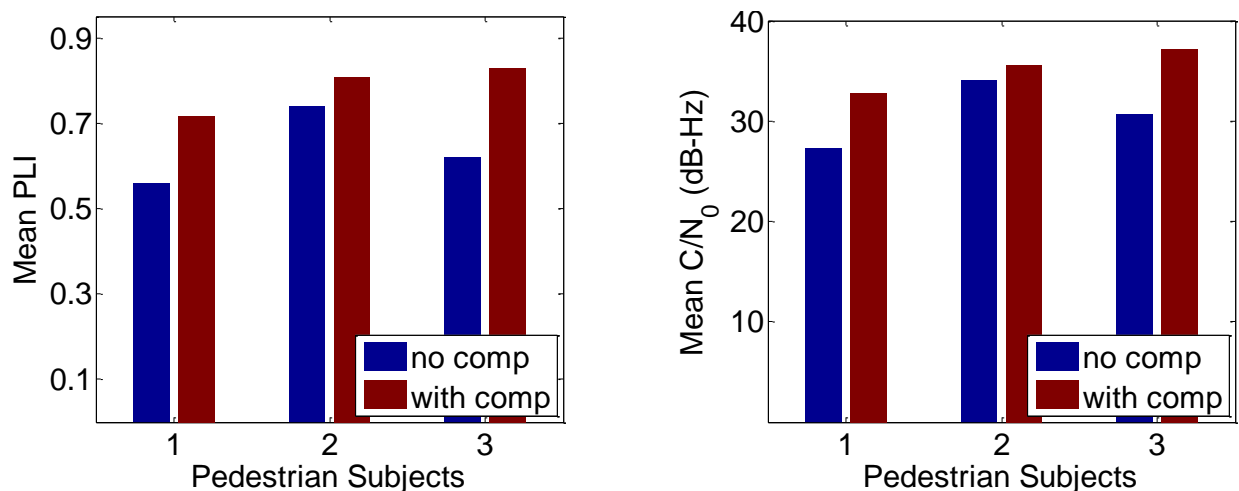


Figure 5-17 Mean PLI and C/N_0 values computed across all visible satellites for different pedestrian subjects corresponding to Ped-D datasets

This demonstration indicates that the proposed algorithm is relatively insensitive to variation in the walking patterns of the individual pedestrian subjects. However, the duration of carrier frequency data used for STFT was 0.64 seconds for subjects 1 and 2, whereas it was 1.28 seconds for subject 3. The length of the FFT buffer was modified after analyzing the fundamental period corresponding to subject 3 motion patterns, as discussed in Section 5.5.

5.7 Summary

A novel feed-forward dynamic prediction algorithm was proposed to measure quasi-periodic components of the receiver dynamics using short-term Fourier transforms. The prediction enables generation of appropriate corrections to the carrier lock loops, which inherently lag in their responses to changing pedestrian dynamics and thereby improves carrier synchronization. The carrier tracking enhancements were demonstrated on a series of datasets collected in various pedestrian scenarios via PLI and C/N_0 metrics. Carrier phase tracking performance enhancement was also evaluated through cycle slips analysis using heuristic methods. In addition to improved synchronization, the feed-forward compensation of dynamics enabled the lowering of effective noise bandwidth, which is demonstrated through the decrease in signal acceleration spectral density from $1 \text{ m/s}^3/\sqrt{\text{Hz}}$ to $0.1 \text{ m/s}^3/\sqrt{\text{Hz}}$. The improvements were also demonstrated with low-cost consumer grade equipment suitable for pedestrian applications.

Chapter Six: Investigation of kinematic positions for pedestrian receivers

6.1 Introduction

One of the requirements for uninterrupted kinematic solutions is the continuity of carrier phase measurements without cycle slips. Section 6.2 discusses quantification of cycle slips in pedestrian receivers using a technique that involves beginning and ending the data collection at a known location of the pedestrian antenna. However, in realistic navigation scenarios this is not possible and, so, single frequency receivers, which are employed in most low-cost hand held devices such as cell phones, use the *phase rate method* or *phase velocity trend method*. The limitations of phase rate method are discussed in Section 6.3. Section 6.4 explores the possibility of kinematic solutions in the pedestrian hand held environment.

6.2 Cycle slips analysis using known receiver location

Carrier cycle slips can be quantified by computing carrier phase measurement errors using an accurate reference trajectory and monitoring discontinuities in the phase trajectory. However, computation of measurement errors require a known reference trajectory of the rover antenna, which is difficult to obtain for pedestrian application experiments unless a high quality IMU is strapped-down with the pedestrian antenna to obtain an integrated solution. However, preliminary analyses of cycle slips were conducted in Chapters 4 and 5 based on heuristic methods without quantification. In this section, the cycle slips occurring in a pedestrian hand held environment are quantified by extending the method used in Section 5.3.3. The single difference carrier phase technique

discussed in Section 5.3.3 is implemented by mounting a survey tribrach that snap-lock the antenna at an accurately known location, as shown in Figure 6-1 (a) during the data collection. The carrier phase measurements corresponding to the pedestrian and reference antennas for a particular satellite can be mathematically expressed as

$$\begin{aligned}\theta_{ped}(t) &= \rho_{ped}(t) + c(dt - dT_{ped}) + \lambda N_{ped} - d_{iono,ped} + d_{tropo,ped} + \varepsilon_{MP,\theta,ped} + \eta_{\theta,ped} \\ \theta_{ref}(t) &= \rho_{ref}(t) + c(dt - dT_{ref}) + \lambda N_{ref} - d_{iono,ref} + d_{tropo,ref} + \varepsilon_{MP,\theta,ref} + \eta_{\theta,ref}\end{aligned}\tag{6-1}$$

where θ represents the carrier phase measurements at time t , the subscripts ref and ped represent the reference and pedestrian antennas, ρ represent the geometric range between the satellite and the user antenna, dt and dT represent satellite and receiver clock biases, N represent the carrier phase ambiguity, d_{iono} and d_{tropo} represent the ionospheric and tropospheric delays, ε_{MP} represents error due to multipath, η represents the noise, the constants c and λ represent speed of light and carrier wavelength, which is about 19 cm for GPS L1.

The carrier phase single difference between the reference and pedestrian receivers can be written as

$$\Delta\theta(t) = \rho_{ref}(t) - \rho_{ped}(t) + c(dT_{ped} - dT_{ref}) + \lambda\Delta N + \Delta\varepsilon_{MP,\theta} + \Delta\eta_{\theta}\tag{6-2}$$

where the terms $\Delta\theta$, ΔN , $\Delta\varepsilon_{MP,\theta}$ and $\Delta\eta$ represent the single-differenced carrier phase measurement, ambiguity, multipath and noise. The differential GPS data collection setup used for this analysis has a 10 m baseline. Therefore, it is assumed that the differential ionospheric and tropospheric delays are negligible. The geometric ranges corresponding to the reference antenna and the pedestrian antenna's known location can be computed

using satellite broadcast ephemeris and removed. The oscillator effects are removed using a common clock across the reference and test receivers, except for the initial clock bias due to potentially different receiver switch-on times and different receiver GPS time initializations.

The single difference in Eq. 6-2 can be simplified after removing satellite motion and clock effects as

$$\delta\Delta\theta(t) = \underbrace{\delta\rho_{ped}(t)}_{\text{pedestrian antenna displacement from the known antenna location}} + \Delta cdT_{const} + \lambda\Delta N + \Delta\varepsilon_{MP,\theta} + \Delta\eta_{\theta} \quad \mathbf{6-3}$$

where the difference term $\delta\Delta\theta$ consists of the carrier phase changes due to pedestrian motion denoted by $\delta\rho_{ped}(t) = \rho_{ped}(t) - \rho_{ped}^{known}(t)$, ρ_{ped}^{known} is the geometric range that corresponds to the known snap-locked location. The term $\Delta cdT_{const} = c(dT_{ped}(t_{ped}^{begin}) - dT_{ref}(t_{ref}^{begin}))$, which is constant, is due to the difference in receiver time initializations across reference and rover receivers and t_{ped}^{begin} and t_{ref}^{begin} represent pedestrian and reference receiver switch-on times.

The test procedure involves beginning and ending the data collection at a known location of the pedestrian antenna. Therefore, the term $\delta\Delta\theta$ in Eq. 6-3 is expected to contain two constants, namely $\lambda\Delta N$ and ΔcdT_{const} , the latter being single-difference multipath and noise at the beginning of the data collection. If there are no cycle slips or losses of lock, the term $\delta\Delta\theta$ should return to its initial static value at the beginning of the test due to $\lambda\Delta N$ and ΔcdT_{const} being constant, except for multipath and noise. The theoretical maximum for carrier phase multipath has been shown to be a quarter of the wavelength,

which is about 4.75 cm for GPS L1. The carrier phase noise is generally in the order of millimetres. Therefore, any significant deviation from the initial constant value, other than the multipath and noise margins, can be interpreted as cycle slips or losses of lock. If a common oscillator cannot be used across reference and pedestrian receivers, double differencing can be used to eliminate clock effects, in which case Eq. 6-3 can be modified as

$$\delta\nabla\Delta\theta(t) = \delta\nabla\rho_{ped}(t) + \lambda\nabla\Delta N + \nabla\Delta\varepsilon_{MP,\theta} + \nabla\Delta\eta_{\theta} \quad \mathbf{6-4}$$

where the operator ∇ indicates differencing across two satellites. In this case, the term $\delta\nabla\Delta\theta$ is expected to begin and end at the double differences constant after executing a pedestrian trajectory, if no cycle slips occur for any of the satellites.



(a) Snap-lock device



(b) pedestrian motion

Figure 6-1 (a) Antenna snap-locking device used to precisely locate the pedestrian antenna (b) Pedestrian exhibited hand held dynamics during data collection

The data collection setup used in this analysis is shown in Figure 6-2. As an extension to the differential GPS setup employed in Section 5.3.1, this setup includes a commercial

survey-grade receiver from NovAtel Inc. (Propak-V3 2011) for comparative performance analysis with the modified version of the software receiver GSNRx™ used in this thesis. The receivers and front-ends were synchronized using a common OCXO (Morion 2012). Pedestrian motion was achieved by carrying the antenna mounted on a short mast that extends overhead as shown in Figure 6-1 (b). The pedestrian antenna was placed at the snap-locked fixed location during the data collection, except for certain intervals of time during which the antenna was unlocked carried through a series of manoeuvres typical of pedestrian motion and, subsequently returned to its initial static position. The data collection lasted for thirty minutes with intermediate pedestrian motion segments lasting for about two to five minutes.

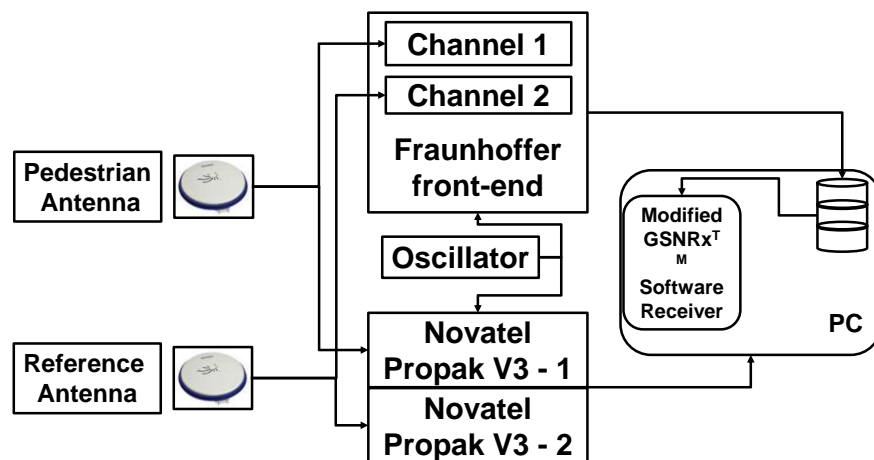


Figure 6-2 Differential GPS data collection setup to detect and quantify cycle slips in pedestrian hand held environment

The single difference phase measurements described by Eq. 6-3 are shown in Figure 6-3 for the NovAtel receiver. Static mode initial values in the single difference measurements were removed to analyze all plots in the same scale. The same plots are shown in three vertical scales, namely 2 million, 20 and 0.4 cycles. If there are no cycle slips, the plots

wander around zero due to multipath and carrier noise when the pedestrian antenna is stationary; during pedestrian dynamics, the phase differences deviate from the constant terms due to motion, but should settle at the initial value after returning the antenna to the initial location. However, upon the recovery from a loss-of-lock or cycle slips, ambiguities change; hence jumps in single difference carrier phase measurements can be observed. Two such instants can be seen in the top subplot of Figure 6-4 where one of the blue curves, corresponding to PRN 30, suffered a measurement discontinuity of one measurement period and exhibited a jump of about 1.3 million cycles after it is recovered. Another plot corresponding to PRN 26 also exhibited a jump of about 1.3 million cycles, but without measurement discontinuity. The former can be referred to as loss-of-lock and the latter a cycle slip.

Mode:	Static	Dynamic	Static	Dynamic	Static	Dynamic	Static
# observations available throughout the mode:	10	10	10	8	8	5	5
# observations without cycle slips from the beginning:	10		8		7		4

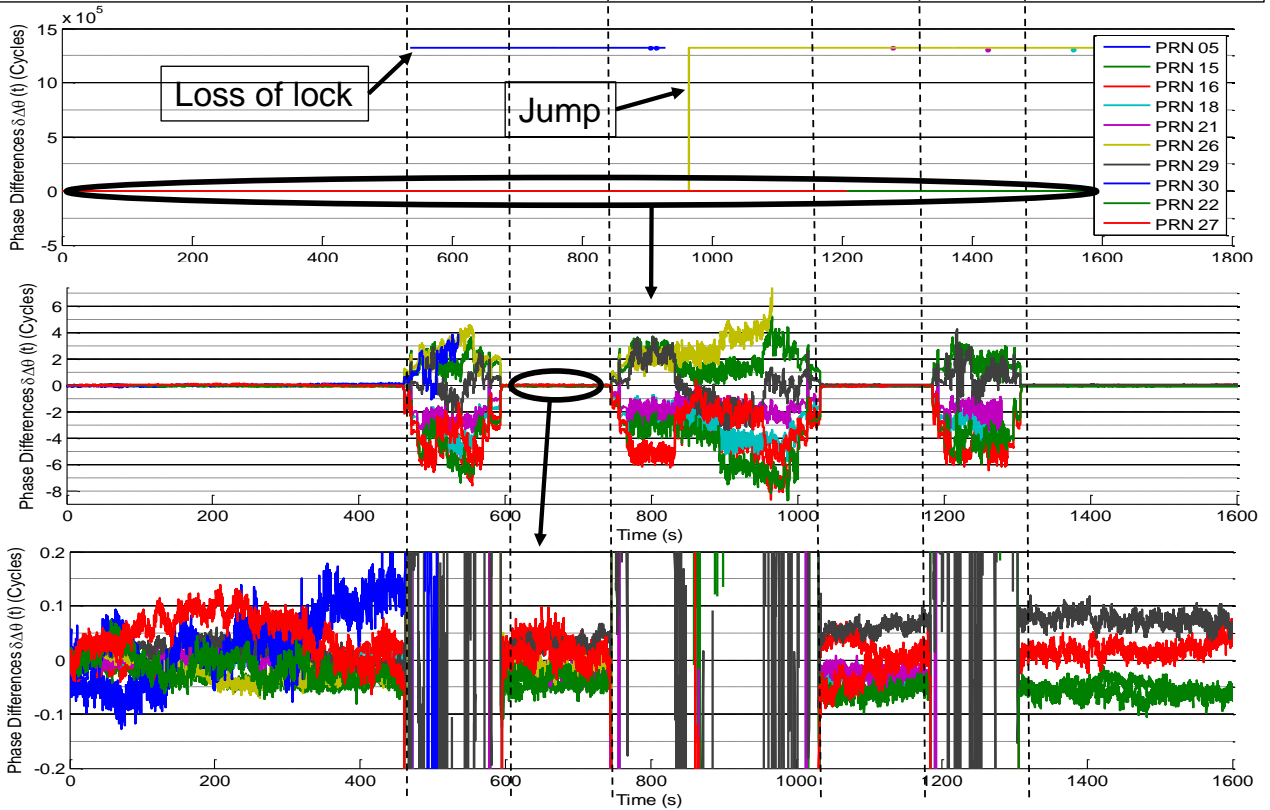


Figure 6-3 Phase difference plots for NovAtel receiver described by Eq. 6-3 shown with gradual reduction in vertical scales from the top to the middle to the bottom subplots

In addition, PRNs 5, 18, 21, 27 and 30 suffered measurement unavailability for a significant amount of time after losing lock until the end of data collection. Overall, it can be concluded that the continuity in carrier phase observations is lost from time to time when the receiver is subject to pedestrian dynamics. Notice the reduction in the number of satellites that revert to the initial phase difference value after the preceding dynamics segment in the bottom subplot of Figure 6-4. The number of satellites that maintained

phase continuity without cycle slips reduced from 10 to 8 to 7, and finally to 4 from the first static segment to the last.

Mode:	Static	Dynamic	Static	Dynamic	Static	Dynamic	Static
# observations available throughout the mode:	10	10	10	10	10	10	10
# observations without cycle slips from the beginning:	10		10		8		7

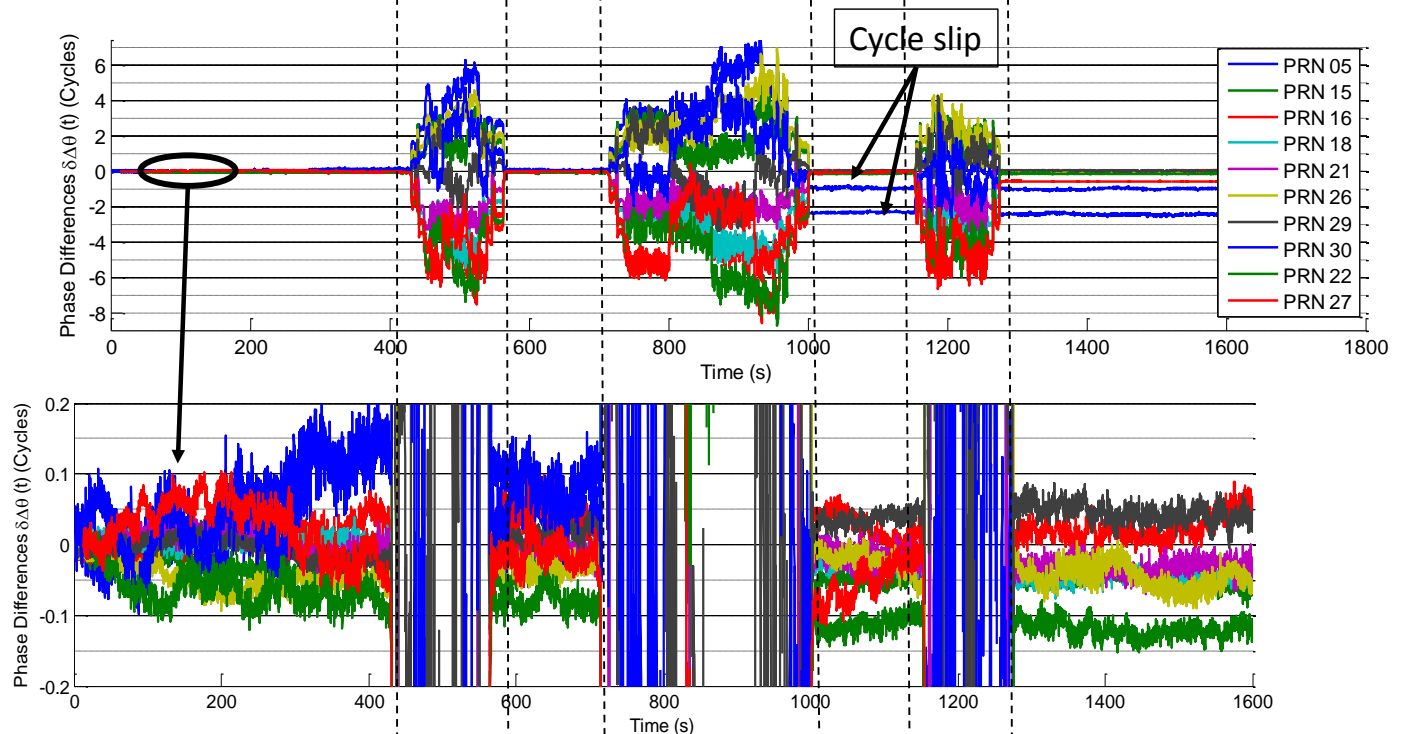


Figure 6-4 Phase difference plots for the modified GSNRx™ receiver, as described by Eq. 6-3 shown with gradual reduction in vertical scales from the top to the bottom subplots

The single difference phase plots for GSNRx™ receiver is shown in Figure 6-4. The plots are shown in only two vertical scales: 20 and 0.4 cycles, as no loss-of-lock was observed and therefore no large jumps in phase difference in millions of cycles. However, an offset of 1 and 2.5 cycles were observed for PRNs 30 and 5, noticeable in the top subplot of Figure 6-4, after the second pedestrian dynamic segment that lasted for about five

minutes, and an offset of 0.5 cycles was observed for PRN 27 after the third dynamic segment. It appears that cycle slips of such a magnitude are a result of severe dynamic stress due to momentary spikes in acceleration that exceeds the carrier phase discriminator's dynamic range (Voutsis et al 2014), and hence not followed by the tracking loop appropriately. In order to further explore this hypothesis, the tracking loop outputs corresponding to a satellite that exhibited cycle slips, for instance PRN 27, were analyzed. GSNRx™ outputs correlation values that correspond to the loop update period, which is 20 ms for GPS L1 C/A code signal considered herein.

The C/N_0 values estimated from the correlation values are shown in Figure 6-5. Notice that the filtered C/N_0 estimates mask momentary signal power level fluctuations. In particular, a series of spikes with significant magnitude resulted in a C/N_0 reduction to 13 dB-Hz during the third dynamic segment. Therefore, it is possible that the tracking loops, which use filtered C/N_0 estimates for decision making purposes, failed to recognize this momentary signal loss. It is likely that these spikes represent momentary losses of phase lock that resulted in an effective 0.5 cycle slip when the antenna returned to its initial static position. However, variations in the estimated C/N_0 , in general, are due to numerous factors such as multipath, signal obscuration, antenna tilt, improper dynamic response of tracking loops leading to correlation loss and thermal noise. Multipath and signal obscuration could not be the causes for C/N_0 fluctuations of such magnitude due to the following reasons: (a) as the antenna was in motion, the multipath effects are likely to be reduced due to spatial de-correlation effects; (b) the data collection site was the roof of a building that contain limited reflections; (c) as the data was collected in open-sky conditions with the antenna extending over the head of the pedestrian, no severe

amplitude fading can be expected; (d) finally, no significant C/N_0 fluctuations were observed when the antenna was static.

The antenna was always kept normal to the ground during pedestrian motion except for the vibrations that resulted in tilts with less than 30 degrees from the normal. According to the radiation pattern specifications of the antenna used for this experiment (GPS-702-GG 2010), the gain roll-off from zenith to an elevation of 60 degrees is only about 6 dB. Furthermore, momentary C/N_0 spikes, especially in the third pedestrian dynamics segment, occur at the same time as the acceleration spikes shown in Figure 6-7. The accelerations were obtained by attaching the 3-space sensor IMU data logger (TSS-DL-HH-S 2012) to the pedestrian antenna during the experiment and time-synchronized manually with the GPS time. It is evident that the momentary spikes in the unfiltered C/N_0 values occur almost at the same time when the acceleration spikes occur. Therefore, it can be concluded that the cause of such cycle slips are pedestrian dynamics that exceed the expected pedestrian dynamics magnitudes. In addition, notice the magnified portion of the correlation values shown in Figure 6-6 indicating that the in-phase correlation values drop below the quadrature values supporting the above observations. The effects of these cycle slips on navigation solutions are discussed, via phase residuals, in Section 6.4.

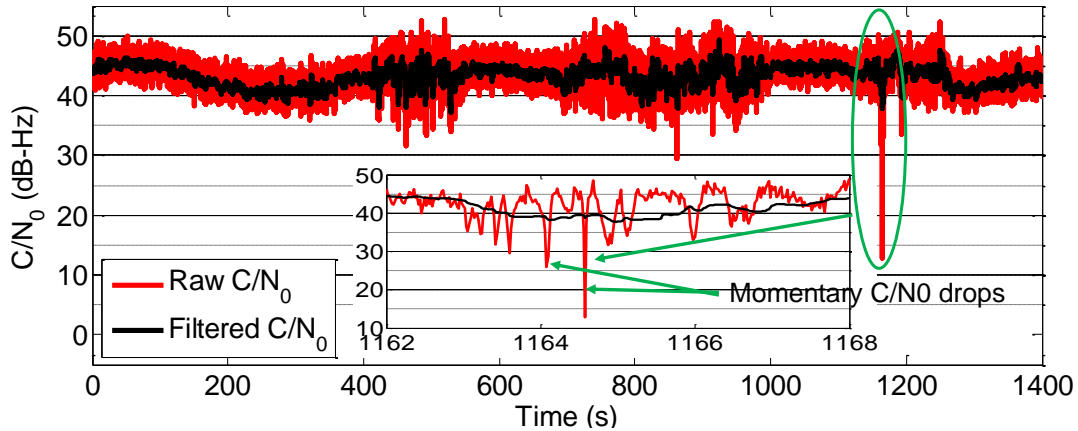


Figure 6-5 Raw and filtered C/N_0 values corresponding to PRN 27 computed from correlation values output by GSNRx™

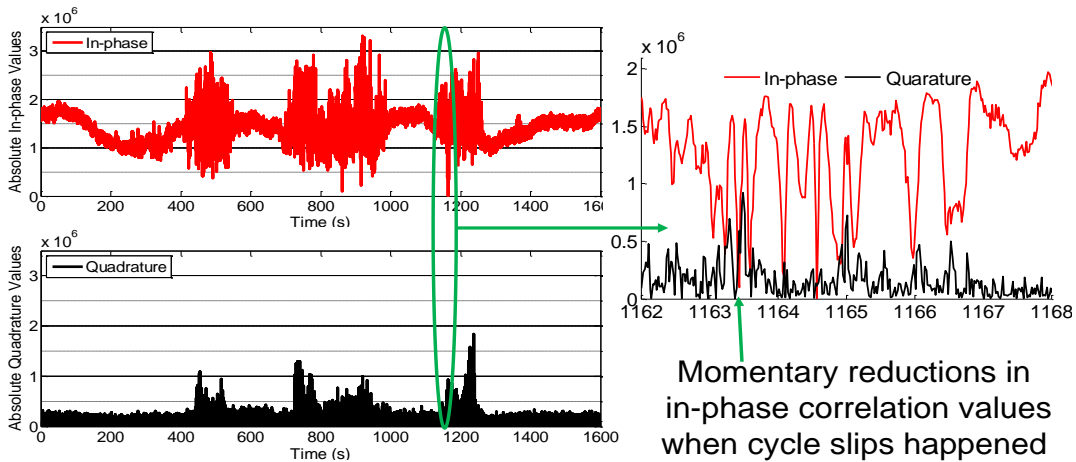


Figure 6-6 Correlation values corresponding to PRN 27 obtained from GSNRx™

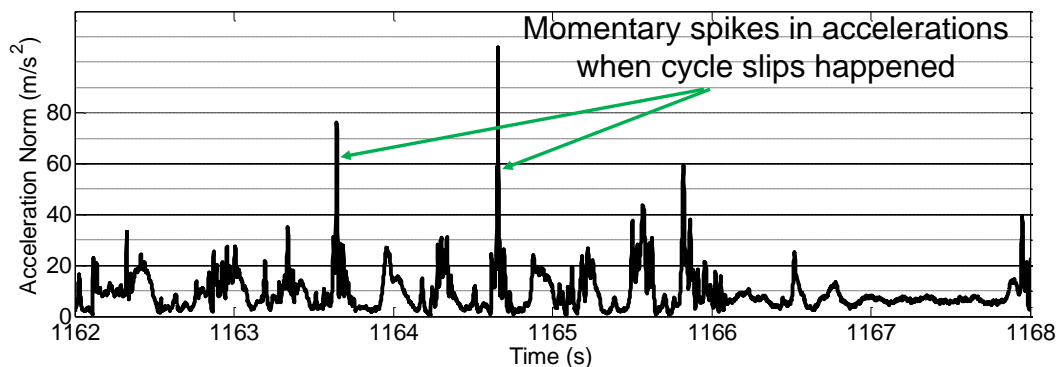


Figure 6-7 Acceleration norm for the time duration corresponding to the spikes observed in correlation values and C/N_0 . IMU time was manually synchronized with GPS time and deemed sufficient for the analysis conducted herein

Although spikes in accelerations were prevalent throughout the dynamic portion of the dataset, cycle slips occurred only for a few times. Cycle slipping is a non-linear phenomenon that is caused due to complex interaction of non-linearity in tracking loops with noise. Cycle slips can be induced by various factors such as abrupt changes in incoming signal dynamics or transients, oscillator phase noise, thermal noise, etc (Gardner 2005). A tutorial survey of cycle slips in PLLs was conducted by Ascheid & Meyr (1982). A detailed analysis of the cycle slip phenomena is beyond the scope of this thesis. One remedy to this problem is to increase the tracking loop bandwidth, but at the cost of reduced thermal noise performance and reduced sensitivity. However, good tracking sensitivity is also a key requirement for pedestrian receivers that suffer satellite signal attenuation due to the human body, as discussed in Chapter 3. Therefore, the tracking loop bandwidth can be, if possible, adapted to changing signal conditions to enhance carrier phase tracking performance. Overall, the number of satellites that maintained phase continuity reduced from 10 in the first static segment to 8 in the third and to 7 in the last corresponding $\text{GSNR}_x^{\text{TM}}$ output.

It is evident from Figure 6-3 and Figure 6-4 that both receivers behave almost identically for static receiver conditions without noticeable degradation in performance in terms of losses-of-lock. Identical trends in carrier phase difference plots are also observed in both receivers; for example, notice that the brown color curves that correspond to PRN 29 in the bottom subplots of Figure 6-3 and Figure 6-4 from 1300 to 1600 s exhibit almost identical trend. The magnitude of these carrier phase difference variations range from 0.05 to 0.2 cycles. This common trend can be attributed mainly to single difference carrier

phase multipath and thermal noise, as all other errors are removed, as per Eq. 6-3. Antenna phase centre variations are negligible, as a survey grade antenna was used for this test. Similar observations can be made for other satellites for other static receiver duration, albeit not clearly visible from the overlapping plots.

Overall, it is noticed that the GSNRx™ receiver demonstrated the availability of more continuous carrier phase measurements compared to the NovAtel receiver. The performance enhancement may be attributed to appropriate choice of the tracking architecture in GSNRx™ specifically tuned for the pedestrian environment under test, whereas the NovAtel receiver probably adopted a more conservative approach to loop design that suits most receiver operating environments. The dynamics tolerated by the NovAtel receiver is specified in its datasheet as sustained tracking with 4 g vibrations (Propak-V3 2011). However, this specification is for nominal signal levels with receivers operating in open-sky conditions. Furthermore, pedestrian accelerations corresponding to the dataset used in this section exhibited momentary acceleration spikes that exceeded 4 g in magnitude, which can be inferred from the acceleration spikes shown in Figure 6-7 and in a short portion of the third pedestrian dynamics segment shown in Figure 6-8.

Although the method discussed in this section to analyze and quantify carrier phase cycle slips can be used for research and testing purposes, it cannot be employed in pedestrian applications to detect cycle slips. The method requires the antenna to be placed at an accurately known location, which is a limitation for commercial pedestrian receivers. However, there are other methods of cycle slips detection which can be employed in the measurement domain. One of the simplest methods is the phase rate method that is used

for single frequency receivers, and it will be discussed next in the context of pedestrian receivers.

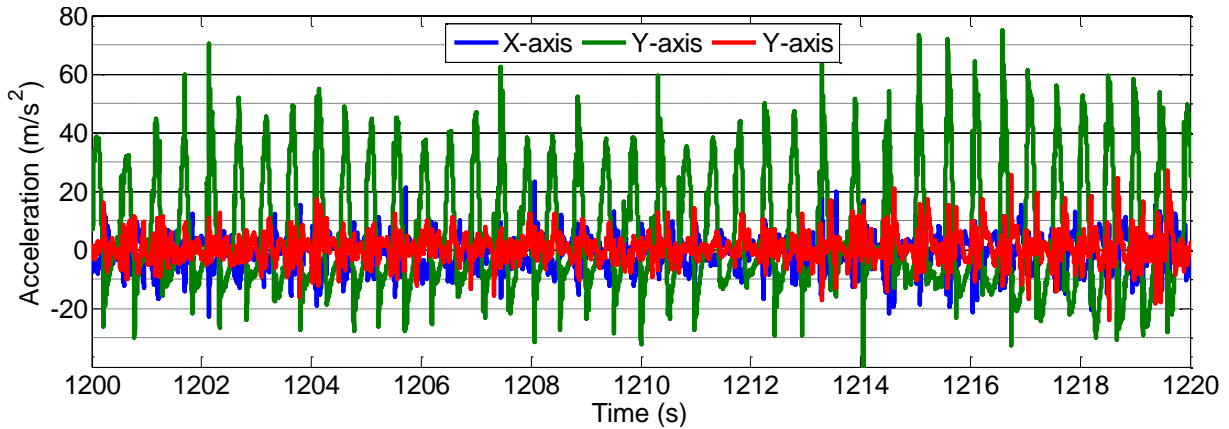


Figure 6-8 A short portion of accelerations in the pedestrian antenna-frame corresponding to the third dynamic segment

6.3 Phase rate method

The phase rate cycle slip detection method works on the principle of mutual agreement between the carrier phase and the carrier frequency observations over a measurement period. The carrier phase and carrier frequency measurements for a particular satellite can be represented as

$$\begin{aligned}\hat{f}_i[k] &= f_i[k] + \eta_{\hat{f}_i}[k] \\ \hat{\theta}_i[k] &= \theta_i[k] + \eta_{\hat{\theta}_i}[k]\end{aligned}\tag{6-5}$$

where \hat{f}_i and $\hat{\theta}_i$ represent carrier frequency and phase measurements in [Hz] and [Cycles] for i^{th} satellite at the measurement instant k . The actual carrier frequency and phase has values f_i and θ_i are corrupted by composite noise terms $\eta_{\hat{f}_i}$ and $\eta_{\hat{\theta}_i}$, which consists of thermal noise effects and dynamic stress errors due to variations in the incoming signal parameters.

The carrier phase value at any measurement instant can be predicted using carrier frequency through linear interpolation, mathematically expressed as

$$\hat{\theta}^p[k] = \hat{\theta}[k-1] + \left(\frac{\hat{f}[k-1] + \hat{f}[k]}{2} \right) \Delta t \quad \mathbf{6-6}$$

where $\hat{\theta}^p$ represents the predicted carrier phase at the k^{th} measurement instant, Δt is the measurement period in seconds. It is also possible that the time-difference carrier phase measurements can be used rather than the carrier frequency measurements in Eq. 6-6 to reduce noise prevalent in the predicted carrier phase. However, it is irrelevant for the purpose of the discussion conducted in this section. Nonetheless, the carrier phase time-difference delivers smoother prediction of carrier phase measurement when implemented in navigation processor. The carrier phase discontinuity between two measurement instants can be detected by a simple binary hypothesis testing with test statistic being the difference between the predicted and measured carrier phases expressed as

$$\begin{aligned} \zeta_{CS} &= \hat{\theta}^p[k] - \hat{\theta}_i[k] \\ H1: \quad &|\zeta_{CS}| \geq \lambda_{CS} \rightarrow \text{Cycle slip detected} \\ H0: \quad &|\zeta_{CS}| < \lambda_{CS} \rightarrow \text{No cycle slip} \end{aligned} \quad \mathbf{6-7}$$

where λ_{CS} is the cycle slip detection threshold that depends on the choice of a tolerable false alarm. The chosen threshold should accommodate thermal noise effects in carrier frequency. If there is significant change in carrier frequency between the measurement instants, the test static ζ_{CS} can easily surpass λ_{CS} set for static receiver conditions. Therefore, the threshold should also accommodate any significant non-linear changes in

carrier frequency process. The limitations of phase rate method of cycle slips detection in the context of pedestrian receivers are discussed next.

6.3.1 Limitations of phase rate method

The phase rate cycle slips detection test statistics were computed for the dataset used in Section 6.2 with the GSNRxTM receiver and are shown in Figure 6-9 for PRN 5 for the reference and pedestrian receivers. The test statistics variance for a 5 Hz measurement rate, shown in Figure 6-9, is significantly higher in dynamics mode compared to the static mode. This is a result of sampling the continuous time carrier frequency process that exhibits significant changes over time, as shown in Figure 6-10, during pedestrian motion. When the measurements are obtained at a higher rate, namely 20 ms that corresponds to the tracking loop update rate, a stark reduction in variance under the dynamic receiver condition is noticed, which is rather expected due to the reason explained later in this section and as shown in Figure 6-9. It was demonstrated from Figure 6-4 in the previous section that a slip of 2.5 cycles was observed for PRN 5 after the second pedestrian dynamic segment that ended at about 1000 s. However, it is not known whether 2.5 cycles slipped at once or in steps. In either case, such slips should be detected. Nevertheless, it is evident from Figure 6-9 that the test statistic does not show any prominent spikes that correspond to a significant discrepancy between predicted and measured carrier phase values. This limitation of the phase rate method should be due to the unavailability of independent carrier frequency measurement at a higher rate in the tracking loops. The carrier frequency error in the tracking loop frequency discriminator is derived by time-differencing the successive carrier phase measurements over a coherent integration

period (Ward et al 2006a). Therefore, the carrier frequency estimate is, almost, entirely dependent on the carrier phase discriminator output, except for the loop filtering effects. In other words, the carrier frequency process is not directly observable in the receiver, but derived through the carrier phase measurements. Therefore, any unwanted jumps in the carrier phase at the tracking loop-level due to thermal noise, or any lack of right jumps due to significant dynamics, will also manifest itself in carrier frequency estimates; the carrier phase and carrier frequency processes always operate in coherence, as per the tracking loop design, except for the filtering effects. Therefore, the phase rate method is not expected to detect such subtle slips.

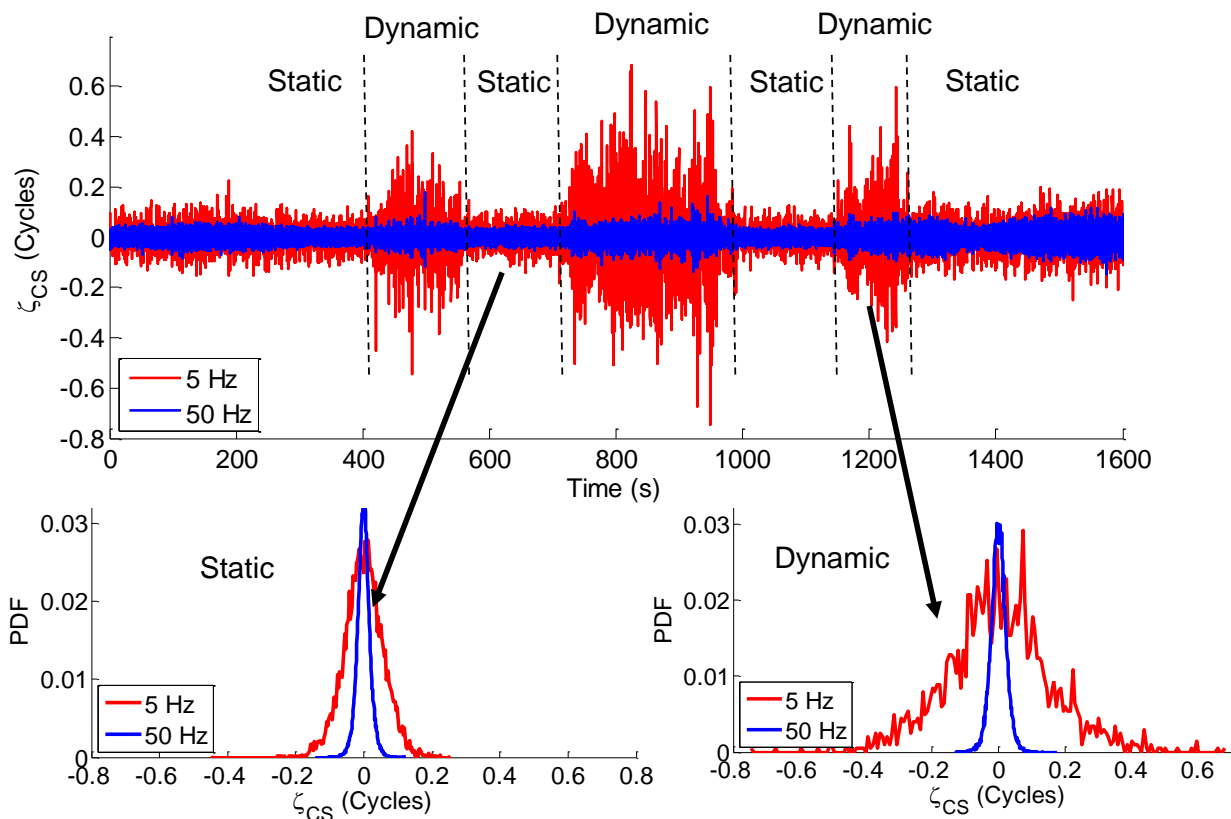


Figure 6-9 Phase rate test statistic for PRN 5 for pedestrian receivers and corresponding PDFs under static and dynamic conditions

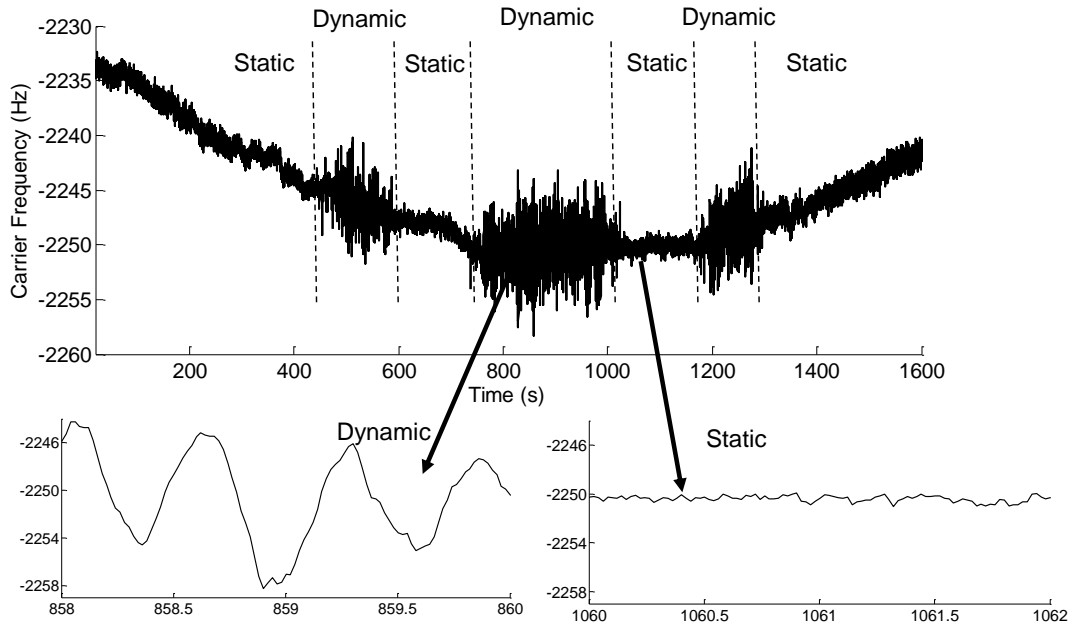


Figure 6-10 Carrier frequency process for PRN 5 for the pedestrian receiver

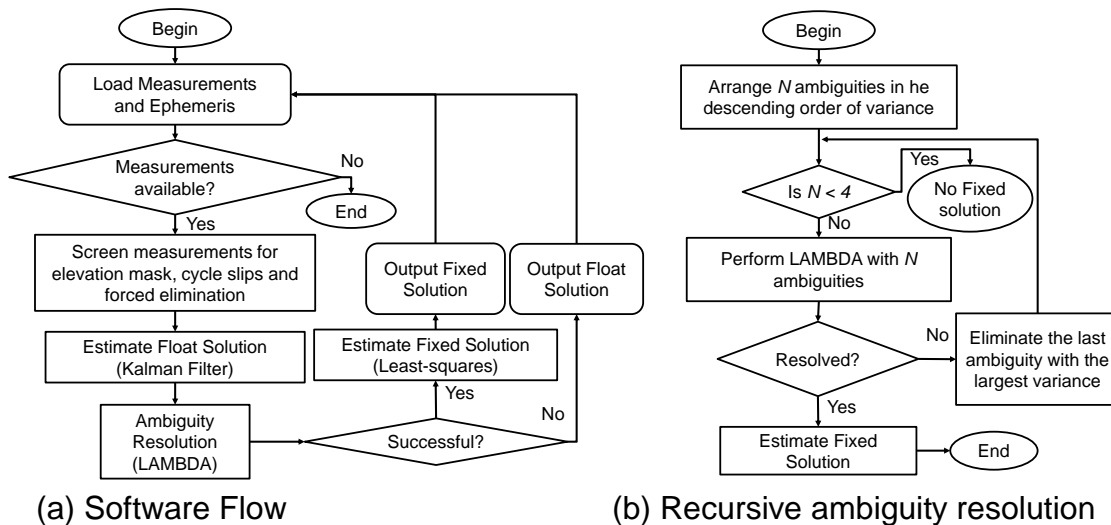
However, the phase rate method detects carrier phase slips with magnitude more than the threshold value that might occur due to various causes as discussed in Gardner (2005) and Ascheid & Meyr (1982). The phase rate method detects large slips in carrier phase which are also caused by momentary loss-of-lock in tracking. When signals are lost momentarily and recovered within the measurement interval, the carrier phase values are likely to contain a large jump. If these momentary glitches are not explicitly indicated, for example through time-since-phase-lock indicator, the navigation processor interprets these discontinuities as cycle slips. Phase rate method may be employed to detect such discontinuities. Overall, subtle jumps in carrier phase needs to be addressed in the receiver to obtain accurate kinematic solutions. These subtle slips can be readily detected by forming carrier phase double differences utilizing frequency diversity. For example, receivers which can track GPS L1 and L2 frequencies, the first difference can be formed across time epochs, and the second difference between-frequencies. Assuming the

occurrence of cycle slips in two frequencies is mutually exclusive, any outlier in the double difference thus formed can be interpreted as cycle slips. However, such methods are not applicable for single frequency receivers, which are mostly employed in lower-cost pedestrian applications.

6.4 Kinematic positioning

This section attempts to analyze the performance of kinematic solutions for pedestrian receivers. Software was developed in Matlab™ to process GPS L1 C/A observations and resolve ambiguities in double-differenced mode. The software flow is depicted in Figure 6-11 (a). The software accepts observations and ephemeris files in a predefined binary format and estimates the position and velocity solutions along with float ambiguities by forming double-difference (DD) measurements. After the float solution converges, the software attempts to fix the DD ambiguities to integer values using the Least-Squares AMBiguity Decorrelation Adjustment (LAMBDA) method (Teunissen 1995) on an epoch-by-epoch basis. The ambiguities are arranged in the descending order of their estimated variances to facilitate iterative search for integer fixing, as described in the flow chart shown in Figure 6-11 (b). The iterative search is designed to discard the ambiguities with large variances that have not converged, but to fix those with smaller variances that appear to have converged. If the ambiguities are successfully resolved as integers, the software estimates a, so-called, fixed solution with carrier phase and Doppler measurements using least-squares technique. The least-squares technique is used to estimate fixed solution, rather than the Kalman filter, so that the position domain performance can be readily compared across receivers without filtering effects.

The measurements from the experiment discussed in Section 6.2, from both GSNRx™ and the NovAtel receivers were processed using the above software. Position accuracy assessment can be performed only for static duration of the experiment, when the pedestrian antenna was located at the known position. During dynamic periods the performance cannot be assessed fully due to the lack of reference trajectory. If the carrier phase ambiguities are resolved correctly however, the estimated kinematic solution will be accurate to the centimetre-level, and therefore can be used as a reference trajectory. Position differences were formed by subtracting the coordinates of the position at which the pedestrian antenna was in static mode, from those obtained from the Matlab™ based software. The position differences obtained from float solutions are shown in Figure 6-12, during the initial convergence period when the antenna was static.



(a) Software Flow (b) Recursive ambiguity resolution
Figure 6-11 Overview of the flow of software developed for kinematic solution analysis and the flow chart for recursive ambiguity resolution

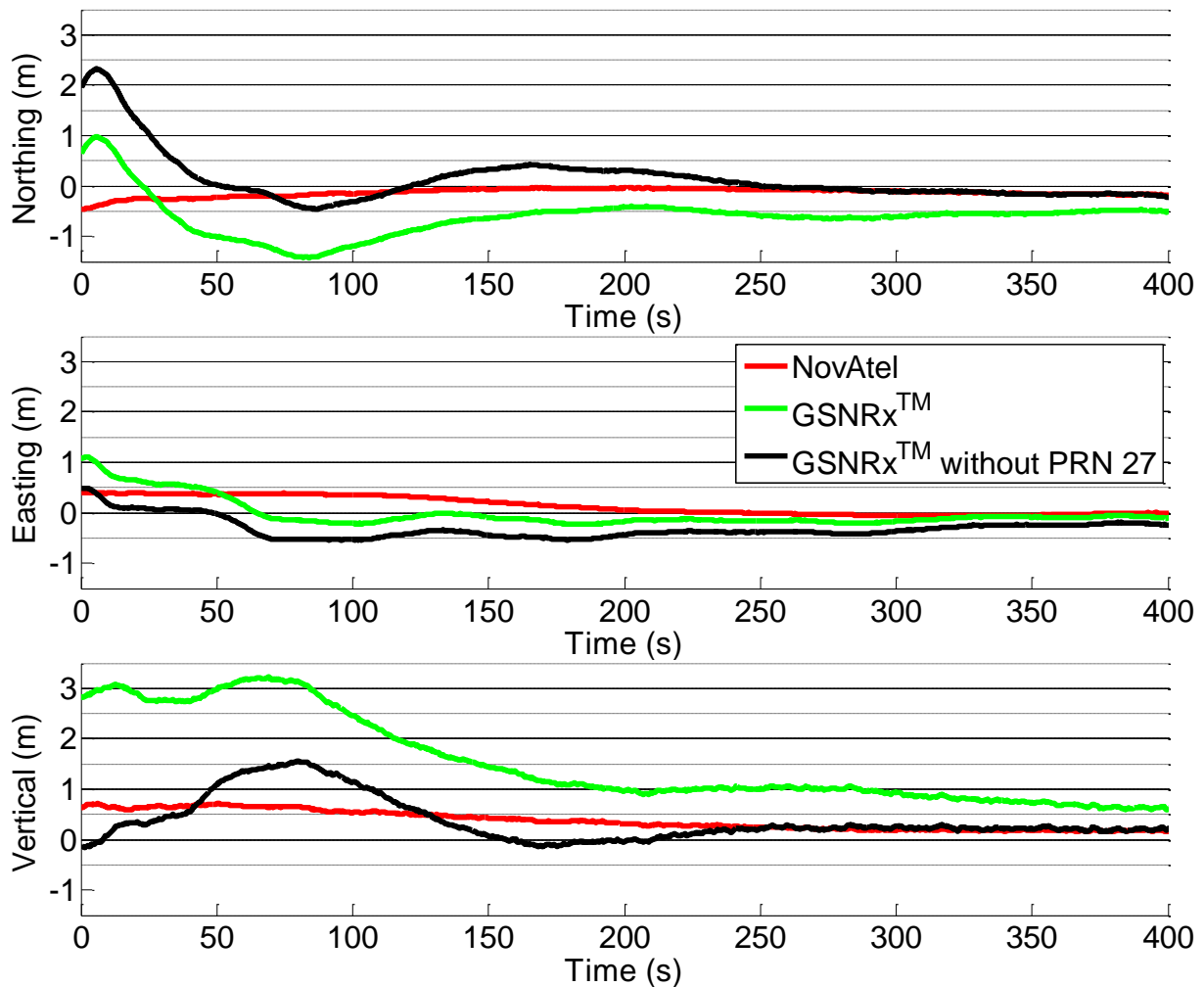


Figure 6-12 Position differences obtained from float solutions when the antenna was static at its initial location

The solutions corresponding to the NovAtel receiver is shown in red and GSNRx™ in green and black. The green curves correspond to the solutions obtained by processing all the available observations, whereas the black curves were obtained by processing satellites that did not contain exhibit cycle slips. The color selection remains the same for fixed solutions, which will be discussed later in this section. A total of three satellites, namely PRNs 5, 27 and 30, exhibited cycle slips in the GSNRx™ output, as discussed in Section 6.2. However, the mask angle setting of 10 degrees eliminated low elevation

PRNs 5 and 30 in all the three versions, namely NovAtel and two GSNRx™. The effect of half cycle slip in PRN 27 on kinematic solutions is now analyzed by comparing the two solutions, the green curves with PRN 27 and the black curves without.

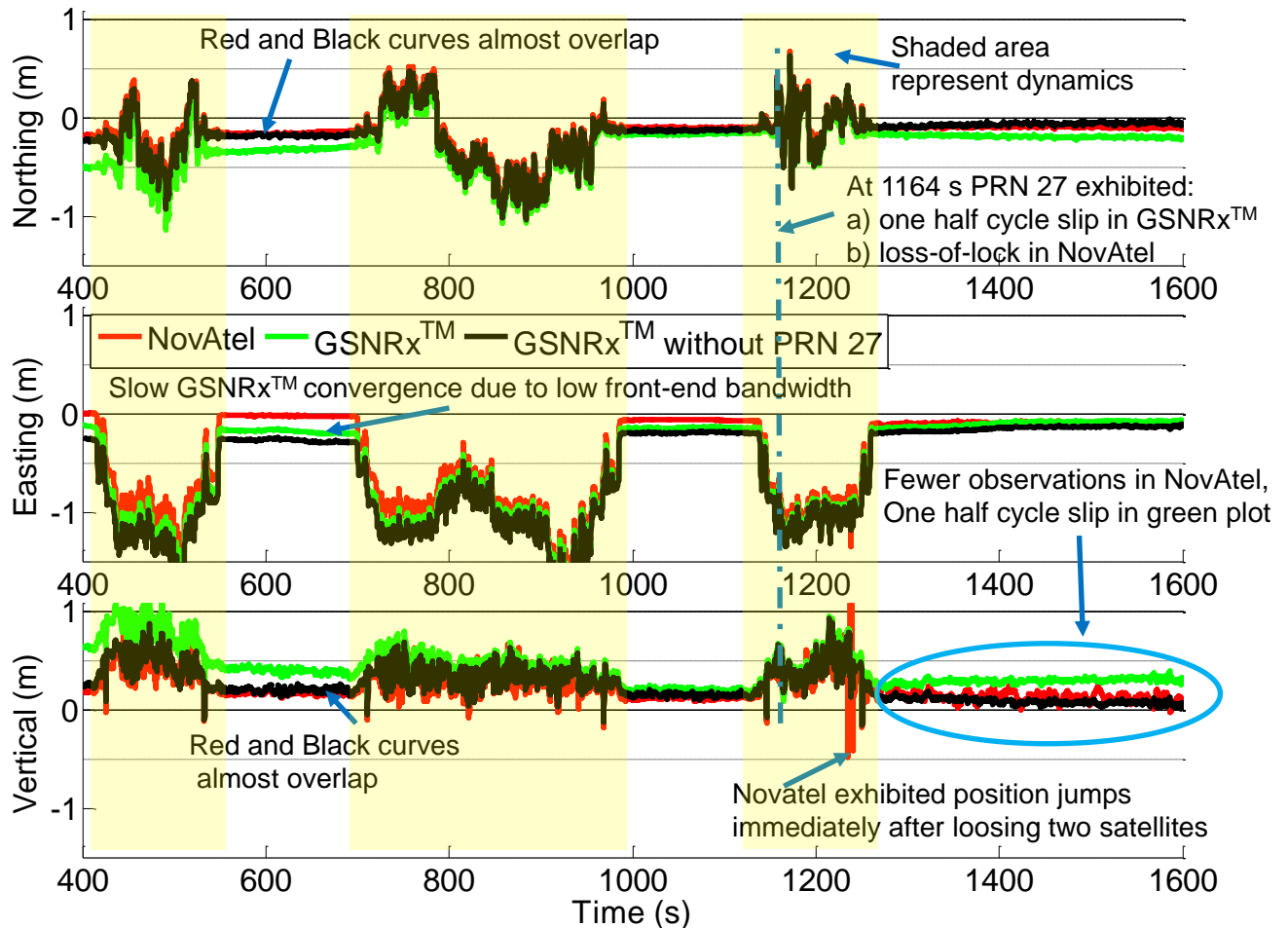


Figure 6-13 Position differences are shown for float solutions after convergence. No noticeable jumps in positions when one half cycle slip happened for PRN 27, but the overall divergence of float solution is apparent

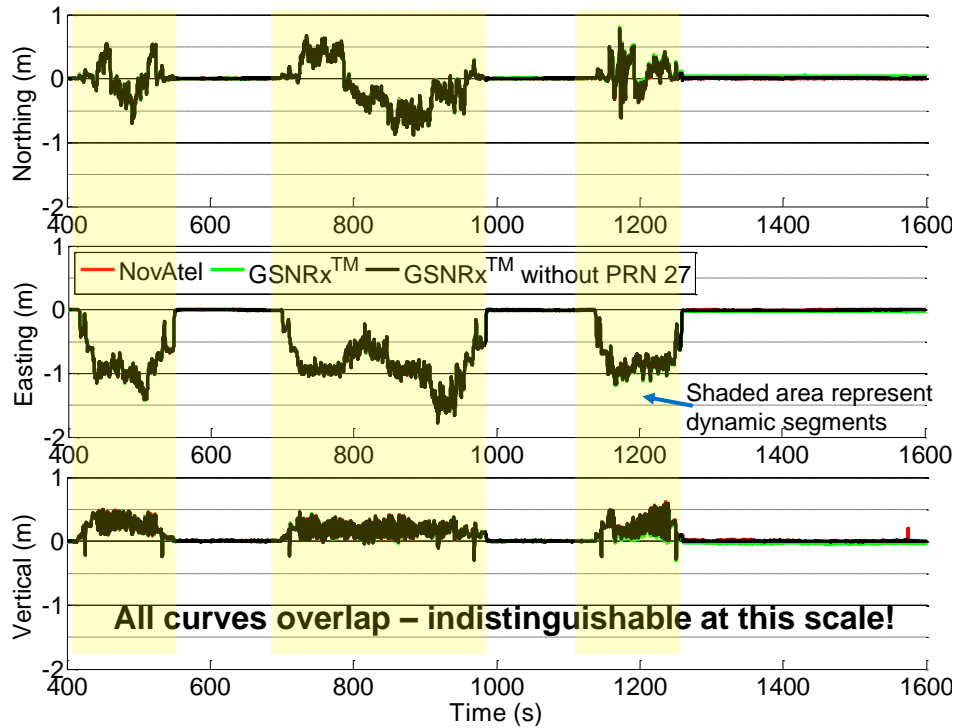
Figure 6-12 indicates that the NovAtel receiver exhibits significantly faster convergence to the reference static position, in all the three directions, compared to GSNRx™. This can be attributed to the use of the full 20 MHz bandwidth by NovAtel receiver, whereas the baseband data processed using GSNRx™ was collected with front-end bandwidth of

2.5 MHz. The higher bandwidth in the NovAtel allows the use of the, so-called, Narrow Correlator technique that can result in reduced code phase biases and jitter (Dierendonck et al 1992). Improved code phase accuracy can lead to faster convergence of the float solution, as code phase measurements influence the initial convergence.

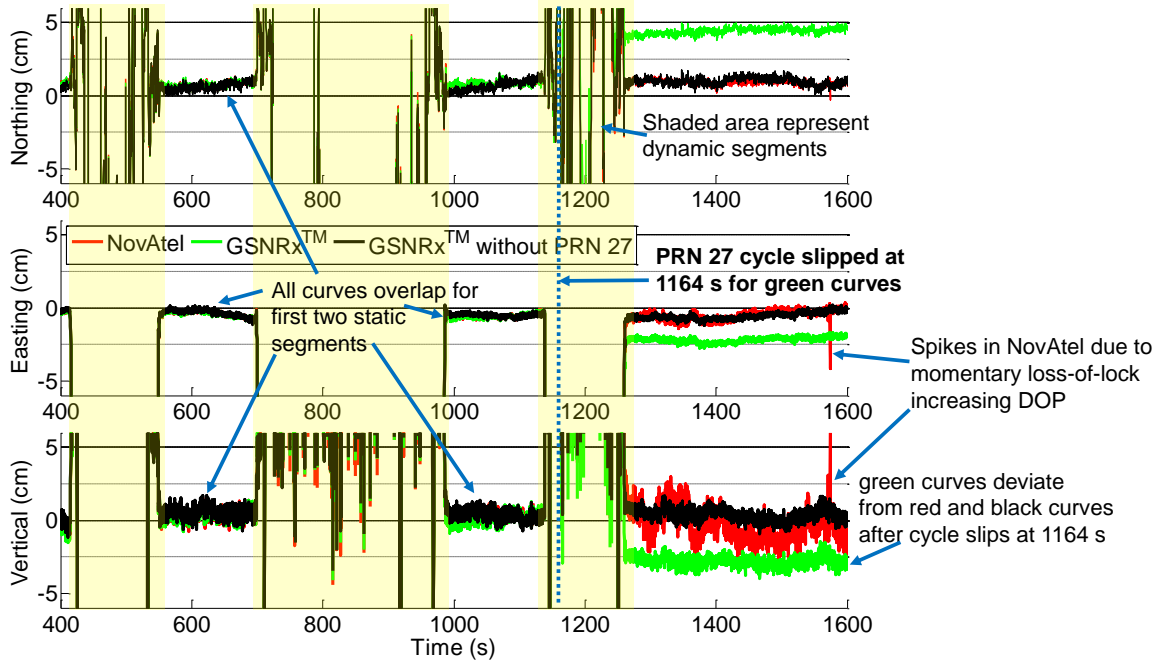
The float solutions corresponding to a kinematic portion of the dataset are shown in Figure 6-13 with semi-transparent shaded areas. It appears that the red and black curves, corresponding to NovAtel and GSNRx™ without PRN 27, overlap for almost the entire duration of the plots, except during the third dynamics segment at about 1230 seconds when the NovAtel receiver exhibited abrupt jumps in the vertical component with a magnitude of about 1.5 m. These jumps occurred immediately after losses-of-lock were observed for two satellites. Therefore, it is likely that the NovAtel receiver suffered pseudorange and Doppler measurement inaccuracies due to pedestrian dynamics in the third segment. Furthermore, the NovAtel receiver exhibited more variance in the vertical direction from approximately 1300 to 1600 seconds. This behavior is explained by reduced number of satellites in the NovAtel receiver during that portion of the dataset leading to increased DOP. This observation is more evident when using phase measurements, as will be discussed later in this section. Comparing the relative performance of green and black curves, it appears that the green curve started comparatively farther from the initial coordinates, and therefore, converged slowly. However, even after converging to the other two curves, the green curve appears to diverge again after the third dynamics segment, which is more visible in the vertical direction shown in the bottom subplot of Figure 6-13. The only difference between green and black curves is the elimination of PRN 27, which exhibited a half cycle slip after the

third dynamic segment, in the latter; therefore, it may be possible that the measurements from PRN 27 are a primary cause of such behaviour. The effect of this half cycle slip is explored further in the kinematic solutions as discussed next.

The kinematic least-squares solutions with integer ambiguities resolved are shown in Figure 6-14 both in full scale and magnified vertical scale. It is evident that the NovAtel and GSNRx™ outputs behave almost identically until the third pedestrian segment. Notice in Figure 6-14 (b) that the green curve deviates from the red and black curves, which was due to PRN 27 that slipped by 0.5 cycles and was used in kinematic solutions computation. Cycle slips of such magnitude can also be detected at the navigation-level by statistical testing of carrier phase residuals. The phase residuals with respect to the least-squares solution are shown in Figure 6-15, for green and black versions of GSNRx™. It is evident that the residuals increase when PRN 27 slips an effective 0.5 cycles at about 1164 s. Further investigation of carrier phase residuals revealed that cycle slips on PRN 27 occurred two times: a first time at 1163.4 s when it quickly recovered after two measurement epochs; a second time at 1164 s, after which it did not recover until the end. These slips occurred when the pedestrian antenna was in motion. Therefore, these could not be detected by the single difference carrier phase analysis conducted in Section 6.2. While PRN 27 cycle slipped in GSNRx™, NovAtel receiver exhibited a loss-of-lock for the same satellite at the time. Furthermore, notice in Figure 6-15 (b) that the residuals corresponding to all other satellites are bunched together on the positive side, whereas the curve corresponding to PRN 27 is offset from the others, indicating the presence of a systematic bias in PRN 27.

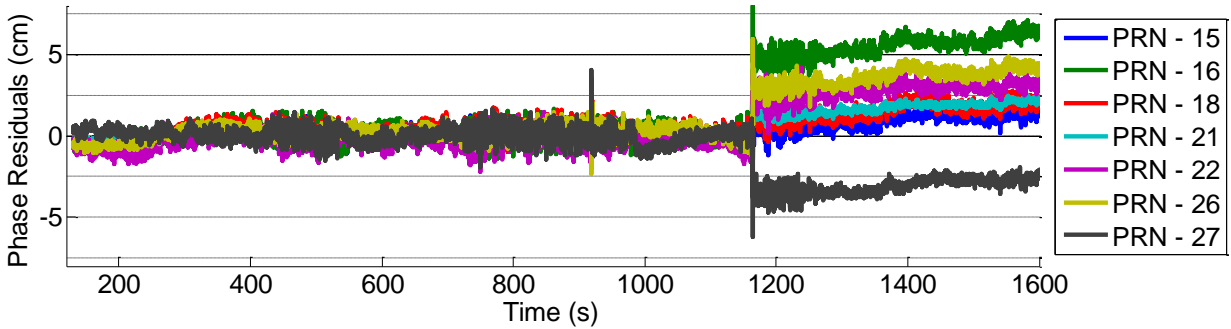


(a) Kinematic solutions at full vertical scale to show the trajectory

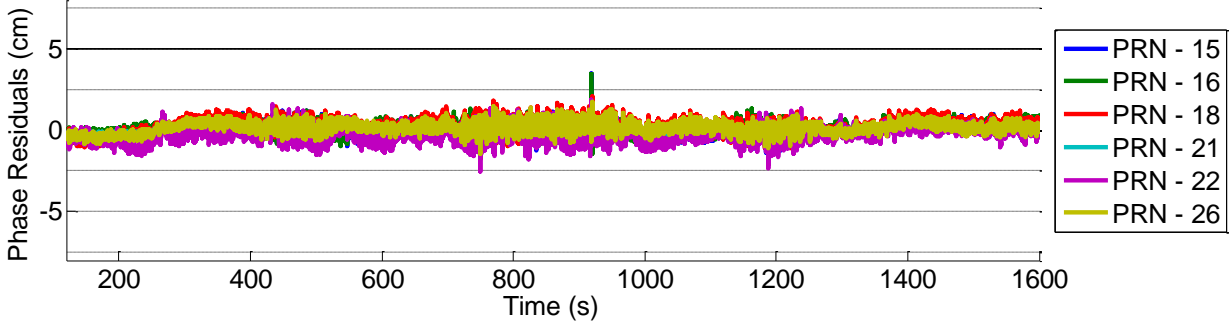


(b) Kinematic solution in magnified vertical scale for performance comparison

Figure 6-14 Position differences obtained from fixed kinematic solution with NovAtel and GSNRx™ observations at (a) full scale and (b) magnified vertical scales. Notice the change of unit from metres in (a) to centimetres in (b).



(a) Phase residuals for GSNRxTM version when all satellites included



(b) Phase residuals for GSNRxTM version when PRN 27 is eliminated

Figure 6-15 Least-squares phase residuals corresponding to two versions of GSNRxTM measurements. The base satellite used was PRN 29 in both cases.

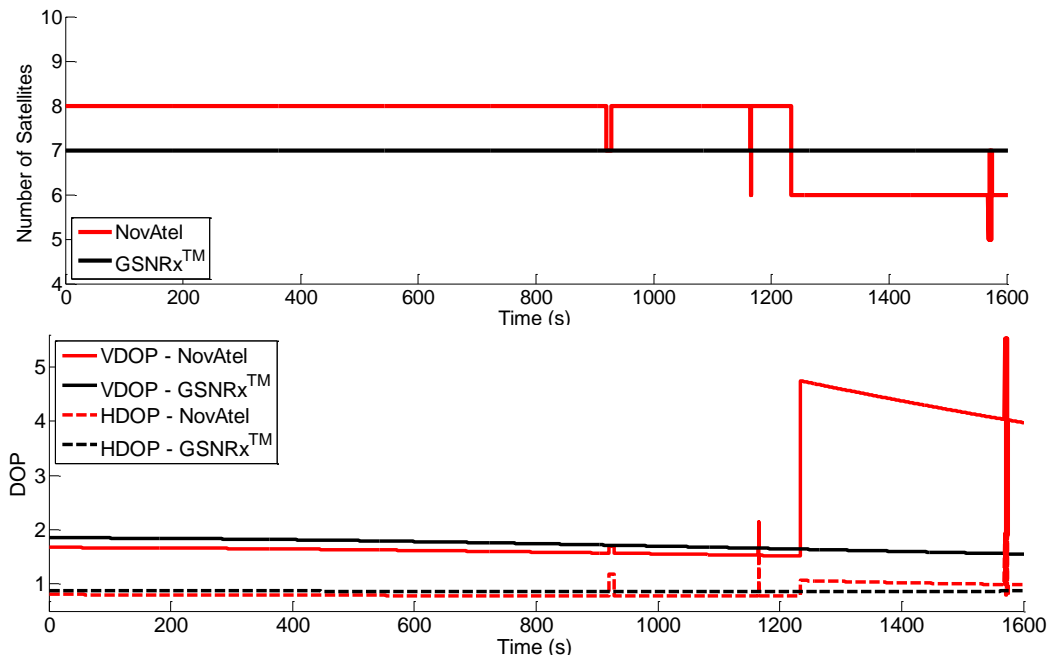


Figure 6-16 Number of satellites used for fix, HDOP and VDOP corresponding to NovAtel and GSNRxTM receivers

Another spike in phase residuals at 919 seconds is noticed in Figure 6-15. Further investigation revealed that it was due to PRN 26 that also likely suffered a momentary half cycle slip, but recovered after two measurement epochs. Although it is possible, when sufficient measurement redundancy is available, to detect and exclude such systematic biases, it is not done in this work to analyze the effect of unidentified cycle slips of such magnitude on kinematic solutions performance. These errors result in precise but inaccurate solutions. It can also be noticed, in the vertical direction subplot in Figure 6-14 (b), that the NovAtel receiver exhibits significantly more variations compared to GSNRx™ after the third dynamics segment. The increase in variation is explained by the reduced number of satellites and increased Vertical Dilution of Precision (VDOP), as shown in Figure 6-16, during the final static segment, extending from approximately 1250 to 1600 s. Overall, it was demonstrated that kinematic solutions is estimated accurately during static receiver conditions as the position coincides with the known antenna location within centimetres, thus validating the integer ambiguity resolution process used herein.

6.5 Effect of human proximity on carrier phase residuals

The effect of human proximity on carrier phase positioning, in particular the carrier phase shift when GNSS signal penetrates the human body to reach the antenna, is analyzed in this section. An experiment was conducted with the data collection setup similar to the one used in Section 3.3. A stationary survey-grade test antenna was mounted on a survey tripod with the antenna height from ground corresponding to the subject's chest-level, or antenna level 6 as shown in Figure 3-15 (b). A stationary reference antenna was also used for differential processing. A survey-grade Novatel receiver was used in the

experiment. During the data collection, the subject walked around the antenna setup at three radial distances, namely 2 m, 1 m and 0.5 m. The measurements were processed using the Matlab™ based software described in the previous section.

The effect of human proximity is analyzed using the carrier phase residuals obtained by a least-squares solution. Short portions of the carrier phase residuals are shown in Figure 6-17 for the three pedestrian-to-antenna distances. The human proximity effects appear to be negligible for the pedestrian-to-antenna distance of 2 m, whereas the effects were pronounced when the pedestrian walks more closely to the antenna. This is due to the increased portion of the body that obscures electromagnetic signals due to increasing proximity. The carrier phase residuals appear to show spikes at regular intervals. For example, notice the green spikes in subplot (b) and blue spikes in subplot (c). These regular time intervals correspond to the time taken by the pedestrian to complete one revolution around the antenna. These spikes can be attributed due to (a) carrier phase shifts when the signal passes through the body and (b) multipath due to reflections from the skin. The carrier phase residuals are a result of a series of signal processing events that happen in the receiver and a detailed analysis of the signal propagation through and in the proximity of human body is beyond the scope of this thesis. Overall, carrier phase residuals spikes of up to 3 cm are noticed for the human-antenna proximity of 0.5 m.

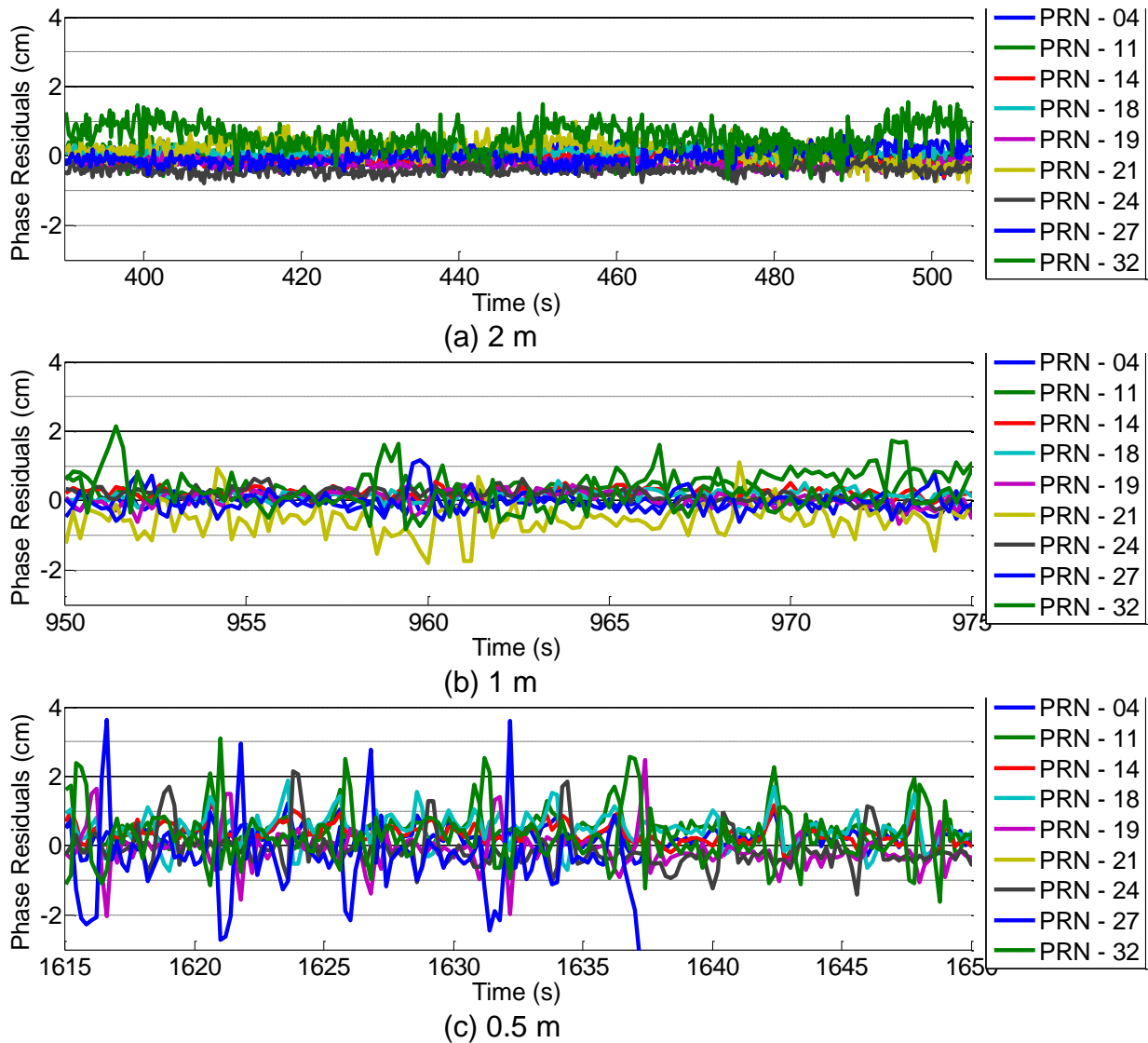


Figure 6-17 Least-squares phase residuals for three pedestrian-antenna distances corresponding to Novatel receiver.

6.6 Summary

A new method of quantification of cycle slips in pedestrian environments by performing prescribed antenna manoeuvres was demonstrated. It was shown that the carrier phase cycle slips of the order of 0.5 cycles can happen in pedestrian environments due to excessive dynamic stress on the carrier tracking loops that are induced by pedestrian dynamics. It was shown that these slips also introduce momentary spikes in estimated

C/N₀ values but were not detected by tracking quality monitors due to filtering effects on the estimated C/N₀ before decision-making. The effect of human proximity on the carrier phase residuals was also analyzed and it was shown that phase residuals of up to 3 cm were observed for a pedestrian-to-antenna of 0.5 m for a scenario in which a pedestrian is walking around the antenna. The performance of a software-defined receiver, in terms of carrier phase continuity, was evaluated through comparison with a commercial survey-grade receiver. It was demonstrated that the survey grade receiver incurs losses-of-lock when subjected to pedestrian dynamics whereas the software defined receiver delivers carrier phase measurements with generally better continuity, which can be mainly attributed to appropriate tuning of tracking loops. It was also discussed that the phase rate cycle slip detection method that can be employed in single frequency receivers is not designed to detect cycle slips within a cycle. It was demonstrated that such slips, when not detected before the navigation solution, can cause precise but inaccurate kinematic solutions. Overall, it was shown that a software-defined receiver can deliver comparable performance to a commercial survey-grade receiver under static conditions and may be able to outperform such receivers, with appropriate tuning of tracking loops as a function of the pedestrian environment.

Chapter Seven: Conclusions and Future Recommendations

7.1 Conclusions

Chapter-wise conclusions from the research work conducted herein are discussed below.

7.1.1 Characterization of pedestrian Environment

Pedestrian accelerations are of significant magnitude: Pedestrian dynamics was characterized in this research to understand the signal propagation effects in a pedestrian GNSS receiver. The dynamics characterization was performed using MEMS grade accelerometers for various motion modes such as gentle walking, running and hiking involving flat terrain and mountains. Maximum peak-to-peak accelerations that were measured during the experiment range from 30 m/s^2 for regular walking with the sensors placed in a backpack to 150 m/s^2 when hiking with sensors mounted on the shin.

Quasi-periodic pedestrian dynamics: It was demonstrated that pedestrian dynamics exhibits strong quasi-periodicities. Therefore, the resulting carrier Doppler and hence, the carrier phase also exhibit quasi-periodicity. The characterization of position and velocity processes, by appropriately processed accelerometer data, was done in the frequency domain. The quasi-periodic dynamics manifest itself as a set of harmonics in the frequency domain. It was demonstrated that the magnitudes and locations of such harmonics depend on the placement of the sensor on the pedestrian as well as the motion mode. The frequency domain attributes of pedestrian dynamics were characterized by power spectral densities and cumulative spectral densities.

Relationship between position and velocity with carrier Doppler and carrier frequency: It was demonstrated that the pedestrian dynamics affects GNSS signal

parameters in two ways: firstly, by LOS frequency and phase perturbations; and secondly, by oscillator g -sensitivity induced apparent dynamics. A theoretical relationship was established between the position and velocity processes derived from processed accelerometers data and GNSS signal parameters, namely carrier frequency and phase. The relationship was verified empirically using live GPS L1 C/A signals. Overall, a major source of dynamics stress was identified to be the pedestrian motion. Of course, the relative magnitudes between the LOS and oscillator g -sensitivity induced dynamics depend on the satellite-receiver locations and g -sensitivity of the oscillator.

Satellite signal attenuation is antenna location dependant: It was shown that the satellite signal attenuation due to human proximity of the antenna depends on the location of the antenna on the pedestrian. The signals are attenuated more when the antenna location goes lower from the head to the torso, which is rather intuitive. It was also shown that the presence of the human body induces momentary spikes in power levels, which are noticeable through raw C/N_0 values computed from correlation values at the loop update rate. However, these momentary spikes were masked due to filtering effects performed on the raw C/N_0 estimates.

Unique operating environment with signal attenuation and high receiver dynamics: Overall, pedestrian GNSS signal propagation was shown to be unique, in the sense that it combines rapid signal power level fluctuations due to the human body, which requires high sensitivity receiver design techniques, as well as high pedestrian dynamics due to the flexibility and degrees of freedom.

7.1.2 Oscillator g -sensitivity effects on GNSS carrier phase tracking

Oscillator g -sensitivity effects carrier phase tracking jitter: The quartz-based oscillators, due to their piezoelectric nature, exhibit sensitivities to acceleration changes. Consequently, when g -sensitive oscillators are used in pedestrian receivers, the tracking loop needs to address changing carrier frequency and phase, essentially by allocating a part of its "bandwidth budget" for these oscillator effects.

Laboratory measurement of oscillator g -sensitivity: It was also shown that it is possible to measure g -sensitivity values with a simple 2- g tip-over test using simulated GPS signals generated by a hardware GPS simulator. The accuracy of such a calibration was also proven to be sufficient to be utilized in the compensation based tracking architecture proposed herein.

Oscillator g -sensitivity effects can be compensated for using accelerometers: One of the important contributions of the thesis is that the oscillator g -sensitivity compensation was achieved by using three-axis accelerometers, which are mounted in close proximity to the oscillator in a strap-down fashion. The compensation was achieved via a tracking loop feed-forward correction of carrier frequency perturbations due to oscillator g -sensitivity, which are estimated by appropriately processed accelerometer measurements. It was demonstrated that the oscillator g -sensitivity effects can almost entirely be compensated for using the proposed method.

The LOS and g -sensitivity effects can be comparable: It was demonstrated with an OCXO measuring a g -sensitivity norm of about 2.18 ppb/ g that, in a typical pedestrian scenario, the carrier phase disruptions caused by LOS variations and apparent dynamics induced through oscillator g -sensitivity are comparable. It was demonstrated that in order

to effectively track carrier phase, g -sensitivity compensation must be activated up on an ultra-tight receiver architecture, where the navigation domain feed-back compensates for the LOS dynamics.

The quality of accelerometers does not matter: The carrier phase tracking enhancement due to oscillator g -sensitivity compensation was demonstrated with various qualities of accelerometers ranging from tactical grade to low cost MEMS based accelerometers available in cell phones. This is a necessary demonstration for the incorporation of the proposed method in low cost pedestrian receivers where cost and size are important considerations. It was also shown that the proposed method is almost entirely insensitive to accelerometers biases. It was demonstrated that the accelerometer scale factor errors and g -sensitivity calibration errors of up to 10% have little effect on the overall carrier phase tracking performance. However, it was shown that low dynamic range of cell phone accelerometers, namely from $-/+ 2$ to $-/+ 4$ g , were insufficient to measure pedestrian dynamics that can generate peak-to-peak accelerations of up to 15 g . Nonetheless, it was demonstrated that the proposed method can deliver improved carrier phase tracking even with such low quality accelerometers. Of course, the proposed method readily incorporates the accelerometers data, when the device with appropriate dynamic range is available.

Compensation rate should depend on the receiver dynamics: It was shown that the feed-forward correction rate should be based on the dynamics, but not on the accelerometers quality. The proposed method delivered similar compensation performance across various qualities of accelerometers, whereas the performance was maximized for a feed-forward correction rate of 25 Hz, which is about twice the typical

frequency content in human gait (Antonsson & Mann 1985). It was also shown that the method delivered improved compensation performance for high feed-forward correction rates in the vehicular scenario that consisted of high frequency receiver platform dynamics. Therefore, the feed-forward correction rate should be chosen based on the receiver dynamics, and not, necessarily, on the accelerometers quality.

The loop bandwidth may be reduced with compensation: It was demonstrated that with the g -sensitivity compensation, it may be possible to reduce the loop bandwidth to reduce thermal noise effects. This observation is intuitive, as external dynamics aiding reduces the tracking loop's dynamics stress, which in turn enables the tracking loop design with a reduced bandwidth. As a result, the receiver designer may cut down on the "bandwidth budget" allocated to track the oscillator g -sensitivity along with other sources of dynamic stress.

7.1.3 Exploiting quasi-periodicity in pedestrian dynamics

Quasi-periodicities in pedestrian dynamics can be isolated: It was demonstrated that a simple STFT based algorithm can be used to detect and separate harmonics resulting from the pedestrian motion. The input to the STFT algorithm was the carrier frequency estimates from the tracking loop itself. It was demonstrated that the tracking loops can be designed to predict pedestrian motion ahead of time.

Performance enhancement via feed-forward compensation of predicted receiver dynamics: The usefulness of dynamics prediction was demonstrated via a feed-forward compensation scheme, which is similar to the technique proposed for the oscillator g -sensitivity compensation. However, the scheme can only compensate for quasi-periodic

dynamics, but not for other sources of carrier phase perturbations, including aperiodic pedestrian motion.

Enables loop bandwidth reduction and minimizing cycle slips: It was demonstrated that the STFT based dynamics compensation scheme may also enable reduction in the loop bandwidth by partly reducing tracking loop dynamic stress. A heuristic method of cycle slips analysis was conducted, where it was demonstrated that the proposed method, with appropriate tuning of the design parameters namely STFT observation window and feed-forward correction gain, results in reduced losses-of-lock and more continuous carrier phase measurements with minimal cycle slips.

Appropriate choices of design parameters are necessary for effective carrier phase tracking: The design parameters, namely carrier frequency observation window length and feed-forward gain, should be appropriately tuned to suit the operating environment. The pedestrian dynamics, when projected on line-of-sight affects various satellites differently based on the location of the satellites with respect to the receiver antenna. Therefore, in principle, an optimal choice of the observation window length via on-the-fly characterization of LOS dynamics can further enhance compensation performance. Nevertheless, it was demonstrated that the algorithm still delivers enhanced carrier phase tracking performance while operating within the constraints imposed.

Performance demonstration across pedestrian subjects with various motion modes: The performance enhancement with the proposed dynamics prediction algorithm was evaluated across three pedestrian subjects involving various walking styles on a flat terrain. The equipment used for the performance evaluation consisted of a consumer-

grade patch antenna and a 1-bit front-end with a TCXO, these being suitable for pedestrian applications.

7.1.4 Investigation of kinematic solutions for pedestrian receivers

A new carrier phase cycle slip quantification method: A new method to quantify cycle slips in a pedestrian environment was described. The method involved prescribed antenna manoeuvres, namely beginning and ending the data collection at a known location using a survey tribrach. It was demonstrated that cycle slips, of the order of 0.5 cycles can happen in a pedestrian hand held environment due to significant dynamics stress that are out of the discriminator linear region, and hence ignored by tracking loops.

Comparative performance evaluation of a software-defined receiver with a commercial survey-grade receiver: It was demonstrated that a commercial survey-grade receiver suffers from losses-of-lock when subjected to pedestrian hand held dynamics. It was shown that a software-defined receiver, when appropriately tuned for pedestrian operating conditions, delivers carrier phase measurements with reduced cycle slips. Furthermore, under static conditions, a software-defined receiver was shown to deliver kinematic solutions comparable to the survey-grade receiver.

7.2 Recommendations for future work

A number of interesting questions were generated throughout this research work. Although a few questions were answered, numerous unanswered questions remain due to the limited scope of the research conducted herein. Some of these unanswered questions may generate continued research interest that may help in continuous availability of kinematic solutions in pedestrian operating environments. A few recommendations for future work, relevant to the chapters written in this thesis, are listed below.

7.2.1 Pedestrian environment characterization

The characterization conducted in this research was limited to only a few pedestrian subjects; in fact, the results discussed correspond to a single subject. It would be interesting to conduct characterization of position and velocity spectral densities across pedestrian subjects. The results obtained from such characterization may be used for many purposes, such as pedestrian GNSS signal simulators, to derive a priori constraints for the STFT based method proposed in Chapter 5.

The study on human attenuation effects of satellites may be extended to include carrier phase disruptions due to multipath effects caused by the presence of the human body. In particular, these results may be used to quantify carrier phase multipath effects caused by the reflections from the skin on kinematic solutions.

Only linear dynamics using accelerometers data were used for the analysis. However, it is interesting to characterize the pedestrian environment in terms of angular dynamics. These results would be useful to understand possible antenna orientation changes that

also affect the carrier phase tracking performance. These results may also be useful to analyze carrier phase wind-up due to antenna rotation, which may happen due to the motion of hand held receivers.

7.2.2 Oscillator g -sensitivity compensation

The oscillator g -sensitivity affects achievable performance across all GNSS applications, albeit in various magnitudes. The study conducted herein in the pedestrian environment could be extended to include high dynamics applications such as fighter aircraft and missiles. It would be interesting to investigate whether the performance of the FLLs, which are typically employed in such high dynamics applications, would improve using the carrier frequency compensation technique proposed herein. Another interesting application where the oscillator compensation technique can be employed is in vehicles used for agricultural purposes. Ploughing tractors, operating in rough fields experience significant high frequency accelerations. However, it would be interesting to investigate whether the accelerations have significant magnitudes that can induce apparent carrier frequency disruptions, which can be compensated using the technique proposed herein. Although g -sensitivity of quartz-based oscillators is examined in this research, it is interesting to investigate MEMS based oscillators. It may be possible that similar to MEMS gyroscopes that are shown to exhibit significant g -sensitivities (Bancroft & Lachapelle 2012b), MEMS based oscillators also suffer from such issues.

7.2.3 STFT based dynamics prediction

The carrier phase tracking performance enhancement was demonstrated using a STFT based prediction. However, it would be interesting to extend this study to include other time-frequency resolution techniques such as wavelets that enables defining of the wavelet shape based on the observed carrier frequency process.

It was shown in Chapter 6 that despite dynamics prediction and compensation, the pedestrian dynamics can still induce significant momentarily acceleration spikes that are ignored by the tracking loop. However, these momentary spikes in acceleration were also recorded by the MEMS based accelerometers attached to the pedestrian antenna. Therefore, it may be possible to extend performance by building a gain scheduling architecture that changes the tracking loop bandwidth on-the-fly to more readily accommodate changing signal conditions.

Although performance demonstration of the proposed methods is conducted using a Kalman filter based architecture, it is interesting to evaluate relative performance when a traditional PI controller based architecture is employed.

The g-sensitivity compensation and STFT based dynamics compensation algorithms are demonstrated independently for research purposes. However, it would be useful to combine the two solutions by appropriate signal processing methods to achieve the overall performance enhancement needed in a commercial product.

It would be interesting to compare the performance of the proposed algorithm with the partially coherent ultra-tight integration scheme proposed in the DINGPOS system (Pany et al 2009a). Furthermore, it would also be interesting to combine the μ -trajectories technique developed therein with the feed-forward architecture proposed in this research.

This could eliminate the need for ultra-tight loop closure at the carrier phase level, but still eliminate significant receiver dynamics stress on the tracking loops.

7.2.4 Kinematic solutions in a pedestrian environment

Performance comparison between a software-defined receiver and a survey-grade receiver were conducted herein. However, the pedestrian operating environment also necessitates enhanced tracking sensitivity due to human body attenuation of satellite signals. Therefore, it would be highly desirable to conduct a relative performance evaluation using high sensitivity receivers that are designed to handle signal obscuration. It would also be useful to understand the effects of using a low-quality antenna for kinematic tests. In particular, it was already demonstrated by Pesyna et al (2014) that kinematic solutions can be estimated using a smartphone-quality antenna for static and wavelength-scale gentle antenna motions. However, it would be interesting to evaluate the performance of the proposed tracking architecture using such low-quality antennas in a pedestrian operating environment.

References

Akos, D. and M. Pini (2006) "Effect of Sampling Frequency on GNSS Receiver Performance," *NAVIGATION, Journal of The Institute of Navigation*, Vol. 53, No. 2, pp. 85-95

Allan, D. W. (1987) "Should the Classical Variance Be Used as a Basic Measure in Standards Metrology?" *IEEE Trans. on Instrumentation and Measurement*, IM-36, pp. 646-654

Angrisano, A., S. Gaglione, C. Gioia, M. Massaro, and S. Troisi (2013) "Benefit of the NeQuick Galileo Version in GNSS Single-Point Positioning," *Hindawi Publishing Corporation*, Volume 2013, Article ID 302947, 11 pages

ANN-MS (2006) ANN-MS Active GPS Antenna, *Product Datasheet*, u-blox AG, Zuercherstrasse68, CH-8800 Thalwil, Switzerland

Antonsson, E. K. and R. W. Mann (1985) "The frequency content of gait," *Journal of Biomechanics*, vol. 18, no. 1, pp. 39–47, 1985

Ascheid & Meyr (1982) "Cycle slips in Phase-Locked Loops: A Tutorial Survey," *IEEE Transactions on Communications*, Volume 30, Issue 10, pp. 2228-2241

Bancroft, J. B., V. Renaudin, A. Morrison, and G. Lachapelle (2011) "GNSS Antenna-Human Body Interaction", *Proceedings of ION GNSS 2011*, Session F6, Portland, OR, 20-23 September 2011, 7 pages (Available at <http://plan.geomatics.ucalgary.ca>)

Bancroft, J. B. and G. Lachapelle, (2012a) "Performance of pedestrian navigation systems as a function of sensor location", *Symposium Navigation Sensors and Systems in GNSS Denied Environments*, Izmir, Turkey, 10 pages (Available at <http://plan.geomatics.ucalgary.ca>)

Bancroft, J. B. and G. Lachapelle, (2012b) "Estimating MEMS Gyroscope G-Sensitivity Errors in Foot Mounted Navigation", *2nd International Conference on Ubiquitous Positioning, Indoor Navigation and Location-Based Service*, Helsinki, 2-5 Oct 2012 (Available at <http://plan.geomatics.ucalgary.ca>)

BeiDou ICD (2012) BeiDou Navigation Satellite System Signal In Space Interface Control Document, Open Service Signal B1I, Version 1.0, China Satellite Navigation Office, December 2012, pp. 1

Benson, D. (2007) "Interference Benefits of a Vector Delay Lock Loop (VDLL) GPS Receiver," in Proceedings of the 63rd Annual Meeting of the Institute of Navigation, Cambridge, Massachusetts, Institute of Navigation, April 2007, pp. 749-756

Besson, R., J. Boy, and F. Deyzac (1996) "Acceleration sensitivity of BVA resonators," Frequency Control Symposium, 50th Proceedings of the 1996 IEEE International, June 1996, pp. 457 – 463,

Bloch, M., O. Mancini, T. McClelland, and L. Terracciano, (2009) "Acceleration 'g' compensated quartz crystal oscillators," in Frequency Control Symposium, 2009 Joint with the 22nd European Frequency and Time forum. IEEE International, April, pp. 175–180.

Borio, D. (2008) *A Statistical Theory for GNSS Signal Acquisition*, Doctoral Thesis, Dipartimento di Elettronica, Politecnico di Torino, Italy

Brown, R. G. and P. Y. C. Hwang (1997) *Introduction To Random Signals and Applied Kalman Filtering*. Third ed. John Wiley & Sons, Inc, pp.198-206

Buckely, J., K. G. McCarthy, B. O'Flynn, and C. O'Mathuna (2010) "The detuning effects of a wrist-worn antenna and design of a custom antenna measurement system," published in *IEEE Microwave Conference (EuMC), 2010 European*, 28-30 Sept. 2010, pp. 1738-1741

Cady, W. G. (1955) "Composite piezoelectric resonator," *American Journal of Physics*, vol. 23, no. 1, p. 31, January 1955

Chen, X., C. G. Parini, B. Collins, Y. Yao, and M. U. Rehman (2012) *Antennas for Global Navigation Satellite Systems*, John Wiley & Sons, Ltd., West Sussex, United Kingdom, 2012, pp. 149-180.

Chowdhary, M., M. Sharma, A. Kumar, K. Paul, M. Jain, C. Agarwal, G. Narula (2009) "Context detection for improving positioning performance and enhancing user experience," in *Proceedings of the 22nd International Meeting of the Satellite Division of the Institute of Navigation*, September, Savannah, GA, pp. 2072-2076

CSR (2015) *Handsets Technologies and Solutions*,
<http://www.csr.com/products/application/handsets>, last accessed January 6, 2015

Curran, J. T. (2010) *Weak Signal Digital GNSS Tracking Algorithms*, PhD Thesis, National University of Ireland, November 2010, p 20

Curran, J., G. Lachapelle and C. Murphy (2012) "Digital GNSS PLL Design Conditioned on Thermal and Oscillator Phase Noise," *IEEE Transactions on Aerospace and Electronic Systems*, volume 48, issue 1, 180-196.

Daneshmand, S., A. Broumandan, J. Nielsen and G. Lachapelle (2013) "Interference and multipath mitigation utilising a two-stage beamformer for global navigation satellite systems applications," *IET Radar, Sonar & Navigation*, volume 7, number 1, pp. 55-66

Daneshmand, S., A. Jafarnia-Jahromi, A. Broumandan, G. Lachapelle (2012) "A Low-Complexity GPS Anti-Spoofing Method Using a Multi-Antenna Array," *ION GNSS12 Conference*, Session B3, Nashville, TN, Sep 18-21, 2012, 11 pages

Dierendonck, A. J. V., P. Fenton, and T. Ford (1992) "Theory and performance of narrow correlator spacing in a GPS receiver," *NAVIGATION*, Journal of the Institute Of Navigation, 39(3), Fall 1992, pp. 265-283

Dierendonck, A. J. V. (1996) "GPS Receivers," [Chapter 8] in *Global Positioning System: Theory and Applications*, volume I, B. Parkinson and J. J. Spilker, Jr., eds., American Institute of Aeronautics and Astronautics, Inc., Washington D.C., USA, pp.329-408.

Diggelen, F. V. (2002) "Indoor GPS Theory & Implementation," *published in Position Location and Navigation Symposium, 2002 IEEE*, pp.240-247

Diggelen, F. V. (2009) *A-GPS: Assisted GPS, GNSS and SBAS*, Artech House, Boston/London

Emmons, D. A., R. M. Garvey, and B. T. Milliren (1984) "Acceleration sensitivity compensation and symmetry in quartz oscillators," in 38th Frequency Control Symposium, May 29-Jun 1 1984, pp. 80– 85

Filler, R. L., (1988) "*The Acceleration Sensitivity of Quartz Crystal Oscillators: A Review*", IEEE Transactions on Ultrasonics, Ferroelectrics, and Frequency Control, Vol. 35, No. 3.

Fortes, L. P. S., T. Lin, and G. Lachapelle (2014) "Effects of the 2012-2013 Solar Maximum on GNSS Signals in Brazil," *GPS Solutions*, published online 19 June 2014, DOI 10.1007/s10291-014-0389-1, 20 pages, (available in <http://link.springer.com/>)

Fry, S. and G. Burnett, (2010) "Reducing the acceleration sensitivity of at-strip quartz crystal oscillators," in *Frequency Control Symposium (FCS)*, 2010 IEEE International, June, pp. 25–30

Gaggero, P. (2008) Effect of Oscillator Instability on GNSS Signal Integration Time, MSc Thesis, University of Neuchâtel, Switzerland, pp. 79-109

GALILEO ICD (2014) European GNSS (Galileo) Open Service Signal In Space Interface Control Document, Revision 2, Issue 1, European Union, February 2014, Available at http://ec.europa.eu/enterprise/policies/satnav/galileo/open-service/index_en.htm

Gardner, F.M. (2005), Phase Lock Techniques, Third Edition, Jhon Wiley & Sons, Inc., USA

Ghafoori, F (2012) *Modeling the Impact of Equatorial Ionospheric Irregularities on GPS Receiver Performance*, PhD Thesis, Department of Geomatics Engineering, University of Calgary, Canada, pp. 218 (Available at <http://plan.geomatics.ucalgary.ca>)

GPS ICD (2012) Navstar GPS Space Segment/Navigation User Interfaces, Interface Specification, IS-GPS-200G, Rev G, <http://www.gps.gov/technical/icwg/IS-GPS-200G.pdf>

GPS-702-GG (2010) High performance pinwheel® antenna, *Product Datasheet*, (Available at <http://www.novatel.com>)

GPS-703-GGG (2014) High performance pinwheel® triple-frequency antenna maximizes tracking capabilities, *Product Datasheet*, (Available at <http://www.novatel.com/assets/Documents/Papers/GPS-703-GGG.pdf>)

Groves, P., C. Mather and A. Macaulay (2007) "Demonstration of Non-coherent Deep INS/GPS Integration for Optimised Signal-to-noise Performance," ION GNSS 20th

International Technical Meeting of the Satellite Division, 25-28 September, Forth Worth, TX, pp. 2627 - 2638

Groves, P. D., H. Martin, K. Voutsis, D. Walter, and L. Wang (2013) "Context Detection, Categorization and Connectivity for Advanced Adaptive Integrated Navigation," *Proceedings of the Institute of Navigation GNSS+ 2013*, 16-20 September 2013, Nashville, TN, USA, 18 pages

Groves, P. D. (2008) *Principles of GNSS, Inertial, and Multisensor Integrated Navigation Systems*, Artech House, Boston, London.

Hanson, W. and T. Wickard (1989) "Acceleration sensitivity as a function of temperature," in *Frequency Control*, 1989., Proceedings of the 43rd Annual Symposium on, May-2 Jun, pp. 427–432

Haykin, S. (2001) *Communication Systems*, John Wiley & Sons, Inc., New York

Hopfield, H. S. (1969) "Two quartic tropospheric refractivity profile for correcting satellite data", *Journal of Geophysical Research*, Volume 74, No. 18, pp. 4487-4499

IT3200C (2014) *SMD Temperature Compensated Crystal Oscillators, datasheet*, Rakon, New Zealand (available at www.rakon.com)

Kamel, A. M. (2010) "Adaptive GPS Tracking Loop Bandwidth Tuning Using Fuzzy Control and Inertial Aiding for Missile Applications", in *Proceedings of the 7th ICEENG Conference, 25-27 May, 2010* (Available at <http://plan.geomatics.ucalgary.ca/>)

Kantola, M., M. Perttunen, T. Leppanen, J. Collin, and J. Rieki (2010) "Context Awareness for GPS-Enabled Phones", in *Proceedings of ION Technical Meeting*, Manassas, VA, USA, 25–27 January 2010, pp. 117–124

Kavanagh, J. J. and H. B. Menz (2008) " Accelerometry: A technique for quantifying movement patterns during walking," *North American Society of Gait and Clinical Movement Analysis, Gait & Posture*28 (2008) 1-15, 15 pages

Kay, S. M. (1993) *Fundamentals of Statistical Signal Processing, Volume I: Estimation Theory*, Prentice-Hall, Inc

Kay, S. M. (1998) *Fundamentals of Statistical Signal Processing, Volume II: Detection Theory*, Prentice-Hall, Inc, New Jersey

Klobuchar, J. A. (1996) "Ionospheric Effects on GPS," [Chapter 12] in *Global Positioning System: Theory and Applications*, volume I, B. Parkinson and J. J. Spilker, Jr., eds., American Institute of Aeronautics and Astronautics, Inc., Washington D.C., USA, pp.485-515

Kolpekwar, A., R.D. Blanton, and D. Woodilla (1998), "Failure Modes for Stiction in Surface-Micromachined MEMS," in *Proceedings of International Test Conference*, 18-23 October, Washington, DC, pp. 551- 556

Kwakkel, S. P. (2008) *Human lower limb kinematics using GPS/INS*, MSc Thesis, Department of Geomatics Engineering, University of Calgary, Canada (Available at <http://plan.geomatics.ucalgary.ca>)

Lachapelle, G. (2004) "GNSS Indoor Location Technologies," *Journal of Global Positioning Systems* (2004), Vol. 3, No. 1-2: 2-11, 11 pages (Available at <http://plan.geomatics.ucalgary.ca/>)

Ladetto, Q., V. Gabaglio, and B. Merminod, (2001) "Combining Gyroscopes, Magnetic Compass and GPS for Pedestrian Navigation", Banff, Canada, June 5-8, pp. 205-212

Lafortune, M. A. (1991) "Three-dimensional acceleration of the tibia during walking and running," *Journal of Biomechanics*, volume 24 (2000), No. 10, pp. 877-886

LCI (2014) *Tactical grade, low noise IMU datasheet*, Novatel, Canada (available at www.novatel.com)

Lee, K., T. Lee, and K. Song (2007) "A Study on the Tracking Loop Design for Weak Signal in High Dynamic Environment", *in proceedings of the 63rd annual meeting of The ION*, Cambridge MA, 23-25 April 2007, pp.589-594

Leeson, D. B. (1966) "A simple model of feedback oscillator noise spectrum," *IEEE Proceedings*, vol. 54, no. 2, Feb 1966, pp. 329–330

Lin, T, M. Abdizadeh, A. Broumandan, D. Wang, K. O'Keefe, and G. Lachapelle (2011) "Interference Suppression for High Precision Navigation Using Vector-Based GNSS software Receivers," *Proceedings of ION GNSS 2011*, Portland, OR, 20-23 September, The Institute of Navigation, pp. 372-383

Lin, T., C. O'Driscoll, and G. Lachapelle, (2011) "Development of a Context-Aware Vector-Based High-Sensitivity GNSS Software Receiver", *Proceedings of International Technical Meeting*, Session C4, San Diego, CA, pp. 1043-1055

Marrison, W. A. (1930) "The crystal clock," *National Academy of Sciences Proc.*, vol. 16, pp. 496–507, July 1930

Mezentsev, O., G. Lachapelle, and J. Collin, (2005) "Pedestrian Dead Reckoning - A Solution To Navigation In GPS Signal Degraded Areas?" *Journal of Geomatics*, Vol. 59, No. 2, 2005, pp.175-182

Milliren, B. T., D. W. Martin, and D. A. Emmons, (1988) "An acceleration compensated precision quartz oscillator," in Frequency Control, 1988., Proceedings of the 42nd Annual Symposium on, 1988, pp. 334– 341

Misra, P. and P. Enge (2011) *Global Positioning System - Signals, Measurements, and Performance*, Revised Second Edition, Ganga-Jamuna Press, P.O. Box 692, Lincoln, Massachusetts 01773

Moe-Nilssen, R. (1998) "Test-retest reliability of trunk accelerometry during standing and walking", *Archives of Physical Medicine and Rehabilitation*, volume 79, issue 11, November 1998, pp. 1377-1385

MORION (2012), *DOUBLE OVEN ULTRA PRECISION OCXO MV89*, Datasheet, Morion Inc

Muthuraman, K., D. Borio, R. Klukas, and G. Lachapelle (2010) "Adaptive Data/Pilot Carrier Phase Tracking for Modernized GNSS Signals", *Presented in ION ITM 2010*, Session C3, San Diego, CA, 25-27 January 2010, pp.736-749 (Available at <http://plan.geomatics.ucalgary.ca/>)

Nebel, M. and B. Lankl (2010) "Oscillator Phase Noise As A Limiting Factor In Stand-Alone GPS-Indoor Navigation," published in *Satellite Navigation Technologies and*

Niedermeier, H., B. Eissfeller, J. Winkel, T. Pany, B. Riedl, T. Wörz, R. Schweikert, S. Lagrasta, G. López-Risueño, and D. Jiménez-Baños (2010) "DINGPOS: High Sensitivity GNSS platform for deep indoor scenarios," 2010 International Conference on Indoor Positioning and Indoor Navigation (IPIN), 15-17 September 2010, Zürich, Switzerland, 10 pages, European Workshop on GNSS Signals and Signal Processing (NAVITEC), 2010 5th ESA Workshop on, 8 pages

O'Driscoll, C. (2007) *Performance Analysis of the Parallel Acquisition of Weak GPS Signals*, PhD Thesis, Department of Electrical and Electronic Engineering, National University of Ireland, Cork, Ireland

O'Driscoll, C., M.G. Petovello and G. Lachapelle (2008) "*Impact of Extended Coherent Integration Times on Weak Signal RTK in an Ultra-Tight Receiver*", Proceedings of NAV08 Conference, London, UK, Royal Institute of Navigation (Available at <http://plan.geomatics.ucalgary.ca/>)

O'Driscoll, C. and G. Lachapelle (2009) "Comparison of traditional and Kalman filter based tracking architecture," in *proceedings of the European Navigation Conference*, Naples Italy, May 2009 (Available at <http://plan.geomatics.ucalgary.ca/>)

O'Driscoll, C., M.G. Petovello, and G. Lachapelle (2011) "Choosing the coherent integration time for Kalman filter-based carrier-phase tracking of GNSS signals", *GPS Solutions*, vol. 15, issue. 4, October 2011, pp. 345-356.

Pany, T., J. Winkel, B. Riedl, M. Restle, T. Wörz, R. Schweikert, H. Niedermeier, G. Ameres, B. Eissfeller, S. Lagrasta, and G. López-Risueño (2009a) "Performance of a Partially Coherent Ultra-Tightly Coupled GNSS/INS Pedestrian Navigation System Enabling Coherent Integration Times of Several Seconds to Track GNSS Signals Down to 1.5 dBHz," Proceedings of the 22nd International Technical Meeting of The Satellite Division of the Institute of Navigation (ION GNSS 2009), 22-25 September, 2009, Savannah, GA, pp.919-934

Pany, T., B. Riedl, J. Winkel, T. Wörz, R. Schweikert, H. Niedermeier, S. Lagrasta, G. López-Risueño, D. Jiménez-Baños (2009b) *Coherent Integration Time: The Longer, the Better*, working papers, InsideGNSS, Nov-Dec 2009, pp.52-61

Papoulis, A. (1991) *Probability, Random Variables and Stochastic Processes*, McGraw Hill, New York

Parkinson, B. W. (1996) "Introduction and Heritage of NAVSTAR, the Global Positioning System," [Chapter 1] in *Global Positioning System: Theory and Applications*, volume I, B. Parkinson and J. J. Spilker, Jr., eds., American Institute of Aeronautics and Astronautics, Inc., Washington D.C., USA, pp.1-28

Pesyna, K. M., Jr., R. W. Heath, and T. E. Humphreys (2014) "Centimeter Positioning with a Smartphone-Quality GNSS Antenna," in *proceedings of ION GNSS+ 2014*, Tampa, FL, pp. 1568-1577

Peters, K and Kay, S. M. (2004) "Unbiased estimation of the phase of a sinusoid," in *Acoustics, Speech, and Signal Processing, Proceedings (ICASSP '04), IEEE International Conference on*, volume 2, 17-21 May 2004, pp.493-496

Petovello, M.G. and G. Lachapelle (2006) "Comparison of Vector-Based Software Receiver Implementations With Application to Ultra-Tight GPS/INS Integration", Proceedings of GNSS06 (Forth Worth, 26-29 Sep, Session C4), The Institute of Navigation.

Petovello, M.G., C. O'Driscoll and G. Lachapelle (2007) "Ultra-Tight GPS/INS for Carrier Phase Positioning In Weak-Signal Environments," *Proceedings of NATO RTO SET-104 Symposium on Military Capabilities Enabled by Advances in Navigation Sensors*, Antalya, Turkey, NATO 2007

Petovello, M.G., C. O'Driscoll, G. Lachapelle D. Borio, H. Murtaza (2008) "Architecture and Benefits of an Advanced GNSS Software Receiver," *Journal of Global Positioning Systems 2008*, volume 7, no. 2, pp 156-168

Petovello, M.G., C. O'Driscoll and G. Lachapelle (2008a) "Carrier Phase Tracking of Weak Signals Using Different Receiver Architectures," *Proceedings of ION National Technical Meeting*, San Diego, CA, Institute of Navigation, pp. 781-791

Petovello, M.G., C. O'Driscoll and G. Lachapelle (2008b) "Weak Signal Carrier Tracking Using Extended Coherent Integration with an Ultra-Tight GNSS/IMU Receiver," *Proceedings of European Navigation Conference*, Toulouse, France 2008

Proakis, J. G. and D. G. Manolakis (2001) *Digital Signal Processing*, 3rd edition, [Prentice Hall of India](#), Delhi, India, 2001

Propak-V3 (2011) Durable, High-Performance GNSS Enclosure Delivers Advanced Positioning Capabilities, *product datasheet*, Novatel Inc., Canada (Available at www.novatel.com)

Przyjemski, J. M. (1978) "Improvement in system performance using a crystal oscillator compensated for acceleration sensitivity," in 32nd Annual Symposium on Frequency Control, 1978, pp. 426–431

Psiaki, M.L. and H. Jung (2002) "Extended Kalman Filter Methods for Tracking Weak GPS Signals", *Proceedings of ION GPS 2002*, pp. 2539-2553.

Ray, J. K., M. E. Cannon, and P. C. Fenton (1999) "Mitigation of Static Carrier-Phase Multipath Effects Using Multiple Closely Spaced Antennas," *NAVIGATION, Journal of The Institute of Navigation*, Vol. 46, No. 3, Fall 1999, 193-201 (Available at <http://plan.geomatics.ucalgary.ca/>)

Ray, J. (2000) Mitigation of GPS Code and Carrier Phase Multipath Effects Using a Multi-Antenna System, PhD Thesis, published as UCGE Report No. 20136, Department of Geomatics Engineering, University of Calgary, Canada

Razavi, A., D. Gebre-Egziabher, and D. M. Akos (2008) "Carrier Loop Architectures for Tracking Weak GPS Signals," in *IEEE Transactions on Aerospace and Electronic Systems*, volume. 44, No. 2 April 2008, pp.697-710

Saastamoinen, J. (1973) "Contribution of the theory of atmospheric refraction," *Bulletin Géodésique*, No. 105, pp. 279-298, No. 106, pp. 383-397, No. 107, pp. 13-34

Saeedi, S., A. Moussa, and N. El-Sheimy (2014) "Context-Aware Personal Navigation Using Embedded Sensor Fusion in Smartphones", *Sensors*, vol. 14, pp 5742-5767

Salem, D. R., C. O'Driscoll, and G. Lachapelle (2012) "Methodology for comparing two carrier phase tracking techniques," *GPS Solutions* April 2012, Volume 16, Issue 2, pp 197-207 (Available at <http://plan.geomatics.ucalgary.ca/>)

Shrestha, S. M. (2003) Investigations into the Estimation of Tropospheric Delay and Wet Refractivity Using GPS Measurements, MSc Thesis, Department of Geomatics Engineering, University of Calgary, Canada (Available at <http://plan.geomatics.ucalgary.ca/>), pp. 38-50

Sokolova, N., D. Borio, and B. Forssell (2011) "Loop Filters with Controllable Doppler Jitter for Standard and High Sensitivity GNSS Receivers", in *Proceedings of the International Conference on Indoor Positioning and Indoor Navigation (IPIN)*, Portugal. (Available at http://ipin2011.dsi.uminho.pt/PDFs/Shortpaper/29_Short_Paper.pdf)

Spilker, J.J. Jr. and B. W. Parkinson (1996) "Overview of GPS Operation and Design," [Chapter 2] in *Global Positioning System: Theory and Applications*, volume I, B. Parkinson and J. J. Spilker, Jr., eds., American Institute of Aeronautics and Astronautics, Inc., Washington D.C., USA, pp.29-56.

Spilker, Jr., J. J., (1996a) "GPS Signal Structure and Theoretical Performance," [Chapter 3] in *Global Positioning System: Theory and Applications*, volume I, B. Parkinson and J. J. Spilker, Jr., eds., American Institute of Aeronautics and Astronautics, Inc., Washington D.C., USA, pp.57-120

Spilker, Jr., J. J., (1996b) "Fundamentals of Signal Tracking Theory," [Chapter 7] in *Global Positioning System: Theory and Applications*, volume I, B. Parkinson and J. J. Spilker, Jr., eds., American Institute of Aeronautics and Astronautics, Inc., Washington D.C., USA, pp. 245-327

Spilker, Jr., J. J., (1996c) "Tropospheric Effects on GPS," [Chapter 13] in *Global Positioning System: Theory and Applications*, volume I, B. Parkinson and J. J. Spilker, Jr., eds., American Institute of Aeronautics and Astronautics, Inc., Washington D.C., USA, pp.517-546

Susi, M. (2012) *Gait Analysis for Pedestrian Navigation Using MEMS Handheld Devices*, MSc Thesis, Department of Geomatics Engineering, University of Calgary, Canada, (Available at <http://plan.geomatics.ucalgary.ca>)

Susi, M., V. Renaudin, and G. Lachapelle (2011) "Detection of quasi-static instants from handheld MEMS devices," in *Proceedings of the International Conference on Indoor Positioning and Indoor Navigation (IPIN)*, Session 20, Guimarães, Portugal, 21-23 September 2011, p. 9 (Available at <http://plan.geomatics.ucalgary.ca>)

Sullivan, D. B., D.W. Allan, D.A. Howe, and F.L. Walls (1990) *Characterization of Clocks and Oscillators*, NIST Tech Note 1337

Svitek, R. and S. Raman (2005) *DC Offsets in Direct-Conversion Receivers: Characterization and Implications*, Application Note, IEEE Microwave Magazine, volume 6, issue 3, September 2005, pp. 76-86

Takeda, R., S. Tadano, M. Todoh, and S. Yoshinari (2009) "Human Gait Analysis using Wearable Sensors of Acceleration and Angular Velocity," 13th International Conference on Biomedical Engineering: ICBME, volume 42, issue 3, pp. 223-233

Tas, N., T. Sonnenberg, H. Jansen, R. Legtenberg, and M. Elwenspoek (1996), "Stiction in surface micromachining," in *Journal of Micromechanics and Microengineering*, Vol. 6, No. 4, pp. 385-397

Terrier, P., Q. Ladetto, B. Merminod, and Y. Schutz (2000) "High-precision satellite positioning system as a new tool to study the biomechanics of human locomotion," *Journal of Biomechanics volume 33 (2000)*, pp. 1717-1722

Teunissen, P. J. G. (1995) "The least-squares ambiguity decorrelation adjustment: a method for fast GPS integer ambiguity estimation," in *Journal of Geodesy*, Vol. 70, Issue 1-2, pp. 65-82

TSS-DL-HH-S (2012) 3-Space Sensor Data-Logging Miniature Attitude & Heading Reference System User Manual, YEI Technology 630 Second Street Portsmouth

u-blox (2014) *UBX-M8030-Kx-DR, product summary*,
[http://www.u-blox.com/images/downloads/Product_Docs/UBX-M8030-Kx-ADR_ProductSummary_\(UBX-13003445\).pdf](http://www.u-blox.com/images/downloads/Product_Docs/UBX-M8030-Kx-ADR_ProductSummary_(UBX-13003445).pdf), last accessed January 9, 2015

Voutsis, K., P. G. Groves, M. Holbrow, and C. Ford (2014) "The Importance of Human Motion for Simulation Testing of GNSS," in *Proceedings of the 27th International Technical Meeting of the Satellite Division of the Institute of Navigation*, 8-12 September, Tampa, FL, 14 pages

Wang, C., G. Lachapelle, and M. E. Cannon (2004) "Development of an Integrated Low-Cost GPS/Rate Gyro System for Attitude Determination," *The Journal of Navigation*, volume 57, pp.85-101

Wang, J. J. H, (2012) "Antennas for Global Navigation Satellite System (GNSS)," *Proceedings of the IEEE*, Vol. 100, No. 7, July 2012, pp 2349-2355

Ward, P. W., J. W. Betz and C. J. Hegarty (2006a) "Satellite Signal Acquisition, Tracking, and Data Demodulation," [Chapter 5] in *Understanding GPS: Principle and Applications*, E. D. Kaplan and C. J. Hegarty, eds., Second Edition, Norwood, MA, Artech House, p153-240

Ward, P. W., J. W. Betz and C. J. Hegarty (2006b) "Interference, Multipath, and Scintillation," [Chapter 6] in *Understanding GPS: Principle and Applications*, E. D. Kaplan and C. J. Hegarty, eds., Second Edition, Norwood, MA, Artech House, p243-299

Watson, R., G. Lachapelle, and R. Klukas (2006) "Testing Oscillator Stability as a Limiting Factor in Extreme High-Sensitivity GPS Applications", Proceedings of ENC-GNSS 2006, Manchester, UK. p. 20 (Available at <http://plan.geomatics.ucalgary.ca>)

Watson, R., M. Petovello, G. Lachapelle, and R. Klukas (2007) "Impact of Oscillator Errors on IMU-Aided GPS Tracking Loop Performance", Proceedings of ENC-GNSS 2007, Geneva, Switzerland, May 29-31, 2007, p. 15 (Available at <http://plan.geomatics.ucalgary.ca>)

Welch, P. (1967) "The use of fast Fourier transform for the estimation of power spectra: A method based on time averaging over short, modified periodograms"

Zaheri, M., A. Broumandan, V. Dehghanian, and G. Lachapelle (2012) "Detection Performance of Polarization and Spatial Diversities for Indoor GNSS Applications,"

Hindawi Publishing Corporation, International Journal of Antennas and Propagation,
Volume 2012, Article ID 879142, 10 pages (Available at
<http://plan.geomatics.ucalgary.ca>)